1-1-2015

Estimating Cold Nuclear Matter Effects Using Jets In P-Pb Collisions At √snn = 5.02 Tev With The Alice Detector

Christopher Ghanim Yaldo
Wayne State University,

ESTIMATING COLD NUCLEAR MATTER EFFECTS USING JETS IN p-Pb COLLISIONS AT $\sqrt{s_{NN}} = 5.02$ TeV WITH THE ALICE DETECTOR

by

CHRIS YALDO

DISSERTATION

Submitted to the Graduate School

of Wayne State University

in partial fulfillment of the requirements

for the degree of

DOCTOR OF PHILOSOPHY

2015

MAJOR: Physics

Approved by:

_____

Advisor Date

_____

_____

_____

TABLE OF CONTENTS

Chapter 1: Introduction **1**

Chapter 2: Theoretical Background **4**

2.1 The Fundemental Forces 4

2.2 The Standard Model 5

2.3 The Nuclear Force: Quantum Chromodynamics 7

2.4 The Quark Gluon Plasma 9

2.5 Jets: Calibrated Probes 11

2.6 Jet Energy Loss and Jet Tomography 13

2.7 The Nuclear Modification Factor 16

2.8 Cold Nuclear Matter 19

2.8.1 Nuclear Parton Distribution Functions 20

2.8.2 Color Glass Condensate 22

Chapter 3: Experimental Setup **25**

3.1 The Large Hadron Collider 25

3.2 The ALICE Detector 26

3.2.1 Time Projection Chamber (TPC) 28

3.2.2 Inner Tracking System (ITS) 30

3.2.3 VZERO 31

3.2.4 Zero Degree Calorimeter (ZDC) 32

3.2.5 EMCal 33

Chapter 4: Data Analysis and Selection Criteria **37**

4.1 Event Selection 39

4.2 Charged Particle Tracking 40

4.3 EMCal Clustering 45

4.4 Jet Selection 50

4.5 Underlying Event 54

4.5.1 Signal Removal Approach 54

4.5.2 Occupancy Median Approach 55

4.5.3 Scale Factor . . . 58
4.6 Background Fluctuations: δp_T . . . 59
4.7 Detector Response . . . 61
4.8 Unfolding . . . 69
4.8.1 Bayesian Approach . . . 71
4.8.2 Singular Value Decomposition (SVD) . . . 73
4.8.3 Jet Finding Efficiency . . . 75
4.8.4 Kinematic Efficiency . . . 75
Chapter 5: Minimum Bias Jet Results **77**
5.1 Normalization . . . 77
5.2 Unfolding the Jet Spectrum . . . 79
5.2.1 Unfolding Algorithm . . . 79
5.2.2 Unfolding Regularization . . . 79
5.2.3 Unfolding Ranges . . . 80
5.3 Statistical Uncertainties . . . 81
5.4 Systematic Uncertainties . . . 82
5.4.1 Regularization Strength . . . 83
5.4.2 Unfolding Method . . . 88
5.4.3 Unfolding Prior . . . 88
5.4.4 Unfolding p_T Range . . . 88
5.4.5 Tracking Efficiency Uncertainty . . . 89
5.4.6 Hadronic Correction . . . 90
5.4.7 Underlying Event Subtraction (UE) . . . 90
5.4.8 Background Fluctuations (δp_T) . . . 91
5.4.9 Unfolding Response for Different Run Periods . . . 92
5.4.10 Scale Factor . . . 93
5.5 Nuclear Modification Factor for Jets . . . 93
5.5.1 pp Reference Spectrum . . . 93
5.5.2 R_{pPb}^{PYTHIA} . . . 95
5.5.3 Comparison of R_{pPb} to other LHC experiments . . . 97
5.6 Jet Structure Ratio . . . 98
Chapter 6: Centrality Dependent Jet Results **102**
6.1 Centrality in p-Pb Collisions . . . 102
6.2 Centrality Dependent Observables . . . 106
6.2.1 Centrality Dependent Jet Spectra . . . 106

6.2.2 R_{CP} 107
Chapter 7: Conclusions **113**
Appendices **115**
Chapter A: Relativistic Kinematics **116**
Chapter B: Jet Algorithms **118**
Chapter C: Centrality Estimation in p-Pb Collisions **122**
Chapter D: Centrality Integrated Jet Systematics (Cross-Section & R_{pPb}^{PYTHIA}) **125**
Chapter E: Jet Structure Ratio $\frac{R=0.2}{R=0.4}$ Systematics **128**
Chapter F: Centrality Dependent Jet Systematics **134**
F.1 0-20% Jet Cross Section Systematics 134
F.2 40-90% Jet Cross Section Systematics 141
Chapter G: R_{CP} Systematics **148**
Bibliography **155**
Abstract **161**
Autobiographical Statement **162**

CHAPTER 1

Introduction

Most if not all cosmological models assert that the universe started out as a point of infinitesimal size and infinite density. Then there was an event, *The Big Bang*, that resulted in the universe rapidly expanding, causing the matter to become less dense and to cool. Of interest to physicists are the properties of this matter and what laws govern its dynamics.

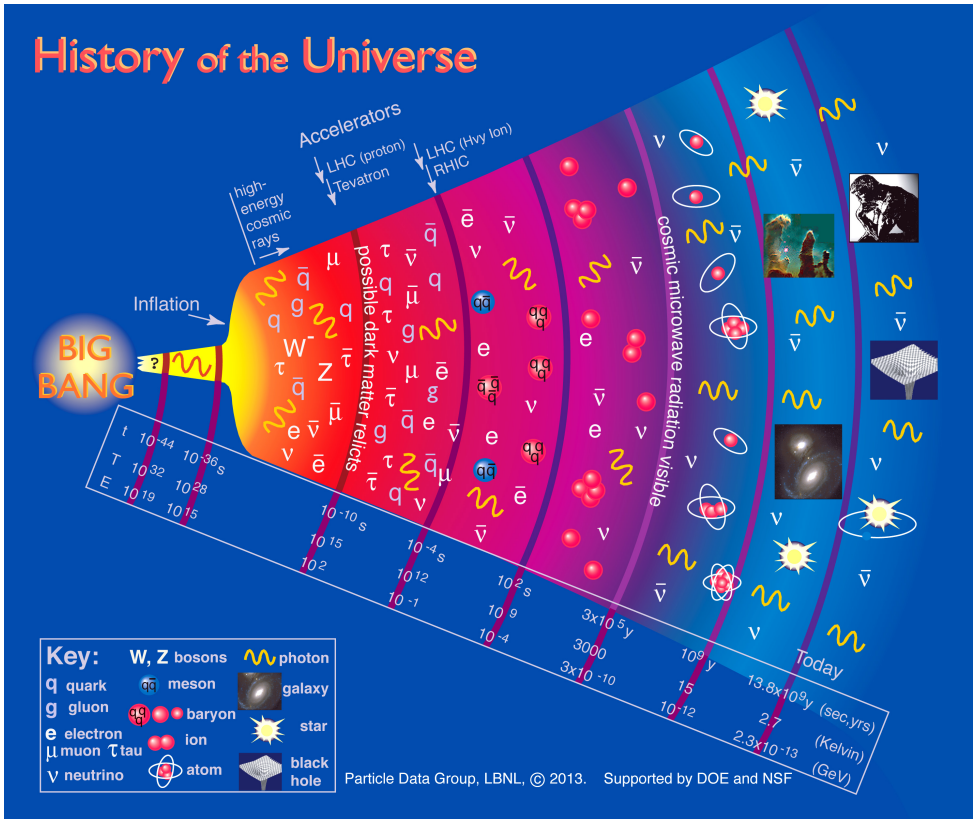

Figure 1.1: Particle Data Group chart of the history of the universe.

As can be seen from figure 1.1, different epochs of the universe have different temperatures and densities. This leads to quasi-equilibrium states being reached in which particles could be formed in pairs due to background energy fluctuations, exist for a certain period of time, and then annihilate back into energy. This procedure would continue until either the temperature or density became insufficient to allow further particle pair creation. As a result, when the universe would transition from one epoch to another, the reduced temperature and density would cause various aspects of those laws to be dominant when compared to other factors.

Of paramount importance would be a complete understanding of the fundamental physical laws which govern all epochs of the universe; from its state of near infinite density and infinitesimal size, to the present day and perhaps even its death (if it has one). Such a theory, referred to as a *Grand Unification Theory* (GUT) would allow an understanding of the properties of matter and the laws that govern it at times before $\sim 10^{-43}$s after the Big Bang. At times before this, all quantities of interest (length, energy, density, temperature, ect.) were on the order of the Plank scale ($\sim 10^{19}$ GeV); at such extremes, the current formalism of Quantum Chromodynamics (QCD) and General Relativity breakdown. A more complete theory of Quantum Gravity is needed to explain the dynamics before this time.

As the universe expended, it cooled until the universe reached an epoch where QCD plays a dominanting role in particle dynamics which occured at roughly $\sim 10^{-12}$s after the Big Bang and lasts for $\sim 1\mu$s. During this epoch, the temperature of the universe was extremely hot, orders of magnitude hotter then the center of the sun (T$\sim$ 1 KeV $\sim 10^7$ °K). so that partons (quarks and gluons) were too energetic (T$\sim$ 1 GeV $\sim 10^{13}$ °K) to hadronize (to form *hadrons*); the process by which a group of partons coalesce together to form either *mesons* (a quark and anti-quark along with gluons) or *baryons* (a group of either three quarks or three anti-quark along with gluons). Instead, they existed in a hot and dense de-confined partonic QCD matter that is referred to as a *Quark-Gluon Plasma* (QGP).

QCD predicts many properties for this state of matter that can be tested utilizing heavy-ion collisions. In particular, one of these predictions is that any parton traversing a QGP should suffer energy loss via scattering processes (the QCD equivalent of bremsstrahlung). In an attempt to produce systems where a QGP might be formed, accelerators collide heavy nuclei (e.g. gold or lead) with each other at the highest energies possible. In essence, the conditions that existed during the QCD epoch of the Big Bang are reporoduced. These collisions can be thought of as producing "little bangs". Mea-

surements performed on these systems are then compared to the same measurement of a system where it is suspected that a QGP was not formed (e.g. a proton-proton [pp] collision) to see what modification(s) occured in the heavy-ion collisions. These modifications are attributed to the QGP formation. In order to unambiguously show that such energy loss is due to the QGP, the effect of the presence of the nucleus referred to as so-called *Cold Nuclear Matter* effects (CNM) must be measured.

In order to discriminate between cold nuclear matter effects and those of the QGP, it is desirable to have a collisional system in which cold nuclear matter effects are present without producing a QGP. Then, using all three collisional systems, knowledge regarding QCD matter under extreme conditions can be derived in a coherent manor. This is the main motivation for proton-lead collisions (p-Pb), as it is expected that p-Pb collisions lack the energy density to produce a QGP while at the same time modifications of p-Pb collisions to pp collisions are expected to be dominated by CNM effects. Presented in this thesis are the first results from full jet measurements: the jet spectra, jet structure ratio, and nuclear modification factor in p-Pb collisions using the ALICE detector.

CHAPTER 2

Theoretical Background

2.1 The Fundemental Forces

In nature, there are four fundemental forces which govern the dynamics of particles. All physical bodies are attracted to each other by the force of *Gravity*. The proportionality of this intereaction is referred to as mass. Mass comes in a single "polarity" in that all objects that have been observed that have mass have "positive" mass. Thus, there is no shielding of the gravitational force and as a consequence it is the dominant force over astronomical distances. However, over short ranges, the magnitude of this force is extremely small when compared to the other forces and therefore its impact on sub-atomic particles is negligible.

Another force of nature is the *Electromagnetic* force. All particles which have an electric charge interact with each other through this force. Electric charge comes in two polarities, positive and negative. They are opposite to one another and objects that contain equal amounts of these charges are neutral and are not subjected to the electromagnetic force. It is observed in nature that there is an equal amount of positive and negetive electric charge and that macroscopic objects tend to be electrically neutral. As a consequence, although the electromagnetic force acts over all distances, because objects (in particular, atoms) tend to be electrically neutral, the force is not dominant over long ranges.

The other two forces are referred to as the *Nuclear* force because their effects are mostly felt on nuclear scales (< 1 fermi $= 10^{-15}$ m). They are divided into the *Weak* and *Strong* nuclear forces. The weak nuclear force is responsible for radioactive decay which causes particles to "transform" into other particles. The strong nuclear force

is responsible for the dynamics of the constituents of subatomic nuclei (protons and neutrons, among others). The theoretical description of the the nuclear forces, along with the electromagnetic force is referred to as the *Standard Model* and is explained in detail in the next section.

2.2 The Standard Model

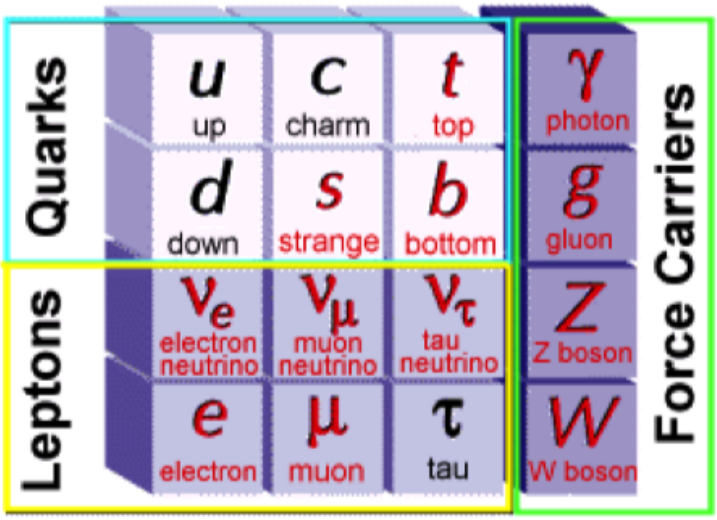

Figure 2.1: A chart organizing the various elementary particles in the Standard Model into groups. Columns are refered to as *generations* with the lightest (i.e. least massive) particles being the left most. The last column (Force Carriers) are the subatomic particles responsible for mediating the fundemental forces of nature (except graviation, which isn't included in the standard model).

Figure 2.1 shows the various families (quarks being one family, leptons a second, along with their respective force carriers a third) of elementary particles grouped together in so-called *generations* (the members in the same column). Collectively, the laws that govern the dynamics of these three families of particles is what is called the *Standard Model*. The significance of structuring these particles into generations is that each generation (starting with the first column to the left) becomes significantly more massive and as a result, less stable (with the exception of neutrinos, which do not decay). Particles in the first column (the up and down quarks along with the electron and electron neutrino) are stable, i.e. they have not been observed in nature to decay into other particles. All matter is either composed of leptons or hadrons (baryons or mesons). Because leptons and hadrons have mass, they are all subject to gravitational interactions. However, due to their small masses and the weak gravitational coupling

constant G, the gravitational interaction is several orders of magnitude smaller than the other interaction and is thus, in the context of particle physics negligible.

Leptons can interact via the electromagnetic and weak nuclear force. These interactions are mediated by photons, $W^{\pm}$, and Z bosons, which are collectively referred to as *Gauge Bosons*. These gauge bosons are not self-interacting, because they do not carry the "charge" of their force (e.g. photons carry no electric charge), but may contain the "charge" of other forces. The unified theory that describes these two forces is referred to as the *Electroweak Force*. Any lepton that contains electric charge is subjected to an electromagnetic interaction (which is a part of the electroweak interaction) plus weak interactions, whereas neutral particles are only subjected to the weak interaction. Furthermore, due to the fact that the photon has no mass, the range of the electromagnetic interaction is infinite. The large masses of the $W^{\pm}$, and Z bosons cause the weak interaction to have a limited range. None of the leptons in figure 2.1 have been observed to have constituent structure.

Particle	**Symbol**	**QCD Mass (MeV)**	**Charge (e)**	**Anti-Particle**
Up	u	5	2/3	$\bar{u}$
Down	d	10	-1/3	$\bar{d}$
Strange	s	~ 200	-1/3	$\bar{s}$
Charm	c	~ 1500	2/3	$\bar{c}$
Bottom	b	~ 4500	-1/3	$\bar{b}$
Top	t	~ 170000	2/3	$\bar{t}$

Table 2.1: General properties of quarks.

Unlike leptons, hadrons have sub-structure and are composed of particles that are collectively referred to as partons. The principal partons that comprises hadrons are referred to as *quarks*. There are six quarks: up, down, strange, charm, bottom, and top. Furthermore for each exists a corresponding anti-particle referred to as an *anti-quark*. Since all quarks are fermions, they have an intrinsic angular momentum (spin) of 1/2. The general properties of quarks are summarized in table 2.1.

Quarks contain an electric charge and are subjected to electroweak interactions. Additionally, their dynamics are also governed by the strong nuclear force. The particle that mediates the strong force is called the *gluon*. It is these gluons along with the quarks that are the partons hadrons are composed of. Like the photon, the gluon has no mass. However, it can interact with itself. This is in contrast to the mediator particles of the electroweak interaction, which cannot self-interact. This is because the gluons carry

the "charge" of its governing force, whereas the electroweak particles do not carry the charge of its governing forces (although the $W^{\pm}$ has charge, it should be noted that this is electric charge and not weak charge, and this boson facilities the weak force, not the electromagnetic). We call this "charge" for the strong force "color". Color comes in three flavors (polarities): "red", "green", and "blue" along with their respective anti-colors. For quarks, they contain only one color (e.g. a red up quark, an anti-blue anti-strange quark, ect.). For gluons, they contain one out of the eight combinations of a color and an anti-color pairs in accordance to the SU(3) color group model [2] (table 2.2).

$(r\bar{b} + b\bar{r})/\sqrt{2}$	$i(r\bar{b} - b\bar{r})/\sqrt{2}$
$(r\bar{g} + g\bar{r})/\sqrt{2}$	$i(r\bar{g} - g\bar{r})/\sqrt{2}$
$(b\bar{g} + g\bar{b})/\sqrt{2}$	$i(b\bar{g} - g\bar{b})/\sqrt{2}$
$(r\bar{r} - b\bar{b})/\sqrt{2}$	$(r\bar{r} + b\bar{b} - 2g\bar{g})/\sqrt{6}$

Table 2.2: The SU(3) color group model.

2.3 The Nuclear Force: Quantum Chromodynamics

The mathematical description of the strong force is *Quantum Chromodynamics* (QCD). An observed feature ot QCD is that all hadrons observed thus far are colorless. This means that the color sum within a hadron adds to zero. Another consequence of QCD is that the quark number (all quarks have a quark number of 1/3 and anti-quarks have a quark number of -1/3 by definition) within a hadron must be an integral value (,-1,0,1,).

Hadrons form two groups: the first being a quark and an anti-quark which is called a *meson*, while the other being a "bag" of three quarks or anti-quarks which is called a *baryon*. This description is what is referred to as the *MIT Bag model* [3] or just *bag model*. It is a phenomenological model in which the partons (quarks and gluons) are treated as quanta of a field. Particles (hadrons) are created in this field via creation and annihilation operators that act on this field. When there is an excitation of this field, a hadron is created and likewise, when there is a de-excitation of the field a hadron can be annihilated. Thus, this field can be thought of as existing throughout all space, but the degrees of freedom (partons) exist only in local disruptions (within the hadron) of this field. To that end, it makes no sense to talk about these degrees of freedom

existing outside these disruptions. Within the bag, the partons are free to move around because the force between them is weak (asymptotic freedom); however these partons are confined within these particle structures (bags).

QCD has two remarkable properties that set it apart from Quantum Electrodynamics (QED) [5]. The first property is *asymptotic freedom*. This property basically states that at very large momenta or short distances, the QCD coupling constant is small and calculations can be done using perturbation theory. This arises from anti-shielding of color charge (which is opposite to that of QED, where the two flavors of charge, positive and negative, effectively shield one from another). The mathematical description of asymptotic freedom is referred to as *perturbative QCD* (pQCD).

The second property is *confinement*, in that quarks and gluons are effectively trapped within hadrons. Mathematically, this is accomplished by a strong, non-linear coupling constant (see figure 2.2). To paint an analogy, imagine that two balls (quarks) are attached by a rubber band (gluon). If the distance between the two balls increases, the rubber band exerts a larger and larger restoring force that causes the balls to return to their original displacement.

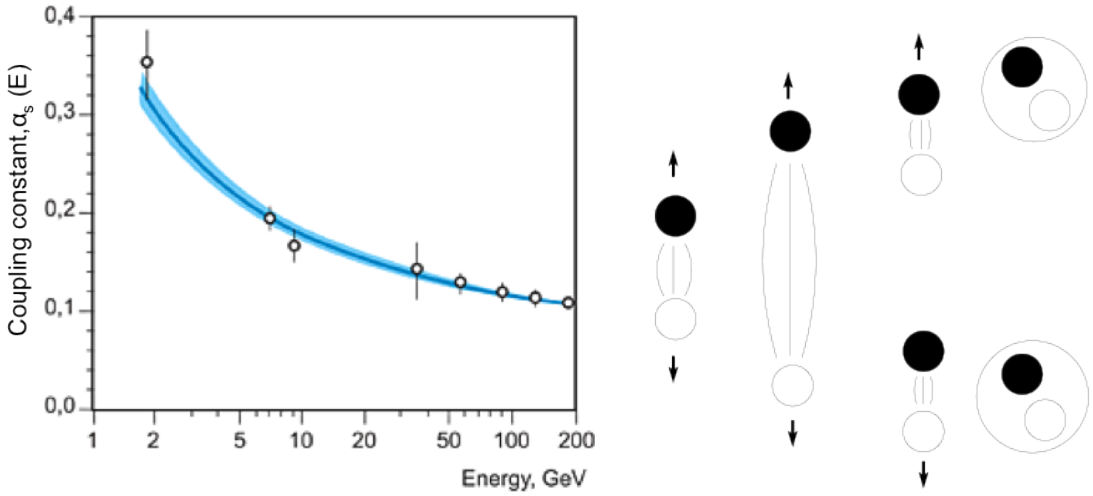

Figure 2.2: Left: The value of the "Running Coupling Constant" vs Energy showing asymptotic freedom in QCD [4]. Right: A pictorial representation of quark anti-quark pair production from sea quarks.

Present within hadrons are valence quarks, which are the quarks that effectively make up the hadron. When the distance between two quarks increases, their potential

energy increases which results in an increase in these energy fluctuations. At some separation distance between the quarks, it becomes energetically favorable to form a quark anti-quark pair between the original pair (see figure **??**). This quark anti-quark pair was created from the vacuum and these quarks are referred to as "virtual" quarks (or "sea" quarks), which essentially only exists within the hadron. These "virtual" quarks also have color and interact with the valence quarks. The system now has an additional quark and an anti-quark. This leads to the system containing four quarks, which QCD predicts is not stable and decays to a less energetic state, of two hadrons. It is akin to taking a magnet and trying to cut it in half in an attempt to isolate the north and south poles, but the net result is two separate magnets each with a north and south pole. This effectively means that a quark or gluon cannot exist in free space, and to date, no experiment has detected a "free" quark or gluon.

2.4 The Quark Gluon Plasma

What occurs when QCD matter is compressed and/or equivalently is heated? Does confinement still exist? A Heavy Ion Collision (HIC), either gold-gold (Au-Au) or lead-lead (Pb-Pb), can produce a system in which the density is much higher than that in normal nuclear matter. These HICs can be very energetic, producing a mean energy density in excess of $1\text{GeV}/\text{fm}^3$. With energy densities so high, lattice QCD calculations predict that a phase transition should occur (see figure 2.3). Such systems would be "weakly" confined, meaning the partons can interact with each other almost as if they were not confined at all. In other words, the coupling constant in this dense system is such that the interaction scale is much larger than the nucleon scale. Such a system is called a *Quark-Gluon Plasma* (QGP). This system is theorized to have occured early in the universe, about 1μs after the Big Bang and can be created and studied in colliders.

This system can be viewed as an entirely new "state" of matter. This is analogous to ice; when it is heated, it melts and becomes liquid water. Although chemically identical, they have different physical properties (viscosity, speed of sound, ect.). One of the principal goals of this research is to have a better understanding of the quantitative properties of this state of matter. Ultimately by creating this state, one learns about the dynamics of the universe during the quark dominated epoch. Furthermore, because this state highlights the interaction between partons, knowledge regarding the strong force can also be gained. Also, by creating this de-confined system of partons, a better understanding of confinement (which currently is not fully understood) can be

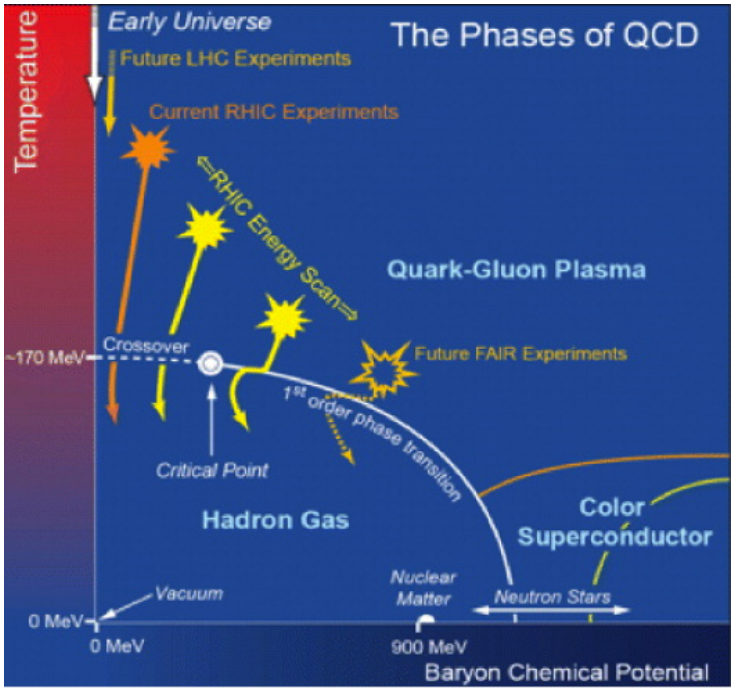

Figure 2.3: Phase diagram of QCD matter [6].

derived. Given that the QCD mass of quarks that make up hadrons are much smaller then the hadron's mass (e.g. the proton which is composed of two up quarks and a down quark has a mass of ~ 938 MeV/c whereas the QCD mass from the quarks is only 15 MeV/c), this implies that most of the mass-energy in the hadron is due to QCD confinement. Hence a more complete understanding of confinement is also a more complete understanding of where most of the mass of hadrons originates from

To study QCD matter under these extreme conditions and/or to detect the existence of the QGP, conditions similar to those that existed early in the universe must be replicated in a controlled fashion. These conditions can be produced at large colliders using heavy-ion collisions. The first attempt to create a QGP was done at The European Organization of Nuclear Research (CERN) using the Super Proton Synchrotron (SPS) in the 1980s. Progress continued at Brookhaven National Laboratory to produce this phase of matter and the first experimental signatures of its existence were detected at the Relativistic Heavy Ion Collider (RHIC) in 2000 [7].

The first unambiguous signatures of a QGP were produced at RHIC in Au-Au collisions. One of the signatures was that the mean energy density (measured at about 5 GeV/fm^3) of the HIC greatly exceed the theoretical value of 1 GeV/fm^3 needed to form a QGP. Furthermore, there was an observed collective behavior of partons in these collisions that can be quantified as harmonic coefficients of their dispersive behavior,

which is referred to as flow (v_n). The first of these harmonic terms v_1, is referred to as directed flow. The second term v_2 is referred to as elliptic flow. Of crucial importance is that from the STAR experiment [8], v_2 has large values approaching the hydrodynamic limit, indicating that the system reaches equilibrium quickly. Subsequent model calculations showed that if such an azimuthal momentum anisotropy is reached, it indicates that the medium is strongly interacting, which is yet another requirement of a QGP. The STAR experiment also found the universal nature of v_2 normalized to the number of quarks in the constituent hadron to scale with the hadrons transverse momentum p_T (see appendix A for defination of p_T). This means that it is not the hadrons that are "flowing" but rather the constituent particles (quarks), which are "flowing". The QGP has also been called the "Perfect Liquid", in that it has extremely low sheer stress, heat conduction, and viscosity [9].

2.5 Jets: Calibrated Probes

In principal there are two ways to study the QGP. As outlined in the previous section, the properties of the system can be studied by analyzing the "bulk" behavior of the system (i.e. flow). Another way of studying the properties of the system is done via scattering experiments; where a probe whose properties are well known can be incidented on the system and the subsequent kinematics (angles, energy, momentum, ect.) of the probe can be observed/measured after the scattering. Such experiments in particle physics are generally referred to as *Rutherford Scatterings* and led to the discovery of the atomic nucleus. These experiments were highly successful at studying the properties of the atomic nucleus because the probes were well callibrated (the properties of the incident alpha particles were well known), and the nucleus was in the same state before and after the probes were incidented on the nucleus (i.e. it didn't fragment or dissipate).

One can estimate how long a QGP phase exists. Assuming that all partons in the collision cannot go faster than the speed of light, and that the system dissipates once the distance between the partons is greater than that of the strong force ($\sim$1 fm), the time scale is $\sim 10^{-23}$ seconds. This brings up an interesting question: How does one study such a system that exists on a time scale several orders of magnitude less than our fastest probing techniques? Externally calibrated probes, those that were used to study the atomic nucleus, can't be produced quickly enough to be incidented on the system. Fortunately, heavy-ion collisions contain internal probes; when the QGP

phase is produced, sometimes collisions between the constituent partons are energetic enough to produce a "spray" of highly collimated hadrons which are visable in a detector. This spray of hadrons is referred to as a *jet*. Although rare, jets serve as an important tool for probing the QCD medium.

The production rates and transverse momentum distributions of primary hard scattered partons can be calculated from first principles. The reason for this is that a jet is produced from a partonic interaction which involves a large transverse momentum (p_T) and energy (Q^2) transfer. In these collisions, the coupling constant is small (see figure 2.2) and pQCD can be used to calculate the necessary kinematics and rates of the reaction. It is important to note that because the kinematics of these probes are calculable from pQCD, they are thus calibrated which is a requirement for any scattering experiment. The jet production cross section can be calculated using pQCD and is written as:

$$d\sigma_{AB}^{hard} = PDF \otimes \sigma_{pQCD} \tag{2.1}$$

where σ_{AB}^{hard} is the jet production cross section from a hard scattering of two partons (A and B), σ_{pQCD} is the cross section for a parton from pQCD, and PDF is the *Parton Distribution Function* of the colliding nuclei (i.e protons for pp collisions or a proton or neutron within a nuclei in HIC). In many experiments, single hadrons are experimental easier to measure and are used as a proxy for jets. This leads to complications in that additional factors to the jet production cross section that takes into account the production of hadrons must be accounted for. These additional factors are referred to as the *Fragmentation Function* (FF). Thus, what is really measured with single hadrons is not the inclusive jet cross section, rather the production cross section of single hadrons: the transverse momentum spectrum of hadrons given a jet p_T [13]. Schematically, it differs from 2.1 and looks like:

$$d\sigma_{AB\to h}^{hard} = f_{a/A}(x_1, Q^2) \otimes f_{b/B}(x_2, Q^2) \otimes d\sigma_{ab\to c}^{hard}(x_1, x_2, Q^2) \otimes D_{c\to h}(z, Q^2) \tag{2.2}$$

Where $f(x, Q^2)$ is the PDF and $D_{c\to h}(z, Q^2)$ is the FF. "Universality" is also assumed when calculating these cross-sections in that the PDFs and FFs measured in e^-e^+ and e^--p collisions can be used in pp collisions. The calculation of this production cross section is also further complicated by geometric effects in the presents of partonic en-

ergy losses [14].

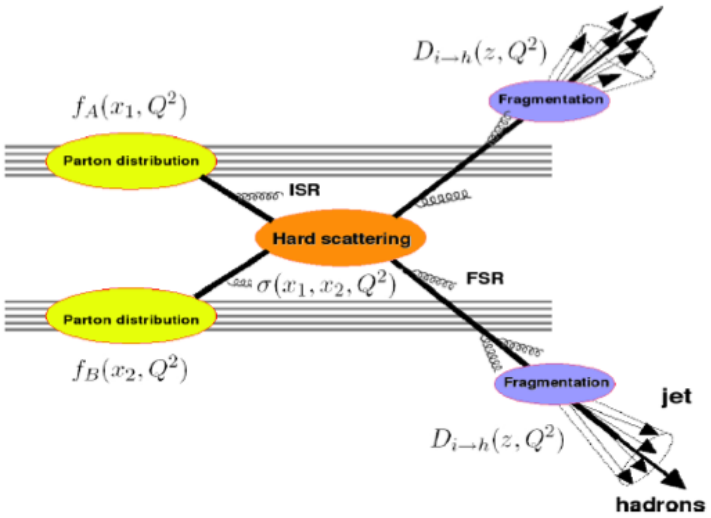

Figure 2.4: Pictorial representation of calculating a Production Cross Section [13].

One of the properties of QCD that seems to hold in practice is factorization, which allows the hadronic jet cross section to be broken up into three factors (see 2.2). That means that each piece of this formula is independent. When all three separate parts are convoluted, the cross section can be obtained. Although pQCD can be used to calculate the cross section of partons, the PDFs and FFs cannot be obtained from first principals and must be obtained from measurement. What is desired is the inclusive jet cross section, which would allow a direct comparison of a theoretical model of partonic energy loss to measured data. This is due to the fact that the inclusive jet cross section is related to the parton kinematics, which is needed to preform calculations from first principals and are not complicated by hadronization. All of these factors along with an excellent agreement with theoretical calculations (see figure 2.5) allow a jet to be used as a calibrated probe of the QGP medium.

2.6 Jet Energy Loss and Jet Tomography

All experiments at RHIC showed a suprpression of high p_T single hadrons from Au-Au collisions when compared to pp collisions [20]. This was the final conclusive piece of evidence that the QGP had been observed at RHIC. However, single hadrons are a proxy for jets and as such their measurements are not as strongly correlated to the parton kinematic of the initial hard scattering as jets are. Thus, a measurement of jet

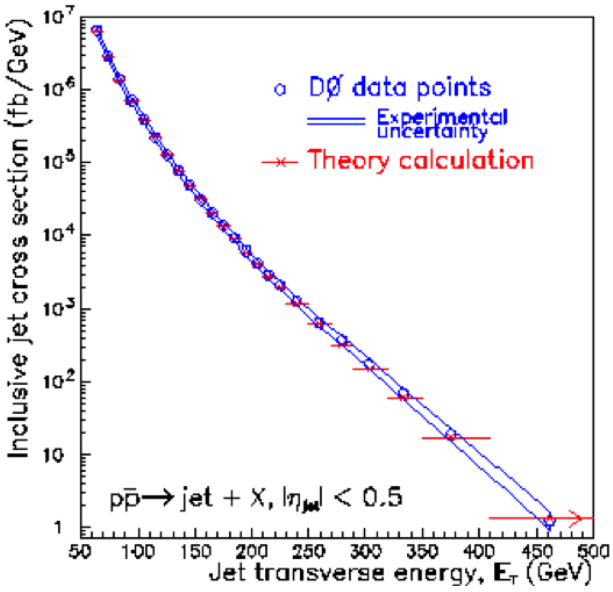

Figure 2.5: The inclusive jet cross section vs transverse energy in pp collisions at mid-pseudorapidity [10].

suppression in heavy-ion collisions relative to pp collisions would be more sensitive to "hot" nuclear effects then single hadrons.

As previously mentioned, the formation time and subsequent evolutions of the system is so short, that no externally produced probe is able to acquire any information about this system. As such, jets and their modification relative to pp collisions provide an excellent tool to study the properties of this medium. For example, the longitudinal redistribution of hadron energy within the jet in Pb-Pb collisions is sensitive to the color charge density of the medium as well as the primary parton dE/dx in the de-confined medium. Alternatively, the modification of the transverse shape of the jet, i.e. the energy distribution transverse to the jet axis, is sensitive to possible multiple soft interactions with the medium in analogy with the multiple scattering of electric charges in QED.

The theoretical interpretation of in medium jet propagation is expected to approximately factorize into jet production in elementary parton-parton collisions and jet propagation modified in medium. The modification in medium is expected due to the constituents of the jet being colored objects. Parton-parton interaction can also produce photons (i.e. photon-jet interactions [11]) which do not interact via the strong force and hence they should not be modified in a QGP. The modification in medium, including the possible modification of the "cold" medium, is one of the primary focuses of this thesis and is likely to be highly non-perturbative.

To further disentangle medium effects, it is important that events can be selected according to the impact parameter (the distance between the centers of the nuclei that are colliding) in HICs via a centrality measurement of the collision. Because this impact parameter cannot be measured directly in experiment, some other method such as the produced particle multiplicity in the collision must be used to infer the impact paramter along with some model calculations to correlate this particle multiplicity with the geometery of the collision (see appendix C for more details). From such studies, the in medium path length of the jet (the distance the jet traverses while in the medium) can modify the jet signal and this modification should be a function of the average path length.

This idea is analogous to studying energy loss of charged particles in a QED plasma in order to deduce properties of the Bethe-Bloch formula and the underlying energy loss mechanisms. While a jet traverses the partonic QCD medium, it can suffer significant energy loss. This energy loss is generally referred to as *Jet Quenching* [15, 16]. Mechanisms contributing to the energy loss in jet quenching include (elastic) scattering, which dominates in the QED case; and gluon radiation or *Gluon Bremsstrahlung* [17], which is expected to dominate the QCD case. The process of gluon bremsstrahlung is caused by multiple soft partonic scattering of the initial hard scattering partons and is expected to be enhanced by the medium. For high Q^2 scatterings, as the initial hard scattered parton that traverse the medium, they suffer energy loss which can be characterized via a time integrated parameter of the medium that is referred to as $\hat{q}$. This radiative energy loss can be thought of as arrising from Landau damping of soft modes in the QGP [18].

Once the jet is reconstructed from hadrons (measured in the detectors) produced from the partons involved in the hard scattering, the effect of this gluon radiation is that the energy and momentum is "diffused" over a large region. Some of these hadrons that were formed early on from gluon emmission of the hard scattering may not be reconstructed in the jet if the jet resolution parameter (or jet radius) is not sufficiently large. This is then interpreted as energy loss of the jet in medium.

This radiative energy loss mechanism causes the FF with respect to pp collisions to broaden and soften (a lower avegare transverse momentum per hadron). This effectively reduces the energy of the original parton in a similar fashion to electrons emitting x-rays when they de-accelerate around a nucleus. As bremsstrahlung radiation causes the electron spectrum to be broadened and soften, a similar effect is expected to be observed in jets, which will be measured and compared to existing theories. An-

other description of energy loss is the AdS/CFT model [19] which states that once a jet interacts with its medium it is completely absorbed by the medium. Quantitative measurements of how the jet signal is broadened and softened will help distinguish which theory of jet quenching is appropriate. This information will reveal a deeper and more quantitative understanding about QCD matter under extreme conditions. The is what is referred to as *Jet Tomography*. Ultimately what a jet provides is a calibrated probe (the production of the jet occurs before the medium is formed, hence the jet production is independent of the medium it is produced in) that can be used to "visualize" the time evolution of the QCD matter. This is very similar to how a radio-isotope injected into a patient can be used to visualize the morphology and physiology of an organ being imaged through a PET scanner.

To summarize, what makes jets useful are:

1. Using pQCD, jets can be calibrated by calculating their inclusive cross sections in e^-e^+ and pp collisions (figure 2.4), and show an excellent agreement between theoretical calculations and measurement for the inclusive cross section (figure 2.5) along with other jet observables.

2. Studying jets is the closest way of studying the kinematics of the initially hard scattered partons. It is less complicated by fragmentation in the way that single hadrons are.

3. Using the Nuclear Modification Factor (figures 2.6 - 2.8), an objective formalism of comparing the production of various particles in two different systems can be achieved to study the properties of these systems.

2.7 The Nuclear Modification Factor

If partons lose energy in the medium than QCD predicts that high p_T partons should experience energy loss as they traverse the QGP causing the production of high p_T hadrons to be suppressed. To verify this, an observable is needed to compare this energy loss in a system where there is a QGP believed to exist to a system where a QGP is not believed to exist. The so-called *Nuclear Modification Factor* R_{AA} defined as:

$$R_{AA} = \frac{\frac{dN^{AA}}{dp_T}}{\langle N_{coll} \rangle \frac{dN^{pp}}{dp_T}} \tag{2.3}$$

is such an observable, in that it compares the production cross section of particles produced in an "A-A" system (could be a heavy-ion collisions like Pb-Pb, or p-Pb collisions) to the production of the same particles in pp collisions. By measuring R_{AA} in different collisional systems, different effects (hot and cold nuclear matter effects) can be studied.

Perturbative QCD predicts that the production cross section should scale with the number of binary collisions. The *Glauber Model* [12] treats a HIC as a superposition of N_{coll} pp collisions (see appendix C). Although the production cross section scales with N_{bin}, the energy loss of particles as they traverse the medium depends on whether the object is colored or not. If a suppression of colored particles to non-colored particles is observed, then that is an indication that a QGP is formed.

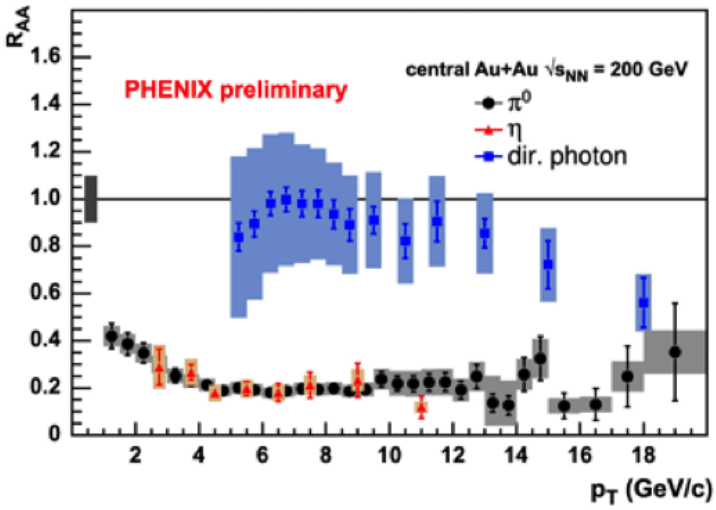

Figure 2.6: Nuclear Modification Factor R_{AA} for π^0, η, and photons in Au-Au collisions [20].

From figure 2.6, non-colored objects (such as direct photons which originate from hard processes [mainly Compton Scattering] within the QGP) do not interact strongly with the medium. This is evident by R_{AA} close to unity indicating that regardless of the path length that the photon traverses through the colored medium, its signal is not modified. However, when the R_{AA} for π^0 and η mesons are measured, it deviates significantly from unity. This is because these hadrons are produced from colored partons (quarks and gluons) that were either the initial hard scatterings in the collision, or the fragements of the initial hard scattering. These partons interact strongly with the medium as they traverse it, eventually hadronizing. For all hadrons, including heavy flavor (hadrons containing charm or bottom quraks), a strong suppression has been

observed [21]. This observed suppression is a consequence of the partons having color charge and can be interpreted as energy loss. Likewise it should be expected that if a colored object traverses a medium that either is not very dense or the path length it traverses is small, its net interaction should be small and thus the R_{AA} measurement should be closer to unity [22].

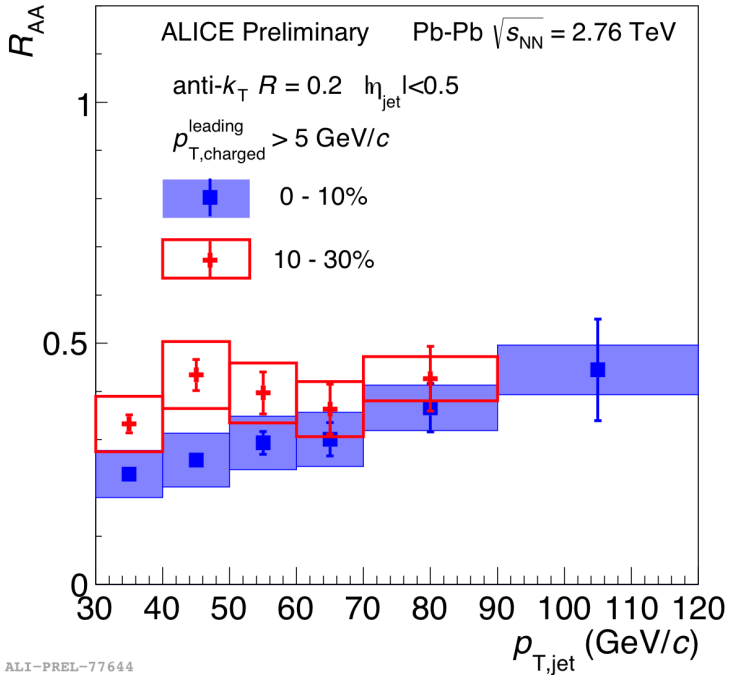

Figure 2.7: Jet R_{AA} for PbPb collisions at $\sqrt{s_{NN}} = 2.76$ TeV in ALICE [24].

It is desirable to use jets as opposed to single hadrons because jets are strongly correlated to the original partonic kinematics of the initial hard scattering, whereas the dynamics of single hadrons are further complicated by fragmenation, which is non-perturbative and cannot be calculated from pQCD and relies on further experimental measurement. As can be seen from figure 2.7, there is a persistant supression in the Jet R_{AA} at all p_T. However, it is not entirely clear whether this supression is due to hot nuclear matter effects (i.e QGP), or cold nuclear matter effects. One of the major goals of understanding the QGP phase is to differentiate between the dynamics of this hot QCD matter to that of ordinary (i.e. cold) nuclear matter.

2.8 Cold Nuclear Matter

To study *Cold Nuclear Matter* (CNM) effects, collisions involving a heavy-ion (e.g. Au, or Pb) and a "light" nucleus (e.g. protons or deuterons) are utilized because these collisions exhibit nuclear effects from the presence of an extended nuclear mass (the heavy-ion) yet lack sufficient energy density to produce a QGP. At RHIC, d-Au collisions were used to measure R_{dAu} for single hadrons and compared with the measured single hadron R_{AA}. Figure 2.8 shows that for single hadrons in d-Au, no suppression was observed over a p_T range of 1-10 GeV/c as compared to Au-Au collisions were a significant suppression is observed. One of the principal observables to be presented in this analysis is an analogous plot of figure 2.8 for jets in p-Pb collisions in ALICE.

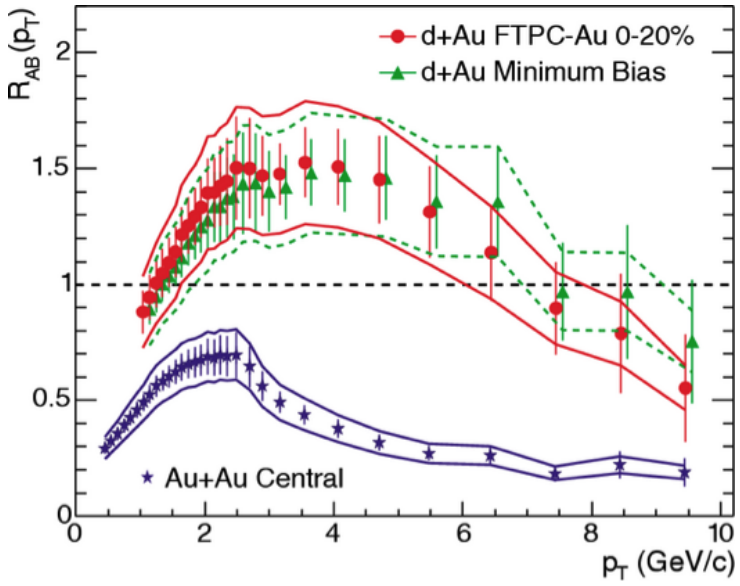

Figure 2.8: Nuclear Modification Factor for hadrons in dAu and AuAu collisions [23].

Figure 2.7 shows a suppression of the Jet R_{AA} in Pb-Pb collisions compared to pp collisions at $\sqrt{s_{NN}} = 2.76$ TeV. What needs to be experimentally verified is that is this suppression caused by the hot medium.

Cold Nuclear Matters (CNM) can be seperated into two effects: modified parton distribution function from the colliding heavy-ion (compared to the PDFs in pp collisions) and initial state radiative effects from the participant nucleons in the heavy-ion nuclei that are not colliding with each other (i.e. spectator nucleons). In Pb-Pb collisions, both QGP and CNM effects are expected to be present. Ideally a measurement of each one of these effects independently of the others would be able to determine which effect is dominant in the Pb-Pb case. In theory, ultra high energy pp collisions could produce

a system with properties similar to the QGP [25] but to date no conclusive evidence that this system has been produced has been observed. Furthermore, there currently exists no experiment which can measure nuclear PDFs (nPDF), as such a measurement would require lepton-nuclei collisions. However, p-Pb collisions are able to measure the cumulative effects of both CNM effects. Thus if an observable is measured in p-Pb collisions and Pb-Pb collisions, the difference is most likely attributed to hot nucelar matter effects.

2.8.1 Nuclear Parton Distribution Functions

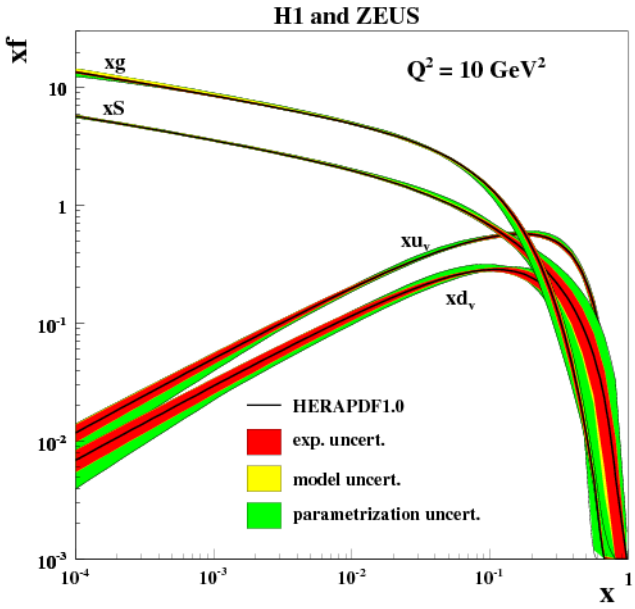

Figure 2.9: Parton distributions in a proton, measured in e^-p Deep Inelastic Scattering (DIS) at HERA [26].

Part of the sucess in being able to use jets as calibrated probes in pp collisions is due to a precise measurement of the single parton distribution functions of protons from e^-p which can be used to calculate the production cross section of jets in pp collisions (2.1). As the fraction of energy carried by a parton compared to the collisional energy of the particles decreases, the PDF of nucleons becomes dominated by gluons (see figure 2.9). In order to have precise measurement of the production cross section of jets in p-Pb collisions, knowledge of nPDF must be known precisely. Until e^-A DIS collisions are performed, this knowledge will be unavaliable. What is currently done is to take the PDF from e^-p DIS and to model it using various schemes [27] to produce nPDF.

Ultimately what the models produce are the relative modification of the PDF for the given nucleus to that of a proton. This ratio, $R^A_{I_s}$ can be defined as:

$$R^A_{I_s} = \frac{I^A_s(x, Q^2)}{A I^p_s(x, Q^2)} \tag{2.4}$$

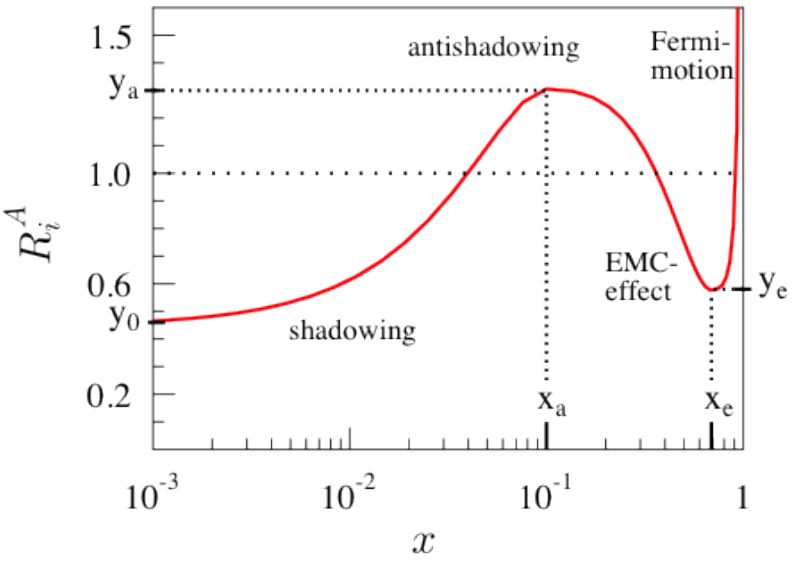

Figure 2.10: Phenomonological model of $R^A_{I_s}$ [28].

where x is the Bjorken scaling x variable and defined in terms of the 4-momentum squared of the system (Q^2) and as the energy transferred to the parton by the scattering ($p \cdot q$):

$$x = \frac{Q^2}{2p \cdot q} \tag{2.5}$$

At low x, the number of gluons increases rapidly. At the LHC, it is expected that the typical jet energies prodcued in p-Pb collisions will produce partons with x$\sim 10^{-3}$ for collisions at $\sqrt{s_{NN}} = 5.02$ TeV with a $Q^2 \sim 100$ GeV for hard scatterings. As the gluonic density increases, because of self interactions, they can scatter off each other producing distructive interferance [29]. The net result is that at low x, the incoming nucleon will "experience" a decreased flux of gluons relative to a proton (when corrected for the number of nucleons). This phenomenon is called *nuclear shadowing* (see figure 2.10). As x increases, this effect diminishes and at x$\sim$ 0.1 there can be an enhancement in the nPDF. This is called the *anti-shadowing* region.

In the x regime between 0.1 and 1 two effects known as the EMC-effect and Fermi-motion can be collectively described by the so-called *Cronin Enhancement* [30]. This effect which produces a hardening of the transverse momentum spectrum in p-A collisions relative to pp collisions is assumed to be caused by multiple scatterings of partons from the proton with partons from the nucleus. The result of successive scatterings is that the partons receives a "kick" in transverse momentum, shifting their p_T spectra from lower to higher p_T and causing the observed depletion (EMC-effect) and enhancement (Fermi-motion).

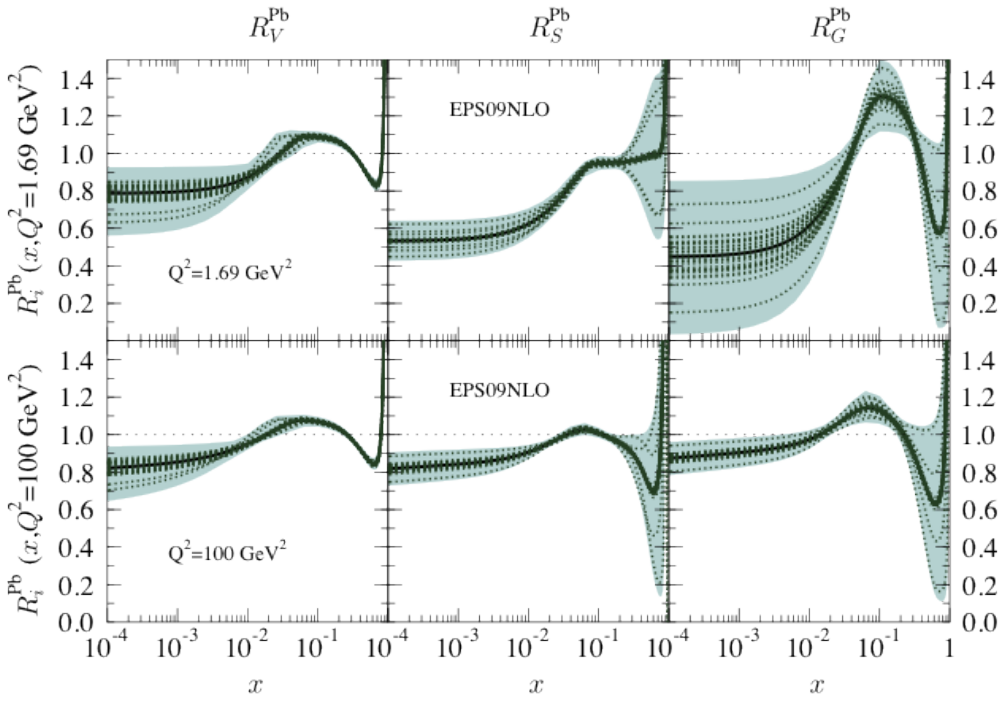

Figure 2.11: nPDF model of $R_{I_s}^A$ for lead at various Q^2 [28].

The various effects described previously can be seen in model calculations using the EPS09NLO model [28]. Of particular interest to p-Pb collisions is the lower right panel in figure 2.11, where the nPDFs for lead nuclei are calculated for hard scatterings with a Q^2 = 100 GeV^2. At these energies, the modified nPDFs are expected to produce only a small effect of roughly 10% relative to proton PDFs at x$\sim 10^{-3}$.

2.8.2 Color Glass Condensate

As two nuclei collide, partons interact with each other scattering in various directions. At low x, since most of these partons are gluons (see figure 2.9), the region

becomes dense and no longer is it appropriate to use pQCD to calculate processes in this regime [32] (see figure 2.12). In the extreme situation where the number of gluons increases to $\sim 1/\alpha_s$, it becomes necessary to compute an infinte number of Feynman diagrams due to multi-parton interactions to obtain the cross section resulting in an infinite amount of gluons being produced. Since this is not energetically possible, at some scale saturation must occur. In these extreme situations (which are expected to be produced in p-Pb collisions at the LHC), in order to obtain the cross secton, one must also have knowledge of multigluon states of the wavefunctions of the two colliding nuclei.

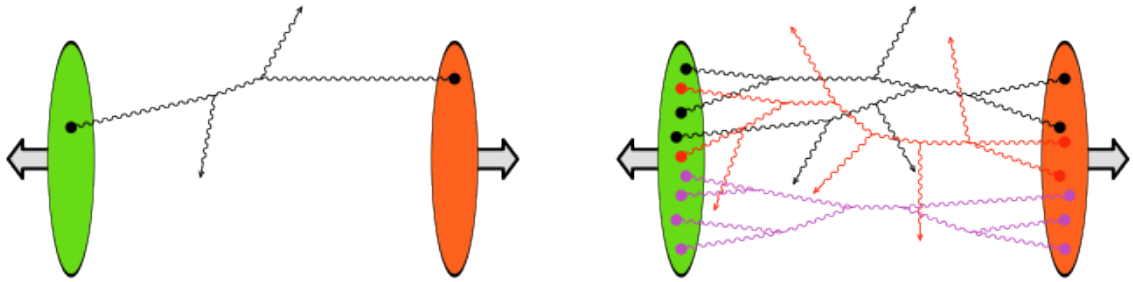

Figure 2.12: Left: typical interaction is a dilute region in a hadronic collision. Right: typical interaction is a dense region in a hadronic collision [32].

This region where strongly interacting particles are "compressed" to extreme densities (see figure 2.12) and pQCD is no longer applicable is referred to as a *Color Glass Condensate* (CGC). This is important because the CGC is proposed as an intrisic property of all high-energy strongly interacting matter. The CGC could also explain how particles are produced in high-energy collisions and provide an effective theory on the distribution of matter within particles [31]. Weak coupling methods can be used in order to compute cross sections by realizing that the dynamical generation of gluons is much larger than the non-perturbative scale Λ_{QCD} (the scale were the strong nuclear force is expected to dominate and confinement is crucial) [32] inside a CGC. This scale, referred to as the *saturation momentum* Q_s is caused by the non-linearality of gluon-gluon interactions. At this scale, gluon recombination becomes large and any momenta smaller than Q_s may be affected by *gluon saturation* (see figure 2.13).

When a CGC is produced in a heavy-ion collision, each nuclei can be envisioned as a "wall" of gluons. When these walls collide, the overlapping region between these walls will be producing the QGP. If a suppression in R_{AA} is observed in such a system, it is unknown whether this suppression is due to the QGP (interaction of the walls) or

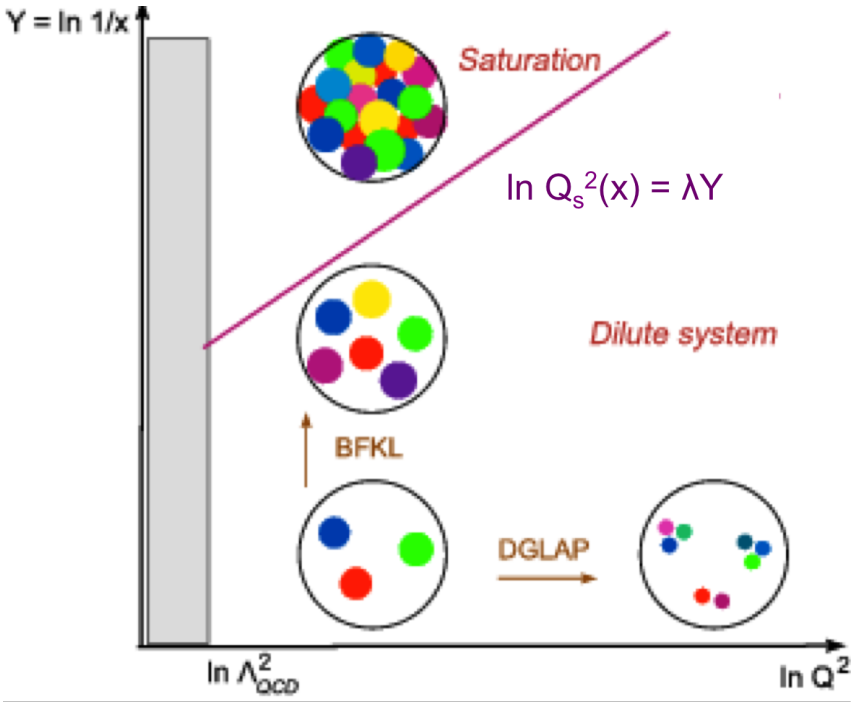

Figure 2.13: The "Phase-Diagram" for parton evolution in QCD; each colored blob represents a parton with transverse area $\Delta x_\perp \sim 1/Q^2$ and longitudinal momentum $k_z = xP$. The straight line $lnQ_s^2(x) = \lambda Y$ is the saturation line, which separates the dense and dilute regimes. Adapted from [33].

cold QCD matter (the wall itself). What is needed is a "control experiment" where one can actually probe the properties of the wall iteself. Proton-lead collisions are ideal for this control experiment. When the lead nucleus is accelerated to sufficently high energies, it acts like a CGC. Now, as a proton colldies with the lead nucleus, the energy density in the overlap region of the proton and the lead nucleus is not sufficent to create a QGP, thus any observable of this system (e.g. nuclear modification factor R_{pPb}) will probe the "cold" QCD matter.

Given the typical $Q^2 \sim 100$ GeV/c that produces jets in p-Pb collisions (for this analysis), and the expected Bjorken $x \sim 10^{-3}$, it is expected that effects due to the CGC (in the "dilute" phase in figure 2.13) will be small or negligible. Hence no suppression should be observed in the production of jets in p-Pb collisions relative to pp collisions. Thus, if no suppression in R_{pPb} is observed, then a reasonable conclusion is that any suppression observed in R_{PbPb} is due to the QGP.

CHAPTER 3

Experimental Setup

This chapter will provide a brief introduction of the LHC and a more detailed discussion of the ALICE experiment with a focus on describing the relevant detector systems used in this analysis

3.1 The Large Hadron Collider

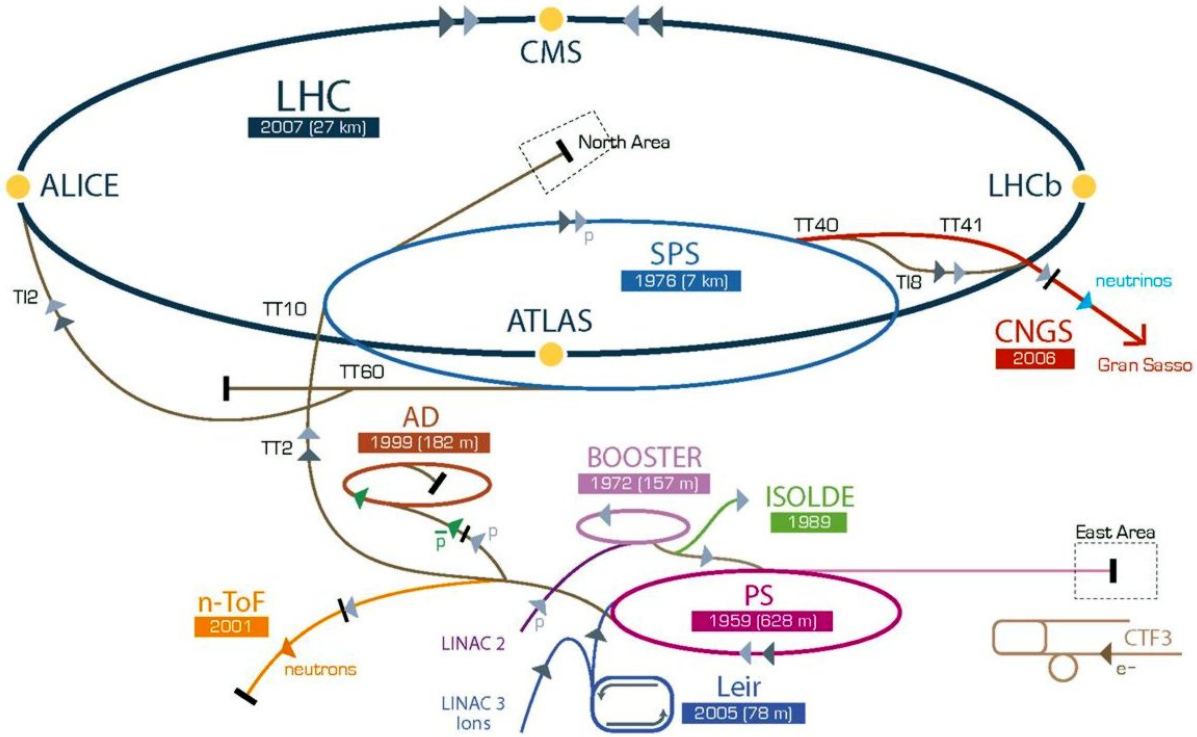

Figure 3.1: Map of LHC accelerator

The Large Hadron Collider (LHC), located on the French-Swiss border, is the world's largest and most complex particle accelerator. With a circumference of approximately 27 km, the LHC can accelerate and collide bunches (a group of ions containing approximately 10^{11} particles) of protons up to a center of mass energy of 14 TeV and bunches of heavy-ions (Pb) up to 5.52 TeV per nucleon pair. The protons or lead nuclei are accelerated in opposite directions in two rings. These rings contain super conducting magnets with can produce magnetic fields up to 8.33 T to keep the beams circular. Prior to March 2013, the LHC has been running at half its nominal collisional energies: $\sqrt{s}$ = 7 TeV for pp collisions and $\sqrt{s_{NN}}$ = 2.76 TeV for Pb-Pb collisions. In 2012, the collisional energy for pp was increased to $\sqrt{s}$ = 8 TeV. A p-Pb run in late 2012 and early 2013 was done with collisional energy of $\sqrt{s_{NN}}$ = 5.02 TeV.

The LHC hosts seven experiments, of which only three contain heavy-ion programs:

- ATLAS (A Torodial LHC Apparatus) [34,35]
- CMS (Compact Muon Solenoid) [36,37]
- ALICE (A Large Ion Colliding Experiment) [38,39]

ATLAS and CMS are general purpose detectors designed for studying the Higgs boson and physics beyond the standard model (supersymmetries in pp collisions, ect.). They also contain heavy-ion programs, with complementary capabilities to ALICE. The ALICE experiment, a dedicated heavy-ion detector, is mainly designed to study the strongly interacing matter that is created from Pb-Pb colisions and to study the properties of the Quark-Gluon Plasma. The proceeding sections will describe the components and capabilities of the ALICE detector.

3.2 The ALICE Detector

The ALICE collaboration currently consists of member from 36 countries, 131 institutions, and over 1200 reserach scientists and engineers[1]. The ALICE experiment is a general purpose detector designed to measure and identify charged hadrons, leptons (electrons and muons), and photons with very high particle densities, up to 8000 charged particles per unit rapidity at mid-rapidity [38,39]. Furthermore, ALICE has

[1] As of November 2013

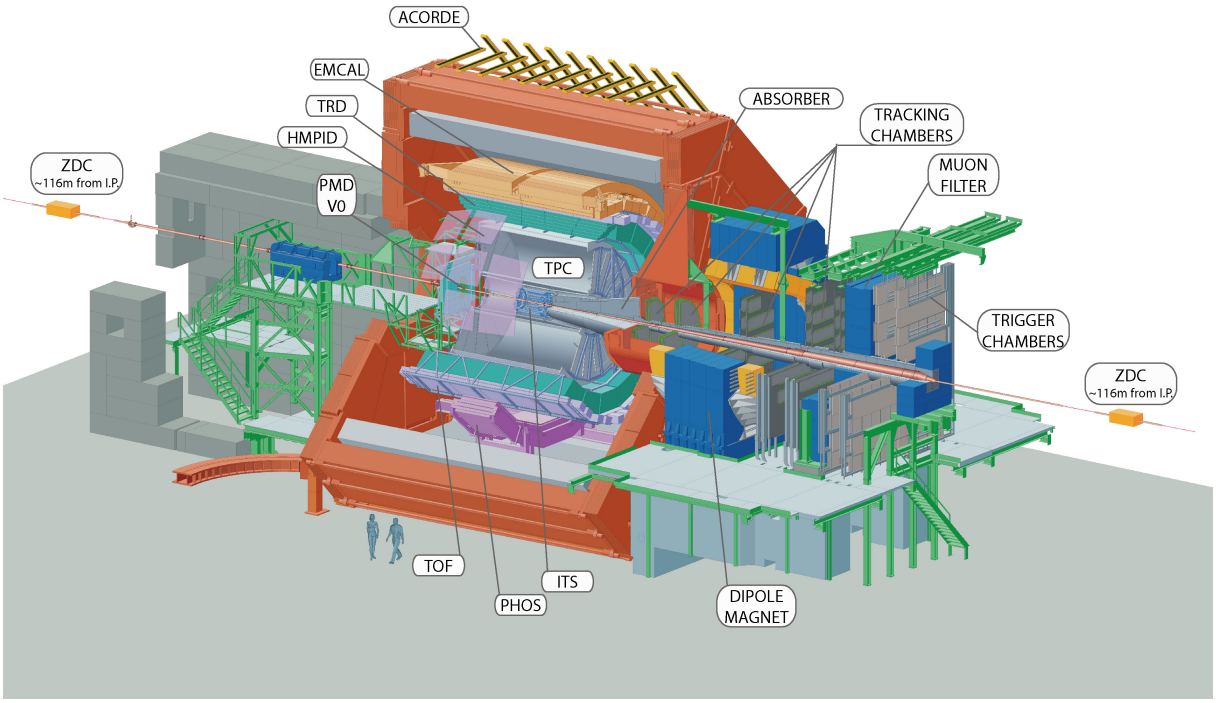

Figure 3.2: Schematic view of the ALICE detector

tremondous capabilites to detect particles over a large range of transverse momentum p_T (from $\sim$ 100 MeV/c to $\sim$ 100 GeV/c). The ALICE experiment consists of 18 sub-detectors which are shown in figure 3.2.

The ALICE coordinate system is a right-handed orthogonal Cartisian system with its origin at the nominal bunch-crossing point in the center of the L3 magnet. The axes are defined as follows: x-axis is perpendicular to the mean beam direction, aligned with the local horizontal and pointing to the accelerator center; y-axis is perpendicular to the x-axis and to the mean beam direction, pointing upward; z-axis is parallel to the mean beam direction. Hence the positive z-axis is pointing in the direction opposite to the muon spectrometer [38] (see figure 3.2).

Due to the cylindrical geometry of ALICE, it is more convient to use a cylindrical coordinate system. The azimuthal angle φ is defined as the angle in the x-y plane, with $\varphi = 0$ corresponding to pointing along the x-axis. The polar angle θ is substituted for the nearly relativistic invarient pseudorapidity. Appendix A contains definitions and an introduction to the kinematic variables that will be used in this analysis.

The central detectors are located within the ALICE magnet, which provides field strengths varying from T = 0.2 to T = 0.5 (default) which is paralell to the beam axis

(z-axis). The central detector systems have full azimuthal coverage and an acceptance of $|\eta| < 1$ in pseudorapidity.

This analysis utilizes 5 of the 18 sub-detectors of ALICE for jet reconstruction in order to assess the charged and neutral constituents of jets, to improve momentum resolution of those constituents, and to determine event centrality. A brief technical explanation of each of these 5 sub-detectors is provided in the proceeding sections.

3.2.1 Time Projection Chamber (TPC)

The main detector within ALICE for measuring charged particles and reconstructing charged tracks is the Time Projection Chamber (TPC) [40]. The TPC consists of an enclosed large volume cylindrical chamber filled with gas and with high voltage electrode discs in the center. The TPC has two multi-wired proportional chambers (MWPC) as endplates producing an electric field between the center and each endplate. This electric field also amplifies the signal of charged particles. When particles traverse the TPC, they produce electron ionizations in the gas. These electrons drift towards the endplates (which are positive) at a drift velocity which is characterized by the gas. In order to reduce diffusion of these drift electrons, a magnetic field is applied parallel to the electric field. The magnetic field also causes these electrons to gyrate in helical trojectories around the beam axis, which allows a measurement of the curvature of the particle, that is related to the particles momentum. As these electrons pass through the MWPCs, the polar coordinate θ is recorded which is related to the radial component of the particle's trajectory. The z-coordinate of the particle can be obtained by measuring the drift time of the ionization event to the MWPCs. Each MWPC is divided into strips along the radial direction which can reveal the azimuthal component of the particle's trajectory. The TPC can be visualized as a "3D camera", in that the trajectory of particles are reconstructed in (η,φ,z) and not just points on an η-φ surface. Figure 3.3 shows an ALICE event display in which the curved trojectories are the reconstructed particle tracks in the TPC.

The TPC is capable of reconstructing charged particles with $0.1 < p_T < 100$ GeV/c. The TPC has full azimuthal coverage along with coverage in pseudorapidity $|\eta| < 0.9$. Outside this pseudorapidity widow, partial tracking can still be done but with a reduced mometum resolution until $\eta \sim 1.5$. Particle identification can also be done on reconstructed tracks by measuring the dE/dx (energy loss per unit distance) of the track in the TPC gas using the Bethe-Bloch formula.

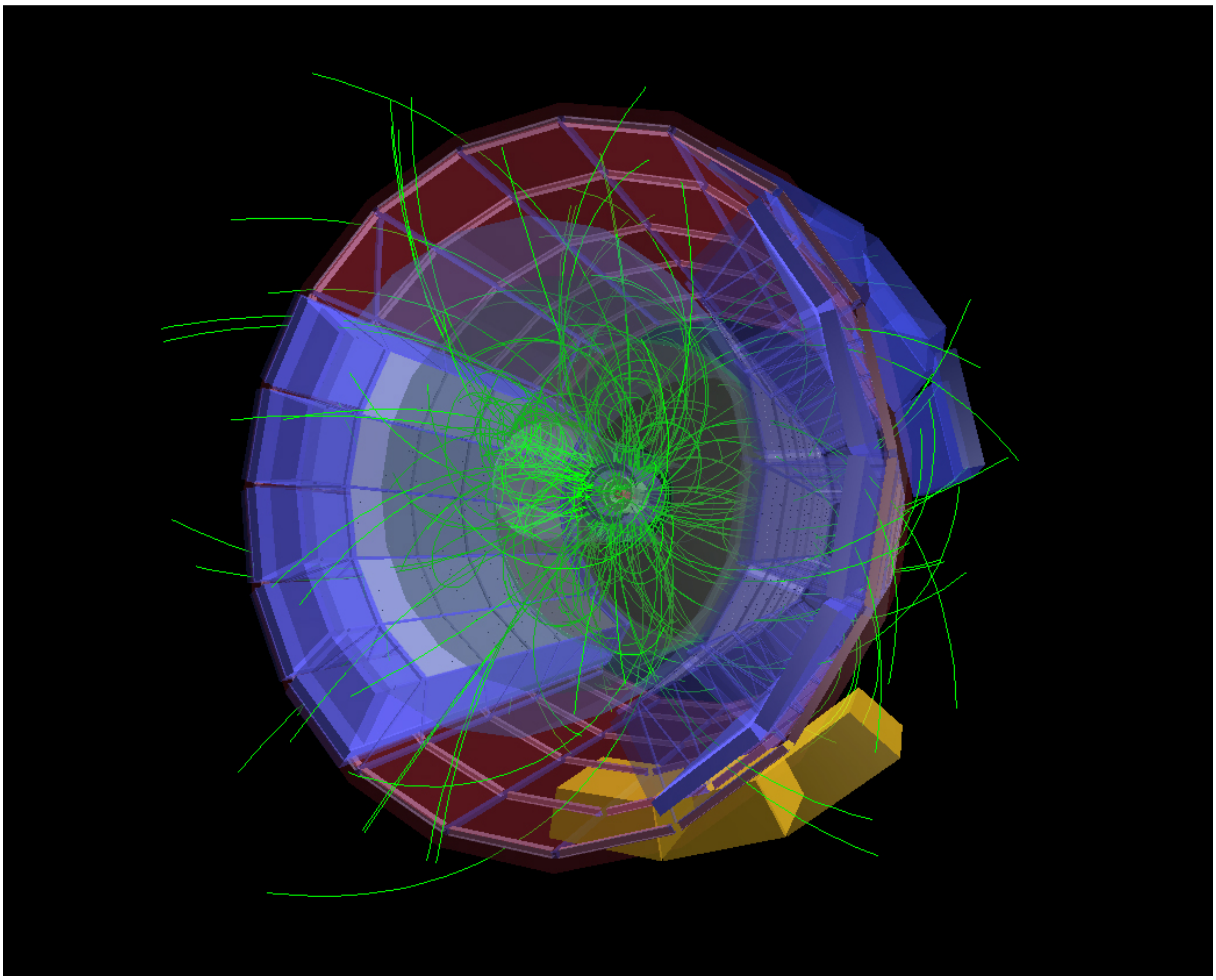

Figure 3.3: An ALICE event display. Green trajectories represent tracks.

The TPC is a cyclindrical shaped detector with a length along the beam axis of 500 cm and an active gas volume between 84.1 cm to 246.6 cm in the ridial direction (see figure 3.4). Charged particles are detected in the TPC by the ionization they produce in the gas (a mixture of 90% Ne and 10% CO_2) within the drift chamber as they traverse the chamber. The diffusion constant is an essential parameter that must be closely monitored as a low diffusion constant and large ion mobility are required to achieve good momentum and high rate capacity.

The TPC is divided by two regions of which one contains a high voltage electrode which is maintained at a potential of 100kV with respect to the end plate which is 250 cm away. As charged particles traverse the TPC, interactions between the charged particles and the gas cause electrons from the gas to be liberated and drift towards the ends of the chamber. The maximum drift time is 90μs. Furthermore, the electric field within the field cage is highly uniform, with irregularities in the field no greater than

1% [40]. The potential strip network is held in place by 18 support rods that are spread equidistant across over azimuth and placed 31 mm from the cylinder wall.

More details about the TPC can be found in [40].

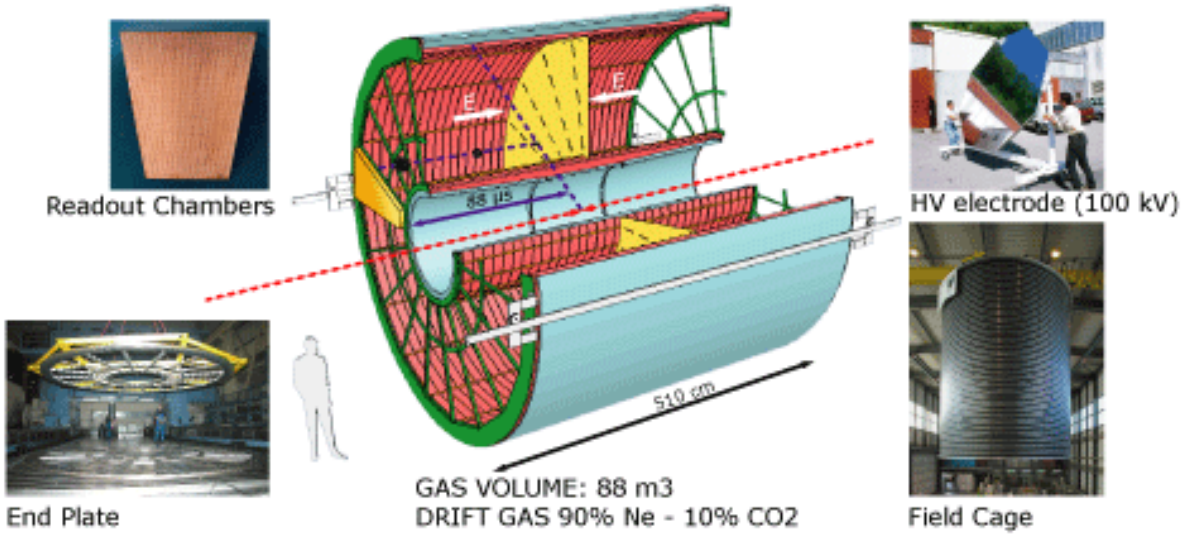

Figure 3.4: Schematic of the Time Projection Chamber TPC.

3.2.2 Inner Tracking System (ITS)

Located within the central barrel of the TPC, the Inner Tracking System (ITS) is composed of six layers of concentric silicon detectors [41]. Due to its location near the interaction vertex and its design (high spatial resolution), the ITS is able to make precision measurements of a charged particle's primary and secondary verticies which allows improved momentum resolution of charged particles, which is important for jets.

The ITS can be divided into three regions. The inner region which consits of the first two concentric rings of silicon detectors located radially from the beam axis at 3.9 and 7.6 cm are referred to as the Silicon Pixel Detectors (SPD). The SPD is an integral part of the reconstruction of the particle verticies with high precision and is used in global tracking. The middle region consisting of another two concentric rings 15.0 and 23.9 cm away from the beam axis are called the Silicon Drift Detectors (SDD). Their design

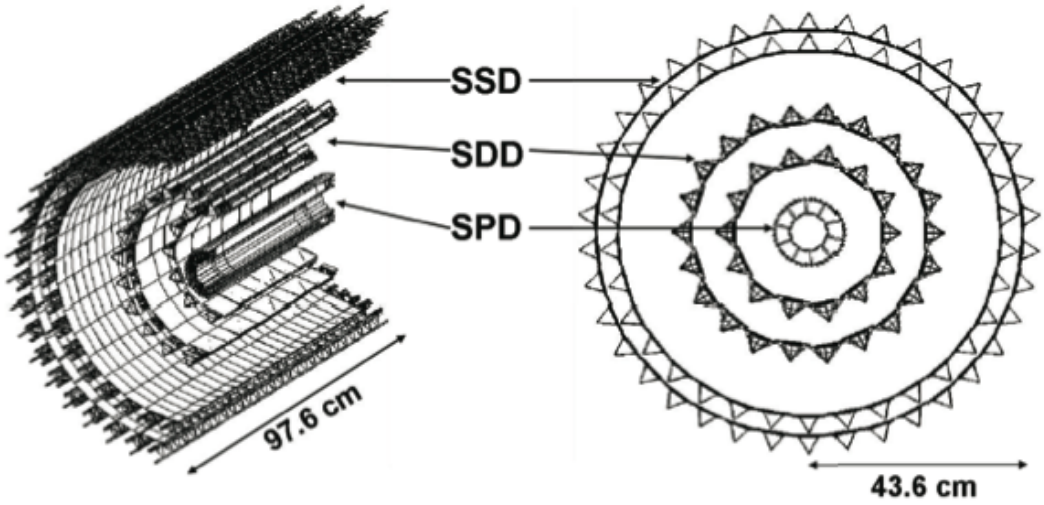

Figure 3.5: Schematic of the Inner Tracking System ITS.

is intended to provided good tracking ability to the SPD along with a measurement of the dE/dx of the particle. The outer region which consists of two concentric rings of double sided SSDs located at 38 and 43 cm from the beam axis is called the Silicon Strip Detectors (SSD). Like the SDDs, they also are used for dE/dx measurements which allows more precise measurements of high momentum charged particles. The SSD is crutical for connecting tracks from the ITS to the TPC. Due to the extremely high particle density environment that ALICE was designed for, the two innermost regions (SPDs and SDDs) were designed for charged track densities up to 90 tracks per cm^2 whereas typical charged track densities $\sim$ 1 per cm^2 are observed at the SSDs.

The ITS has full azimuthal acceptance along with a pseudorapidity coverage of $|\eta| < 0.9$ for all verticies located in the region of the interaction diamond ($|z| < 5.3$ cm along the beam axis). The innermost pixel layer has an extend pseudorapidity coverage of $|\eta| < 1.98$ for interactions occuring at z = 0 cm.

More details regards the technical specifications of the ITS can be found in the ITS Technical Design Report [41].

3.2.3 VZERO

The VZERO [42] is a detector consisting of two silicon counters on opposite sides of the ALICE collision vertex in the forward regions. These two small angle silicon counters are located at a pseudorapidity $2.8 < \eta < 5.1$ for V0A while V0C is at $2.8 < \eta < 5.1$. Each silicon counter consists of 32 elementary counters arranged in 4 rings

with 8 sectors per ring covering full azimuth (see figure 3.6).

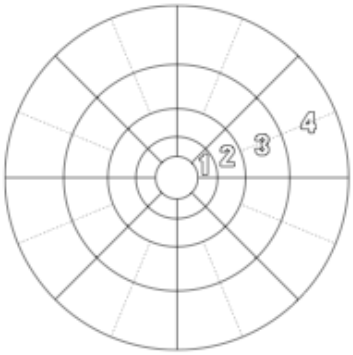

Figure 3.6: Layout of the VZERO silicon rings.

The VZERO serves as an online trigger for minimum-bias (MB) pp and ion-ion collisions. This is acheived by the VZERO measuring deposited energy of emitted charged particles (MIPs) crossing through the detector and firing once a minimum threshold energy has been recorded. The deposited energy of MIPs traversing the detector is proportional to the number of charged particles in the event, thus the VZERO detector can be used to measure the event centrality.

3.2.4 Zero Degree Calorimeter (ZDC)

The ZDCs [43] consists of four modules designed to measure spectator nucleons (nucleons that do not participate in the interaction). Two of these modules are located at 116.13 m from the interaction point (IP) on each side and are designed to measured energy from spectator neutrons. Since neutrons are not deflected by the magnetic fields, the calorimeters need to be close to the beam. The modules are located 1 cm off the beam axis to account for the 100 μrad per beam crossing angle of the two beams at the IP. The modules themselves are 7 x 7 x 100 cm^3, made of quartz fibres embedded in a tantalum matrix allowing 80% of the shower generated by spectator neutrons to be contained. The fibres have a core diameter of 365 μm and are oriented at 0^o with respect to the beam axis. The resolution for a 2.7 TeV neutron is 10.5%, according to simulation [43].

Two other modules are placed at 115.63 m from the IP on each side and are designed for measuring energy from spectator protons. Since protons can be deflected by the magnetic fields, these modules will have to be off the beam axis at a larger distance then those for neutron detection. 90% of the protons are contained in an area 12.6 x

2.8 cm^2, centred at 19 cm from the beam axis, on the outgoing beam side. To obtain a shower containment and an energy resolution similar to that of the neutron ZDCs, two devices of 20.8 x 12 x 150 cm^3 made of quartz fibres embedded in a brass matrix are centered at 19 cm from the beam axis. The fibres have a core diameter of 550 μm and are oriented at 0^o with respect to the beam axis.

The ZDC detector operates by detecting so-called "slow" nucleons moving through the detector: protons in the proton ZDC (ZPA) and neutrons in the neutron ZDC (ZNA). The multiplicity of these slow nucleons has been shown to be monotonically correlated to N_{coll} (nucleon-nucleon collisions. See appendix C) in lower energy experiments [67]. In order to relate the energy deposited in the ZDC to N_{coll}, a model must be used to explain the slow nucleon production. The *Slow Nucleon Emission Model* [67] was used to detemine the event centrality in the ZDC detectors as outlined in [53] and will be used in this analysis. The ZNA spectrum is preferred since for the proton calorimeter the acceptance is affected by the LHC optics and magnetic field settings.

3.2.5 EMCal

Of the 18 subdetectors within ALICE, only two are capable of measuring neutral particles: The ALICE Photon Spectrometer (PHOS) [44] and the Electromagnetic Calorimeter (EMCal) [45]. For this analysis, the EMCal will be used for neutral particle detection which are used in full jet reconstruction.

The EMCal is located within the large solenodial magnet of ALICE. Situated $\sim$ 450 cm from the beam line and with a length of $\sim$ 7 m, the EMCal has an azimuthal acceptance of 107° and a pseudorapidity acceptance of $|\eta| < 0.7$. Several components of the EMCal were built at Wayne State University along with software developement and hardware testing.

The EMCal (see figure 3.7) consists of an array of 10 full Super Modules which are assembled from 12 x 24 = 288 modules along with 2 one-third size Super Modules with 4 x 24 = 96 modules. The modules have a fixed width in the φ direction and a tappered width in the η direction of 1.5°. Each module is an identical, self contained detector unit with four independent channels/towers/cells. Thus each Super Module contains 1152 towers giving the entire EMCal Super Module Array 12288 towers in total

The active readout of the EMCal is a 5 x 5 mm^2 active area Avalanche PhotDiode (APD), with high quantum efficiency, low dark current, and very high stability and reliability. The APDs are connected to Charge Sensitive Preamplifer (CSP) with an

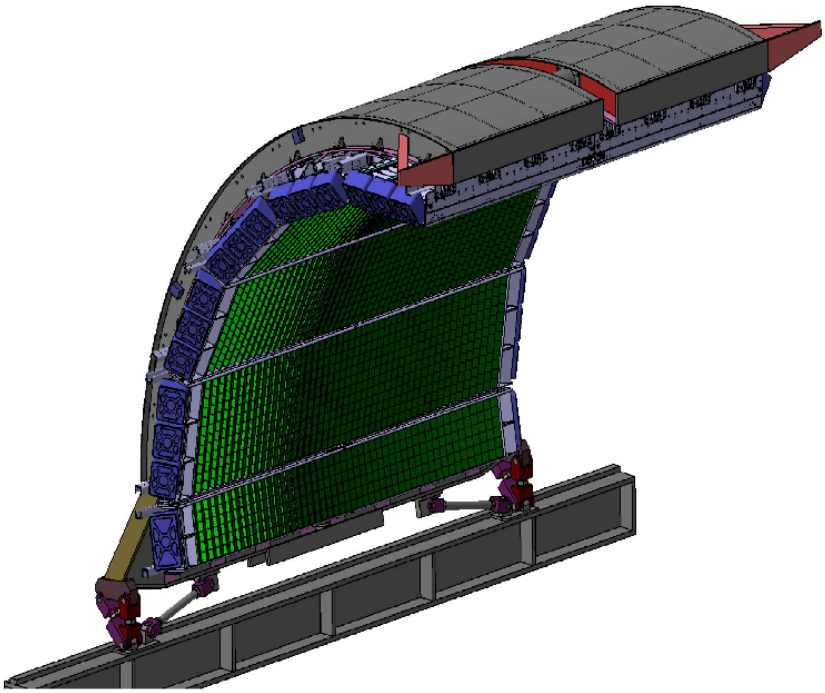

Figure 3.7: EMCal Super Module array.

integrated charged output from the APD over a 1 pF capacitor into a voltage step pulse.

The EMCal works by measuring the energy deposition of particles as they traverse the towers. For photons (which are either produced directly in the collisions or as decays products of hadrons produced in the collisions) with energies higher than $E \sim$100 MeV, they lose their enegy via production of e^+e^- pairs [46]. Electrons produced from pair production (or from the hard scatterings themselves) will still have large energies and will lose their energy almost exclusively by bremsstrahlung. Neutral hadrons (e.g. neutrons, κ_L^0, ect.) induce nuclear interactions with the lead-tungsten crystals which in turn produce electrons and photons. The radiation loss has a characteristic length X_0 (which is a property of the lead-tungsten crystals [$PbWO_4$]), of which the particle losses 50% of its energy. Thus an incident particle showers into many particles which lose energy rapidly in what is referred to as a cascade, or a *mip response* .

To illustrate this effect (see figure 3.9), consider a $E_0 = 100$ GeV photon incidented on a module. After a length X_0 on average the photon will produce an e^+e^- pair. In turn, the e^+ and e^- will radiate a photon each. At this stage, the process can repeat itself until bremsstrahlung is no longer the dominant source for energy lose for electrons and pair production is no longer the dominant source of energy lose for photons. Assuming the energy loss is symmetrically shared between the particles produces at

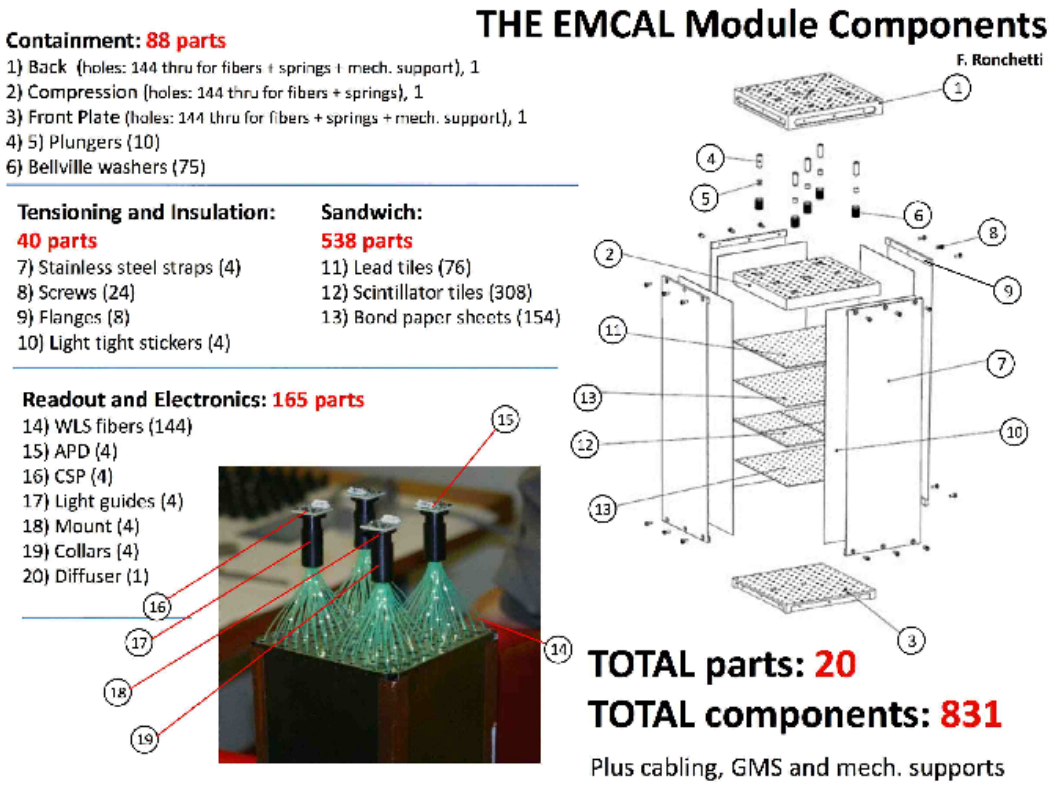

Figure 3.8: Schematic of EMCal module with components.

each stage, the shower peak will occur after $t = \frac{E_0}{E_c}$ radiation lengths. Thus, the energy deposited in the calorimeter is proportional to the depth of the position of the shower peak.

Neutral particles are not the only particles that will shower in the EMCal. Charged particles (not just electrons and positrons) will also deposit energy in the EMCal via bremsstrahlung which will trigger a cascade. Therefore, not all energy deposited in the EMCal are from particles that have not been measured in another ALICE subdetector (e.g. a charged hadron's energy has already been measured in the ITS and TPC). Thus, a correction must be applied offline to remove this double counting (see section 4.3 for more details).

Figure 3.9: Schematic representing an electromagnetic cascade. Wavy lines are photons and solid lines are electrons or positrons [46].

CHAPTER 4

Data Analysis and Selection Criteria

Once data are recorded in the detectors, various offline filtering and corrections are performed in order to measure the jet spectrum. A flow chart for the analysis chain has been provided in figure 4.1 to help the reader navigate the complexity of this analysis.

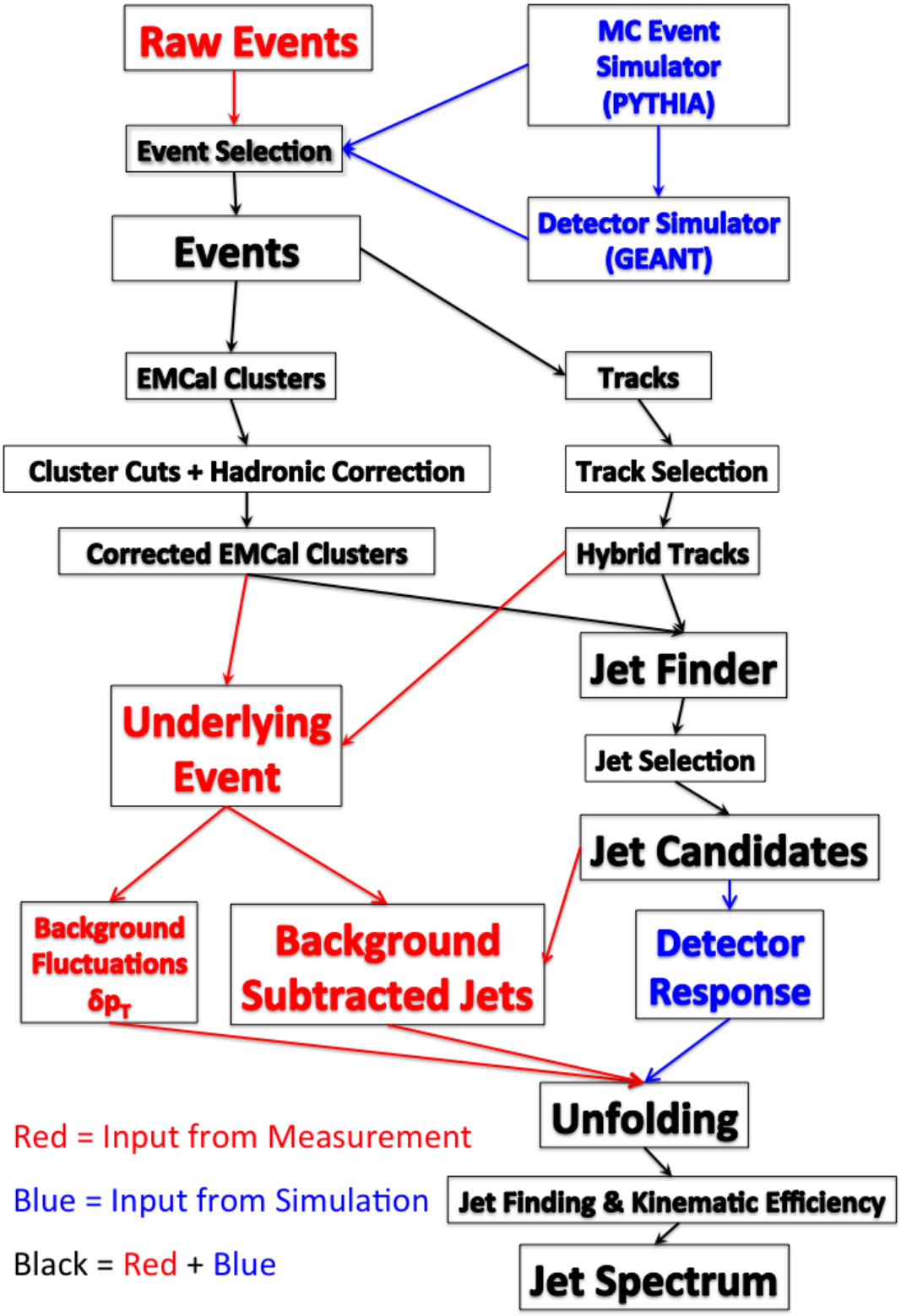

Figure 4.1: Flow chart showing analysis chain for p-Pb analysis presented in this thesis. It should be noted that the final product (i.e. the "Jet Spectrum") should also be normalized for detector acceptance, integrated luminosity, jet finding efficiency, and kinematic efficiency.

4.1 Event Selection

Starting in Feburary of 2013, the ALICE detector recorded collisions between proton and lead nuclei at $\sqrt{s_{NN}} = 5.02$ TeV at an integrated luminosity of $L_{int} = 51\mu b^{-1}$. In total, approximately 126 million events were recorded. The minimum biased (MB - i.e. centrality integrated) dataset was divided into two run periods: LHC13b and LHC13c, because in one of the periods (LHC13c) there is a dip in the ϕ distribution (see figure 4.3) in a region of the TPC due to readout electronic loss. So the LHC13c period in this analysis will be referred to as "semi-good" whereas LHC13b will be referred to as "good". The runs used in each period are listed here for completeness:

LHC13b Good: 195344, 195351, 195389, 195391, 195478, 195479, 195481, 195482, 195483

LHC13c Semi-Good: 195529, 195531, 195566, 195567, 195568, 195592, 195593, 195633, 195635, 195644, 195673, 195675, 195677

These runs were subsequently reprocessed to propogate the tracks (from the TPC) to the EMCal surface to facility hadronic correction (AOD154 reproduction). Afterwards, the events were processed offline through a physics selection task which required certain event quality criteria:

- Reconstructed z-vertex $|z_{vertex}| < 10$ cm (See figure 4.2)
- Reconstructed r-vertex $r_{vertex} < 1$ cm
- $|z_{SPD} - z_{TRK}| < 1$ mm to exclude events where the SPD vertex was not properly reconstructed.

The primary vertex of the interaction is reconstructed along the beam line (z-axis) and then in the x-y plane seperately. Using all the hits recorded in the the first two pixel layers of the silicon detectors, the z_{vertex} is estimated by finding a point which makes that distribution symmetric. When $z_{vertex} > 10$ cm, this estimate becomes inaccurate, which is why this cut is introduced. To find the point in the x-y plane, the tracks (which are reconstructed using the TPC and ITS, see section 4.2) are projected along a straight line from their interation point back to the pixel layers and only those within $4\sigma_z$ of the estimated z-vertex are considered. Once these tracks have been reconstructed, a centroid in the x-y plane is calculated and the vertex is reconstructed in all three spatial dimensions.

The restrictions on the vertex are implemented to insure that events will have high tracking efficiency. After physics selection, about 95 million events remained. These events were used in this analysis.

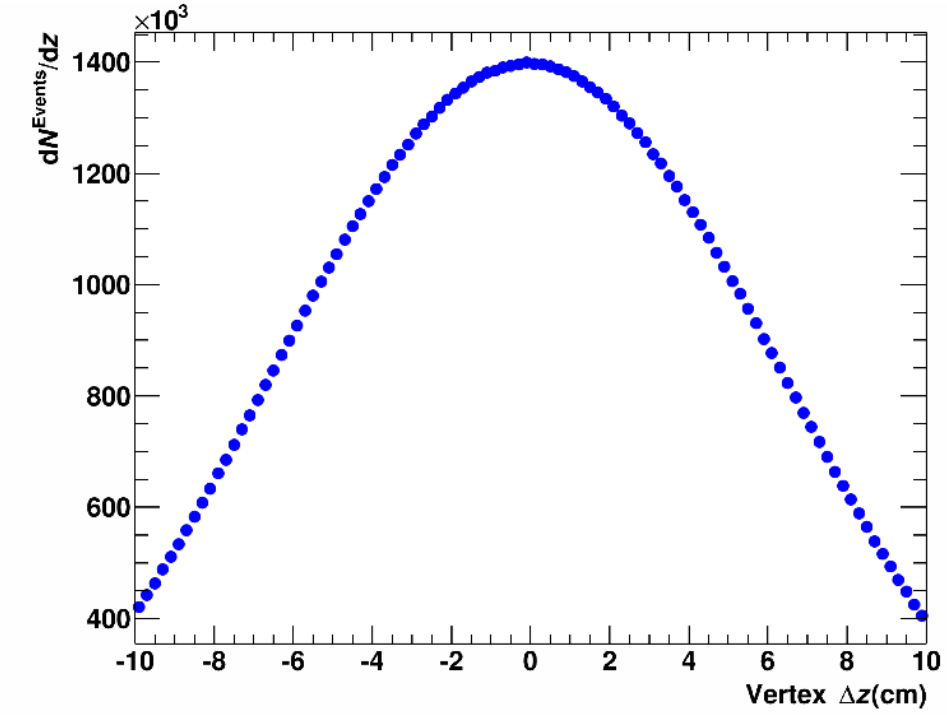

Figure 4.2: Reconstructed z-vertex distribution for p-Pb events [54]

4.2 Charged Particle Tracking

ALICE's central barrel tracking detectors, Inner Tracking System (ITS) and Time Projection Chamber (TPC), provide the charged particle reconstruction for the charged jet component. The track selection described in this section follows a two-component hybrid approach to avoid an azimuth-dependent efficiency that would be caused by the non-uniform SPD response. As a trade-off to increased uniformity within the geometrical acceptance, there will be an overall decrease in the transverse momentum resolution of reconstructed jets due to accepting a portion of reconstructed tracks with lower momentum resolution. On a jet-by-jet basis this could be particularly bad as this uniformity requirement can reject a high p_T track that was reconstructed in a $\eta - \varphi$ region of the TPC with low particle multiplicity. In turn that high p_T track can significantly alter the p_T of the jet and the jet vertex. However, if a procedure for maximizing

the transverse momentum resolution for tracks is favored over track uniformity, then entire regions of the TPC must be excluded which would reduce the geometric acceptance for jets. This would severly limit the statistics of jet observables.

The two track classes used in this approach are *global* and *complementary* tracks. Their selection criteria are given in table 4.1. While for global tracks, at least one SPD hit is required, complementary tracks cover the regions without SPD response. In order to ensure a consistent momentum resolution even without the SPD hits, the complementary tracks are constrained to the main primary vertex.

`AliESDtrackCuts` function	Value	Comment
Global standard and complementary tracks		
`SetMinNCrossedRowsTPC`	70	Number of crossed rows
`SetMinRatioCrossedRowsOver FindableClustersTPC`	0.8	Ratio between number of crossed rows and findable clusters
`SetMaxChi2PerClusterTPC`	4	Maximum χ^2 per TPC cluster
`SetAcceptKinkDaughters`	`kFALSE`	Reject tracks with kink
`SetRequireITSRefit`	`kTRUE`	Require ITS refit
`SetRequireTPCRefit`	`kTRUE`	Require TPC refit
`SetMaxFractionSharedTPCClusters`	0.4	Maximum fraction of shared TPC clusters
`SetMaxDCAToVertexXY`	2.4	Maximum Distance of Closest Approach (DCA) to the main vertex in transverse direction
`SetMaxDCAToVertexZ`	3.2	Maximum DCA in longitudinal direction
`SetDCAToVertex2D`	`kTRUE`	Cut on the quadratic sum of DCA in XY- and Z-direction
`SetMaxChi2PerClusterITS`	36	Maximum χ^2 per ITS cluster
`SetMaxChi2TPCConstrainedGlobal`	36	Maximum χ^2 between global and TPC constrained tracks
`SetRequireSigmaToVertex`	`kFALSE`	No sigma cut to vertex
`SetEtaRange`	-0.9,0.9	Pseudorapidity cut
`SetPtRange`	0.15, 1E+15	Minimum $p_{\mathrm{T}} > 150\mathrm{MeV}/c$
Only for global standard tracks		
`SetClusterRequirementITS`	`AliESDtrackCuts::kSPD, kAny`	Require at least one hit in SPD
Only for complementary tracks		
Global track constrained to primary vertex		

Table 4.1: Overview of the hybrid track cuts.

Hybrid track selection is optimized to recover the tracking acceptance when some parts of the SPD ladders are switched off. To ensure uniform distributions in the (η,φ)-plane, an approach of hybrid tracks of the following types is used:

- global tracks with measured space points in the SPD and a good fit in the full ITS
- global tracks without any space points in the SPD but with a good fit through the remaining ITS layers; track is constrained to the primary vertex

As far as available tracks of first type with SPD hits are used, those give the best resolution in transverse momentum p_T. Tracks of the second type are constrained to the primary vertex of the event to improve the transverse momentum resolution of tracks in spite of a missing hit in the SPD.

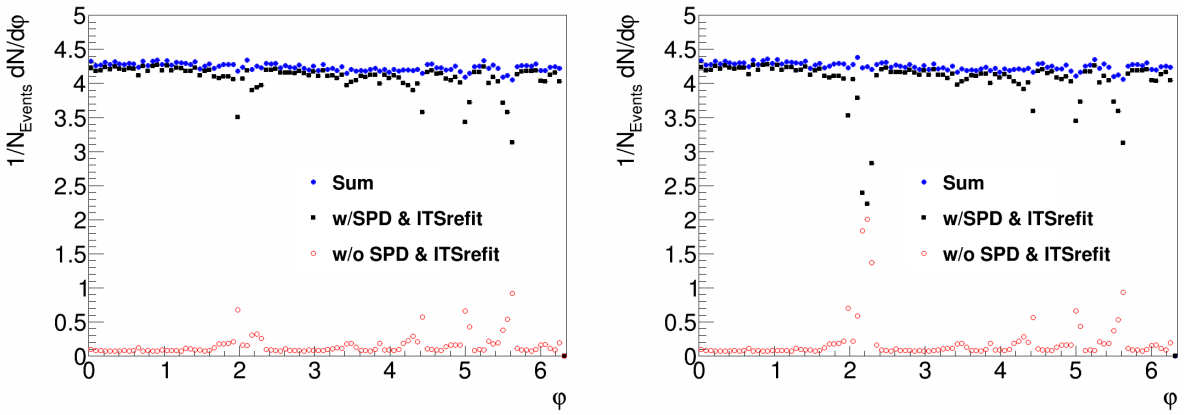

Figure 4.3: φ distribution of hybrid tracks in different p-Pb periods with minimum bias (kINT7) trigger. Left: LHC13b. Right: LHC13c.

Figure 4.3 shows the azimuthal distribution of the two hybrid track categories in minimum bias events. In addition, the figure also shows the sum of the hybrid tracks resulting in a uniform azimuthal track multiplicity distribution. The primary vertex is estimated from all tracks in the event with SPD hits. The different panels in Fig. 4.3 correspond to the different run periods used in the analysis. Runs from the LHC13b period, are called good runs since the fraction of complementary tracks is small, whereas runs from LHC13c period consist of semi-good runs in which the complementary tracks recover the tracks in the region where the SPD was inactive ($\varphi \sim 2$). The pseudorapidity distribution for the two periods are shown in figure 4.4.

As the transverse momentum increase, it is observed that the transverse momentum resolution decreases as shown in figure 4.5. The transverse momentum resolution is assumed to be the same in p-Pb runs as it was for Pb-Pb runs as there have

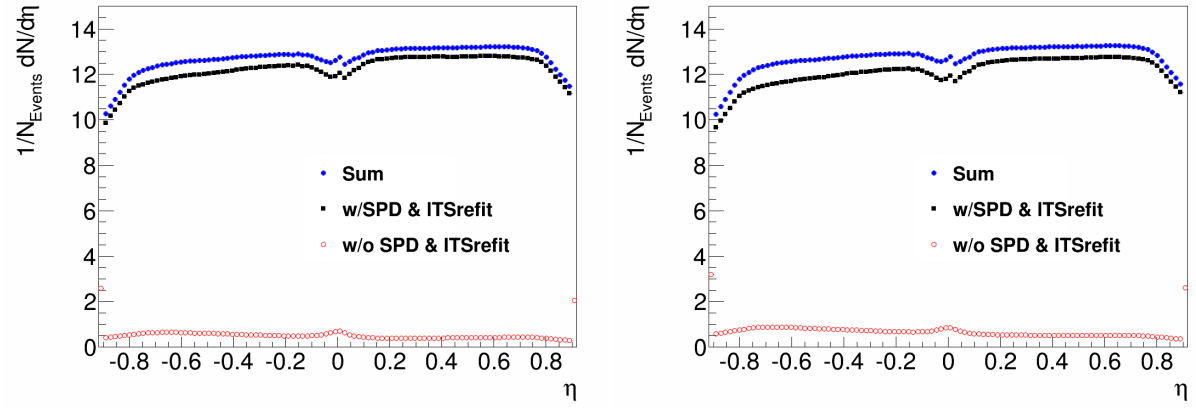

Figure 4.4: η distribution of hybrid tracks in different p-Pb periods with minimum bias (kINT7) trigger. Left: LHC13b. Right: LHC13c.

been no major changes to the TPC that would effect tracking resolution. For the majority of tracks used in this analysis ($p_{T,track} < 40$ GeV/c), the momentum resolution $\sigma(p_T)/p_T < 5\%$.

The tracking efficiency for hybrid tracks reconstructed in the ITS and TPC is evaluated with event and detector simulations. The number of generated particles is defined as all the generated charged primary pions, protons, kaons, electrons and muons within $|\eta| < 0.9$. Reconstructed tracks are all tracks which pass the track selection and originate from a primary particle. The expected tracking efficiency for p-Pb events is around 90% (see figure 4.6). The ratio between the reconstructed and generated tracks defines the tracking efficiency:

$$\epsilon(p_{T,gen}) = \frac{dN^{reco}/dp_{T,gen}}{dN^{gen}/dp_{T,gen}} \tag{4.1}$$

Since there is an uncertainty in what percentage of tracks are reconstructed in an event, a systematic uncertainty due to tracking efficiency on the jet spectrum must be estimated (see section 5.4.5).

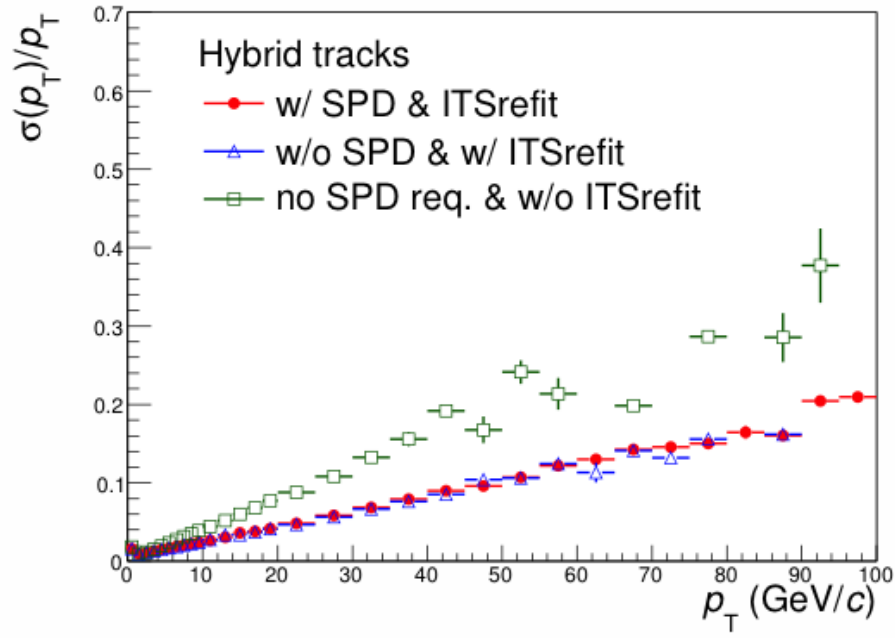

Figure 4.5: Transverse momentum tracking resolution for 0-10% central Pb-Pb events [49].

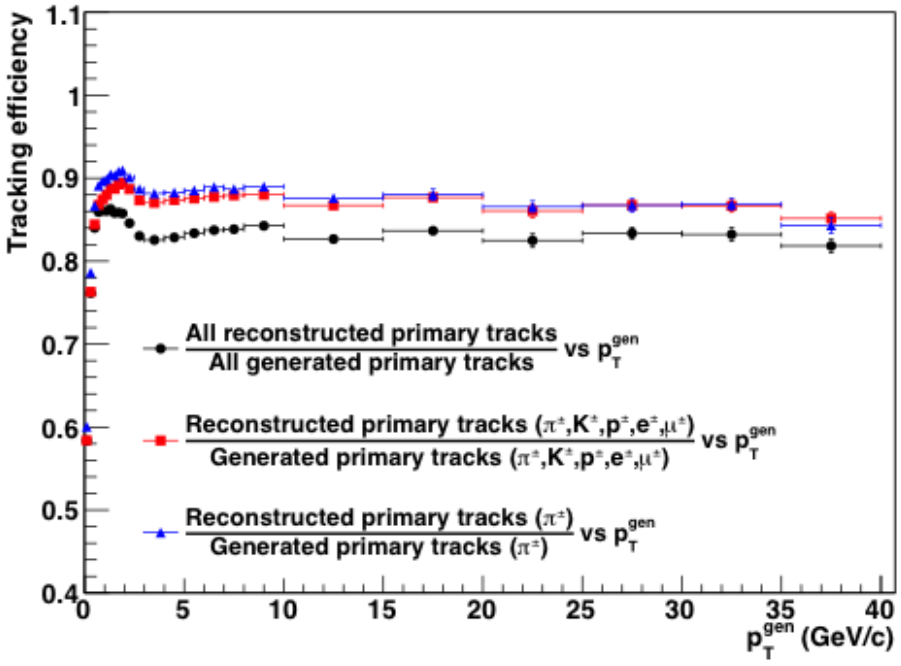

Figure 4.6: Tracking efficiency for three definitions of charged particles from detector-level simulations in PYTHIA [55].

4.3 EMCal Clustering

The clustering algorithm used for this analysis is the so-called V_2 clustering algorithm [44]. This algorithm combines cells in a sprialing outward sequence from the fired tower. Each cell is a $\Delta\eta x \Delta\phi = 0.014$ x 0.014 tower. The seed threshold for this clusterizing algorithm is 300 MeV. The sequence terminates when either a tower has an energy less than 50 MeV, or when the $n^{th} + 1$ cell in the sequence has a greater energy than the n^{th} cell. Figure 4.7 shows a schematic of the V2 clusterizing algorithm compared to the V1 clusterizing algorithm, which is exactly the same as the V2 clusterizing algorithm but without the $E_{n+1} < E_n$ constraint.

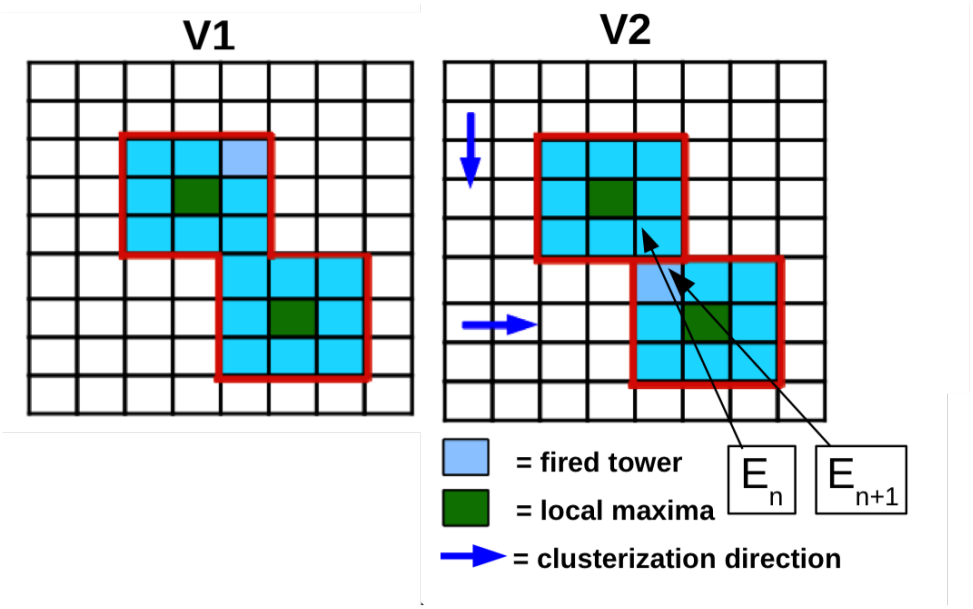

Figure 4.7: Schematic of V1 and V2 clusterizing algorithms. Adapted from [44].

The V2 clusterizer is prefered over the V1 clusterizer in that in events where the occupancy is high, the V1 clusterizer will essentially creates a single cluster for each supermodule whereas the V2 clusterizer will produce clusters where there is a single maximum in each cluster at the center of the cluster, which is a natural assumption to how particles deposit energy in the calorimeter. This means the V2 clusterizer breaks clusters that are created by two or more particles into their constituent parts. In sparse events, the two should give similar result.

As mentioned in section 3.2.5, because charged hadrons can also deposit energy within the EMCal, a correction to the energy of clusters in which at least one track has traversed must be performed in order to extract only the neutral component of en-

ergy from EMCal clusters. This correction is done offline by propogating the charged tracks to the EMCal surface (which is 440 cm from the beam axis), matching any track that is within a particular EMCal cell, and then subtracting the track's energy from the recorded EMCal cell's energy. In this analysis, 100% of the p_T of any and all tracks that are found to be within an EMCal cell are subtracted. This is referred to as a *hadronic correction* factor (hadCorr) of 2.0. However, just because a track is located near or within an EMCal cell, that does not necessary mean all its energy was deposited within the EMCal (some tracks might only traverse a small fraction of the cells depth by entering at a near parallel trojectory to the cell along its depth). Thus in principal a 100% subtraction might seem too large. In practice, the analysis is repeated with only subtracting 70% of the p_T of tracks within the EMCal (hadCorr of 1.7). Figure 4.8 shows the mean relative over-subtracted energy as a function of detector-level jet p_T. Simulation studies of charged particles traversing the EMCal (along with e^-) have shown that a hadCorr of 2.0 is an overall better approximation of the neutral energy compenent of the cluster than some other factor. Only clusters with energies greater than 150 MeV were hadronically corrected even though in this particular analysis, only clusters above 300 MeV are used in jet finding.

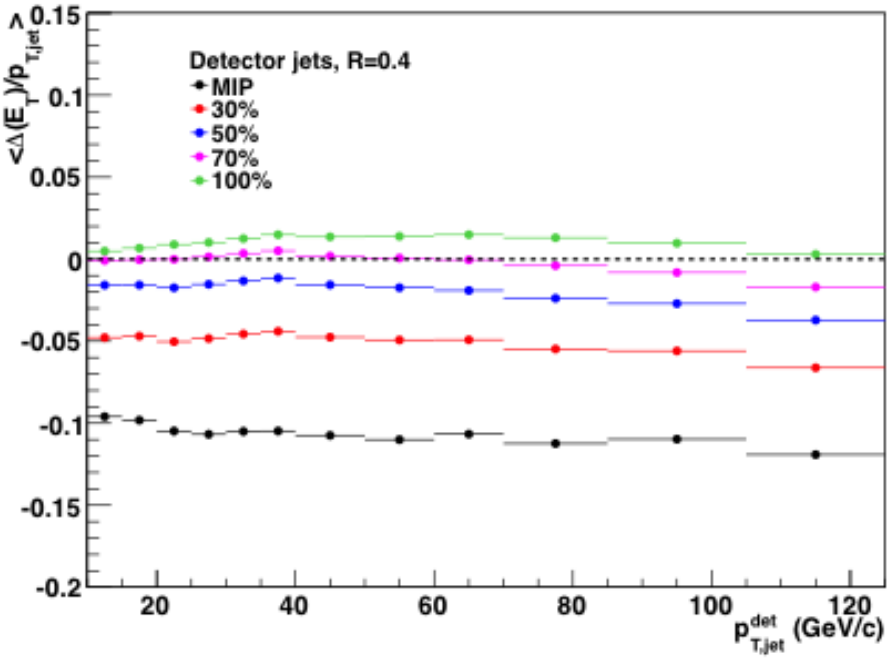

Figure 4.8: Mean relative over-subtracted energy as a function of jet p_T [55]. A subtraction of 70% provides a near zero over-subtraction for a large range of jet p_T.

Shown in figures 4.9 and 4.10 are the EMCal cluster η and φ distributions. Figure

4.11 shows the η-φ distribution in the EMCal which is obtained from a one-to-one matching of an EMCal cell ID to a $\eta - \phi$ position (figure 4.12). In figure 4.11, the EMCal super-module boundries are clearly visable by the white regions that run at constant φ along η. Other regions show a significant reduction of activity (blue and purple colored areas) when comparing to their surroundings. The most likely cause of this is dead electronics in the affected cells. Figure 4.13 shows the p_T distribution of EMCal clusters. Although the EMCal measures energy and not p_T, the p_T of the clusters can be reconstructed by using the event vertex along with the location of the cell (in $\eta - \varphi$ space) and assuming a massless neutral particle (90% of neutral particles will be π^0 with energies much larger than their mass).

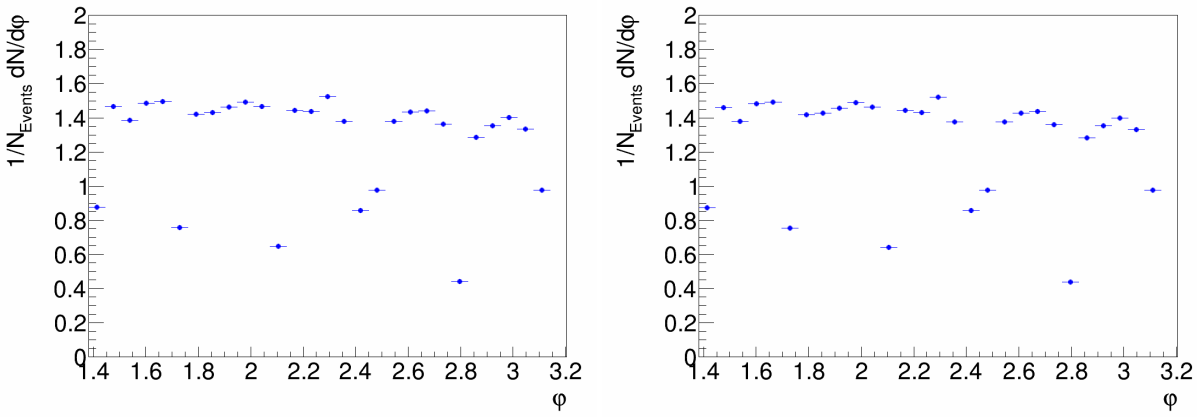

Figure 4.9: φ distribution of EMCal clusters (hadCorr = 2.0) in different p-Pb periods with minimum bias (kINT7) trigger. Left: LHC13b. Right: LHC13c.

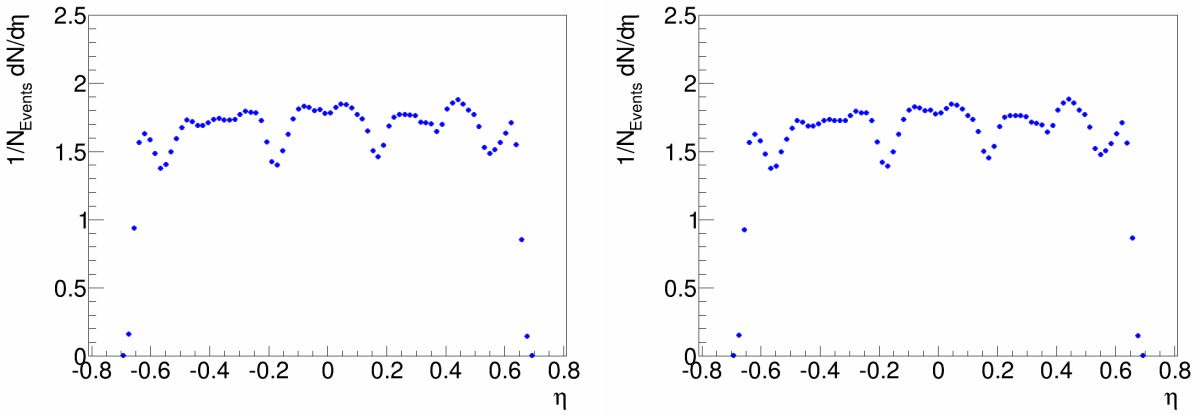

Figure 4.10: η distribution of EMCal clusters (hadCorr = 2.0) in different p-Pb periods with minimum bias (kINT7) trigger. Left: LHC13b. Right: LHC13c.

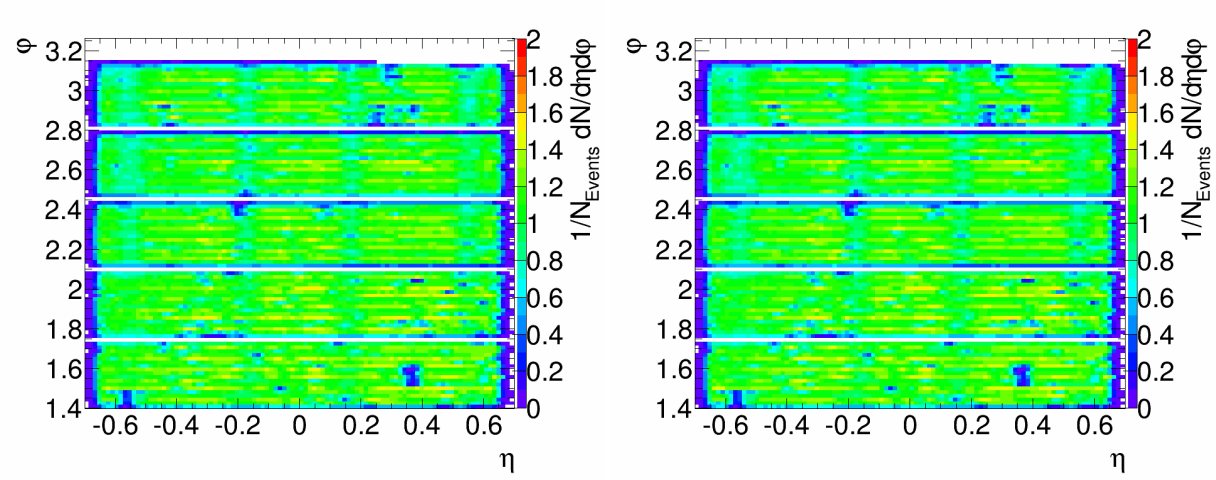

Figure 4.11: η-φ distribution of EMCal clusters (hadCorr = 2.0) in different p-Pb periods with minimum bias (kINT7) trigger. Left: LHC13b. Right: LHC13c.

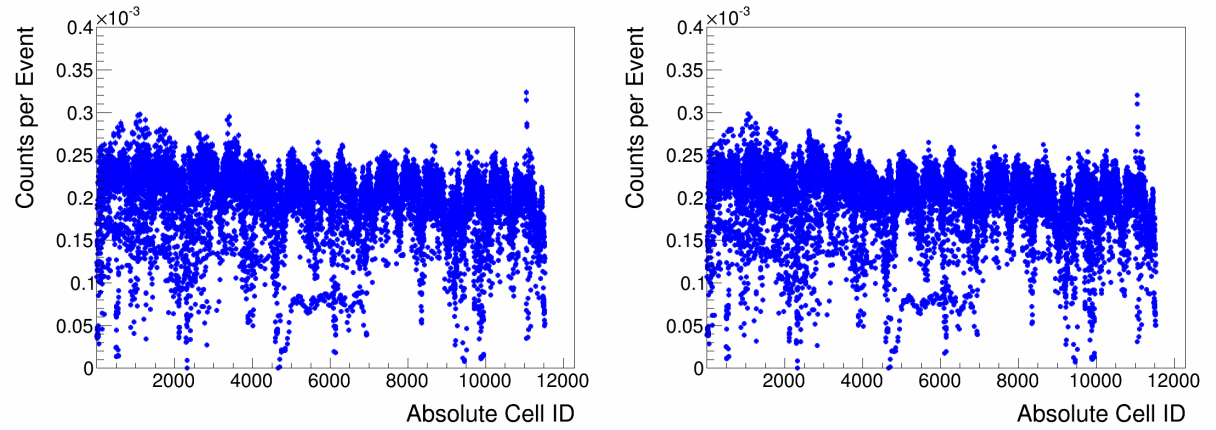

Figure 4.12: EMCal clusters cell ID counts per event in different p-Pb periods with minimum bias (kINT7) trigger. Regions of low cell counts correspond to low activity areas in figure 4.11. Left: LHC13b. Right: LHC13c.

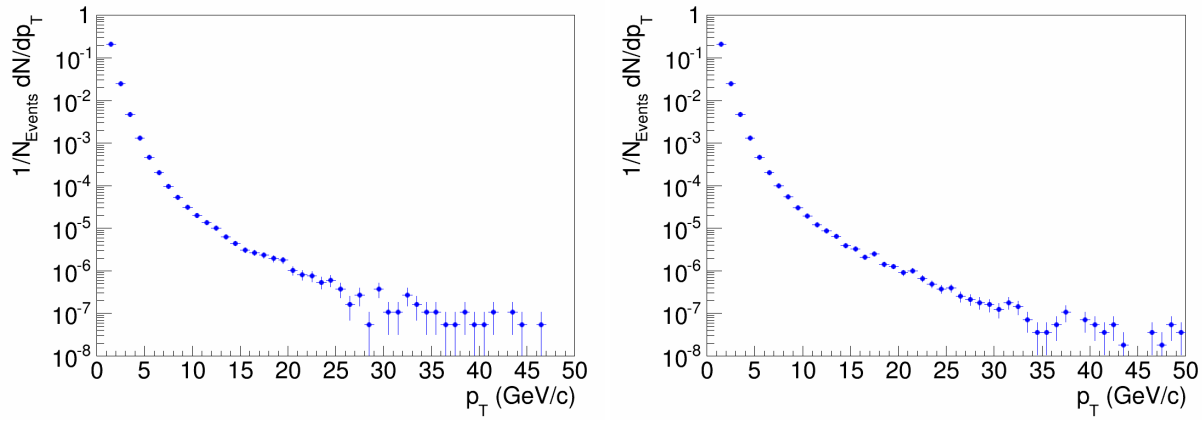

Figure 4.13: p_T distribution of EMCal clusters (hadCorr = 2.0) in different p-Pb periods with minimum bias (kINT7) trigger. Left: LHC13b. Right: LHC13c. The cluster p_T is constructed by using the event vertex.

4.4 Jet Selection

The kinematic properties of jets reflect the kinematic properties of the original hard partons from the hard scattering process. In order to fully recover the kinematic properties of the parton, it is required to recover all the hadrons the parton fragments into. This requires the jet to be sufficiently large (i.e. a large jet radius) such that all (or as much as possible) particles the parton has fragmented into can be recovered in the jet cone, and that the detectors used to measured the particles can detect all charged and neutral fragments. The partons fragment into hadrons which are either directly measured (i.e. the hadron has not decayed yet or is stable. e.g. protons) or the hadron decays into other particles (i.e. $\pi^0 \rightarrow \gamma + \gamma$) which are then measured in one of the ALICE detectors.

Once tracks and EMCal clusters have been measured and reconstructed, they are inputted into a jet algorithm which groups them together using various schemes and criteria. Algorithms of choice which will be used in this analysis are part of the `FastJet` package and described in [47, 48]. Here we shortly describe the jet finding and background subtraction methods to be used in this analysis. A more extensive description can be found in [49, 50]. Generic properties and requirements on jet algorithms are discussed in more detail in appendix B.

For this analysis, a *signal* jet is defined as a jet in which the reconstructed $p_{T,jet} > 5$ GeV/c (before background subtraction) with no constraints on the constituent p_T that make up the jet. All signal jets are reconstructed with the anti-k$_T$ jet algorithm of the `FastJet` package. The jets are only accepted if they are fully contained in the acceptance in which the constituents of the jet are measured. For charged jets: full azimuth and $|\eta_{jet}| < 0.9 - R$; full jets: $1.4 + R < \varphi_{jet} < \pi - R$ and $|\eta_{jet}| < 0.7 - R$. Jets with an area smaller then $0.6\pi R^2$ are rejected (see figure 4.14). This selection mostly removes jets that are at very low $p_{T,jet} < 20$ GeV after background rejection. In addition, jets containing a track with $p_T > 100$ GeV/c, for which the momentum resolution is worse than 20%, are rejected after performing the jet clustering. This selection has a negligible effect in the reported range of jet transverse momenta.

The Pb-Pb analysis uses a much higher $p_{T,jet}$ threshold for signal jets due to the very large background that any jet could "sit" on. Furthermore, due to the high particle multiplicities in Pb-Pb collisions, it is possible to have high p_T "fake" jets in which all its constituents are thermally produced low p_T particles. Thus, a consitituent p_T cut is also used. For p-Pb collisions, these constraints are not required due to much

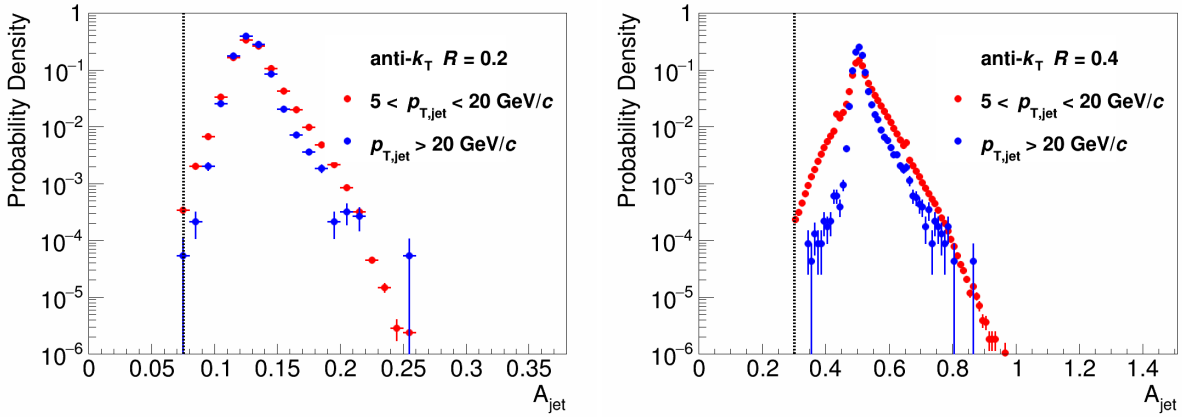

Figure 4.14: Probability density of jet area (A_{jet}) in steradians for signal jets. The area cut, given by $A_{jet} > 0.6\pi R^2_{jet}$ is the vertical black line. Left: $R = 0.2$. Right: $R = 0.4$.

lower particle multiplicities ($dN^{ch}/d\eta \sim 15$ and $\rho \sim 5$ GeV/c) compared to Pb-Pb ($dN^{ch}/d\eta \sim 1200$ and $\rho \sim 150$ GeV/c for 0-10% central events).

Figures 4.15 and 4.16 shows the azimuthal and pseudorapidity distributions of jets for jet radii 0.2 and 0.4 for the two periods of interest. The φ distribution in figure 4.15 at first might seem puzzling in that it has structure dependent on the jet radii. The reason for this is that at $R = 0.4$, because the signal jets must be fully contained within the detector and anti-k$_T$ will group together jet candidates that are sufficently close together to form jets, it isn't possible to have more than 2 jets in a strip of η along φ axis. Furthermore, no matter where one of the signal jets is, it is always possible to have a signal jet besides it. This explains the uniform behavior in φ. When a smaller radius is considered, the situation complicates in that now there is the possibility of several jets in the same strip of η and depending on where 2 jets lie in this strip along η, it is possible to have 0, 1, or 2 additional jets between those jets. This produces a cyclical behavior depending on the $\eta - \varphi$ positions of the 2 jets.

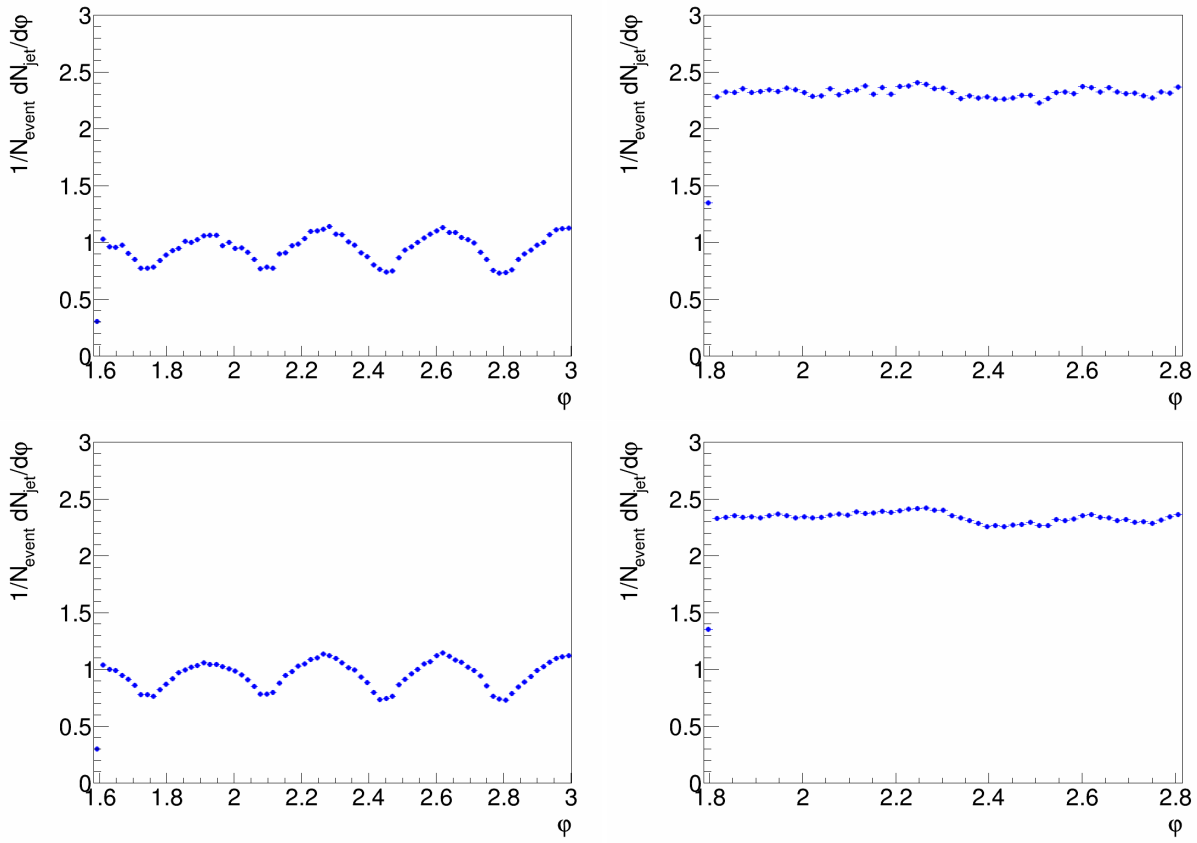

Figure 4.15: φ distribution of anti-k$_T$ full signal jets with $R = 0.2$ (left plots) and $R = 0.4$ (right plots) in different p-Pb periods with minimum bias (kINT7) trigger. Upper plots: LHC13b. Lower plots: LHC13c.

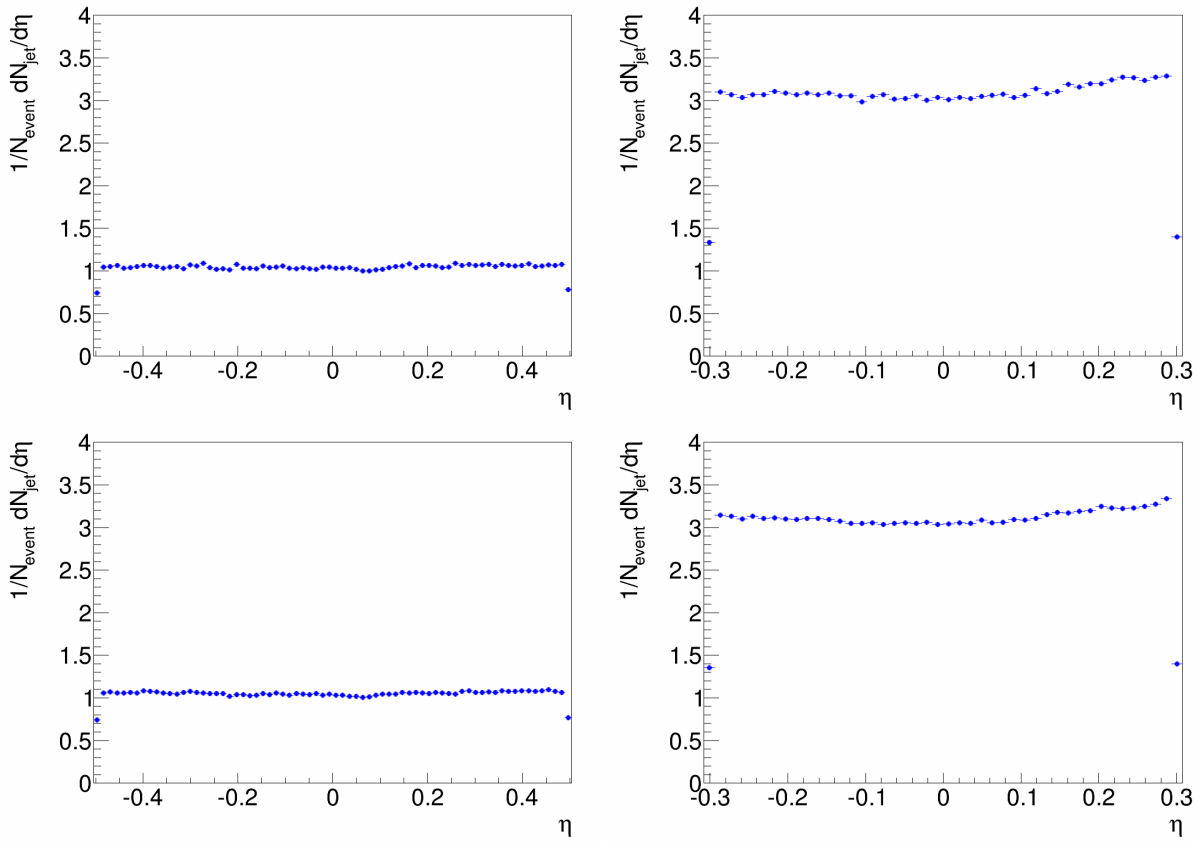

Figure 4.16: η distribution of anti-k_T full signal jets with $R = 0.2$ (left plots) and $R = 0.4$ (right plots) in different p-Pb periods with minimum bias (kINT7) trigger. Upper plots: LHC13b. Lower plots: LHC13c.

4.5 Underlying Event

There exists no unabiguous method to differentiate between a *signal* jet and the background (dominated by thermal production of hadrons [mainly pions] from the collision). As such it is desirable to reduce the contribution of background to the signal by attempting to exclude as much of the soft (i.e. low p_T) uncorrelated particles from the signal. Since it is impossible to detemine on a jet by jet basis which constituents are related to the initial hard scattering and subsequent fragmentation as opposed to those that are produced from uncorrelated background, a probabilistic approach is required.

When considering the background contribution to the signal jet, because it is assumed that the background particles are produced through thermal processes that are uncorrelated to the production of the signal jet, the transverse momentum of the signal jet can be broken into three pieces: the measured transverse momentum of the jet; a pedestal which is essentially the average particle transverse momentum per unit acceptance; and an event-by-event fluctuation which is related to the geometric position of those thermally produced particles relative to the jet vertex combined with the characteristic transverse momentum distribution of the thermal particles themselves. Schematically this can be representd by equation 4.2:

$$p_{T,jet}^{det} = p_{T,jet}^{meas} - \rho A_{jet} + F(p_T, A_{jet}) \tag{4.2}$$

Where ρ is the underlying event transverse momentum density and F(p_T,A_{jet}) is the background fluctuation spectrum (discussed in the section 4.6). The simplest approach for quantifiying ρ is to simply add the p_T of all particles within the detectors acceptance and divide by the acceptance itself. This crude approach would also include the entire signal as well as uncorrelated soft particles and will not be a good estimate of ρ by consistantly over estimating the background. More sophisticated approaches are required to estimate ρ accurately and will be discussed below.

4.5.1 Signal Removal Approach

To better estimate the underlying event density per unit of azimuth and rapidity, one could simply remove all signal jets from the event and calculate ρ:

$$\rho_{SR} = \frac{\sum_i p_T^i - \sum_j p_T^j}{A_{Detector} - \sum_j A_{jet}^j} \tag{4.3}$$

This method tends to over estimate ρ when the event is sparse (low multiplcity) and is thus not the most desirable method for measuring ρ in p-Pb collisions. The reason for this over estimation is that many particles that are produced via fragmentation in the hard partons that form the jet are not reconstructed in the signal jet due to geometric considerations (particles that fragment outside the jet cone radius would be considered background [uncorrelated to the jet] while in reality they are not!). Also, since the definition of the what a signal jet is cannot be unambiguous (just as the background cannot be measured in an unambiguous way), this could also produce potential biases in measuring ρ, particularly in high density environments. This method can provide a useful systematic check to the contribution of the underlying event on the jet spectrum.

4.5.2 Occupancy Median Approach

CMS [51] presents a median based method which also accounts for the emptiness of an event. This is neccessary for sparse events such as those in p-Pb. The emptiness is accounted for in the calculation of ρ:

$$\rho_{OMA} = \frac{median(p_{T,i} of k_T - cluster)}{A^i_{k_T - cluster}} xC \tag{4.4}$$

$$C = \frac{\sum_i A^i_{k_T - cluster}}{A_{Detector}} \tag{4.5}$$

where $C = Covered Area / Total Area$. The covered area is the area covered by real k_T jets and the total area is the covered area plus the area of the ghosts jets (see apendix B). This method was revised in ALICE to exclude signal jets which are defined as jets with $p_T > 5$ GeV/c as was done in the p-Pb charged jet analysis. A pictorial representation of the two algorithms used to calculate ρ are shown in figure 4.17. Figures 4.18 and 4.19 show the spectral and centrality dependent distributions. Measurements of ρ using the signal removal approach tend to produce higher values. This may be a result of jets which were not classified as signal jets and being included in the background estimation. The occupancy median approach estimate of the background is less sensitive to the jet radius then signal removal, which indicates that this method for background estimation is not as strongly correlated to jets (and more importantly what defines a *signal* jet). Both methods yield a higher ρ for more central events.

Figure 4.20 shows a comparison of the jet spectra for different underlying event subtraction methods to the jet spectra which is not corrected for underlying event sub-

traction. As can be seen, the cumulative effect of underlying event subtraction is small for sufficiently large $p_{T,jet}$ and even smaller when comparing between the occupancy median approach and signal removal.

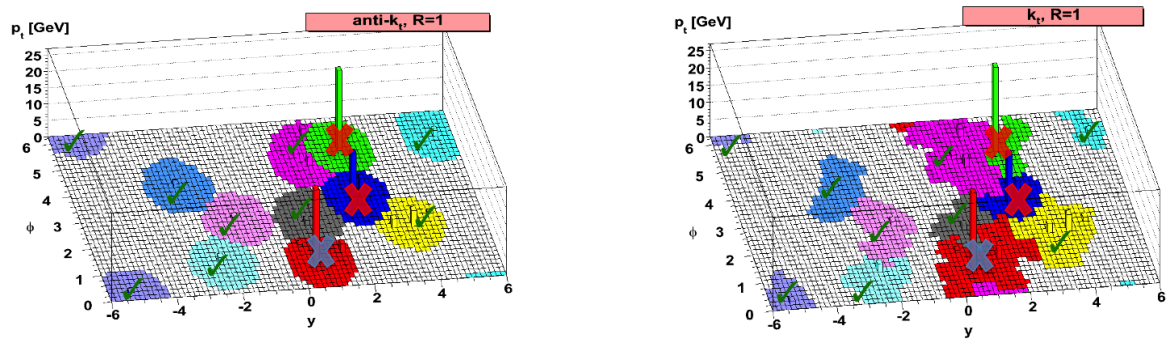

Figure 4.17: Schematic of ρ calcualting algorithms (adapted image from [51]). Left: Signal Removal Approach (section 4.5.1). Right: Occupancy Median Approach (section 4.5.2)

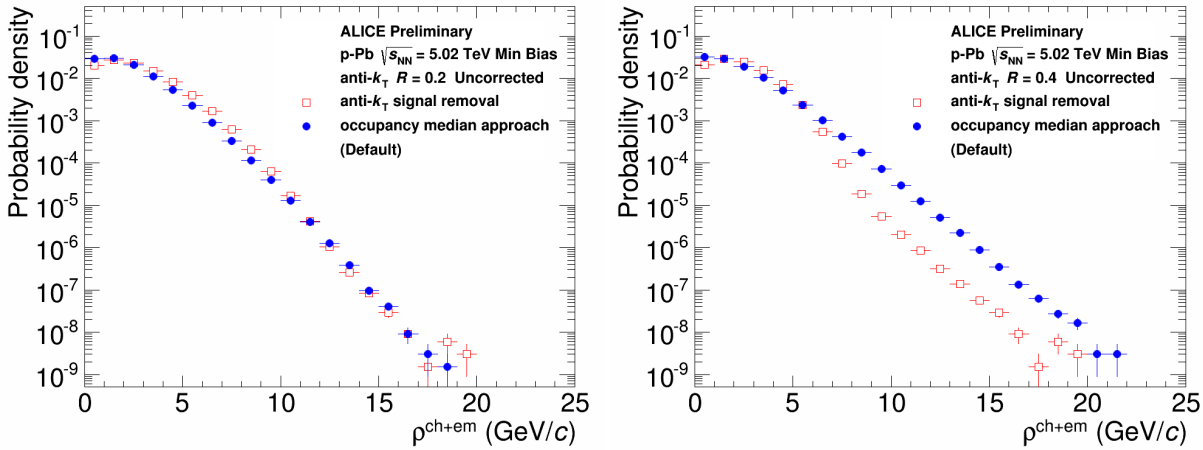

Figure 4.18: Spectral distributions of ρ. Left: $R = 0.2$. Right: $R = 0.4$

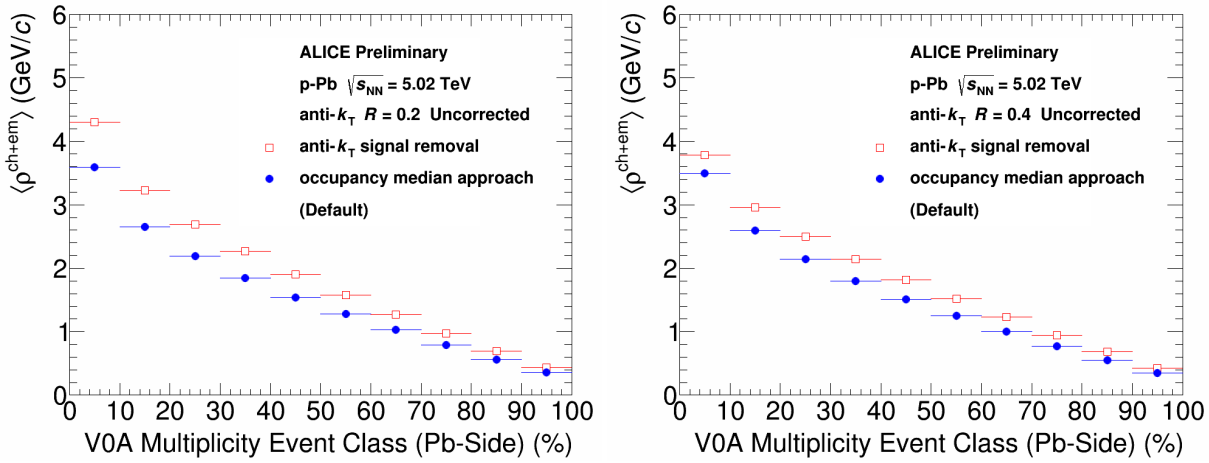

Figure 4.19: $\langle \rho \rangle$ vs V0A multiplicity class estimator. Left: $R = 0.2$. Right: $R = 0.4$

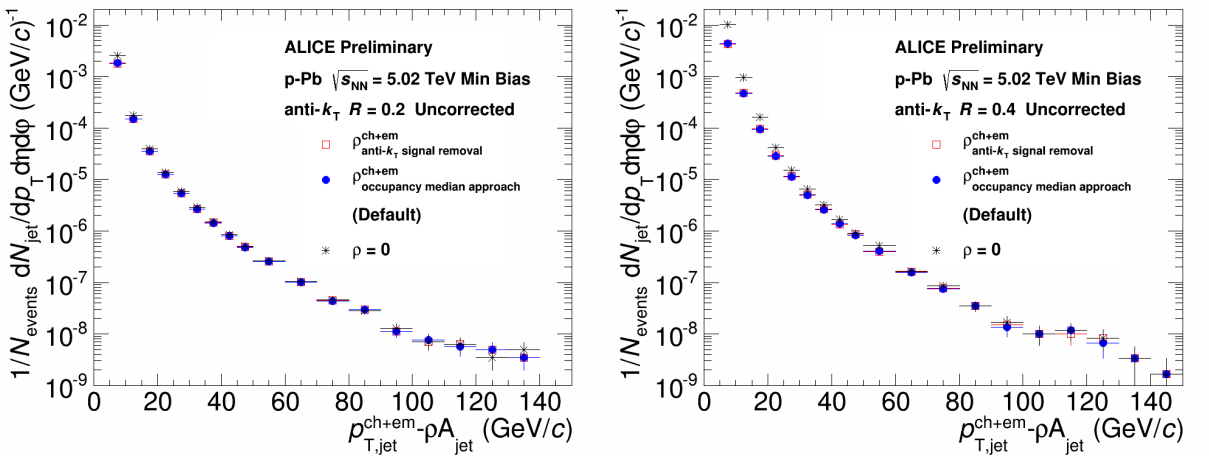

Figure 4.20: Comparison of jet spectra (uncorrected for detector effects) with and without underlying event subtraction. Left: $R = 0.2$. Right: $R = 0.4$

4.5.3 Scale Factor

In the Pb-Pb full jet spectra analysis [50], it was determined that the preferred way to calculate the underlying event for full jets was to measure ρ for charged particles and then multiply the energy density by a scale factor, s_{EMC}, to account for the neutral energy component. This procedure is neccessary to avoid large event-by-event charged to neutral fluctuations due to the limited size of the EMCal. The scale factor is measured according to Equation 4.6. The scale factor is the ratio of the total energy in the EMCal plus the total momentum of all charged track pointing in the EMCal acceptance divided by the total momentum of the charged tracks within the TPC accpetance. This is then normalized by the relative acceptances.

$$s_{EMC} = \frac{E_{EMC} + pT_{EMC}}{pT_{TPC}} \frac{A_{TPC}}{A_{EMC}} \tag{4.6}$$

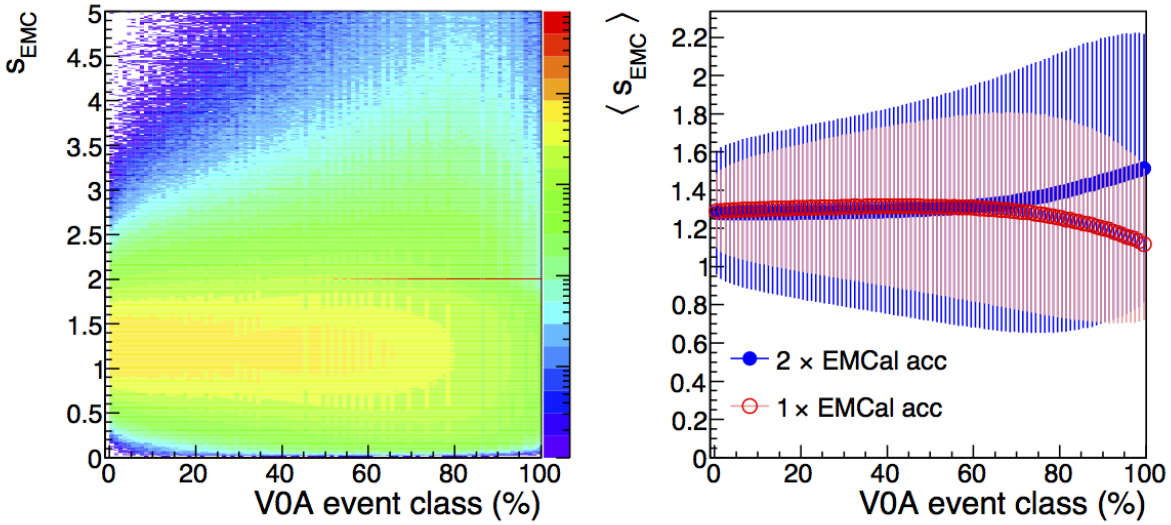

Figure 4.21: Left: 2D histogram showing the probability density of event for measured scale factor S_{EMC} as function of the V0A multiplicity class estimator. Right: $\langle S_{EMC} \rangle$ vs V0A multiplicity class estimator.

Cross checks in which the area is varied to determine the scale factor are also included in Figure 4.21 (right panel). Since it is not expected that the scale factor should have a centrality dependence in p-Pb collisions, s_{EMC} as a function of centrality is fitted with a flat line and a single value of 1.28 is used for all centralities. Figure 4.21 also shows the scale factor extracted considering twice the EMCal acceptance for the energy measured in the TPC. The error bars shown in the figure represent the standard

deviation of the average value. It can be observed that over a large range of V0A event classes, the two methods give consistent results (see appendix C for the definition of centrality in p-Pb collisions). The scale factor is independent of centrality for V0A event classes from 0% to 60% at a value of ∼1.28. For lower multiplicity events the average scale factor increases up to ∼1.43 in case twice the EMCal acceptance is considered and decreases to ∼1.13 in the case only the EMCal acceptance is considered. This deviation from a constant value is due to the 'emptyness' of events meaning there can be events which don't have EMCal clusters or tracks inside the considered acceptance for the calculation of the scale factor. For this analysis the scale factor $S_{EMC} = 1.28$ measured for the high multiplicity events will be used for all events. The scale factor is measured in the minimum bias event sample from the LHC13c p-Pb data period.

4.6 Background Fluctuations: δp_T

Background fluctuations are measured with the random cones technique which is also applied in the Pb-Pb analysis [52]. The contribution to the background fluctuations of different sources is studied by placing rigid cones with a radius equal to the resolution parameter R used for jet finding in the measured p-Pb events at a random position in η and φ while the cone is fully contained in the detector acceptance. This approach of using circular cones in the event to determine the background fluctuation spectrum is effective because the jet finding algorithm used to reconstruct the jets (anti-k_T) tends to produce circular jets (see appendix B). It is further assumed that these background fluctuations are independent of the jet transverse momentum. The background fluctuations are defined by calculating the difference between the summed p_T of all the tracks and EMCal clusters in the random cone (RC) and the estimated background transverse momentum a RC with an area equal to what a jet would have in uniform underlying event transverse momentum density:

$$\delta p_T = \sum_{i \in RC} p_T^i - \rho A \tag{4.7}$$

Where A is the area of the cone $A = \pi R_{jet}^2$. A random cone can overlap with a jet just as two "real" jets in a collision can overlap each other. Properly estimating the contribution of jet-jet overlap in p-Pb collisions is more crucial than in Pb-Pb collisions because the number of binary collisions (N_{coll}) is much lower. In order to avoid oversampling the probability that this happens in p-Pb collisions, a partial exclusion of

overlap with all signal jets in the event is applied. This is done by neglecting random cones overlapping with a signal jet with a given probability:

$$p = \frac{1}{N_{coll}} \tag{4.8}$$

Where N_{coll} is taken from estimates applying a Glauber fit [53]. For MB events, a N_{coll} = 6.88 is used. Three systematic variation for δp_T will be used in this analysis:

- Random cones including all overlaps with leading jets (p=1)
- Random cones with exclusion of all signal jets in every event (p=0);
- Random cones with partial exclusion ($p = \frac{1}{N_{coll}}$). This is the default method to be used throughout this analysis;

Figure 4.22 shows the background fluctuation δp_T for MB p-Pb events. Although significant differences can be seen in the tails ($p_T > 10$ GeV/c), 99% of statistics for δp_T are within 6 GeV/c for R=0.2 (8 GeV/c for R=0.4). Differences in the tails are expected based on which p value is used for signal exclusion because the larger the p value, the higher the probability of jet overlap. As the probability of jet overlap increases, it is expected that the spectrum (which is a power law spectrum) should flatten (i.e. a higher p_T tail). Also, as the radius of the cones increases, the background fluctuations in the cone increase, as expected.

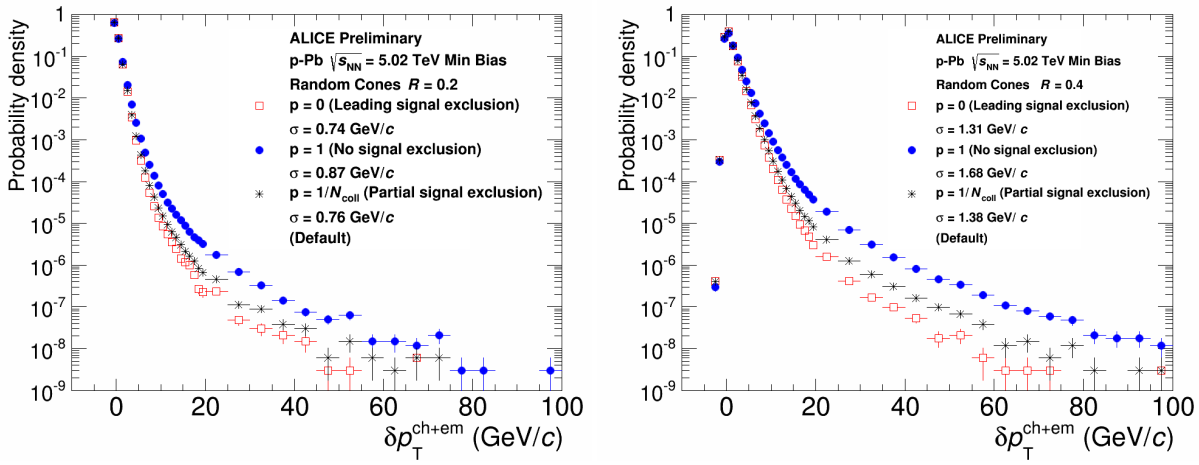

Figure 4.22: Background fluctuation δp_T for MB p-Pb events. Left: $R = 0.2$. Right: $R = 0.4$

4.7 Detector Response

In order to compare measured results from the ALICE detector to results from other experiments and to theoretical calculations, corrections must be applied to the measured spectra to account for detector imperfections, or so-called detector effects such as: tracking efficiency, transverse momentum resolution, faulty electronics, and various other effects. These detector effects will cause jets to be on average reconstructed at a lower p_T then its "true" p_T. This drop in $p_{T,jet}$ can be understood by either a loss in geometrical acceptance (some particles that were produced by the jet can escape the detector), tracking efficiency (not all tracks can be detected), minimum p_T threshold required to be detected in the detector, and other effects. These accumulated effects will be reflected by a shift in the jet energy scale. In order to correct for this shift, it is required to construct a *Response Matrix* which conveys information on how a jet with a given measured p_T compares to a jet measured in an ideal detector.

As done in the Pb-Pb analyses [49, 50] and the charged p-Pb analysis [54], detector effects are estimated using events created with PYTHIA [56] and GEANT [57]. PYTHIA generates the collision event containing the hard collisions and subsequent particle fragmentation from those hard collisions, while GEANT simulates the detector response.

The PYTHIA output is used to generate two distinct but correlated classes of jets: *particle-level* jets which are produced using event selection cuts and assuming a perfect detector (i.e. all particles are detected); and *detector-level* jets in which the PYTHIA output is transported through GEANT and then that output goes thorugh event selection cuts producing tracks and EMCal clusters. Thus, regardless of whether input is data from measurement or simulation, it will go through identical event selection, track cuts, and EMCal cluster cuts (see figure 4.1). For the p-Pb analysis, the following run numbers were choosen, one for each run period, to simulate the detector conditions: LHC13b Good(195351), LHC13c Semigood (195531).

Afterwards, a jet finder is run on both generated particle-level and detector-level particles to construct jets. These jets from particle and detector-level are matched geometrically and a pair is rejected if the angular seperation between detector-level and particle-level, ΔR, is larger than 0.25. Once matched, a probabilistic correspondence between the p_T of a detector-level jet and the p_T of a particle-level jet is achieved. These correspondences are what constitutes the elements of the detector response, which is used to correct measured jets for these detector effects. It should be stressed that the

purpose of this detector simulation is to get the response behavior of the detector to jets from p-Pb collisions which is an asymmetrical collision (see figures 4.4 and 4.10). However, PYTHIA generates jets from pp collisions, which are symmetric. Therefore a Lorentz boost must be applied on simulation to produce the same rapidity shift observed in data. PYTHIA also does not account for effects from the underlying event.

If PYTHIA creates jets with the p_T dependent probability (minimum bias jets) over the entire p_T range, a prohibitively large sample of events would be needed to achieve this high p_T reach with viable statistical precision. To circumvent this problem, PYTHIA can be configured to create events where the hard collisions p_T is in a given range - called a p_T hard bin. The productions used to create the response matrix consists of 10 bins. For each bin, roughly 1M events were created for the two productions. The edges of the common bins are defined by the numbers of the following set:

p_T hard bin edges: 5, 11, 21, 36, 57, 84, 117, 152, 191, 234, ∞ in GeV/c

For each p_T hard bin, the response matrix is created separately. The matricies can not be added directly as the events generated in each p_T hard bin are generated with their corresponding cross sections. The weighting is done with the following factors:

$$w_i = \frac{\sigma_i}{N_{trials}} \tag{4.9}$$

Where i denotes the hard bin, σ_i is the cross section, and N_{trials} is the number of trials needed to produce one event within a given p_T hard bin as defined in PYTHIA. The matrices are scaled with these factors and merged together. The nominal dectector responses for the jet radii are shown in figure 4.23. The jet energy shift, which is referred to as the detector resolution and is given by:

$$\Delta p_{T,jet}(part, det) = \frac{p_{T,jet}^{det} - p_{T,jet}^{part}}{p_{T,jet}^{part}} \tag{4.10}$$

and is the relative fraction of energy missing in a detector-level jet compared to a matched particle-level jet. The detector-level jet can contain more energy then a particle level jet because of boundary effects, tracking efficiency, and particle migration that can occur after transporting through GEANT that can cause additional particles to be clustered in the detector-level jet that are not clustered in the particle-level jet. Figures 4.24 and 4.25 show projections of the detector resolution for a given $p_{T,jet}^{part}$ bin along with the mean jet energy shift vs $p_{T,jet}^{part}$.

Detector imperfections are expected to not recover the full energy of the jet at particle-level which is seen as a negative shift in the JES for all $p_{T,jet}^{part}$ bins. Furthermore, when using a larger jet radius, more particles are captured at detector-level producing a peak in the JES closer to 0.

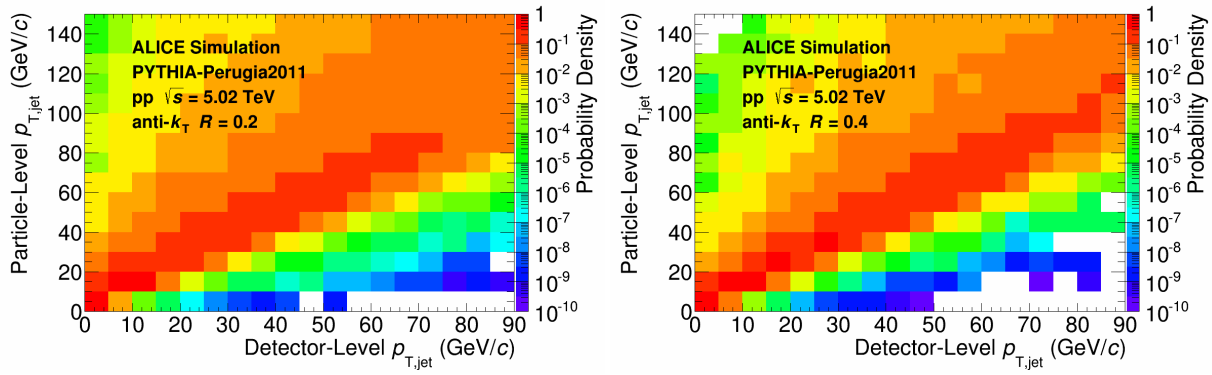

Figure 4.23: Nominal detector response. By nominal it is meant that 100% tracking efficiency is used along with a hadCorr of 2.0 to reconstruct tracks and EMCal clusters once particles are transported through GEANT but before particle are feed into jet finders. Period lhc13c was used for the nominal detector response because it has more p-Pb events then lhc13b. Left: $R = 0.2$. Right: $R = 0.4$

Before the detector response can be used to unfold the measured jet spectra, that can be compared to other experiments and/or theory and to validate the particular PYTHIA tune used, it is necessary to ensure that the detector-level jets have similar characteristics to those that are measured in data. If this holds, then it will be reasonable to assume that the detector response will provide the correct particle-level spectra once the measured data are unfolded. This analysis utilizes two important tests to ensure that the neutral energy fraction (NEF) of jets and the leading constituent p_T distribution in jets shows agreement between simulation (PYTHIA) and measurement. The NEF test was chosen as it shows how well both the tracking and EMCal clusters were simulated (see figures 4.26 and 4.27).

The leading constituent p_T in jets, defined as:

$$z_{leading}^{const.} = \frac{p_{T,leading}^{const.}}{p_{T,jet}} \tag{4.11}$$

shows how well the fragmentation of jets in simulation and measurement agree (see figures 4.28 and 4.29). The excellent agreement between the measured NEF and $z_{leading}^{const.}$ for jets in the given data periods to the simulated PYTHIA events transported

through GEANT anchored to the same data periods detector conditions implies that the detector is properly simulated and these results can be used in unfolding the jet spectrum for detector effects.

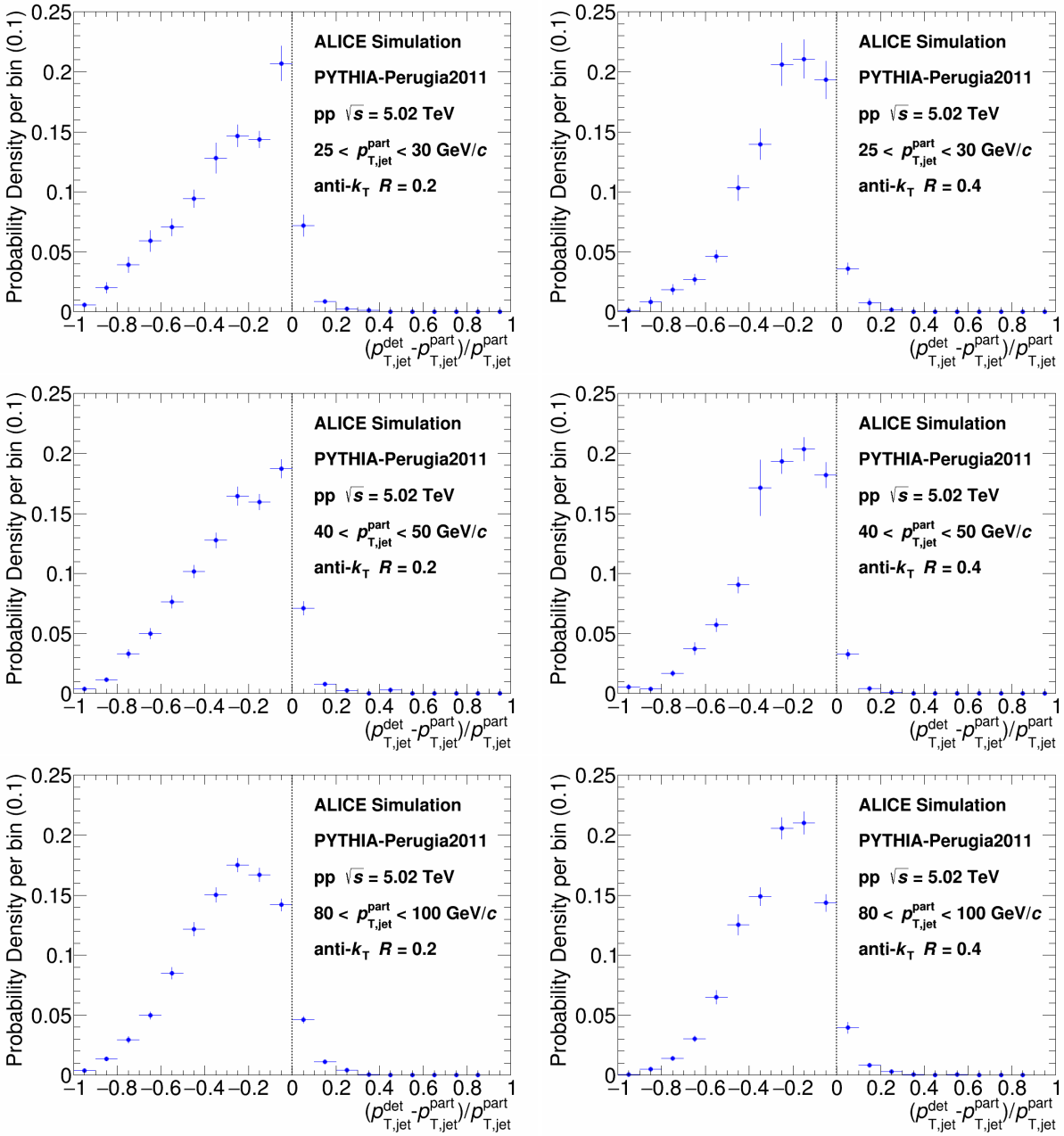

Figure 4.24: Jet energy shift between particle-level and detector-level jets for the nominal detector response. Upper panel: $25 < p_T^{part} < 30 GeV/c$. Middle panel: $40 < p_T^{part} < 50 GeV/c$. Lower panel: $80 < p_T^{part} < 100 GeV/c$. Left: $R = 0.2$. Right: $R = 0.4$.

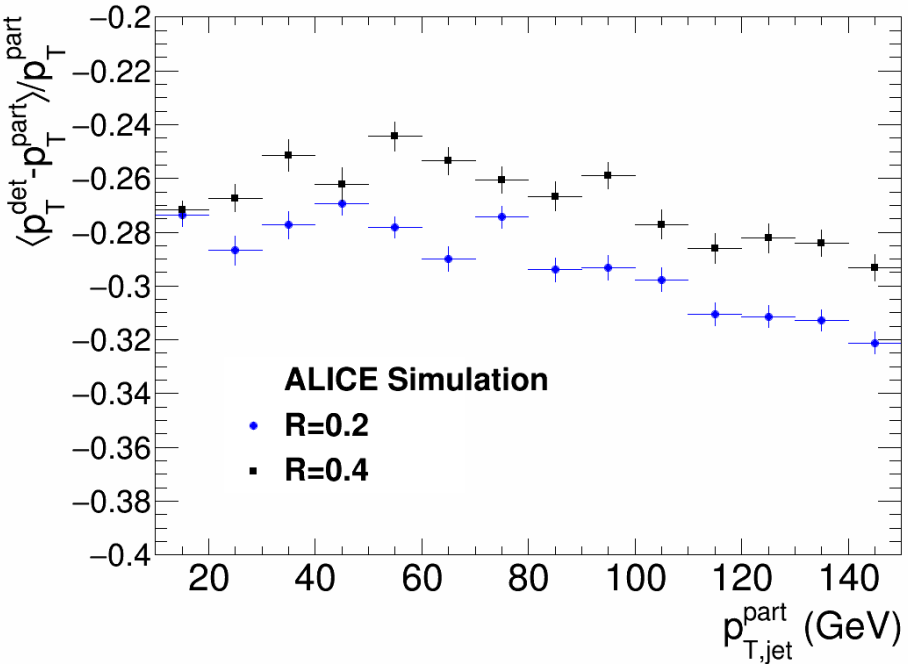

Figure 4.25: Mean jet energy shift between particle-level and detector-level jets for the nominal detector response. Left: R = 0.2. Right: R = 0.4.

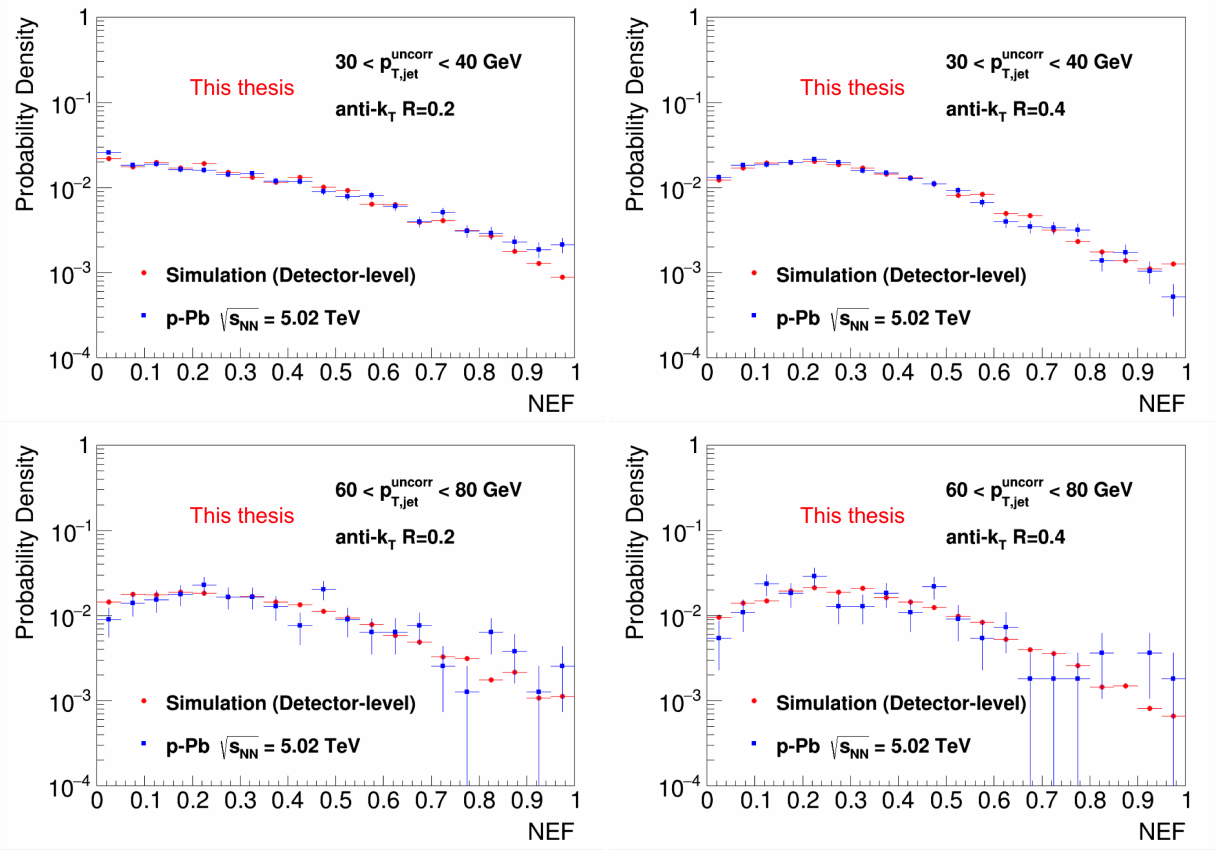

Figure 4.26: Comparison of NEF for measured jets to simulated detector-level jets using the nominal detector response. Upper panel: $30 < p_{T,jet}^{uncorr} < 40$ GeV/c. Lower panel: $60 < p_{T,jet}^{uncorr} < 80$ GeV/c. Left: $R = 0.2$. Right: $R = 0.4$.

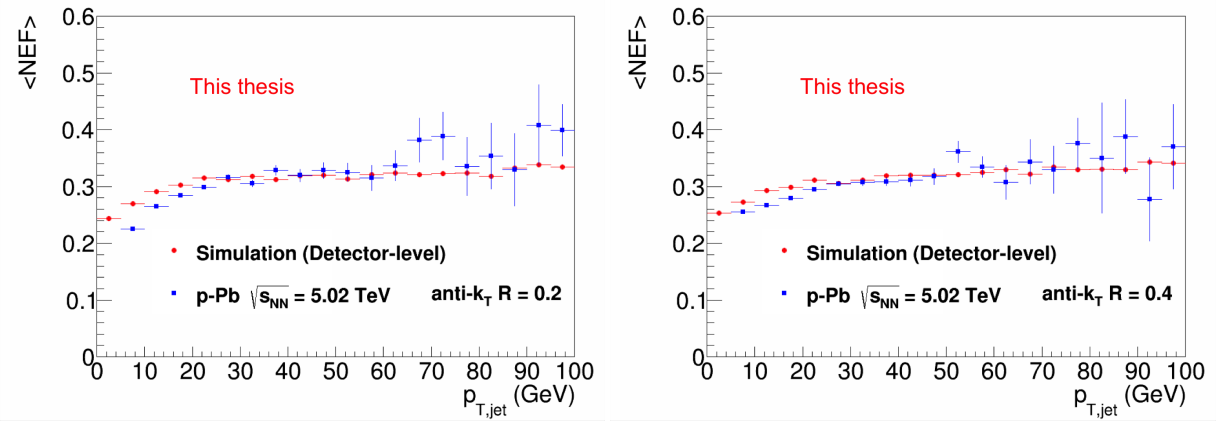

Figure 4.27: Comparison of mean NEF for measured jets to simulated detector-level jets using the nominal detector response. Left: $R = 0.2$. Right: $R = 0.4$.

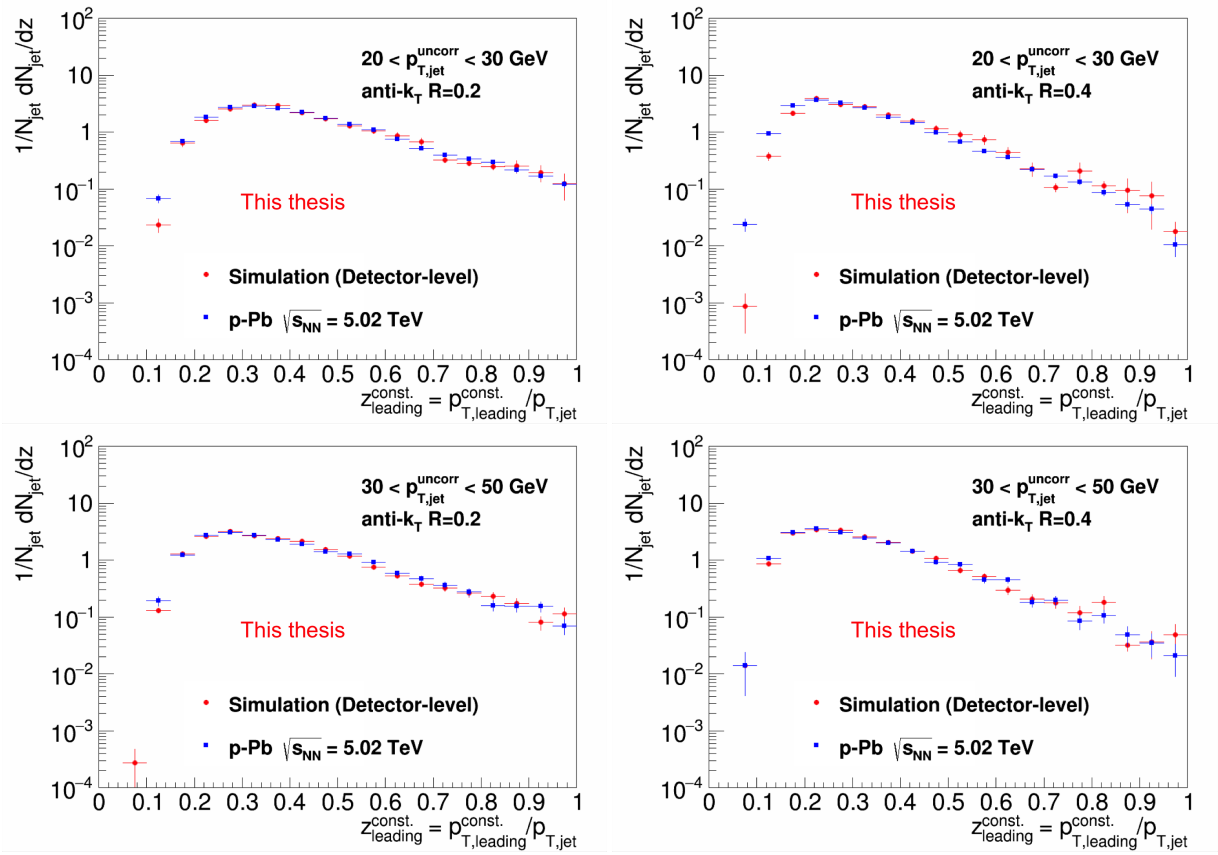

Figure 4.28: Comparison of leading constituent p_T distribution in jets for measured jets to simulated detector-level jets using the nominal detector response. Upper panel: $20 < p_{T,jet}^{uncorr} < 30$ GeV/c. Lower panel: $30 < p_{T,jet}^{uncorr} < 50$ GeV/c. Left: $R = 0.2$. Right: $R = 0.4$.

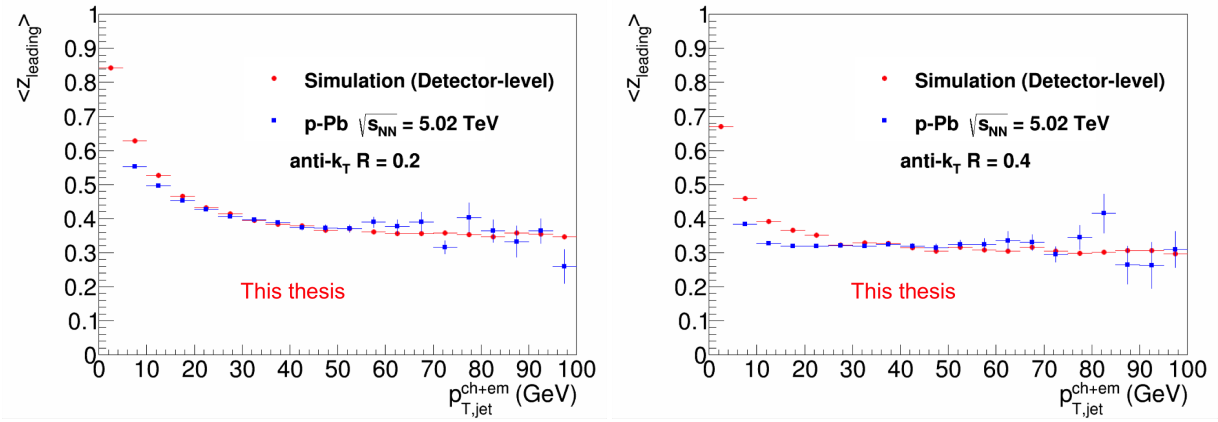

Figure 4.29: Comparison of mean leading constituent p_T distribution in jets for measured jets to simulated detector-level jets using the nominal detector response. Left: $R = 0.2$. Right: $R = 0.4$.

4.8 Unfolding

As mentioned in section 4.7, in order to compare experimental measurements in ALICE to theoretical calculations and to measurements from other experiments, a correction procedure to account for detector effects must be applied. The goal of section 4.7 was to outline how to obtain a correspondence between the measured data in ALICE and the true distribution from MC simulations (PYTHIA). This section address how these detector corrections, along with corrections from background fluctuations explored in section 4.6 are applied to the measured spectrum to recover the "true" distribution. This procedure is referred to as *unfolding*.

The measured spectrum $f(m)$, true distribution $g(t)$, and resolution function $R(m,t)$ are related by the following formula:

$$f(m) = \int g(t)R(m,t)dt \tag{4.12}$$

The resolution function $R(m,t)$ shows the correspondence between the measured data points and the true distribution (the truth). Because there is not a 'one-to-one' correspondence between particular values of measured data points and the truth, the effect of $R(m,t)$ results in a "smearing" of the truth spectrum. What is needed is to invert this process; to recover the truth spectrum from the measured data points. Since the measured data points are not continuous, there is a binning for $f(m)$ and thus $R(m,t)$. Finite resolution alters equation 4.12 to:

$$\mathbf{m} = \mathbf{Rt}, \tag{4.13}$$

where **m** and **t** are vectors representing the measured and truth distributions, and **R** is the response matrix. For this analysis, the response matrix is a combination of two effects: smearing caused by background fluctuations (see section 4.6) along with smearing caused by detector effects (see section 4.7). Detector effects cause the truth distribution to be smeard by **D** resulting in an 'intermediate' jet spectrum referred to in section 4.7 as the detector-level **d**. The background fluctuations further smear **d** producing the measured spectrum **m**. This smearing, which is assumed to be independent of jet p_T, is what is accounted for in δp_T. Its corresponding response matrix **B** is shown in figure 4.30.

These two effects are combined in a singular matrix which is called the *Combined*

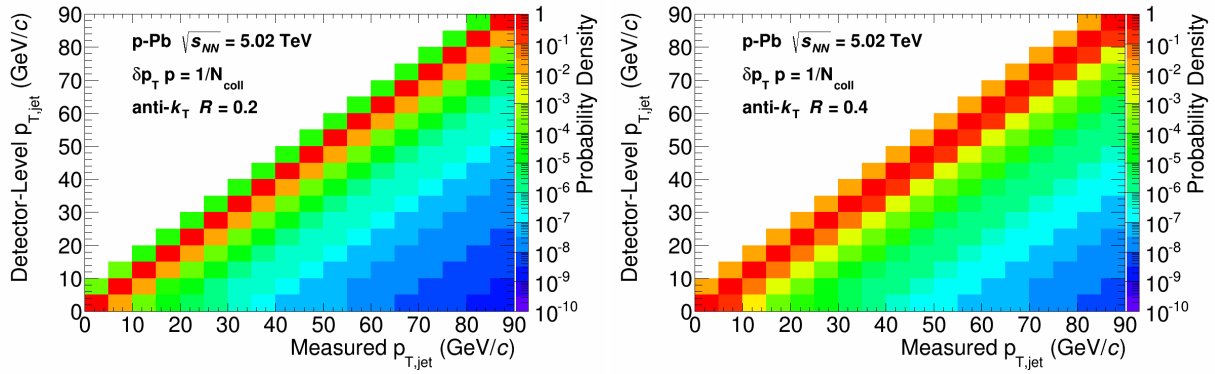

Figure 4.30: δp_T Response Matrix $B(m,d)$. Left: R = 0.2. Right: R = 0.4

Response Matrix and is a convolution of **B** and **D**:

$$R_{mt} = B_{md} D_{dt} \tag{4.14}$$

The combined response matrix will be used thorughout this analysis to unfold the measured spectra, and will be referred to as $R(m,t)$ or simply **R**. Figure 4.31 shows the combined response matrix. As expected, the effect of background fluctuations is reduced for smaller jet radii.

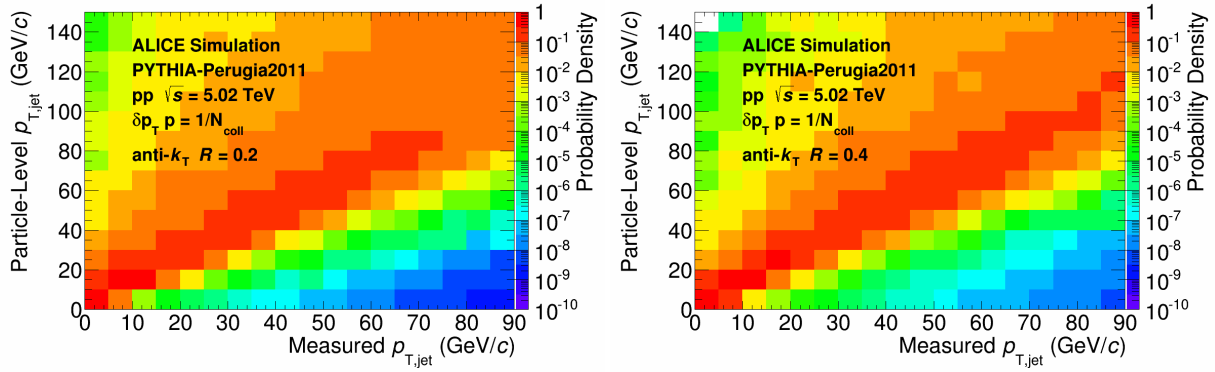

Figure 4.31: Combined Response Matrix $R(m,t)$. Left: R = 0.2. Right: R = 0.4

In principal if an inverse of **R** can be found, then the solution for **t** can be found by: $\mathbf{t} = \mathbf{R}^{-1}\mathbf{m}$. However, the inversion of **R** is only adequate when $R(m,t)$ is nearly diagonal. Unfortunately, this is not the case in all experiments where in practice large 'off-diagnal' terms exist in **R** (see figure 4.31). This causes the inversion of the response matrix to be an *ill-posed problem* and would result in any vector (spectrum) which is obtained from inverting **R** to be highly fluctuating and thus could lead to a non-physical solution to the problem. More sophisticated techniques must be employed to acheive

this inversion. This is accomplished with various unfolding algorithms which use regularization schemes to improve the stability of the unfolded spectrum. The two most commonly used unfolding algorithms, and the only two that will be used in this analysis, are Bayesian [58] and Sigular Value Decomposition (SVD) [59]. These algorithms are implemented in the `RooUnfold` package [60] which is used in this analysis.

To validate the unfolding procedure, it is instructive to compare the measured spectrum to the "refolded" spectrum, which is the truth spectrum from unfolding the measured spectrum folded with the combined response matrix. Figure 4.32 shows the measured spectrum, unfolded (truth) spectrum, and the refolded spectrum. If the refolded spectrum does not agree with the measured spectrum to high precision (in the appropriate kinematic reach, see section 4.8.4), then the recovered truth spectrum from unfolding is a mathematically invalid solution and should be rejected.

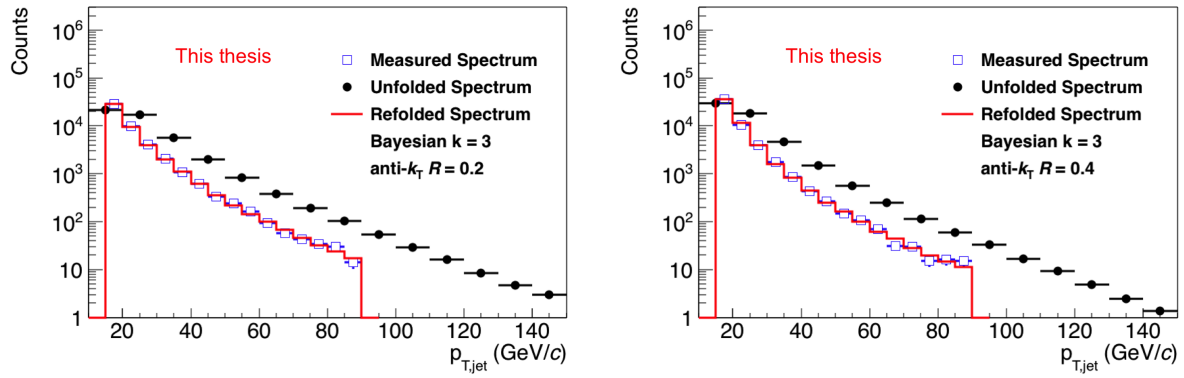

Figure 4.32: Comparison of measured jet spectrum, unfolded (truth) jet spectrum, and refolded jet spectrum. Left: R = 0.2. Right: R = 0.4

4.8.1 Bayesian Approach

In order to obtain the *Unfolding Matrix* $\mathbf{R}^{-1}$ (which will be called M_{ij} in this section), Bayes theorem is applied iteratively to invert $\mathbf{R}$. Starting with Bayes theorem:

$$P(A|B) = \frac{P(B|A)P(A)}{P(B)}, \tag{4.15}$$

and a restatement of the total probability for $P(B)$ given as:

$$P(B) = \sum_j P(B|A_j)P(A_j), \tag{4.16}$$

4.15 can be rewritten as:

$$P(A_i|B) = \frac{P(B|A_i)P(A_i)}{\sum_j P(B|A_j)P(A_j)}, \tag{4.17}$$

where A refers to the truth distribution and B refers to the measured distribution. As such, $P(B|A)$ is the probability of recording a measured event B given a truth of A and is thus the physical interpretation of the response matrix. It's "inverse" is consequently the term on the left-hand side of 4.17 which can be redefined to accommodate discrete distributions as:

$$M_{ij}^k = \frac{P(F_j|G_i)N_{k-1}(G_i)}{\epsilon_i \sum_l P(F_j|G_l)N_{k-1}(G_l)}, \tag{4.18}$$

where F_j are the measured counts for the measured bin j, G_i are the truth counts for truth bin i, ϵ_i is the efficiency for each truth bin i, and N_k is the k^{th} iteration of the unfolded distribution. For M_{ij}^1, which is the result after the first iteration, an initial "guess" of the unfolded distribution is needed in order to initiate the procedure. This guess is referred to as a *Prior Distribution* and can either be the measured distribution itself (after proper rebinning), a distribution obtained from a MC study, or even a uniform distribution. Once M_{ij}^k is calculated, the unfolded spectrum for the k^{th} iteration is given by:

$$N_k(G_i) = \sum_j M_{ij}^k N(F_j) \tag{4.19}$$

Once $N_k(G_i)$ has been calculated, the next iteration of M_{ij} can be computed by taking this result and inserting it back into 4.18. The process is terminated once a certain number of iteration are performed in order to produce a spectrum that is not fluctuating considerably bin-to-bin. If the inversion of $\mathbf{R}$ is stable then the final answer ($N_k(G_i)$) should not vary strongly with regularization strength (k), choice of prior ($N_0(G_i)$), and the unfolding and measurement ranges used (values of i and j). In this analysis, these unfolding parameters will be varied in order to determine the systematic uncertainties associated to the unfolding procedure.

4.8.2 Singular Value Decomposition (SVD)

In linear algebra, any matrix **R** can be factorized as a rotation, followed by a scaling, and finally another additional rotation. Mathematically, it takes the form:

$$\mathbf{R} = \mathbf{U}\Sigma\mathbf{V}^{\top}, \tag{4.20}$$

where matrix **U** is mxm, matrix Σ is mxn, and matrix **V** is nxn. Such a factorization is referred to as a *Singular Value Decomposition*. Since **U** and **V** are complex unitary matricies, then Σ is a rectangular diagonal matrix. The diagonal terms of Σ, s_i, are called the *singular values*. Using this representation, it can easily be seen that the measured distribution can be related to the truth distribution by:

$$\mathbf{U}\Sigma\mathbf{V}^{\top}\mathbf{t} = \mathbf{m} \tag{4.21}$$

If an inverse of Σ exists, then **t** can be computed from **m**:

$$\mathbf{t} = \mathbf{V}\Sigma^{-1}\mathbf{U}^{\top}\mathbf{m} \tag{4.22}$$

The difficulity lies in finding the singular values (s_i). Once these can be found, Σ^{-1} can be calculated using standard inversion techniques for matrices. Furthermore, there are usually statistical uncertainties in **m**. One approach [59] is to minimize the χ^2 of the following:

$$\sum_i \left(\frac{\sum_j R_{ij}t_j - m_i}{\Delta m_i}\right)^2 = (\mathbf{Rt}-\mathbf{m})^{\top}\mathbf{C}^{-1}(\mathbf{Rt}-\mathbf{m}) = min, \tag{4.23}$$

where **C** is the covariance matrix of the measured distribution **m**. Rescaling is done such that $t_j = w_j t_j^{prior}$. The unfolded vector to be recovered is now **w**. This also rescales **R** and **m** to **P** and **q** respectively. This rescaling is desirable because t_j^{prior} is motivated from MC simulation and should be in general close to the true distribution. Furthermore, because **w** should satisfy some "smooth" conditions in that it should not vary considerably bin-by-bin, its decomposition will not require as much regularization which is expected to make its unfolded solution more accurate.

The regularization is achieved using the following integral:

$$s[g(t)] = -\int \frac{d^k g(t)}{dt^k} dt, \tag{4.24}$$

where k is the regularization strength. In principal, this regularization function 'smoothens' the k^{th} derivative of the truth distribution (e.g. if k=2, the 'curvature' is smoothened). The regularization can be applied to 4.23 by adding a term:

$$(\mathbf{Pw}-\mathbf{q})^{\top}(\mathbf{Pw}-\mathbf{q})+s_k^2\cdot(\mathbf{Dw})^{\top}(\mathbf{Dw})=min, \tag{4.25}$$

where **D** is a matrix which specifies conditions on the solution with weights of s_k^2 for regularization strength k. **D** in this application is the "second derivative curvature matrix" (see [59] for more technical details) and can be inverted using standard techniques. SVD can now be used to decompose the matrix $\mathbf{PD}^{-1} = \mathbf{U\Sigma V}^{\top}$. Afterwards, one can rotate **q** and **Dw** and write:

$$\mathbf{d}=\mathbf{U}^{\top}\mathbf{q} \tag{4.26}$$

$$\mathbf{z}=\mathbf{V}^{\top}\mathbf{Dw}, \tag{4.27}$$

so that the system can be written now as:

$$d_i=s_i\cdot z_i \tag{4.28}$$

The effect of introducing the regularization s_k^2 is such that the vector **d** transforms to:

$$d_i^k=\frac{d_i s_i^2}{s_i^2+s_k^2}, \tag{4.29}$$

which leads to the regularized solution $\mathbf{w}^k$:

$$z_i^k=\frac{d_i s_i}{s_i^2+s_k^2} \tag{4.30}$$

$$\mathbf{w}^k=\mathbf{D}^{-1}\mathbf{V}\mathbf{z}^k \tag{4.31}$$

It can now be seen how nonzero s_k regularizes the singularities due to small s_i, effectively working as a cutoff for a low-pass filter [59].

The stability of SVD unfolding relies on not having large bin-by-bin fluctuations. Large bin-by-bin fluctuations in general require larger regularization strength to be needed. Thus, if there are any bins in the measured spectrum which have a "jump-

discontiuity", an infinite curvature (k) would be required in the unfolding. For such spectra, unfolding using the Bayesian method would produce a more stable result. This aspect is highlighted in detail in sections 5.4.1 and 5.4.2 for this particular analysis, and is a feature caused by a sparse background. This is the main motivation behind using the Bayesian unfolding method for the spectras in this thesis.

4.8.3 Jet Finding Efficiency

In the process of generating the detector response matrix **D**, jets on particle-level must be generated, propogated through GEANT, and then the corresponding detector-level jet are created. There is a finite probability that a jet generated on particle-level within the detector acceptance can migrate out of the detector acceptance once propagated through GEANT so that the jet finder when run on detector-level will not be reconstructed (consequently the opposite migration, particle-level jets produced outside the detector acceptance migrating to within the acceptance can also occur). The detector response matrix does not contain this information which is needed to properly normalize the jet spectrum. As such, the *Jet Finding Efficiency* has to be introduced to account for these effects and can be calculated from simulation and used for correcting the jet spectrum. As a function of particle-level $p_{T,jet}^{ch+em}$, it is given by:

$$\epsilon_{jet}(p_{T,jet}^{ch+em}) = \frac{N_{matched}}{N_{particle-level}^{jets \in acceptance}} \tag{4.32}$$

To avoid an artifical decrease in ϵ_{jet} due to edge effects, only particle-level jets which are generated within the detector acceptance are counted in the denominator in 4.32. There are no constraints on the detector-level jets so long as a match is found. Figure 4.33 showns the jet finding efficiency for simulated pp events from PYTHIA Perguia2011. For both radii, it is roughly a percent effect and is therefore negligible.

4.8.4 Kinematic Efficiency

All measured p_T bins are not statistically significant in that if the number of counts are too low, hence causing large statistical uncertainties. This in turn will cause instabilities in the unfolding procedure. Also, if a bin is contaminated by combinatoric jets that are not reproduced in simulation, those measured bins should also not be unfolded because unfolding preserves the integral (number of total jets in the spectrum). As such, for this analysis only measured p_T bins with at least 10 counts are considered

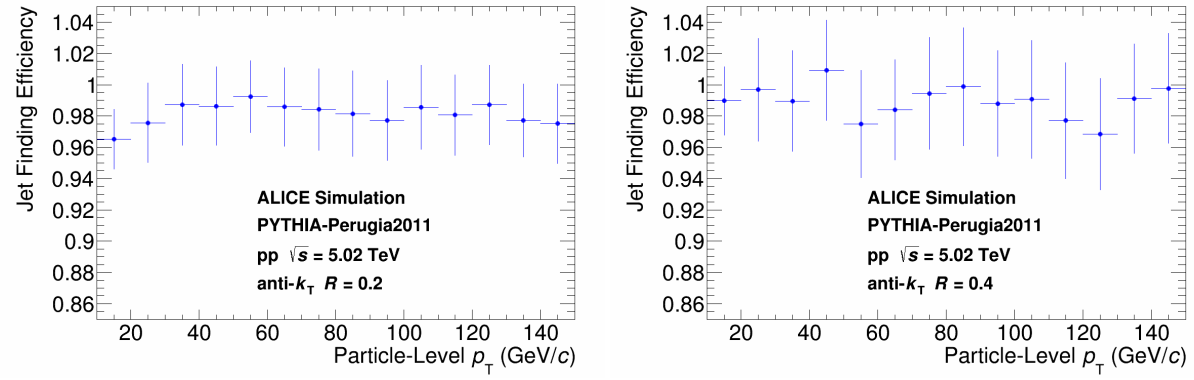

Figure 4.33: Jet Finding Efficiency $\epsilon_{jet}(p_{T,jet}^{ch+em})$ for simulated pp events in PYTHIA Perguia2011. Left: R = 0.2. Right: R = 0.4

(for a high p_T cutoff) and bins with a jet p_T > 10-15 GeV/c (which is the cumulative smearing of detector effects and background fluctuations). These statistical limitations will cause only a certain portion of the p_T range to be unfolded. This truncated kinematic reach will cause some particle-level jets that are reconstructed to 'drift' outside the kinematic reach once they have been smeared by background fluctuations and detector effects. The loss in efficiency of unfolded jets is referred to as the *Kinematic Efficiency*. For this analysis, only p_T ranges in which the kinematic efficiency is larger than 80% are considered, and the jet spectrum is corrected for by this kinematic efficiency by applying the values in figure 4.34 in the appropriate range.

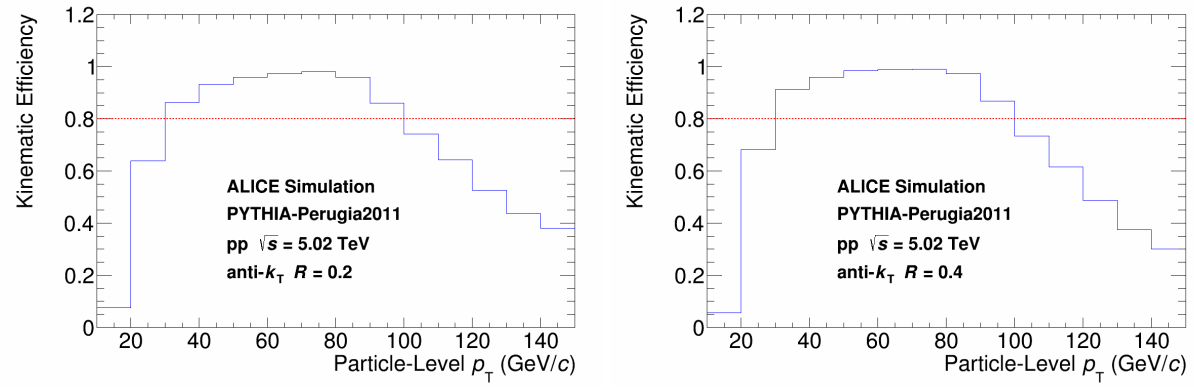

Figure 4.34: Nominal Kinematic Efficiency as a function of particle-level jet transverse momentum $p_{T,jet}^{ch+em}$. Left: R = 0.2. Right: R = 0.4

CHAPTER 5

Minimum Bias Jet Results

In this chapter, so-called *Minimum Bias* results regarding jet observables which are integrated over all centralities will be presented. The three observables that will be discussed are the jet spectra for $R = 0.2$ and $R = 0.4$; the *Jet Structure Ratio* of $\frac{R=0.2}{R=0.4}$; and the *Nuclear Modification Factor* (R_{pPb}) for jets using a PYTHIA pp jet spectrum from simulation as the reference for both $R = 0.2$ and $R = 0.4$. Furthermore, a comparison of various MC tunes and scaling of other measured pp spectra from ALICE and ATLAS will be discussed as well. Statistical uncertainties as well as a comprehensive assessment of all systematic uncertainties pertaining to all observables will be shown in this chapter. Additional material can be found in appendix E.

5.1 Normalization

The jet spectra in both measurement and simulation must be properly normalized in order to compare them. For this analysis, the number of jets per event will be reported normalized per unit η integrated over full azimuth. Since the azimuthal acceptance of the EMCal is limited, a geometric acceptance correction must be applied. The geometrical acceptance of the EMCal is given by equation 5.1:

$$f_{Acc} = \Delta\eta \times \Delta\varphi \tag{5.1}$$

In terms of the raw counts measured in data dN_{jets} or the cross section per p_T bin-width obtained from MC simulations σ_{MC}:

$$\frac{dN_{data}}{d\eta dp_T} = \int_0^{2\pi} \frac{dN_{jets}d\varphi}{N_{events}f_{Acc}dp_T} \tag{5.2}$$

$$\frac{d\sigma_{sim}}{d\eta dp_T} = \int_0^{2\pi} \frac{d\sigma_{MC} d\varphi}{f_{Acc} dp_T} \tag{5.3}$$

In addition, the jet cross sections for p-Pb collisions can be found in appendix D, and its normalization differs from 5.2 by:

$$\frac{d\sigma_{data}}{d\eta dp_T} = \int_0^{2\pi} \frac{f(m) d\varphi}{L_{int} f_{Acc} dp_T} \tag{5.4}$$

where L_{int} is the integrated luminosity which is $51 \mu b^{-1}$ for the p-Pb run. The simulated events are not p-Pb collisions but rather pp collisions. A geometric scaling must be applied to simulation in order to compare. Using the Glauber model, a collision between two nuclei with mass numbers A and B at an impact parameter b, $T_{AB}(b)$ is given by:

$$T_{AB}(b) = \frac{N_{coll}(b)}{\sigma_{inel}} \tag{5.5}$$

For centrality integrated results, $T_{AB}(b)$ should be integrated over the entire cross section area $d^2(b)$, which results in:

$$\int T_{AB}(b) d^2b = AB \tag{5.6}$$

For p-Pb collisions (A = 208, B = 1), an averaged T_{pPb} can be given in terms of 5.5 by:

$$T_{pPb} = \frac{N_{coll}}{\sigma_{pp}^{inel}} \tag{5.7}$$

Where N_{coll} is the average number of binary collisions in a minimum biased (MB) p-Pb collision which has a value of $N_{coll} = 6.8835 \pm 0.5643$ [53] and corresponds to a relative error of 8.2% on the scaled spectra. The total pp cross section, σ_{pp}^{inel}, for pp collisions at $\sqrt{s} = 5.02$ TeV is 70mb [61–63]. This cross section can be used because the kINT7 (MB) trigger only triggers on inelastic events. Using 5.7, a comparison of dN_{data} to $d\sigma_{sim}$ can be made by scaling $d\sigma_{sim}$ by T_{pPb} in order to produce a R_{pPb}.

Furthermore, as mention in sections 4.8.3 and 4.8.4, the jet spectra are corrected for the kinematic and jet finding efficiencies.

5.2 Unfolding the Jet Spectrum

As discussed in section 4.8, there are several different algorithms that can be used for unfolding. Each algorithm must be optimized by adjusting the regularization strength in order to give the most numerically stable and accurate unfolded spectrum. The regularization is not the only parameter that has to be considered in optimization; the unfolded spectrum also depends on the measured range used for the unfolding input, the range of the truth spectrum which is the output, and on the assumption of a shape or functional form of the prior spectrum (i.e. an initial guess). The sensitivity of the unfolded spectrum to these effects will be discussed in section 5.4.

5.2.1 Unfolding Algorithm

The default algorithm used in this analysis to unfold the jet spectra is the Bayesian Method (see section 4.8.1). Bayesian is prefered over SVD in this analysis because the algorithm displays more stability in the unfolding thile changing the regularization strength (see figures 5.7 and 5.8). The default prior used for unfolding is the measured jet spectrum itself.

5.2.2 Unfolding Regularization

If the unfolded spectrum were not regularized, then the spectrum would fluctuate (vary randomly bin to bin) wildly, producing an unphysical spectrum. On the other hand, if the unfolded spectrum is regularized too strongly, then it will also have large fluctuations (do to statistical uncertainties) and will not be physical either. The common way to asses this is to use the *Pearson Coefficients* (figure 5.8) which are obtained from the unfolded covariance matrix:

$$\rho(x,y) = \frac{cov(x,y)}{\sigma_x \sigma_y} \tag{5.8}$$

The Pearson coefficients are analyzed and unfolded spectra with regularization strengths that have large correlations (or anti-correlations) from bin to bin are rejected. Figure 5.1 gives an example of what the Pearson coefficients should look like in a properly regularized spectrum; what is desired is a strong correlation along the diagonal with minimal correlations for off-diagnal terms. The reason for minimizing off diagonal terms is that there is expected to be a strong correlation between jets on particle-

level and measured jets and non-zero off diagonal terms indicate that this correlation is not strong (or possibly anti-correlated). An example of what the Pearson coefficents may look like if not properly regularized is shown in figure 5.2.

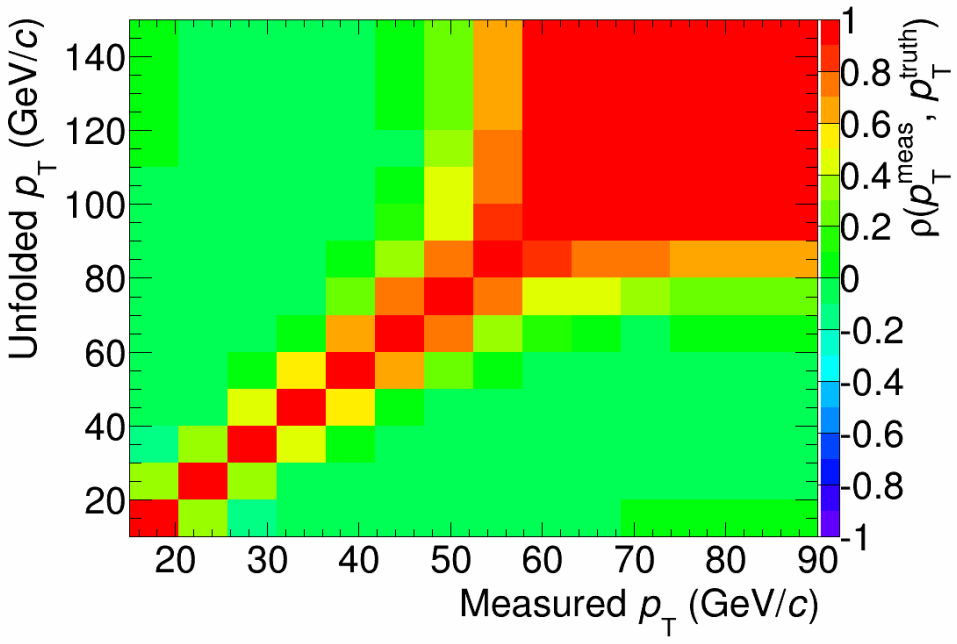

Figure 5.1: Pearson Coefficients for an unfolded spectrum with optimal regularization.

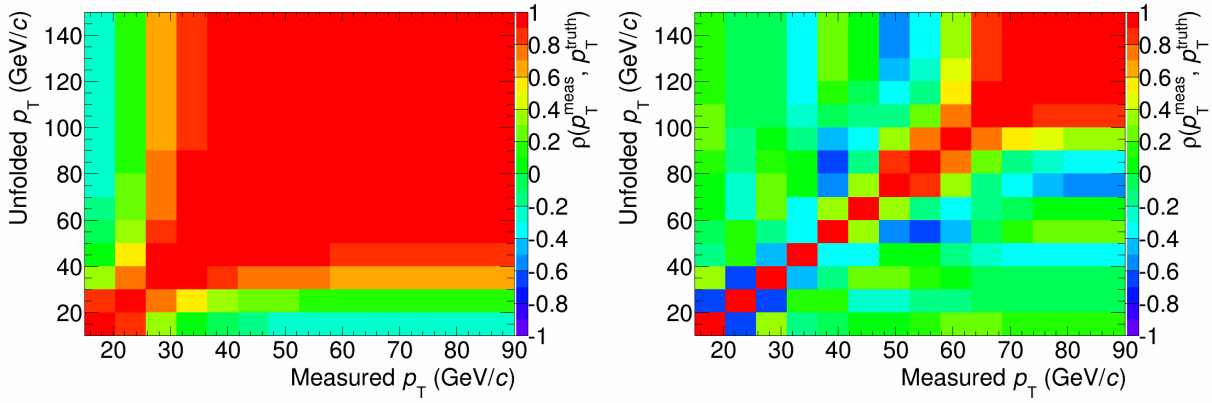

Figure 5.2: Pearson Coefficients for unfolded spectra with regularizations not optimized. Left: Under regularized spectrum. Right: Over regularized spectrum

5.2.3 Unfolding Ranges

The measured spectrum used in the unfolding algorithm can only be used in a restricted p_T range. The minimum measured p_T is chosen such that it is sufficently away

from combinatoric jets (jets which are composed primarly of uncorrelated thermally produced low p_T particles [see section 12.1 in [50] for more details]), so that a large upward fluctuation in the background will not cause a wildly fluctuating spectrum at low p_T. Also, since unfolding preserves the integral of the measured spectrum, combinatoric jets would be wrongly considered as true signal jets and hence the normalization would be incorrect over the whole range. For this analysis, the default minimum measured p_T is 15 GeV/c. The maximum measured p_T is limited by the recorded statistics. For this analysis it is defined by the highest p_T bin containing at least 10 counts which is determined to be 90 GeV/c.

Furthermore, restrcitions are applied on the range of the unfolded spectrum. The minimum unfolded p_T is allowed to be below the minimum measured p_T due to the need to constrain the spectrum in a regime where there is a lot of statistics and the spectrum is steeply falling. The maximum unfolded range can and should extend to very high p_T (in this analysis, up to 150 GeV/c). However the unfolded spectra should only be reported in the p_T range in which the kinematic efficiency is larger than 80% (see section 4.8.4), which for MB jet spectra in this analysis corresponds to the range between 30 and 100 GeV/c in jet transverse momentum.

5.3 Statistical Uncertainties

The statistical uncertainties on the measured spectrum are calculated using simple Poissonian statistics: they are defined by the square root of the number of counts per p_T bin. In order to reduce statistical uncertainties, especially at high p_T, allowing for a higher kinematic reach (in transverse jet momentum $p_{T,jet}^{ch+em}$) in the jet spectrum, both data taking periods (lhc13b & lhc13c) are utilized.

For spectra in which a ratio is computed (jet structure ratio and nuclear modification factor for jets), the statistical uncertainties on those spectra will be computed by assuming that the numerator and denominator of the ratio are independent and thus will be added in quadrature. For the jet structure ratio, the data is split into two independent sets to ensure statistical independence and proper error propagation (see section 5.6). For the nuclear modification factor for jets, the numerator is data while the denominator is simulation; therefore the two datasets are independent.

The measured jet spectra are then unfolded using `RooUnfold`, which also propagates statistical uncertainties by taking the square root of the diagonal elements of the covariance matrix. As a cross check the counts in each bin in the measured spectrum

are randomized assuming a Gaussian distribution with the mean being the nominal bin count and the standard deviation being the uncertainty in that bin. These spectra (from this randomized bin count process) are then unfolded and their spread in each bin is the statistical uncertainty, which coincides with the square root of the diagonal elements of the covaraince matrix.

5.4 Systematic Uncertainties

In addition to statistical uncertainties, it is important that a careful evaluation of the associated systematic uncertainties are performed. In this analysis, the systematic uncertainties can be divided into two catagories: sytematics related to unfolding and systematics due to the jet energy scale (JES). Table 5.1 shows the two classes of systematic uncertainties that will be discussed in this section.

Unfolding	**Jet Energy Scale** (JES)
Regularization	Tracking Efficiency
Method	Hadronic Correction
Prior	Underlying Event Subtraction (UE)
p_T Range	Background Fluctuations (δp_T)
	Detector Response
	Scale Factor

Table 5.1: Overview of the two classes of Systematic Uncertainties.

The division of these systematics into two catagories is natural in that any unfolding systematic will be uncorrelated to any JES systematic. For this analysis it is assumed that all the systematic uncertainities are uncorrelated, so that the total systematic is estimated by adding all the indivdual systematics in quadrature. Although in principal this may not be true, it is difficult to estimate the covariance between any two of the systematics while keeping all others (at least in that category) constant. Furthermore, many of the systematics which one would assume to be highly correlated (e.g. underlying event subtraction and background fluctuations) tend to have small contributions to the overall systematic uncertainty. The approach of assuming independence is a conservative aproach in that the systematic uncertainities are at worst overestimated. The total uncertainty (statistical and systematic) on the jet spectrum is shown in figures 5.3 and 5.4 and will be discussed in detail in the following sections.

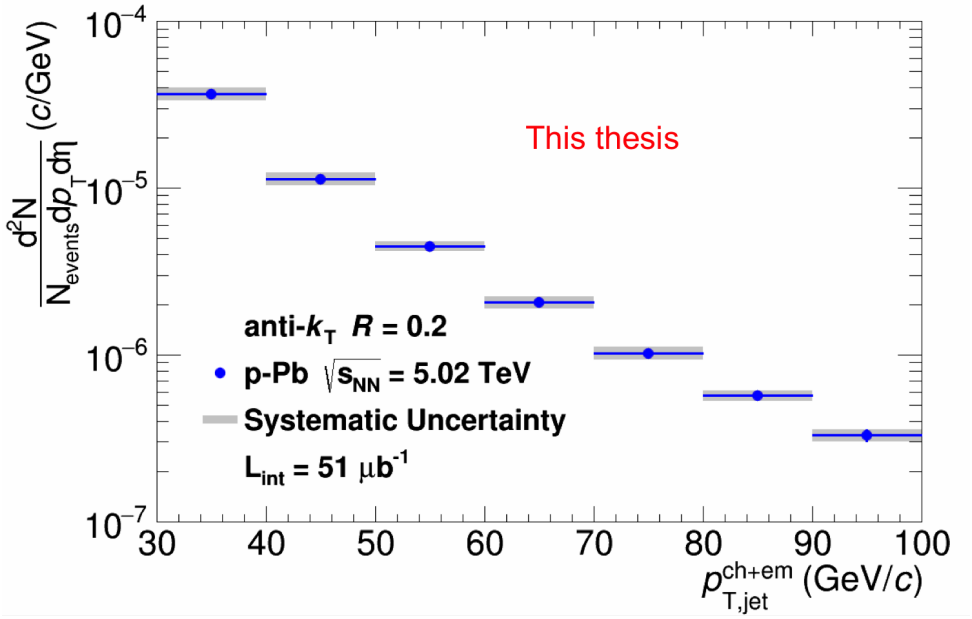

Figure 5.3: Total uncertainty due to statistical and systematic uncertainties for $R = 0.2$ anti-k_T jets.

5.4.1 Regularization Strength

In order to determine which unfolding algorithm and regularization strength is most suitable as a baseline for evaluating the systematic uncertainty in unfolding, all combinations of avaliable algorithms and regularizations are considered in order to determine which combination results in the most stability. The stability will be "judged" in two ways: firstly, it is required that the pearson coefficients exhibit behavior in which their are no strong off-diagonal terms; secondly, varaition from one regularization strength to another in a given algorithm should be minimized.

By comparing figures 5.5 to 5.6 it is clear that the p-Pb jet spectra with the Bayesian method produces pearson coefficients with off-diagonal terms much closer to zero then those using SVD. Furthermore, when looking at figures 5.7 and 5.8, it is clear that the variation between optimal and near optimal regularization strength for bayesian show much less variation than that for SVD. From the results in figures 5.5 to 5.8, we can conclude that Bayesian is the preferred unfolding method for p-Pb jet spectrum.

The sensitivity to the regularization between unfolded spectra using the two different unfolding algorithms is not observed (to this extent) in the Pb-Pb analysis. In that analysis, SVD is used as the default method. Conceptually the SVD algorithm is sensitive to curvature changes in the spectrum and its derivatives. When a spectrum

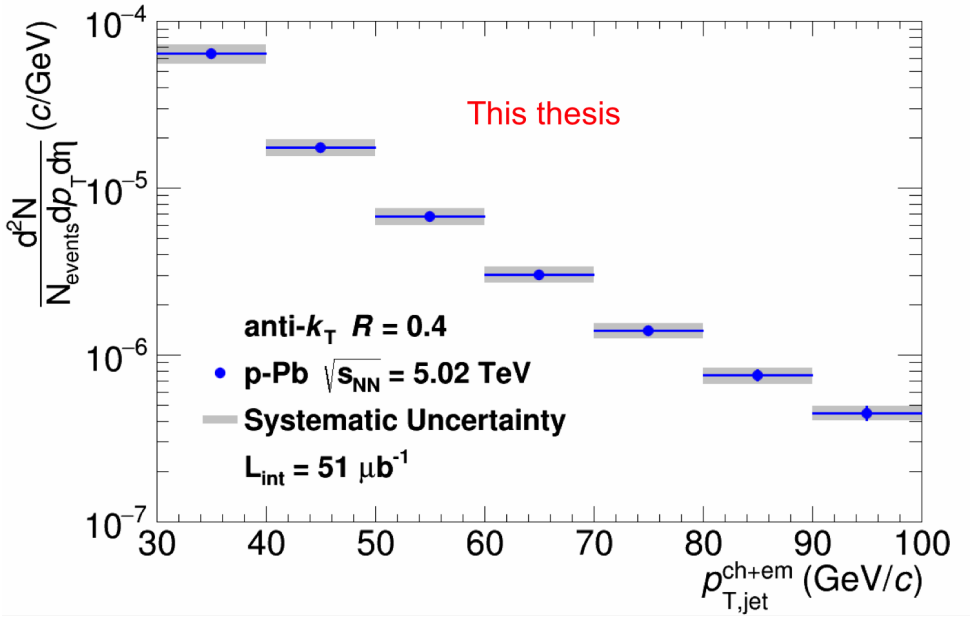

Figure 5.4: Total uncertainty due to statistical and systematic uncertainties for $R = 0.4$ anti-k_T jets.

has a discontinuity, SVD will produce a result which could be more unstable. These discontiniuties could be caused by the proposed background correction procedures utlized in this analysis. In Pb-Pb events, due to the high particle density produced in the collision, it is rare (if not statistically impossible) to have empty events. However in p-Pb collisions, empty events exist and are enhanced in peripheral events. These empty events cause a "jump" discontinuity in the δp_T and lead to instabilities when unfolding with SVD. These empty events have been observed in toy model simulations when a uniform background is simulated and δp_T is measured. The effect is reduced when more particles are simulated, resembeling a central p-Pb collision or even a Pb-Pb collisions. This effect is most likely to be the main reason why Bayesian is more stable in unfolding the p-Pb jet spectrum, in particular the sparse events, than SVD and hence will be used as the default unfolding algorithm.

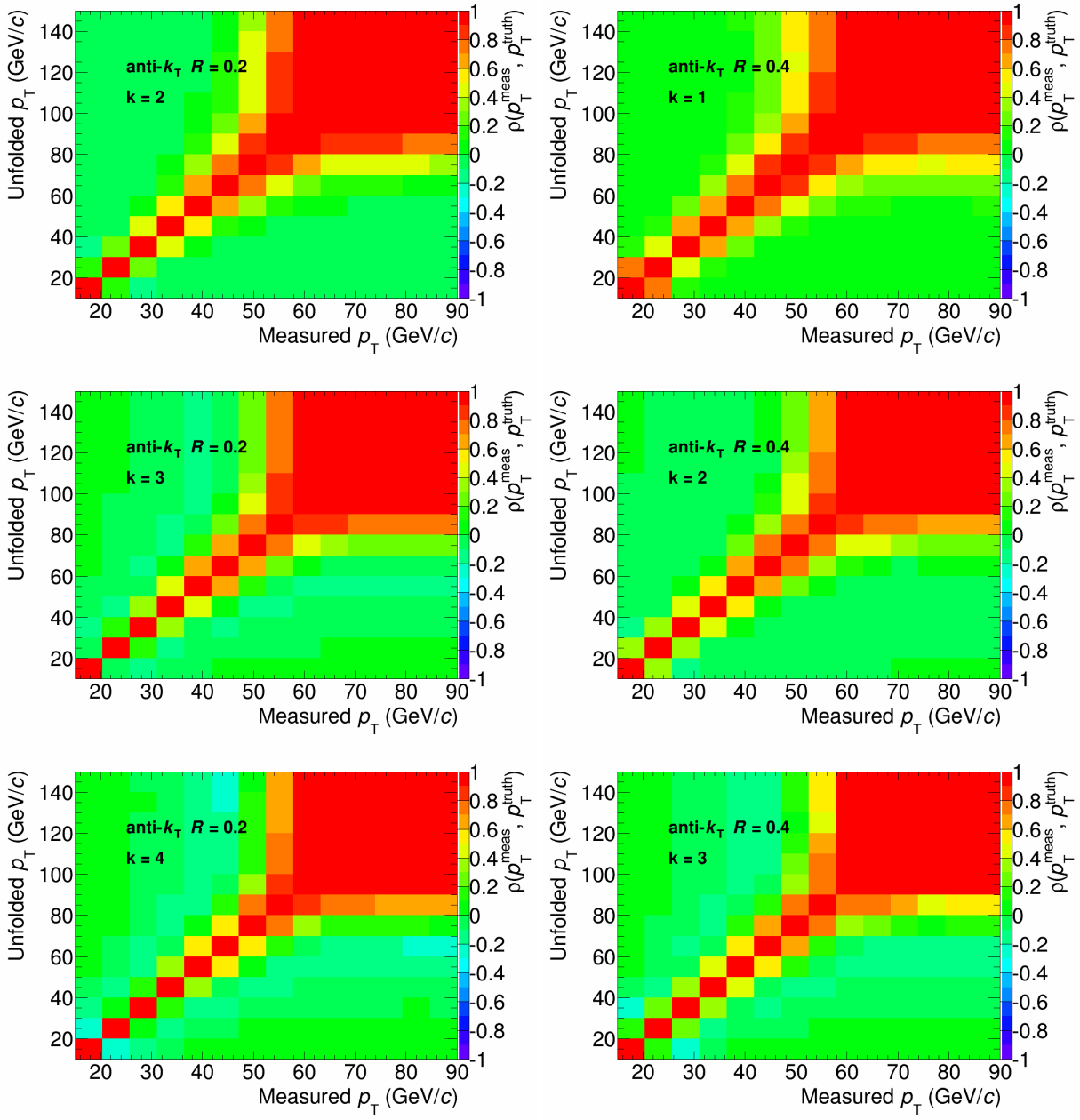

Figure 5.5: Pearson Coefficients for unfolded spectra using bayesian method. The optimal values are $k = 3$ for $R = 0.2$ and $k = 2$ for $R = 0.4$. Upper Left: $k = 2; R = 0.2$. Upper Right: $k = 1; R = 0.4$. Middle Left: $k = 3; R = 0.2$. Middle Right: $k = 2; R = 0.4$. Lower Left: $k = 4; R = 0.2$. Lower Right: $k = 3; R = 0.4$.

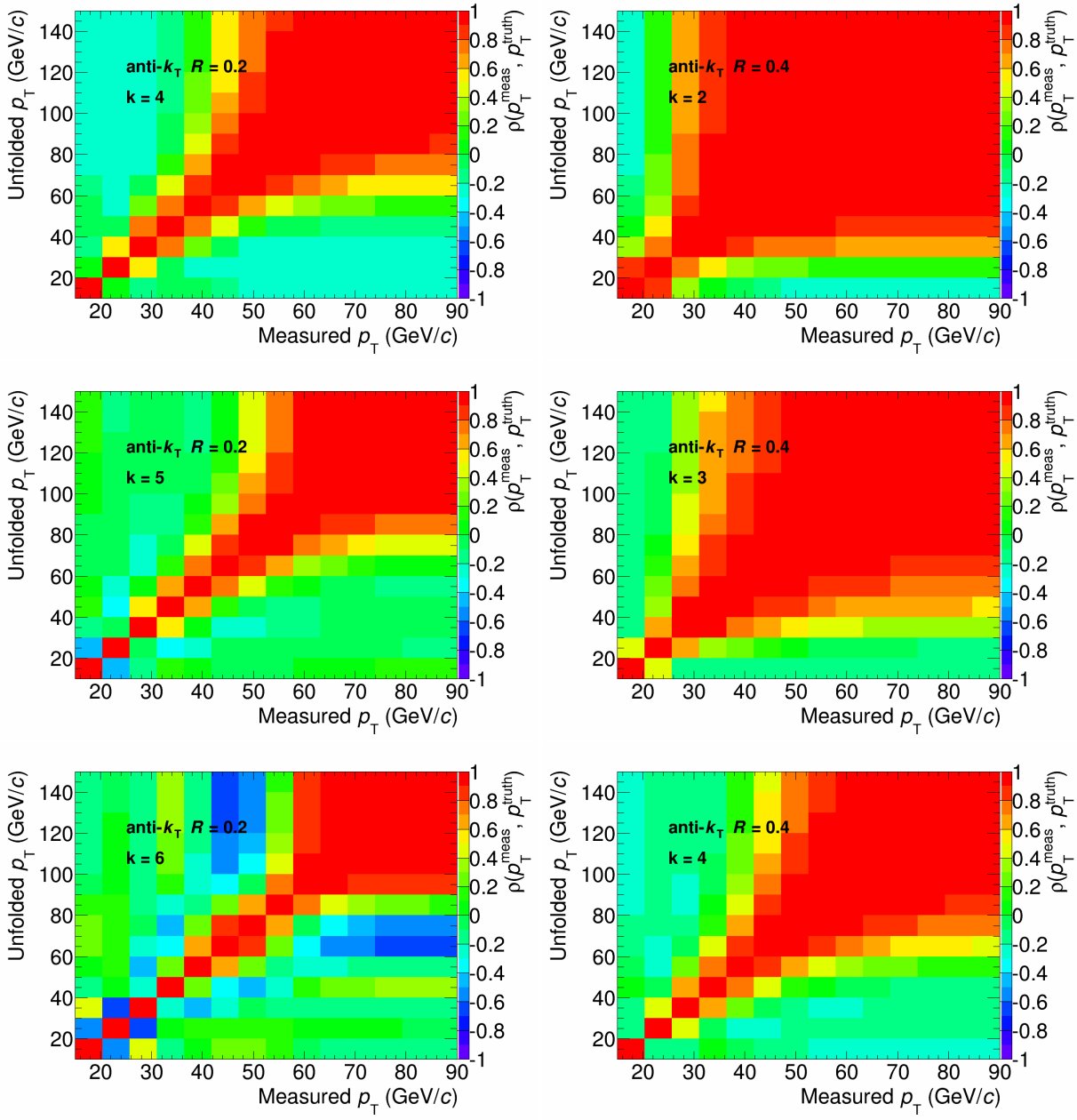

Figure 5.6: Pearson Coefficients for unfolded spectra using SVD method. The optimal values are $k = 5$ for $R = 0.2$ and $k = 3$ for $R = 0.4$. Upper Left: $k = 4; R = 0.2$. Upper Right: $k = 2; R = 0.4$. Middle Left: $k = 5; R = 0.2$. Middle Right: $k = 3; R = 0.4$. Lower Left: $k = 6; R = 0.2$. Lower Right: $k = 4; R = 0.4$.

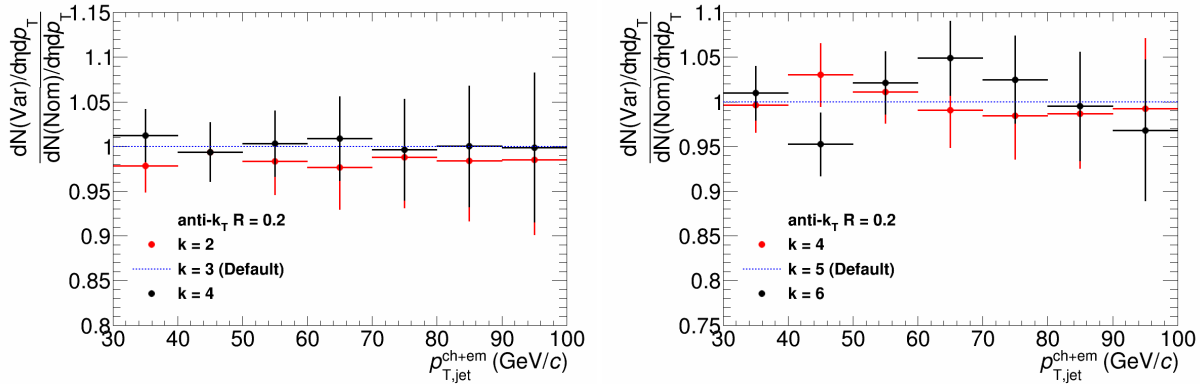

Figure 5.7: Relative systematic uncertainty due to different regularizations in bayesian and SVD unfolding for $R = 0.2$. Left: Bayesian. Right: SVD

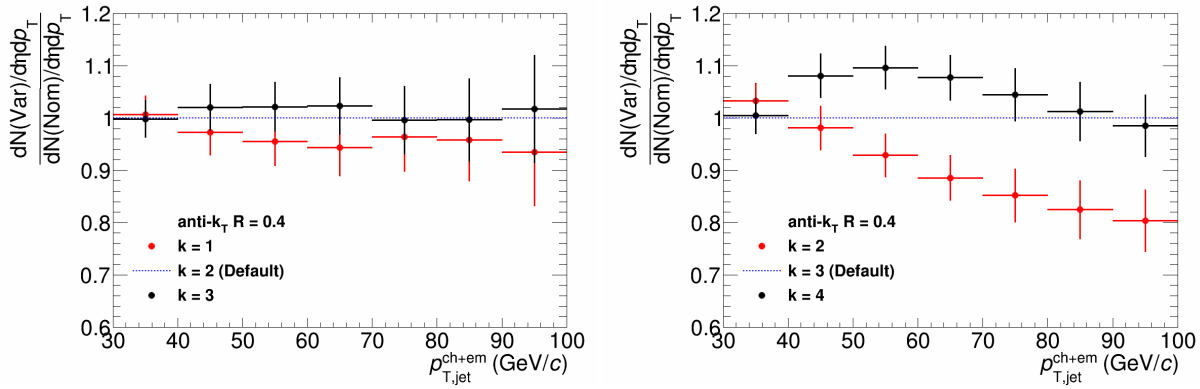

Figure 5.8: Relative systematic uncertainty due to different regularizations in bayesian and SVD unfolding for $R = 0.4$. Left: Bayesian. Right: SVD

5.4.2 Unfolding Method

With the considerations from section 5.4.1, a comparison of the different unfolding methods can be done, with the variation between the two methods producing a systematic unceratinty due to the method being used (figure 5.9). As mentioned in the previous section, since SVD shows signs of instability (when compared to Bayesian) it could be excluded as a proper unfolding method. Hence the systematic uncertainty estimated here can be seen as an extremely conservative estimate.

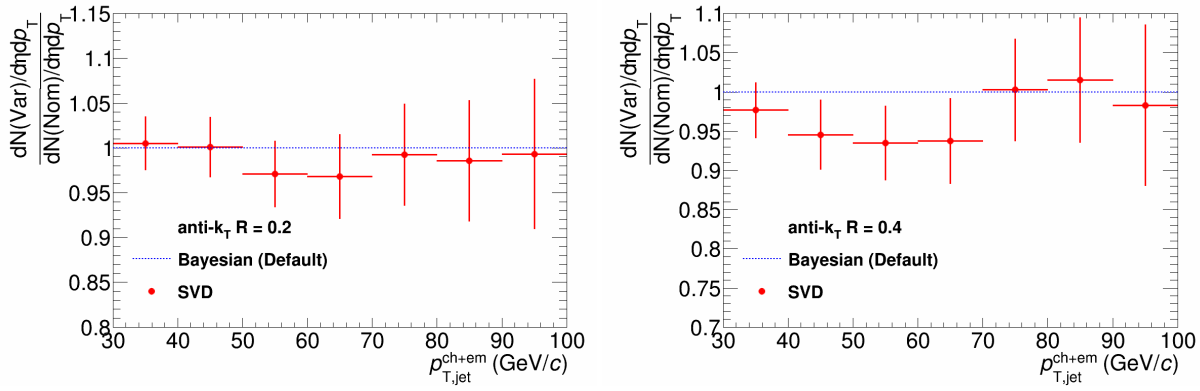

Figure 5.9: Relative systematic uncertainty due to different unfolding methods. Left: $R = 0.2$. Right: $R = 0.4$

5.4.3 Unfolding Prior

The prior, used as a starting point for the unfolding algorithm, is the measured jet spectrum itself. To test the sensitivity of the prior, the PYTHIA Perguia2011 spectrum, which is obtained from MC particle-level simulation, is used instead of the measured spectrum. The further the prior is away from the final unfolded spectrum, the more regularization is required to recover the spectrum. For the regularizations used in this analysis, different priors produce at most a 5% deviation (see figure 5.10).

5.4.4 Unfolding p_T Range

The default p_T ranges for the minimum measured and unfolded p_T (see section 5.2.3) are varied to see what effect they have on the unfolded spectrum. For the unfolded minimum p_T, a minimum p_T of 0 GeV/c is used instead of 10 GeV/c producing a neglegable deviation ($< 0.1\%$). For the measured minimum p_T, as expected reducing the minimum p_T from 15 GeV/c to 10 GeV/c mostly effects the lowest bin, causing a

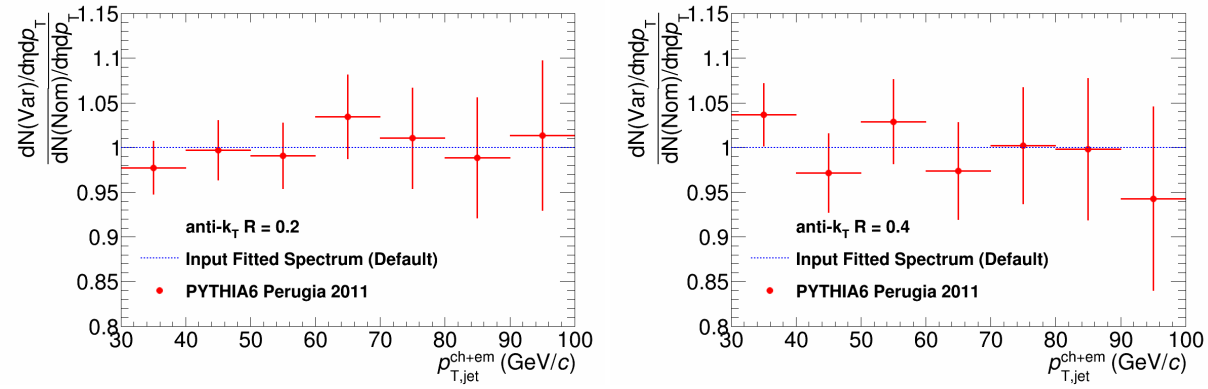

Figure 5.10: Relative systematic uncertainty due to different priors being used. Left: $R = 0.2$. Right: $R = 0.4$

deviation of at most 1% for both radii for other bins ($p_T > 40$ GeV/c). See figure 5.11 for details.

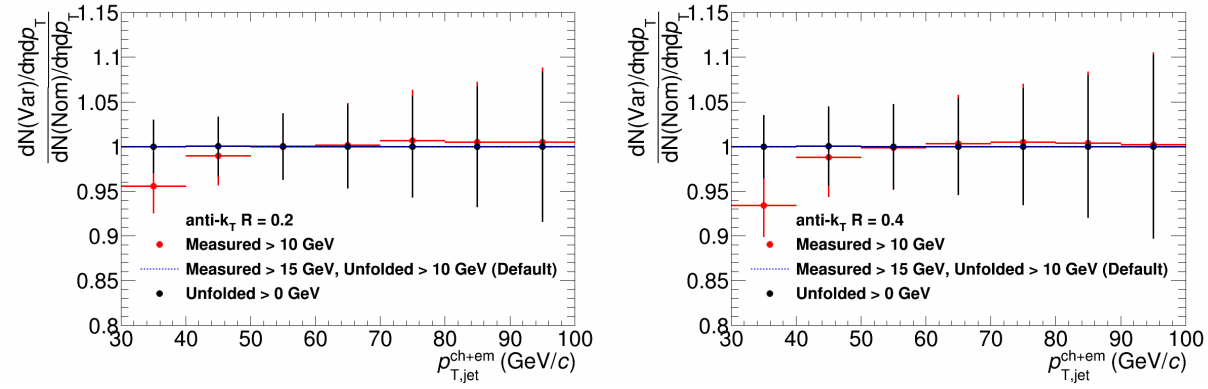

Figure 5.11: Relative systematic uncertainty due to different minimum unfolding p_T cuts. Left: $R = 0.2$. Right: $R = 0.4$

5.4.5 Tracking Efficiency Uncertainty

As seen in figure 4.6, the assumed tracking efficiency uncertainty in the ALICE TPC reconstruction is about 4%. In order to estimate the effect of this uncertainty on the jet spectrum, two detector response matricies are constructed: the default in which the optimal efficiency of track reconstruction is assumed (which is around 90% of all tracks) and another in which 4% of all tracks that were reconstructed using the optimal efficiency in an event are rejected binomially (all tracks reconstructed using the optimal efficiency in a simulated event have a 96% chance of surviving rejection). The relative uncertainty is shown in figure 5.12.

As can be seen when comparing figure 5.12 to all other figures in section 5.4, the tracking efficiency is the dominant systematic uncertainty. This can also be seen in table 5.2. However, when a ratio of two spectra that are obtained from data are compared using the same detector (e.g. the Jet Structure Ratio or R_{CP}), the tracking efficiency is signifcantly reduced (see figures E.5 and G.8 in appendicies E and G respectively).

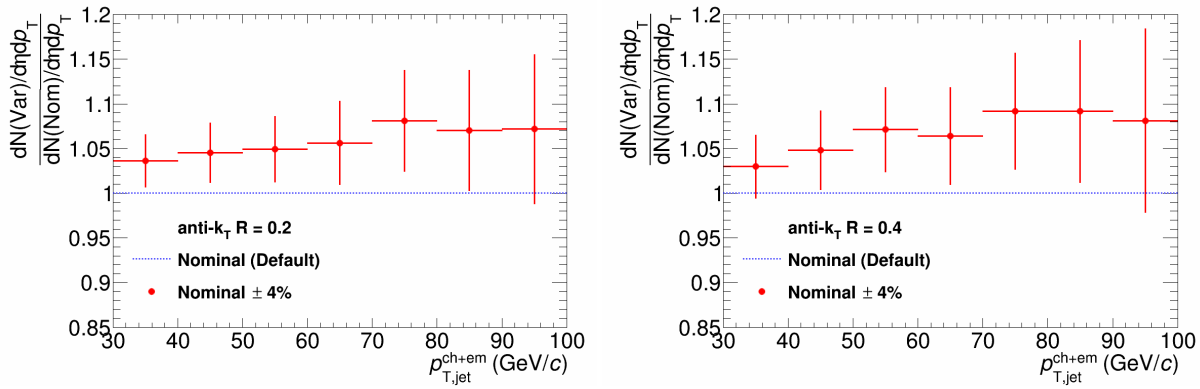

Figure 5.12: Relative systematic uncertainty due to tracking efficiency. Left: $R = 0.2$. Right: $R = 0.4$

5.4.6 Hadronic Correction

In section 4.3 it was mentioned that in order to avoid double counting of energy deposition in the EMCal due to charged particles, a procedure referred to as hadronic correction was employed in which a certain percentage of the energy of the tracks with trajectories passing through an EMCal cell would be subtracted. The nominal fraction of charged energy removed from a cell is taken to be 100% (i.e. all energy deposited by a charged particle traversing a cell is removed). This systematic is varied by removing 70% of the charged energy. Figure 5.13 shows what effect varying subtraction fractions have on the jet spectrum. In order to self consistently estimate this systematic uncertainty, the hadronic correction is done on both simulation and data. The effect on the jet spectrum is a few pecent for both jet radii.

5.4.7 Underlying Event Subtraction (UE)

In sections 4.5.1 and 4.5.2 were presented the two methods of underlying event subtraction that are used in this analysis. The default method of UE subtraction is the occupancy median approach, which is optimized for dealing with sparse events

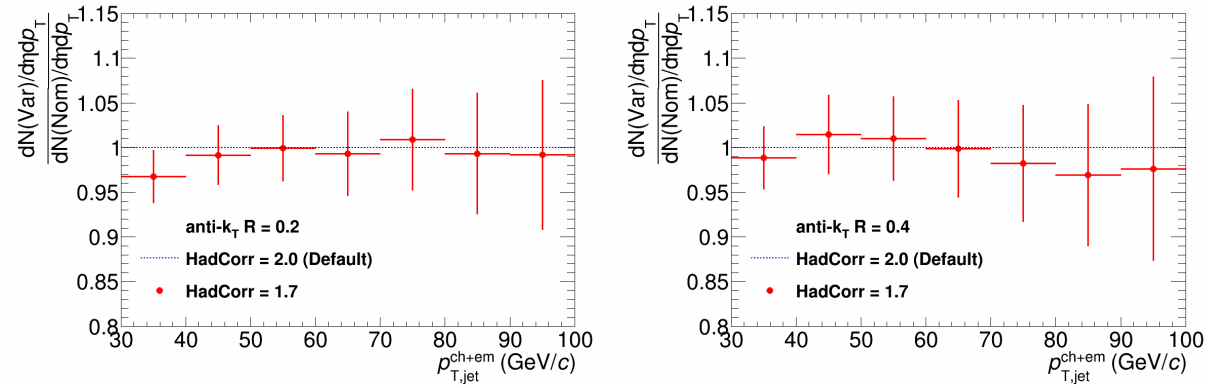

Figure 5.13: Relative systematic uncertainty due to hadronic correction. Left: $R = 0.2$. Right: $R = 0.4$

in which significant portions of the detector(s) contain no particles or energy depositions. Figure 5.14 shows the systematic uncertainty due to different UE subtraction approaches.

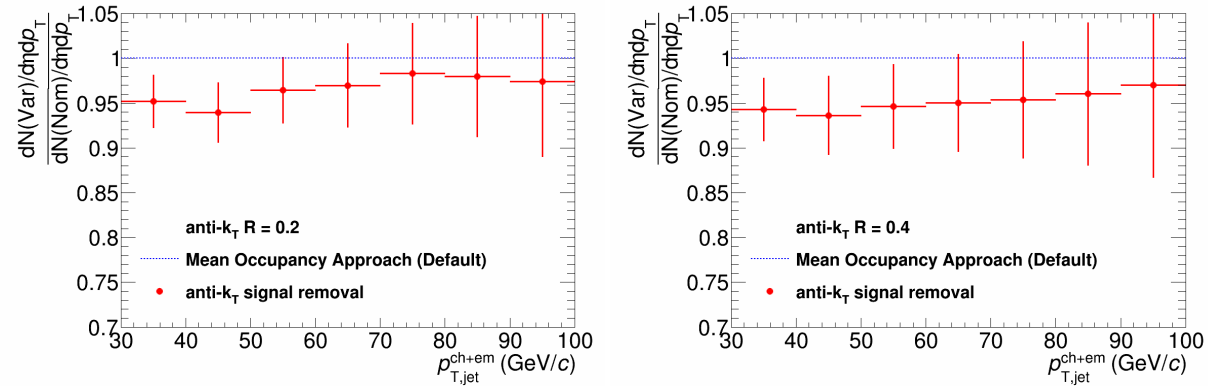

Figure 5.14: Relative systematic uncertainty due to different UE subtraction methods. Left: $R = 0.2$. Right: $R = 0.4$

A systematic offset is observed in figure 5.14 when contrasting the two methods. The difference can be understood based on observations of figures 4.18 and 4.19. When averaged over all events, the estimated background density for the signal removal approach is higher then the median occupancy approach. This translates into a lower yield at a particular jet transverse momentum for the signal removal approach as compared to the median occupancy approach.

5.4.8 Background Fluctuations (δp_T)

The discussion in section 4.6 showed that background fluctuations due to uncorrelated particle production with respect to hard scatterings produce low p_T particles that "smear" the jet spectrum. This smearing is corrected for in the unfolding procedure in which a δp_T response matrix is constructed and multiplied by a detector response matrix to produce the combined response matrix used in the unfolding procedure (see section 4.8). Since there is no unambiguous way of defining a δp_T based on data alone, an estimate of the corresponding systematic uncertainty is performed by varying the p-values (probability of jet-jet overlap, see figure 5.15).

In figure 4.22, a tail is seen at high p_T for larger radii and larger p-values. This translates to a consistent bias in the jet spectra with larger biases due to larger radii and/or larger p-values. When a larger radius is used for random cones, it is expected that there will be larger region-to-region fluctuations in the total energy when compared to the nominal value of ρA. These larger fluctuations cause more smearing in the unfolded spectra when compared to a smaller radius. The same is true for p-values. A p-value of unity means that there is a higher probability of jet overlap. With jet overlap, there is significantly more energy in a cone then a cone comprised of only uncorrelated low p_T particles. This explains the larger and larger tails as the p-values increase, which translates to more smearing and a lower spectral yield for jets at higher p_T.

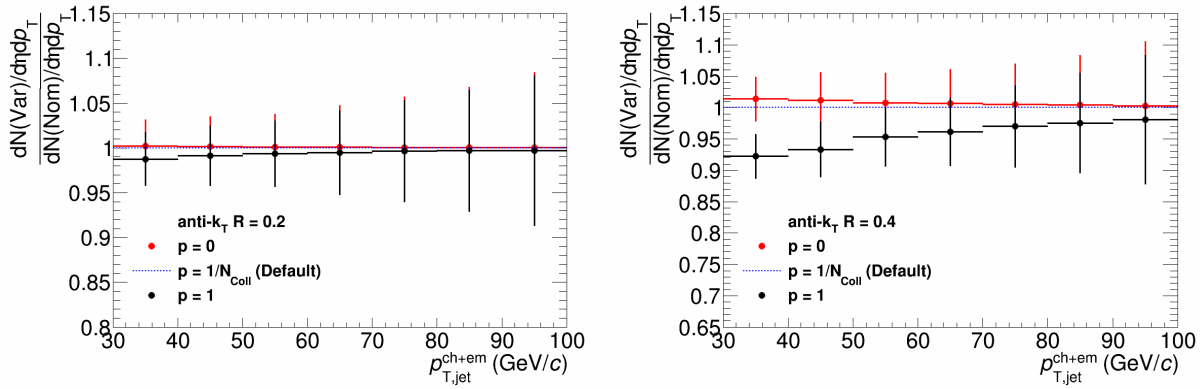

Figure 5.15: Relative systematic uncertainty due to different δp_T definitions. See section 4.6 for definitions of the p values. Left: $R = 0.2$. Right: $R = 0.4$

5.4.9 Unfolding Response for Different Run Periods

As mentioned in section 5.3, both run periods are merged together in order to reduce statistical uncertainties, particularly at high p_T. This benefit comes at a price,

namely that each run period has slighty different detector conditions and that each period should be unfolded with their respective responses, and then merged. Because the merger is done prior to unfolding, an additional systematic is introduced by chosing to unfold with one detector response only. Although this procedure introduces an additional systematic uncertainty, this additional uncertainty is smaller then the additional statistical uncertainty of unfolding both periods seperately and then merging. Figure 5.16 shows the relative uncertainty when comparing good response (anchored to run number 195351 from lhc13b) to the semigood response (anchored to run number 195531 from lhc13c). The uncertainty is on the order of 5% for $p_T > 40$ GeV/c.

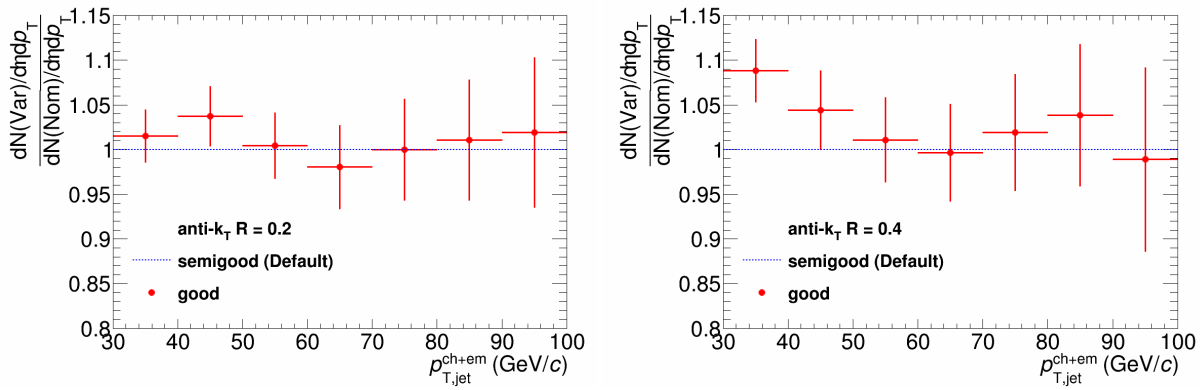

Figure 5.16: Relative systematic uncertainty due to different unfolding response matricies used for detector conditions. Left: $R = 0.2$. Right: $R = 0.4$

5.4.10 Scale Factor

In order to estimate the background density (ρ) of an event, section 4.5.3 outlines a procedure where a scale factor can be measured to allow estimates of the charged particle density in the TPC to be translated into charge + neutral estimate of the background density in the TPC + EMCal. This procedure allows the statistical uncertainty of the background density to be reduced but at a cost of introducing an additional systematic uncertainty due to this scaling. Figure 5.17 shows what effect this scale factor has on the unfolded jet spectrum. This systematic uncertainty produces a negligible effect.

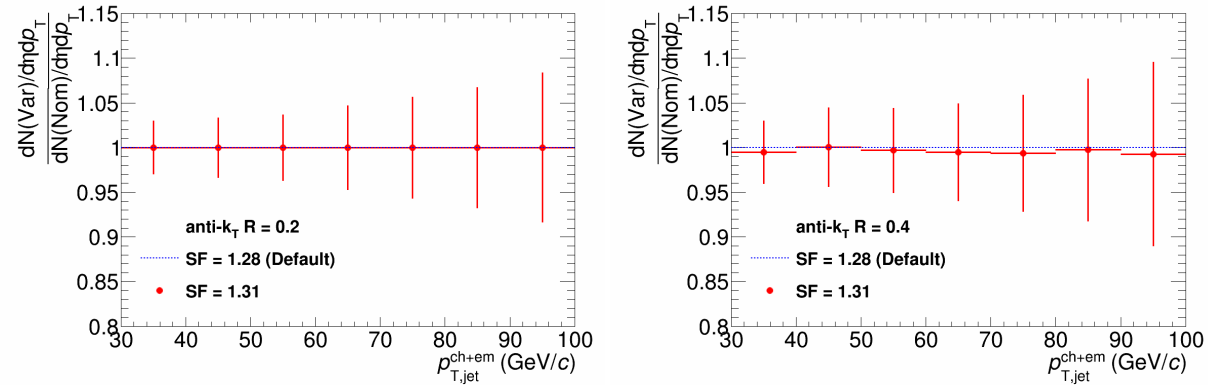

Figure 5.17: Relative systematic uncertainty due to different scale factors. Left: $R = 0.2$. Right: $R = 0.4$

5.5 Nuclear Modification Factor for Jets

5.5.1 pp Reference Spectrum

In order to estimate the nuclear modification factor for jets, a pp reference is required. In the Pb-Pb analysis [50], a pp jet spectrum at 2.76 TeV was available hence allowing a direct comparison of the the PbPb data to the pp data. It is convenient when both spectra are available at the same collisional energies and using the same detectors because many of the systematic uncertainties will be reduced or even eliminated. Unfortunately for this analysis, which is done at $\sqrt{s_{NN}} = 5.02$ TeV, there exists no pp reference from ALICE, or even some other collaboration which could be used as a reference. Once run period 2 commences at the LHC in 2015, ALICE will be able to produce a pp jet spectrum at $\sqrt{s} = 5.02$ TeV which can be used as a reference to produce a "true" R_{pPb}.

To overcome this problem, several different approaches were explored. In the p-Pb charged jet analysis [54], a 7 TeV pp reference was scaled down to 5.02 TeV using PYTHIA in order to obtain a pp jet reference spectrum. This was also done in both ATLAS [64] and CMS [65] p-Pb jet results. Unfortuantely, ALICE does not have a 7 TeV full jet pp reference at the time of this thesis. An attempt to scale the 2.76 TeV spectrum up was made, however the associated systematic uncertainties were too large to be used as a reference. Figures 5.18 and 5.19 shows various MC tunes that were analyzed and compared to p-Pb full jets. The pp jet spectrum is scaled up by T_{pPb} so that the nuclear modification for jet in p-Pb collisions compared to pp collisions, R_{pPb}, can be

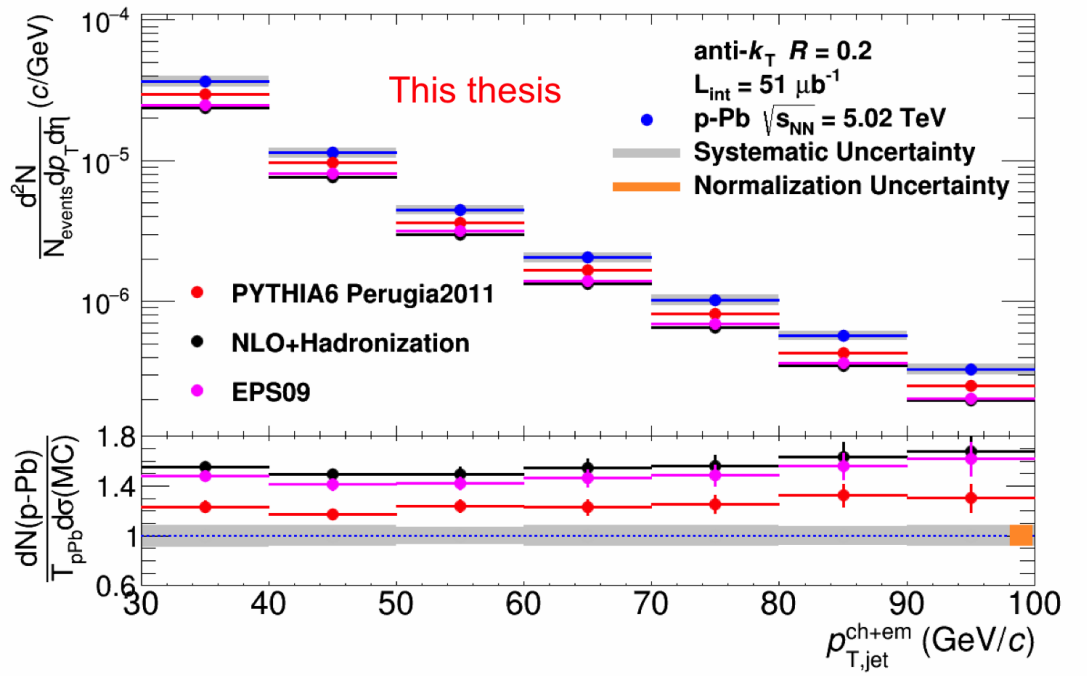

Figure 5.18: A comparison of the p-Pb jet spectrum to various MC tuned pp jet spectra which have been scaled by T_{pPb}. An overall normalization uncertainty of 8.2% to the overall spectrum is also shown on the plot.

measured by:

$$R_{pPb} = \frac{\frac{d^2N_{pPb}}{N_{events} d\eta dp_T}}{N_{coll} \frac{d^2N_{pp}}{d\eta dp_T}} = \frac{\frac{d^2N_{pPb}}{N_{events} d\eta dp_T}}{T_{pPb} \frac{d^2\sigma_{pp}}{d\eta dp_T}} = \frac{\frac{d^2\sigma_{pPb}}{d\eta dp_T}}{A \frac{d^2\sigma_{pp}}{d\eta dp_T}} \tag{5.9}$$

where all the parameters in 5.9 are defined in section 5.1. The R_{pPb} spectra for the various MC tunes are shown in the bottom panels of figures 5.18 and 5.19 along with the corresponding systematic and overall normalization uncertainties on the p-Pb jet spectrum.

Three theoretical models are considered here: a particular PYTHIA tune (PYTHIA6 Perguia2011) [66], next-to-leading order (NLO) pQCD calculations with hadronization and the EPS model which in addition to calculating the jet spectra using NLO pQCD calculations also incorporates modifications to the nuclear PDFs (see section 2.8.1) in the simulated pp collisions at the same collisional energies as the ALICE p-Pb collisions. A comparison between NLO+hadronization and the EPS models highlight differences in the nPDFs which as can be seen from figures 5.18 and 5.19 are small. The PYTHIA tunes produce the 2.76 and 7 TeV pp data more closely then any other MC

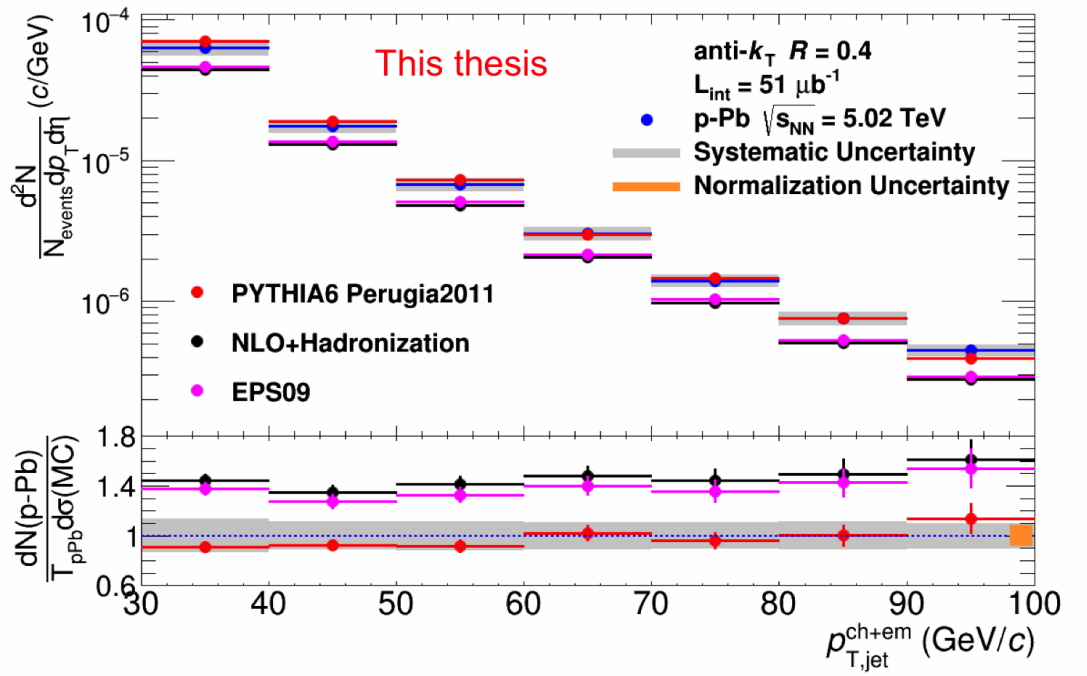

Figure 5.19: A comparison of the p-Pb jet spectrum to various MC tuned pp jet spectra which have been scaled by T_{pPb}. An overall normalization uncertainty of 8.2% to the overall spectrum is also shown on the plot.

tunes. For this reasons, PYTHIA6 Perguia2011 is used as the pp reference for 5.02 TeV. This observable will be referred to as R_{pPb}^{PYTHIA}.

5.5.2 R_{pPb}^{PYTHIA}

Figures 5.20 and 5.21 shows the nuclear modification factor for jets using PYTHIA6 Perguia2011 as the pp jet reference. There is a noticable difference between the two jet radii. This is most likely due to hadronization effects which affects smaller jet radii significantly and could be not properly treated in the PYTHIA tune used. Measured results utilizing larger jet radii are prefered over smaller radii as these observables capture a large fraction of the energy depostied by the initial hard scattering and are thus more strongly correlated to the parton kinematics and less affected by hadronization. When looking at the R_{pPb}^{PYTHIA} for $R = 0.4$, a value consistent with unity is observed within the reported uncertainties (statistical, systematic, and normalization). This uncertainty could be reduced significantly with an experimentally measured pp reference as the effects of model specific hadronization can be removed.

The observed R_{pPb}^{PYTHIA} for $R = 0.4$ indicates that there is little modification of the

jet yield from cold nuclear matter effects of the Pb nucleus. Although this does not conclusivly prove that the supression observed in R_{PbPb} is dominated by to hot nuclear matter effects (e.g. jet quenching from the QGP), it does preclude cold nuclear matter effects from being the dominate source of jet suppression observed in Pb-Pb collisions.

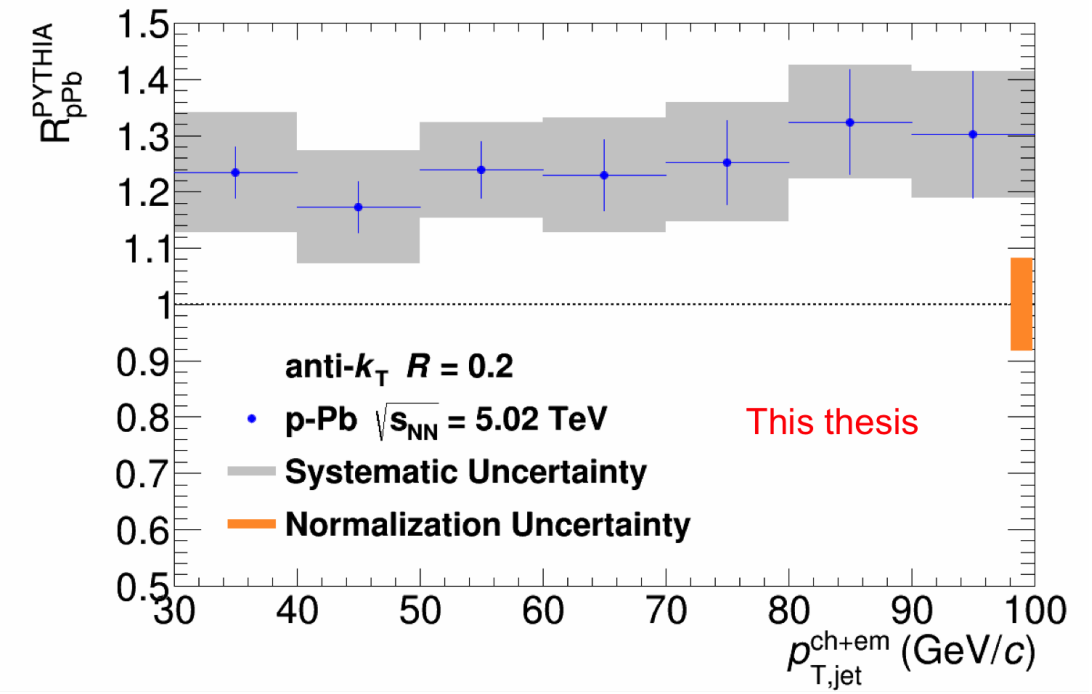

Figure 5.20: Nuclear Modification Factor for jets R_{pPb}^{PYTHIA} for $R = 0.2$. PYTHIA6 Perguia2011 is used as the pp reference and is scaled by T_{pPb}. An additional systematic uncertainty of 8.2% to the overall spectrum is also shown on the plot.

5.5.3 Comparison of R_{pPb} to other LHC experiments

Figure 5.22 shows a comparison of the R_{pPb} measured in this thesis to those measured in ATLAS [64] and CMS [65]. A one-to-one comparison of the ALICE data to the ATLAS data can be made given that both experiments measured the nuclear modification factor for jets with the same radius ($R = 0.4$), using the same jet finding algorithm (anti-k_T), in the same pseudorapidity window ($|\eta_{cm}| < 0.3$), and with an overlap region in jet transverse momentum. In this region the two measurements are consistent with each other within statistical and systematic uncertainties.

CMS measured the nuclear modification factor for jet using a jet radius of $R = 0.3$. Nevertheless, this observable was measured in the same pseudorapidity window ($|\eta_{cm}| < 0.5$) as ALICE $R = 0.2$ full jets and thus a comparison can be made. The two

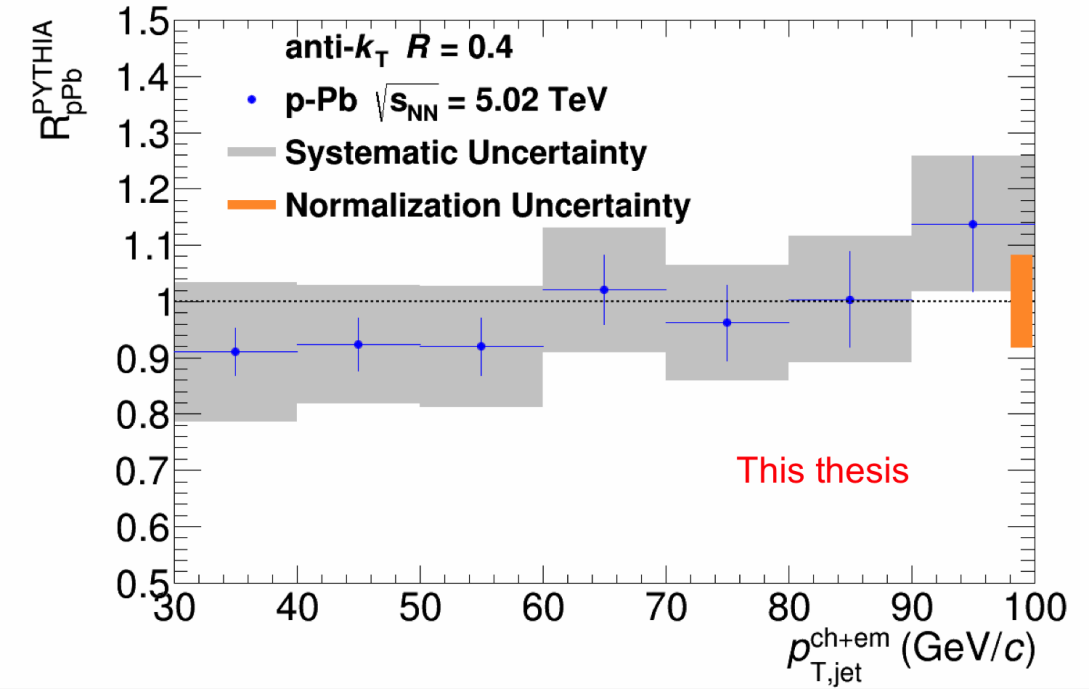

Figure 5.21: Nuclear Modification Factor for jets R_{pPb}^{PYTHIA} for $R = 0.4$. PYTHIA6 Perguia2011 is used as the pp reference and is scaled by T_{pPb}. An additional systematic uncertainty of 8.2% to the overall spectrum is also shown on the plot.

measurements are also consistent with each other in the overlap region.

The value of considering all three experimental results collectively is that they are complimentary with each other. The results from ATLAS and CMS extend to high jet transverse momentum due to the increased integrated luminosity (27.8 nb^{-1} and 35 nb^{-1} for ATLAS and CMS respectively), and their superior tracking abilities for high p_T particles. However these experiments lack the precision to measure low p_T particles as accurately as ALICE, which allows ALICE to measure a R_{pPb} at a much lower jet transverse momentum with higher precision.

5.6 Jet Structure Ratio

One approach to study the structure of jets is to compare jet spectra measured using different cone radii or resolution parameters. Results from the charged jet analysis in ALICE suggest no significant modification to the structure in p-Pb or Pb-Pb when comparing jet spectra at different radii to pp or PYTHIA measurements [54].

To avoid the strong statistical correlations if the same jets at different radii in the

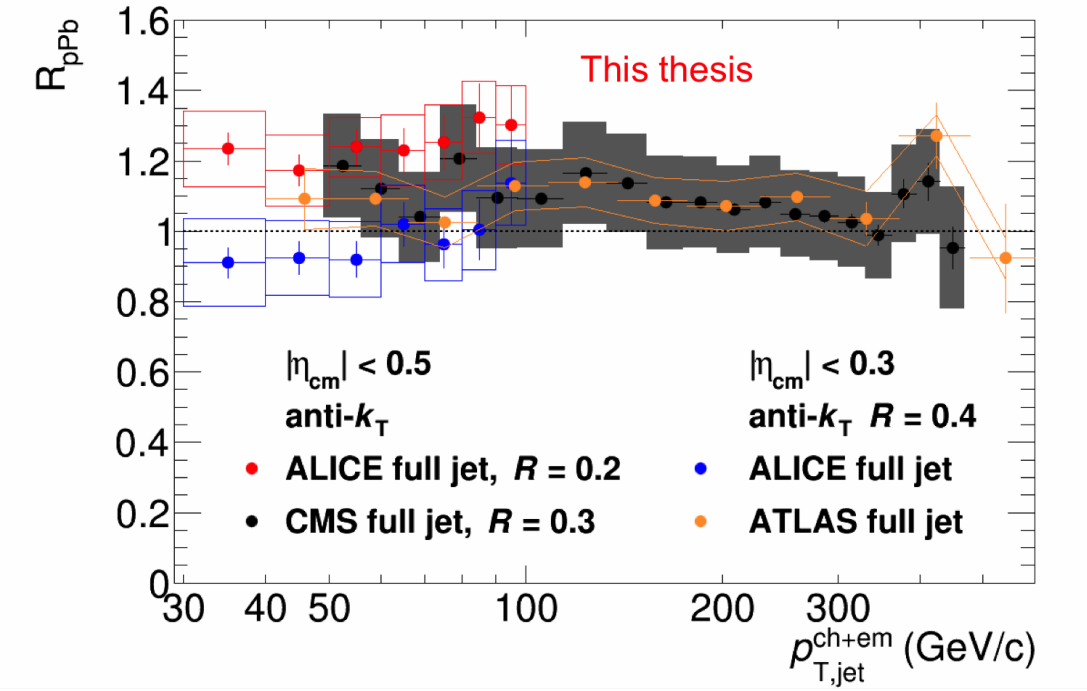

Figure 5.22: Nuclear Modification Factor for jets R_{pPb} for various jet radii from different LHC experiments. Adapted from [64, 65].

same event are used, the two spectra are measured in independent sets of events. These two sets deemed 'lhc13X' and 'lhc13Y' are composed of an equal number of events from lhc13b and lhc13c. The respective run number composition of the two pseudoperiods are:

lhc13X: 195483, 195529, 195531, 195673

lhc13Y: 195344, 195351, 195389, 195391, 195478, 195479, 195481, 195482, 195566, 195567, 195568, 195592, 195593, 195633, 195635, 195644, 195675, 195677

The ratio measured in this analysis is shown in figure 5.23. A comprehensive discussion of all systematic uncertainties analogous to those discussed in section 5.4 can be found in appendix E. In addition to the jet structure ratio for p-Pb and pp collisions, figure 5.23 also shows the jet structure ratios from two theoretical models: next-to-leading order (NLO) pQCD calculations with and without hadronization and the EPS model which in addition to calculating the jet spectra using NLO pQCD calculations also incorporates modifications to the nuclear PDFs (see section 2.8.1) in the simulated pp collisions at the same collisional energies as the ALICE p-Pb collisions.

The jet structure ratio for pp collisions is consistently lower for all observed p_T when compared to p-Pb. This is primarily due to a lower collisional energy in the measured pp system and not the cold nuclear matter effects. Incorporating modified nuclear PDFs produces only a small effect on the jet structure ratio (comparing EPS to NLO without hadronization), and those models are consistent within systematic uncertainties to the ALICE p-Pb measured data. When hadronization is incorporated, the results differ significantly with the measurement. The reason for this discrepancy is that for smaller jet radii, hadronization is a more important effect. This is what is observed in the PYTHIA Perguia2011 tune for $R = 0.2$. PYTHIA underestimates the jet cross section at $R = 0.2$ which causes the jet structure ratio to be reduced compared to other models (and data), and also causes the R_{pPb}^{PYTHIA} for $R = 0.2$ to be enhanced when compared to $R = 0.4$. Overall there is no indication of strong modifications in the jet structure due to cold nuclear matter effects.

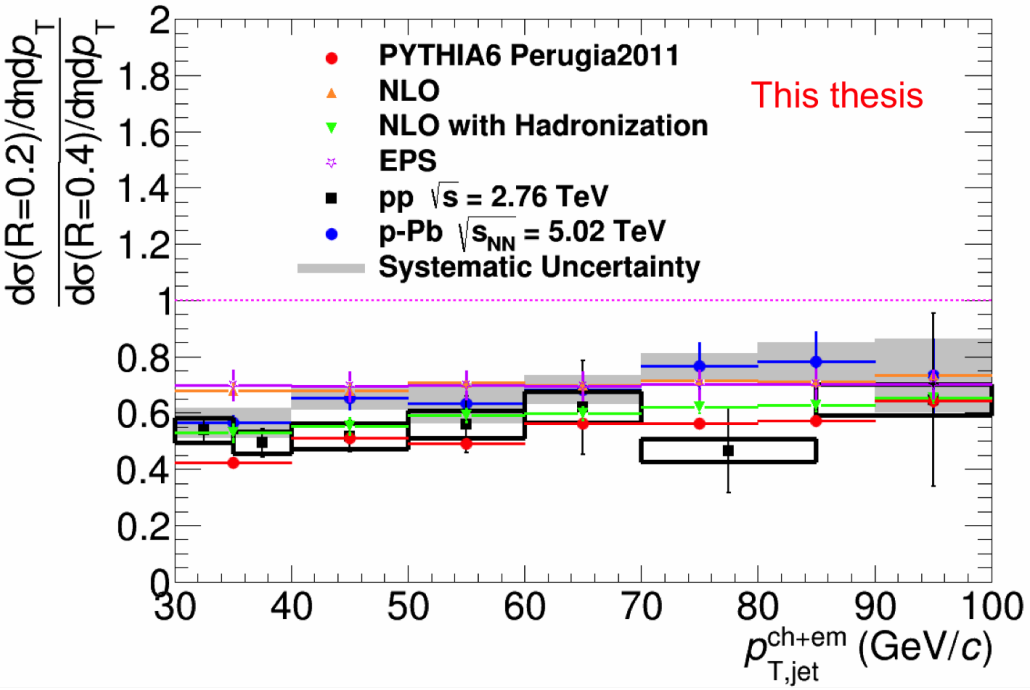

Figure 5.23: Comparison of Jet Structure Ratio for p-Pb collisions to pp collisions at $\sqrt{s_{NN}} = 5.02$ TeV and $\sqrt{s} = 2.76$ TeV respectively. Simulated spectra from various models are also shown

Averaged $30 < p_{T,jet}^{ch+em} < 100$ GeV/c	**Cross Section &** R_{pPb}^{PYTHIA}		**JSR**
Systematic	$R = 0.2$	$R = 0.4$	
Unfolding Systematics			
Unfolding Method	1.3	3.1	1.7
Unfolding Regularization	0.2	0.9	0.6
Unfolding Prior	<0.1	0.2	0.4
$p_{T,min}^{meas}$	0.7	1.1	0.5
$p_{T,min}^{unf}$	negligible		
JES Systematics			
Tracking Efficiency	5.7	6.6	1.1
Hadronic Correction	0.8	0.6	2.2
Underlying Event Subtraction (UE)	3.5	5.2	1.6
Background Fluctuations (δp_T)	0.1	0.8	0.7
Detector Response	0.8	3.3	2.5
Scale Factor	<0.01	0.4	0.4
Total Systematic	8.7%	11.6%	8.3%

Table 5.2: Summary of systematic uncertainties for the jet cross section, jet structure ratio, and nucelar modification factor for jets. The values shown for the systematic uncertainties are the averaged deviation between the nominal parameter set, and the closest variation for each systematic over the entire reported p_T range.

CHAPTER 6

Centrality Dependent Jet Results

In this chapter, results regarding jet observables which are centrality dependent will be discussed. In particular, the jet spectrum for various centrality bins and radii will be shown as well as the R_{CP} for $R = 0.2$ and $R = 0.4$. The R_{CP} observable has three distinct advantages over the observables presented in the previous chapter. Firstly, a reduction in the systematic uncertainty due to many effects canceling out (or reduced) when calculating the ratio. Secondly, nuclear effects should be stronger in more central p-Pb collisions compared to peripheral. Finally, a pp reference from simulation is not needed elminating model dependent effects (used to generate the pp reference) on the jet spectra.

However, the paramount issue with centrality dependent observables, in particular for this analysis, is determining the centrality itself on an event-by-event basis in the sparse environment of p-Pb collisions in a mannor which is not biased. This is discussed at length in section 6.1.

6.1 Centrality in p-Pb Collisions

In ALICE, centrality classes are defined by certain cuts which are placed in event activity estimators which measure charged particle mutliplicity amplitudes in three distinct pseudorapidity regions (the VZERO detector), along with at zero-degree energy (the ZDC detector) [53].

The procedure to estimate centrality (see appendix C) is based upon a percentile class of the observed event activity in a particular detector. In Pb-Pb collisions [49, 50], it was observed that a strong correlation exists between the event multiplicity and the

number of partcipants in the collisions (N_{part}) or the number of binary nucleon-nucleon collisions (N_{coll}). The VZERO detector which is able to precisely measure the total event multiplicity (see section 3.2.3) was favored in Pb-Pb collisions. In contrast to Pb-Pb collisions, in p-Pb collisions it is observed that large multiplicity fluctuations along with a small range of participants, generates a dynamical bias for centrality classes based on observed event activity in the VZERO. However, zero-degree energy is expected to be less sensitive to this bias due to its large η-seperation from the central portion of ALICE (see section 3.2.4 for technical details). These dynamical biases can be seen in figure 6.1. For most central p-Pb collisions (0-20% event centrality), there are more jets when using V0A then ZNA. The opposite effect is observed at peripheral events (40-90% event centrality) where ZNA produces a larger jet yield.

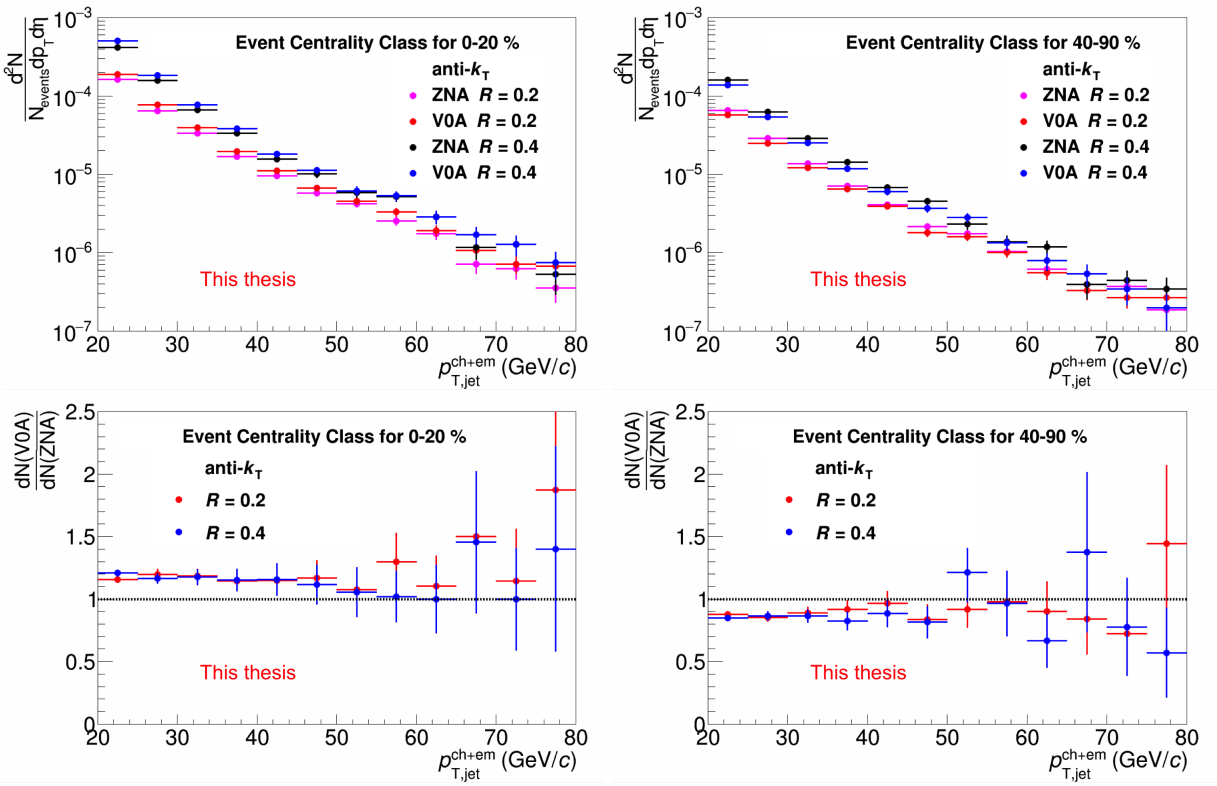

Figure 6.1: Comparison of different centrality class jet spectra (Upper Plots) and ratios (Lower Plots). Left: 0-20%. Right: 40-90%.

The observed bias in the jet spectra for V0A and ZDC are also observed in in the charged hadron Q_{pPb}:

$$Q_{pPb}(p_T; cent) = \frac{\frac{dN_{pPb}^{cent}}{N_{events} d\eta dp_T}}{T_{pPb}^{cent} \frac{d\sigma_{pp}}{d\eta dp_T}} \tag{6.1}$$

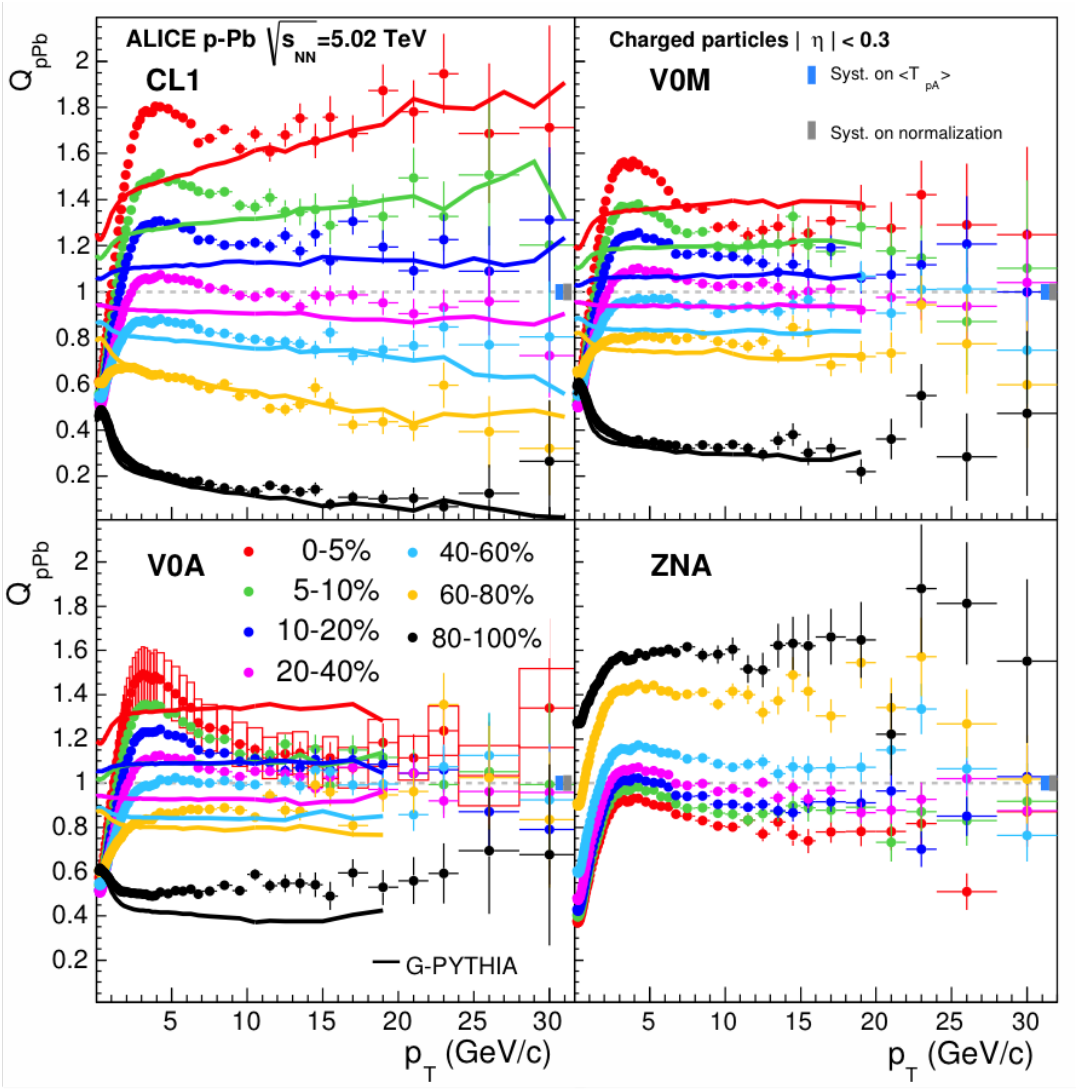

Figure 6.2: Comparison of charged hadron Q_{pPb} for various centrality classes. Adapted from [53].

From figure 6.2, it is observed that the spread between the centrality classes reduces with increasing rapidity gap between the centrality estimator and the measured hadron p_T [53]. This shows a clear indication of jet-veto bias (negative slope in Q_{pPb}) when using the CL-1 centrality estimator and still persits (but to a lesser extent) to the VZERO multiplicity class (V0A and V0M which is a weighted average of V0A and V0C). Furthermore, both VZERO multiplicity classes and the CL-1 show a clear multiplicity bias ($Q_{pPb} < 1$). Given the above studies, the ZDC (ZNA event class) was concluded to be the least biased centrality estimator in ALICE at the time of this thesis and will be used to determine the centrality classes in this analysis.

Figure 6.3 shows the correlation between the VZERO detector and the ZDC detector

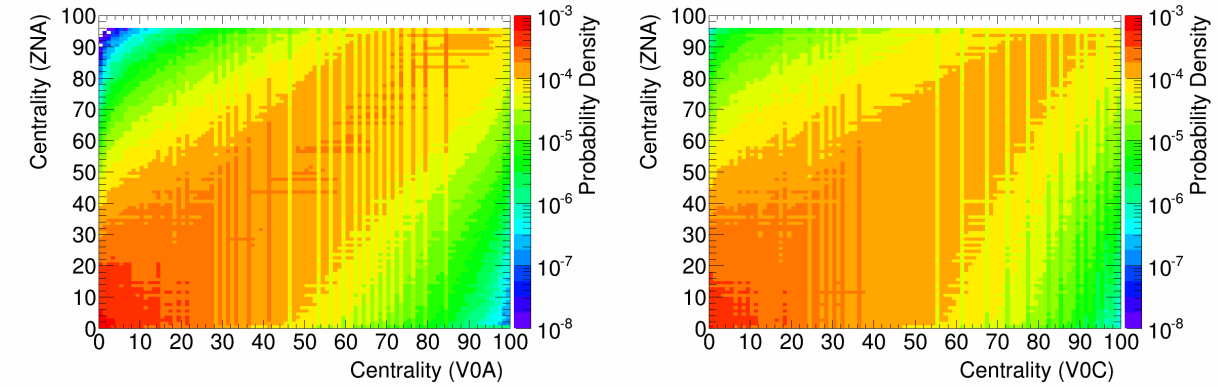

Figure 6.3: Correlation between VZERO and ZDC detector event centrality. Left: V0A vs ZNA. Right: V0C vs ZNA

for event centrality. There is clearly a linear correlation between the detectors, but a rather large spread. Several feature that put constraints on what centralities can be considered for the "central" jet bin and the "peripheral" jet bin are seen in this plot. There are no entries for 95-100% centrality for the ZNA estimator. This requires the analysis to be carried out by not considering ZNA centralities above 95%.

In order to "engineer" an observable which is as sensitive to cold nuclear matter effects as R_{pPb}, it is desriable to have a jet centrality bin which is as central as possible, while also having a peripheral jet bin which is as peripheral as possible. The reasoning for this is that in most central collisions, it is expected that CNM effects will be strongest, while in peripheral collisions, the collisions should be approximately pp "like".

These idealized criteria have to be relaxed given limited statistics along with centrality biases that exists in event centrality measurements. Limited statistics lead us to consider using binning where both central and peripheral jet bins have a similar (and maximal) transverse momentum reach. Finally, given that when comparing one centrality estimator versus another there is a spread, there should be a reasonable gap or seperation between the two jet centrality bins. To account for all the above considerations, the following jet centrality bins were utilized for this analysis: 0-20% for the central jet bin; 40-90% for the peripheral jet bin. The N_{coll} for these two bins are 12.77 (central) and 4.38 (peripheral).

As with the minimum biased results, it was necessary to determine to what extent the jet spectra were statistically significant in terms of the $p_{T,jet}$. The same criteria are used here in which for both jet radii and centrality bins, the spectrum is required to have at least 10 counts. Furthermore, in unfolding it is also desirable to have a

Centrality (%)	N_{coll}^{V0A}	N_{coll}^{ZNA}
0-5	14.8	15.8
5-10	13.0	14.1
10-20	11.7	12.6
20-40	9.36	10.1
40-60	6.42	6.35
60-80	3.81	2.95
80-100	1.94	1.34
0-100	6.87	6.90

Table 6.1: Comparison of $\langle N_{coll} \rangle$ values for various centrality estimators [53].

"smooth" spectrum where there are not wild bin-by-bin fluctuations. This behavior can be observed in figure 6.1 where the peripheral jet bins for $R = 0.4$ has a large jump in the spectrum for $p_{T,jet}^{meas} > 60$ GeV/c. This impacts the unfolded spectra in that any "jumps" in the measured spectrum now amplify the fluctuating behavior of an unfolded spectrum. If such fluctuations occur, they could cause the unfolded spectrum to have large bin-by-bin fluctuations which would render the spectrum unstable. By taking into account this consideration, all measured spectra that are used as input are cutoff at 60 GeV/c.

6.2 Centrality Dependent Observables

6.2.1 Centrality Dependent Jet Spectra

Similar to what was done in sections 5.1 to 5.2, both centrality bins for the jet spectrum are analyzed and corrected for following the same procedure. It is also required to unfold the jet spectra and normalize them properly in order to measure R_{CP}. The normalization of the jet spectra for the two centrality bins are identical that that done in section 5.1 with the exception that N_{events} in 5.2 is now the number of events in the corresponding centrality bin.

All the unfolding systematics along with a comparison of the spectra for ZNA compared to V0A can be found in appendix F. Figure 6.4 shows the 0-20% ZNA centrality estimator jet spectra for $R = 0.2$ and $R = 0.4$. Figure 6.5 shows the 40-90% ZNA centrality estimator jet spectra for $R = 0.2$ and $R = 0.4$. The cross section can also be found in appendix F.

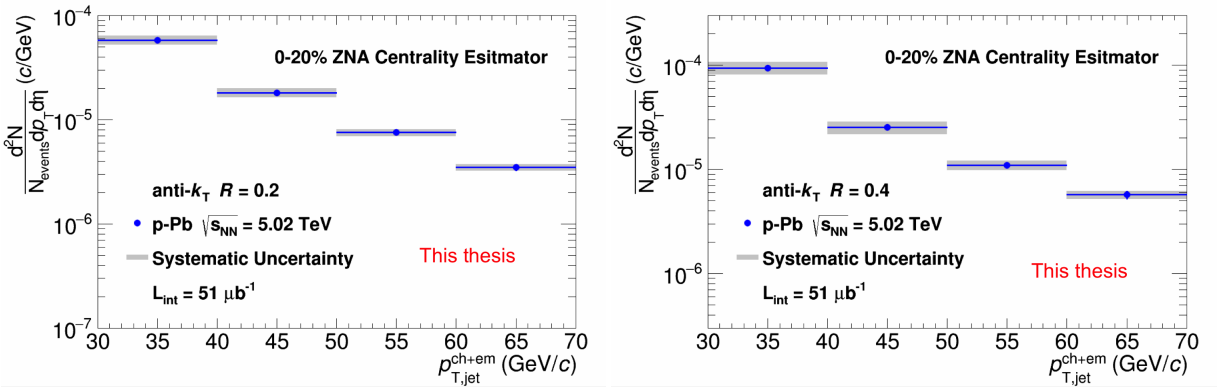

Figure 6.4: 0-20% Central jet spectrum with statistical and systematic uncertainties. Left: $R = 0.2$. Right: $R = 0.4$

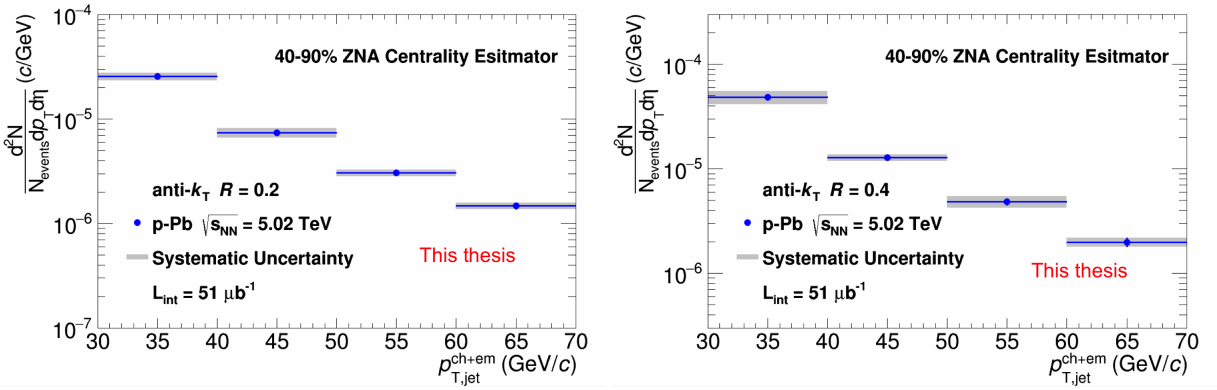

Figure 6.5: 40-90% Peripheral jet spectrum with statistical and systematic uncertainties. Left: $R = 0.2$. Right: $R = 0.4$

6.2.2 R_{CP}

A R_{CP} can be defined analogous to R_{pPb} in 5.9 by:

$$R_{CP} = \frac{N_{coll}^{c2}}{N_{coll}^{c1}} \frac{\frac{d^2N_{jets}^{c1}}{N_{events}^{c1} d\eta dp_T}}{\frac{d^2N_{jets}^{c2}}{N_{events}^{c2} d\eta dp_T}} = R_{coll}^{c1,c2} \frac{\frac{d^2N_{jets}^{c1}}{N_{events}^{c1} d\eta dp_T}}{\frac{d^2N_{jets}^{c2}}{N_{events}^{c2} d\eta dp_T}} \tag{6.2}$$

Where $c1$ is defined to be the central centrality bin (i.e. 0-20% in this analysis) and $c2$ is the peripheral centrality bin (i.e. 40-90% in this analysis). In principal, $c1$ and $c2$ can be any centrality bin (even if $c2$ is 0-100% in which R_{CP} is refered to in literature now as R_{CM}), however a proper treatment of statistical uncertainties must be addressed if there is an overlap between $c1$ and $c2$ when utilizing the same dataset for $c1$ and $c2$ (e.g. $c1$ = 20-50% and $c2$ = 40-80% for the same set of events). The corresponding variables that are dependent on $c1$ and $c2$: namely N_{events}, N_{jets}, and N_{coll} are analogous

to those explained in section 5.1, but for their respective centrality bins. The parameter $R_{coll} = \frac{N^{c2}_{coll}}{N^{c1}_{coll}}$ is the ratio of nucleon-nucleon collisions between $c1$ and $c2$. The means and total uncertainties for N_{coll} and R_{coll} are given in table 6.2.

	Mean	**Total Uncertainty**
$N^{0-20\%}_{coll}$	12.77	10 %
$N^{40-90\%}_{coll}$	4.38	15.5 %
R_{coll}	2.92	18.4 %

Table 6.2: Values for various centrality dependent parameters. Values adapted from [53].

The N_{coll} values were calculated by taking a weighted averaged of the centrality bins considered in [53]. R_{coll} was estimated by assuming independence of the two centrality bins in the Glauber model used to calculate these parameters. This assumption of independence leads to a very conservative estimate of the overall normalization uncertainty, which for R_{CP} is 18.4%.

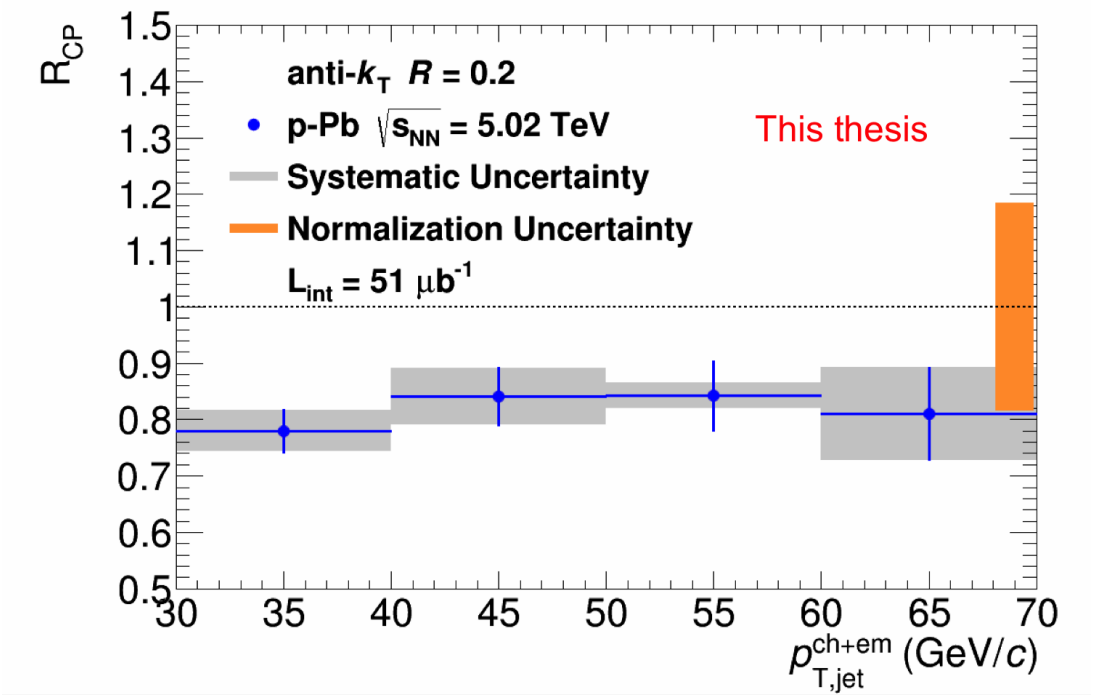

Figure 6.6: Nuclear Modification Factor R_{CP} with statistical and systematic uncertainties. A normalization uncertainty in R_{coll} = 18.4% is also shown for $R = 0.2$.

Figures 6.6 and 6.7 shows the R_{CP} for various jet radii in p-Pb collisions along with statistical, systematic, and normalization uncertainties. Firstly it should be noted that

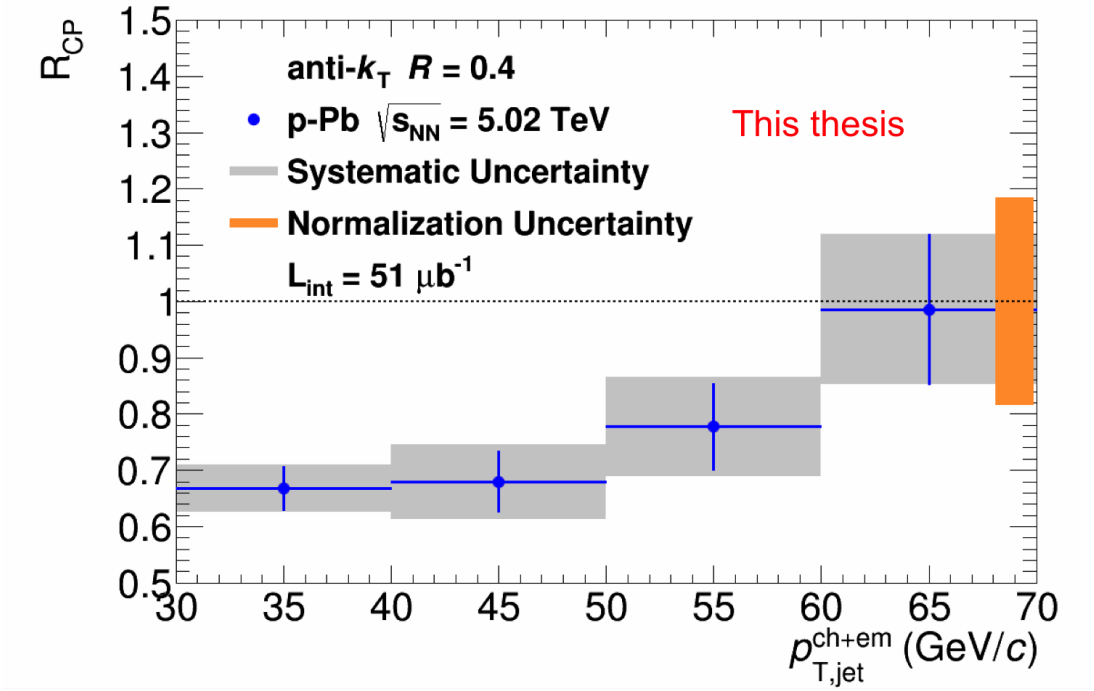

Figure 6.7: Nuclear Modification Factor R_{CP} with statistical and systematic uncertainties. A normalization uncertainty in R_{coll} = 18.4% is also shown for $R = 0.4$

these spectra suffer from a reduced $p_{T,jet}^{ch+em}$ kinematic reach due to lack of statistics in the peripheral jet bin. In order to increase the statistics and the $p_{T,jet}^{ch+em}$ reach, either more statistics are required or the EMCal trigger dataset must be analyzed (see figure 6.8).

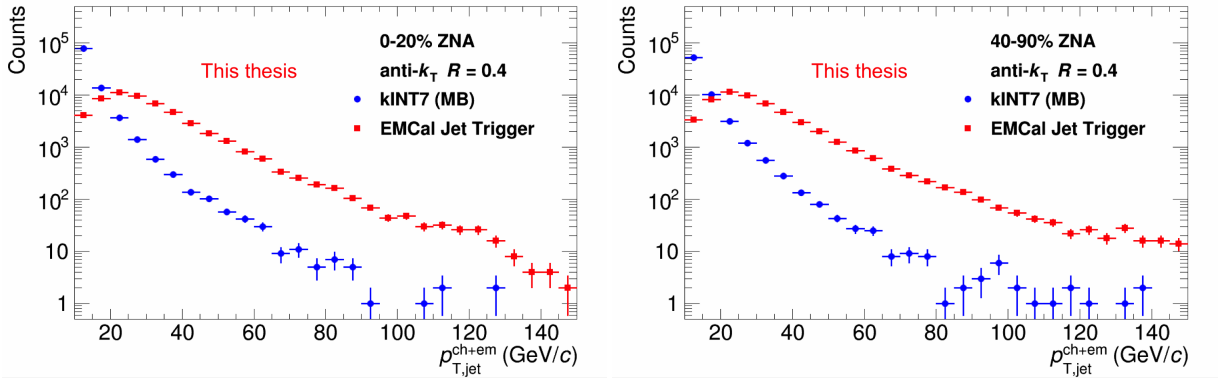

Figure 6.8: Comparison of kINT7 (used for this analysis) to the EMCal jet trigger. The EMCal jet trigger (kJ1) requires an EMCal cell to have an energy deposition of 20 GeV/c or greater to trigger on an event.

As mentioned in the introduction of this chapter, R_{CP} should be more sensitive to nuclear effects then R_{pPb} from MB events. As with R_{pPb}, R_{CP} for $R = 0.2$ is more

sensitive to hadronization effects and is most likely not as strongly correlated to the parton kinematics of the initial hard scattering as $R = 0.4$. Although there is a large uncertainty due to normalization, an increase is observed in R_{CP} for $R = 0.4$ with increasing p_T. The suppression at low p_T in R_{CP} may be due to "cold" nuclear effects (nPDFs and/or CGC), however to unambiguously conclude that such an effect is being observed, a more rigourous assesment of the potential centrality biases must be performed.

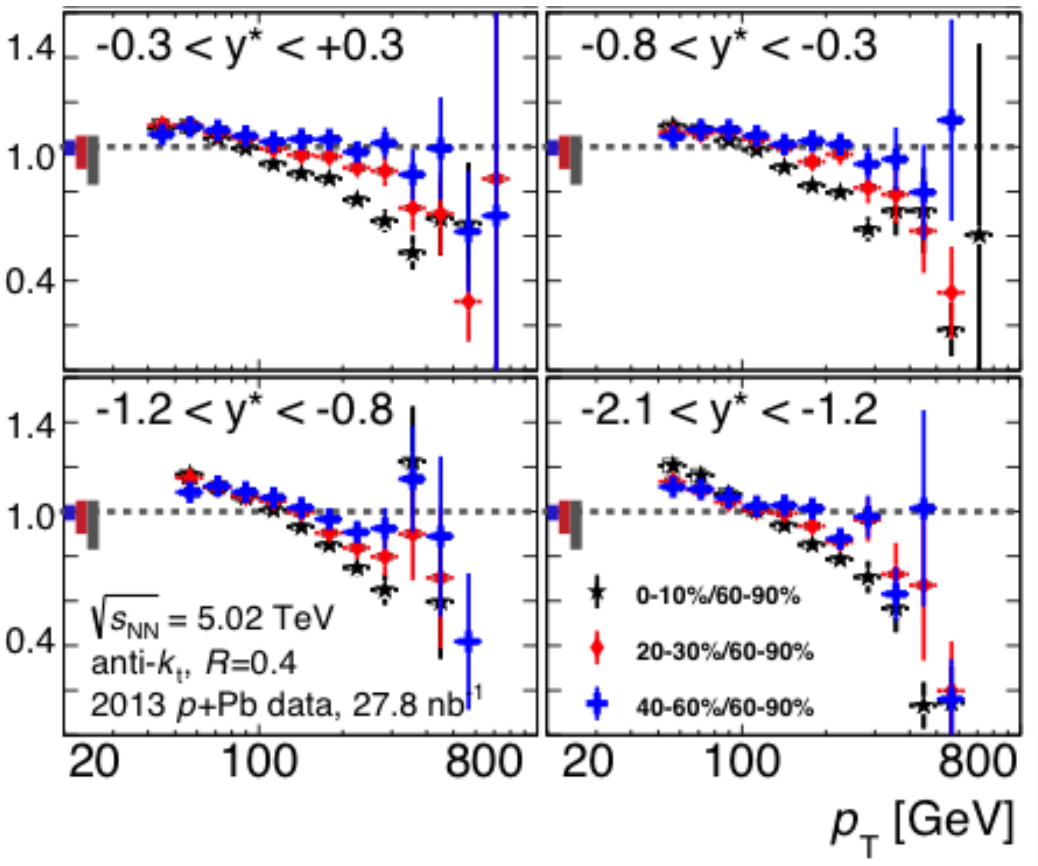

Figure 6.9: Measured R_{CP} values for $R = 0.4$ jets in p-Pb collisions in central (stars), mid-central (diamonds) and mid-peripheral (crosses) events. Each panel shows the jet R_{CP} in a different rapidity range. Vertical error bars represent the statistical uncertainty while the boxes represent the systematic uncertainties on the jet yields. The shaded boxes at the left edge of the $R_{CP} = 1$ horizontal line indicate the systematic uncertainty on R_{coll}. Figure adapted from [64].

Potential centrality biases also make an "apples-to-apples" comparison difficult to other LHC experiments. At the time of this thesis, only ATLAS has produced a R_{CP} for p-Pb collisions which is seen in figure 6.9. A comparison over the same rapidity range ($|y| < 0.3$) to figure 6.7 shows that two R_{CP} measurements are consistent with

one another in the overlap region within uncertainties (statistical, systematic, and normalization). This consistency is observed in spite of the fact that the ATLAS FCAL [68] pseudorapidity window corresponds to roughly the same pseudorapidity window of the VZERO and thus may contain many of the same centrality biases that VZERO has with respect to the ZDC.

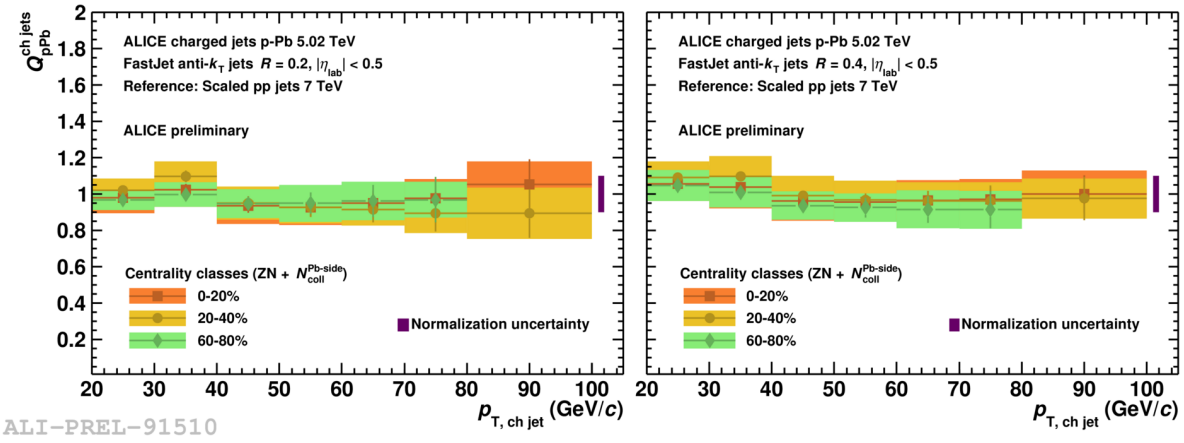

Figure 6.10: ALICE Charged jet Q_{pPb} for various centralities. The pp reference used is the ALICE charged jet 7 TeV scaled down by MC. Normalization uncertainties are also shown. Figure adapted from [54].

Figure 6.10 shows the ALICE charged jet Q_{pPb}. These values of Q_{pPb} are consistent with unity indicating that strong cold nuclear effects are not present. A comparison between the charged jet Q_{pPb} and the full jet R_{CP} can be made but with many caveats. Firstly, the centrality method used and the centrality binning are not identical. Furthermore, the parton kinematics of charged jet at a given p_T are not the same as those at the same p_T for full jets.

Taking these consideration into account, R_{CP} may be treated like a "double ratio" of a Q_{pPb} from a central bin to a Q_{pPb} from a peripheral. In that sense since the Q_{pPb} do not differ from unity appreciably, a charged R_{CP} could be infered to be close to unity. Although the measured R_{CP} for full jets is below unity at low p_T, there are considerable uncertainties on both full and charged jet nuclear modification factors, a large normalization uncertainty due to both Glauber model and pp reference scaling (for charged jets), and unresolved centrality biases. Once these issues are properly resolved, an agreement is expected between the observed R_{CP}.

All the unfolding systematics along with a comparison of the spectra for ZNA compared to V0A can be found in appendix G. Table 6.3 shows an overview of systematic uncertainties in the centrality dependent jet observables. As with the jet structure ra-

tio, some of the systematic uncertainties in R_{CP} are offset by both the numerator and denominator being measured with the same detector.

Averaged $30 < p_{T,jet}^{ch+em} < 70$ GeV/c	**0-20%**		**40-90%**		R_{CP}	
Systematic (R_{jet})	0.2	0.4	0.2	0.4	0.2	0.4
Unfolding Systematics						
Unfolding Method	0.8	6.6	0.3	0.4	0.5	6.1
Unfolding Regularization	1.8	1.0	1.1	0.3	0.3	0.1
Unfolding Prior	1.9	0.6	<0.1	<0.01	1.9	0.5
$p_{T,min}^{meas}$	2.1	0.6	1.4	0.2	0.7	0.4
$p_{T,min}^{unf}$	negligible					
JES Systematics						
Tracking Efficiency	4.3	4.4	4.5	5.3	0.2	0.8
Hadronic Correction	1.6	1.5	0.9	1.4	0.7	2.9
Underlying Event Subtraction (UE)	5.6	4.6	5.0	6.2	0.6	1.8
Background Fluctuations (δp_T)	0.2	1.6	0.1	0.9	0.1	0.7
Detector Response	1.9	4.2	2.0	4.5	0.1	0.2
Scale Factor	<0.1	0.2	<0.01	<0.1	<0.01	0.1
Total Systematic	9.3%	12.7%	8.9%	11.3%	4.5%	9.1%

Table 6.3: Systematic uncertainties for the central and peripheral jet cross section, and R_{CP}.

CHAPTER 7

Conclusions

In heavy-ion collisions at RHIC and the LHC, a suppression of the nuclear modification factor for jets along with other strongly interacting particles has been observed relative to proton-proton collisions. To unambiguously determine if this suppression is due to the creation of a strongly interacting medium of de-confied partons referred to as the *Quark-Gluon Plasma*, or due to *Cold Nuclear Matter* effects, a "control experiment" is required. Proton-lead collisions serve as this control experiment, in that such collisions are expected to be sensitive to cold nuclear matter effects while not producing a QGP at this collision energy ($\sqrt{s_{NN}} = 5.02$ TeV). This thesis reports the first measurements of full jets in p-Pb collisions using the ALICE detector.

Measurements of CNM effects are done via R_{pPb}, R_{CP}, and the jet structure ratio. Measurements of the jet spectrum for charged + neutral constituents along with a detailed and proper discussion of the statistical, systematic, and normalization uncertainties are presented in sections 5.3 and 5.4. A comparison of the *Jet Structure Ratio* for $\frac{R=0.2}{R=0.4}$ is shown in figure 5.23 along with the JSR measured in pp collisions at $\sqrt{s} = 2.76$ TeV and various other simulated pp collisions. No significant modifications in the jet structure ratio are observed.

In order to measure a R_{pPb}, a pp reference at the same collision energy of p-Pb collisions is required. At the time of this analysis, such a measurement was not avaiable. The LHC will run beam for pp collisions at $\sqrt{s} = 5.02$ TeV during run 2. The PYTHIA6 Perguia2011 tune is used to simulate pp collisions for this thesis due to its ability to reproduce the 2.76 and 7 TeV pp jet spectra (see section 5.5.1). Figures 5.18 and 5.19 shows the p-Pb jet spectrum compared to various MC tunes when properly scaled by T_{pPb}.

The principal observable presented in this analysis is R_{pPb}^{PYTHIA} which essentially captures the modification the jet itself "experiences" due to Cold Nuclear Matter effects. As can be inferred from figures 5.20 and 5.21, the measured R_{pPb}^{PYTHIA} is consistent with those measured in ATLAS and CMS. The magnitude of any observed suppression in R_{pPb}^{PYTHIA} even without using a pp reference at $\sqrt{s} = 5.02$ TeV (needed to increase precision) cannot account for the observed suppression in R_{PbPb}. This indicates that CNM effects are small. Given the Bjorken $x \sim 10^{-3}$ and the $Q^2 \sim 100$ GeV/c for jets in p-Pb collisions, it can be assumed that the potential effects of the color glass condensate are negligible. Hence, if the modification in R_{pPb}^{PYTHIA} is due to nPDFs, it is consistent with EPS calculations within uncertainties.

In addition to R_{pPb}, measuring the so-called R_{CP} in which jet spectra from central p-Pb collisions are compared to peripheral collisions is also a measurement of nuclear modification. In principal, peripheral p-Pb collisions can be used to approximate pp collisions. This allows a measurement to be performed without needing a pp reference. The issues here is that the cross section is lower due to a lower N_{coll} and since the jet spectrum is more "pp like", it falls more steeply with increasing transverse momentum. These two effects cause the jet transverse momentum reach to be severly reduced compared to centrality integrated measurements. In order to compensate for this effect either more statistics or a triggered dataset are required (see figure 6.8).

R_{CP} is shown in figures 6.6 and 6.7. Although the transverse momentum reach is limited to 70 GeV/c, the measured R_{CP} is consistent with unity and with the measured R_{pPb}^{PYTHIA} from section 5.5.2. Comparing the measured R_{CP} from this analysis to other experiments is difficult to perform given the unresolved potential centrality biases that exist in measuring event centrality in p-Pb collisions in ALICE. Given these biases, the R_{CP} measured in ATLAS for full jets over the same rapidity range is consistent with the R_{CP} measured in this analysis. In order to further constrain uncertainties, additional studies are required to investigate these centrality biases. Exploration of these centrality biases along with analyzing the EMCal trigger dataset is a natural extension of the work presented in this thesis and should be performed before a more rigourous comparison of the R_{CP} between the experiments can be made.

Given all the measurements performed in this analysis regarding cold nuclear matter effects (R_{pPb}^{PYTHIA}, R_{CP}, and JSR), at this point it can be concluded that no strong cold nuclear matter effects have been observed in p-Pb collisions at $\sqrt{s_{NN}} = 5.02$ TeV in ALICE. Therefore, the jet suppression observed in R_{PbPb} is a QGP hot nuclear matter effect.

Appendices

APPENDIX A

Relativistic Kinematics

In relativistic collisions, coordinate transformations from one system to another follow the common *Lorentz* transformation, with its relation to *Cartisian* coordinates given by A.1:

$$\begin{aligned} t' &= \gamma\left(t - \frac{vx}{c^2}\right) \\ x' &= \gamma\left(x - vt\right) \\ y' &= y \\ z' &= z \\ \gamma &= (1 - \frac{v^2}{c^2})^{-\frac{1}{2}} \end{aligned} \tag{A.1}$$

where it is assumed that one coordinate system (the primed system) is traveling at constant velocity along the x direction (which is arbitrary) realtive to the unprimed system. These 4 components of the transformation can be written in a 4-vector x^μ with x^0 representing the time component. For coordinate systems in which there is azimuthal symmetry (i.e. cyclindrical coordinate systems like those used in ALICE), the 4-vector for position can be written as:

$$x^\mu = \{t, x_T, z\} \tag{A.2}$$

where $x_T = \sqrt{x^2 + y^2}$. The 4-momentum p^μ can be written as:

$$p^\mu = \{E/c, p_T, p_z\} = \{E, p_T, p_z\} \tag{A.3}$$

where $c = 1$ is used in the last equality of A.3. The transverse momentum, $p_T = \sqrt{p_x^2 + p_y^2}$, is the component of momentum that is perpendicular to the beam pipe. This is a useful quantitiy in relativistic collisions in that particles with high p_T must be produced by hard scatterings of partons and cannot be spectator particles from the nuclei involved in the collisions themseleves (e.g. protons or neutrons in lead nuclei). The angle between the y-axis and x-axis in the plane perpendicular to the beam line is the azimuthal angle φ.

A useful quantity in relativistic collisions is the rapidity, which is defined as:

$$y = -\frac{1}{2}\ln\left(\frac{E + p_z}{E - p_z}\right) \tag{A.4}$$

The rapidity is useful because it is Lorentz invarient, i.e. it is additive in the sense that non-relativistic speeds are additive in cartisian coordinate systems. To measure or calculate the rapidity of a particle, the energy and momentum are required. This can be an issue in experiments because the particles mass may not be well known. Thus a more convenient quantity, the *pseudorapidity* is used and defined in terms of the particle angle wrt the beam axis (in this context the z-axis):

$$\eta \equiv -\ln\left(\tan\frac{\theta}{2}\right) \tag{A.5}$$

The pseudorapidity can also be defined in terms of a particles momentum p, and the longitudinal momentum p_z as:

$$\eta \equiv \frac{1}{2}\ln\left(\frac{p + p_z}{p - p_z}\right) \tag{A.6}$$

In terms of the pseudorapidity and azimuthal angle, the angular seperation between two points in ALICE is given by:

$$(\Delta R)^2 = (\Delta\eta)^2 + (\Delta\varphi)^2 \tag{A.7}$$

In this analysis, it is assumed that the mass of particles $m \sim m_\pi$. This assumption doesn't effect the p^μ of particles significantly for two reasons: firstly, about 90% of particles produced in HIC tend to be pions (charged or neutral), and secondly the measured p_T of particles on average tends to be significantly higher then the rest mass of the pion.

APPENDIX B

Jet Algorithms

A *Jet* is an object which is reconstructed from particles in accordance to a specfic set of instructions (i.e. algorithm). A high p_T parton fragments into a collection of particles which can be reconstructed into a jet. Therefore the parton which fragments and the jet are not the same object but share many of the same kinematic properties. The process of constructing jets in a relativistic collision following some set of instructions is referred to as *Jet Finding*.

Because a jet is reconstructed by a jet algorithm, the properties of the jet are dependent of what the algorithm reconstructs. The general "desirable" properties that a jet should have, according to the "Snowmass Accords" [69] are:

- Simple to implement in an experimental analysis;
- Simple to implement in the theoretical calculation;
- Defined at any order of perturbation theory;
- Yields finite cross sections at any order of perturbation theory;
- Yields a cross section that is relatively insensitive to hadronization.

Historically, jet algorithms fall into two classes [70]. The first class are cone algorithms in which a "top-down" algorithm relying on the idea that QCD branching and hadronization leaves the bulk features of an event's energy flow unchanged (specifically, energy flow into a cone). Sequential recombination algorithms use a "bottom-up" algorithms that repeatedly recombines the closest pair of particles according to some distance measure, usually related to the divergent structure of QCD matrix elements.

In order for an algorithm to achieve many of the properties outlined in the Snowmass Accords, it must be *Colinear Safe* and *Infrared Safe* (IR safe).

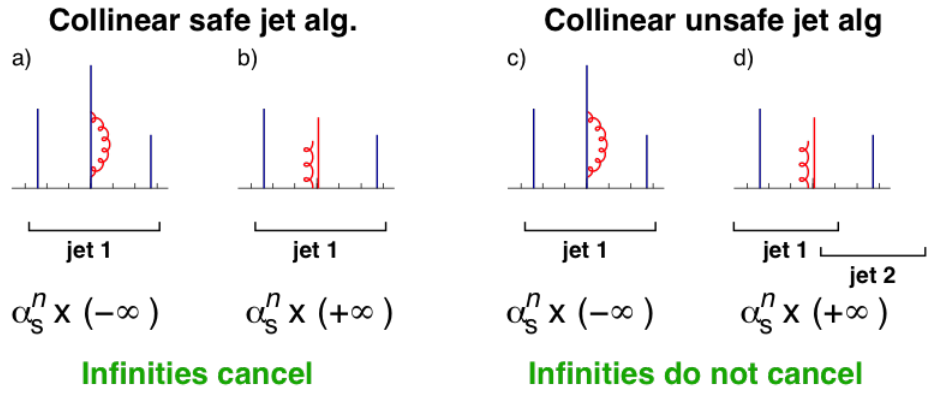

Figure B.1: Left: A colinear safe jet finding algorithm. Right: A colinear-unsafe jet finding algorithm. Particles are verticle line with their height's proportional to their transverse momentum; the horizontal scale is the rapidity. Adapted from [70]

A jet finding algorithm is colinear safe if a colinear splitting of a parton (e.g. a gluon emission from a parton) does not add or subtract the number of jets found in an event (figure B.1). Also, a jet algorithm should not be sensitive to soft particles which are uncorrelated to the hard scattering. If a parton from a soft process were added to the event near two jets, it shouldn't cause the jets to be combined into a single jet (figure B.2). Such a property is referred to as infrared safe.

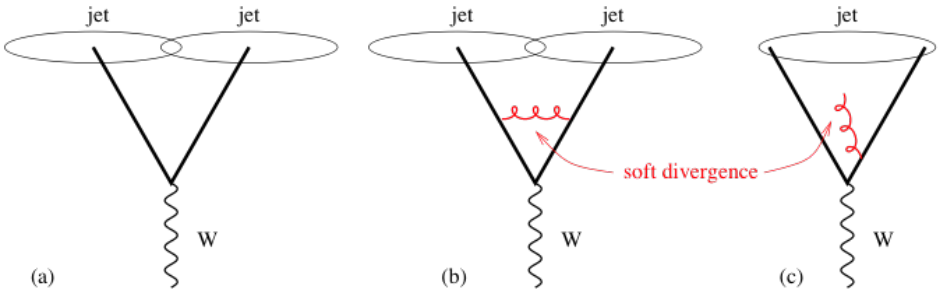

Figure B.2: A diagram of an event containing a W boson and two hard partons. Left: An IR safe jet reconstruction algorithm. Right: An IR unsafe jet reconstruction algorithm. The diagram shows the angular seperation of the jets and not their p_T as a function of rapidity. Adapted from [70]

In this analysis, the jet finding algorithms used are from the `FastJet` package [48]. The two algorithms used are the anti-k_T and [inclusive] k_T algorithms [47, 71]. Both algorithms are sequential recombination algorithms which cluster particles together

based on their transverse momenta and angular seperation. Given a set of n pseudoparticles {1,2,...,n}, the algorithms first calculate the p_T-weighted distance (d_{ij}) between all two pseudoparticle pairs in the set:

$$d_{ij} = min[k_{Ti}^{2p}, k_{Ti}^{2p}]\frac{\Delta_{ij}^2}{R^2} \tag{B.1}$$

$$d_{iB} = k_{Ti}^{2p} \tag{B.2}$$

where k_T is the transverse momentum, $\Delta_{ij}^2 = (y_i - y_j)^2 + (\varphi_i - \varphi_j)^2$ is the distance between two pseudoparticles, y is the rapidity, φ is the azimuthal angle, and R^2 is the dimensionless resolution parameter in the $\eta - \varphi$ plane analogous to the jet radius in cone algorithms. The quantity d_{iB} is the beam distance for the pseudoparticle.

The value of p is what determines how pseudoparticle pairs' distance modulus (d_{ij}) is calculated. Values of $p > 0$ has the effect of preferentially clustering particles of soft transverse momentum first and are thus more sensitive to the underlying event in heavy-ion collisions. The special class of $p = 1$ is the k_T jet finding algorithm and is used throughout this analysis to estimate the underlying event density. Values of $p < 0$ have the opposite effect in that they cluster the hard pseudoparticles first and that any soft pseudoparticles in their vacinity will cluster with them and not other soft pseudoparticle. The case of $p = -1$ is the anti-k_T jet finding algorithm. In addition to clustering soft pseudoparticles with hard ones first and not themseleves, the anti-k_T algorithm will not add two hard pseudoparticles together that are not within 2R. Thus, the jet produced in this case will be all the soft pseudoparticles around each hard pseudoparticle within R from each hard pseudoparticle in the event, with the resulting jets being almost perfectly conical. The case where $p = 0$ corresponds to the inclusive Cambridge/Aachen algorithm [72].

What determines if pseudoparticles are merged into a cluster is if $d_{ij} < d_{iB}$. If this is true, then the two pseudoparticles are summed by adding their 4-momenta into a new pseudoparticle (thus pseudoparticle i and j are removed from the list). If $d_{ij} \geq d_{iB}$, then pseudoparticle i is defined as a *jet candidate* and is removed from the particle list. The process continues until all pseudoparticles have been removed from the list. These jet candidates are then processed in the analysis by removing those that do not meet specfic selection criteria (those outlined in section 4.4).

One of the particular cuts mentioned in section 4.4 is the *Jet Area* cut, which is set to

be:

$$A_{jet} > 0.6\pi R_{jet}^2 \tag{B.3}$$

The area of the jet is estimate by using the active area method in `FastJet` [72]. In this method, a large amount of "ghost" particles with infinitesimal p_T are randomly placed in the event while jets are reconstructed. The amount of ghost particles a reconstructed jet contains is proportional to the area of the jet. The precision of the jet area is related to the number of ghost particles per unit area used in the area method. For this analysis, a ghost area of 0.005 is used.

The remaining jets which satisfy all the selection cuts are then called *Signal Jets* and are the jets used in this analysis.

APPENDIX C

Centrality Estimation in p-Pb Collisions

The *Glauber Model* [73] is generally used to calculate geometrical quantities of nuclear collisions (AA or pA). The model treats a HIC as a superposition of many pp collisions. The main parameterization of this model is the distance between the centers of the nuclei, which in particle physics experiments is generally referred to as the impact parameter (b). In order to relate a HIC to a pp collision, the model calculates two values: N_{bin} (also referred to in this analysis as N_{coll}) which is the number of nucleon-nucleon binary collisions; and N_{part} which is the number of participating nucleons. The values of N_{coll} and N_{part} are dependent on the geometry of the collision and the energy of the incoming nucleons. An expectation of the model is that as the impact parameter of the collision changes, N_{coll} and N_{part} (among many other quantities the model calculates) are changed wrt to a pp collision of the same energy.

Unfortunately, their is no way to measure the impact parameter on an event-by-event basis directly. Thus, the model must be related to an estimator M, the "Multiplicity" (referred to as a *Centrality Estimator*), which is measurable and various paramters or outputs (b, N_{coll}, N_{part}, ect.) of the model can be expressed in terms of M in a probabilistic manor. In order for the model to be useful, there must be a montonic dependence of the centrality estimator on the parameters of the model. The use of centrality estimators based on multiplicity or summed energy in certain pseudorapidity intervals is motivated by the observation that they show a linear dependence with N_{coll} or N_{part} [53].

Although there is a general monotonic correlation in the centrality estimator vs the impact parameter, there isn't a cleary one-to-one correspondance. As the average value of the centrality estimator increases, so does the average value of the impact

parameter. Thus, given a narrow centrality interval, there is a broad distribution to the value of impact parameters. This isn't an issue in collisional systems which produce high multiplicities (e.g. Pb-Pb) because the multiplicity fluctuations used to select a given centrality is much smaller then the multiplicity range of the reported centrality interval. However, in p-Pb collisions, the multiplicity fluctuations for a given centrality are comparable to the centrality intervals themseleves. This presents an issue in that now a measured multiplicity in an event could have a large ranges of centralities (see figure C.1).

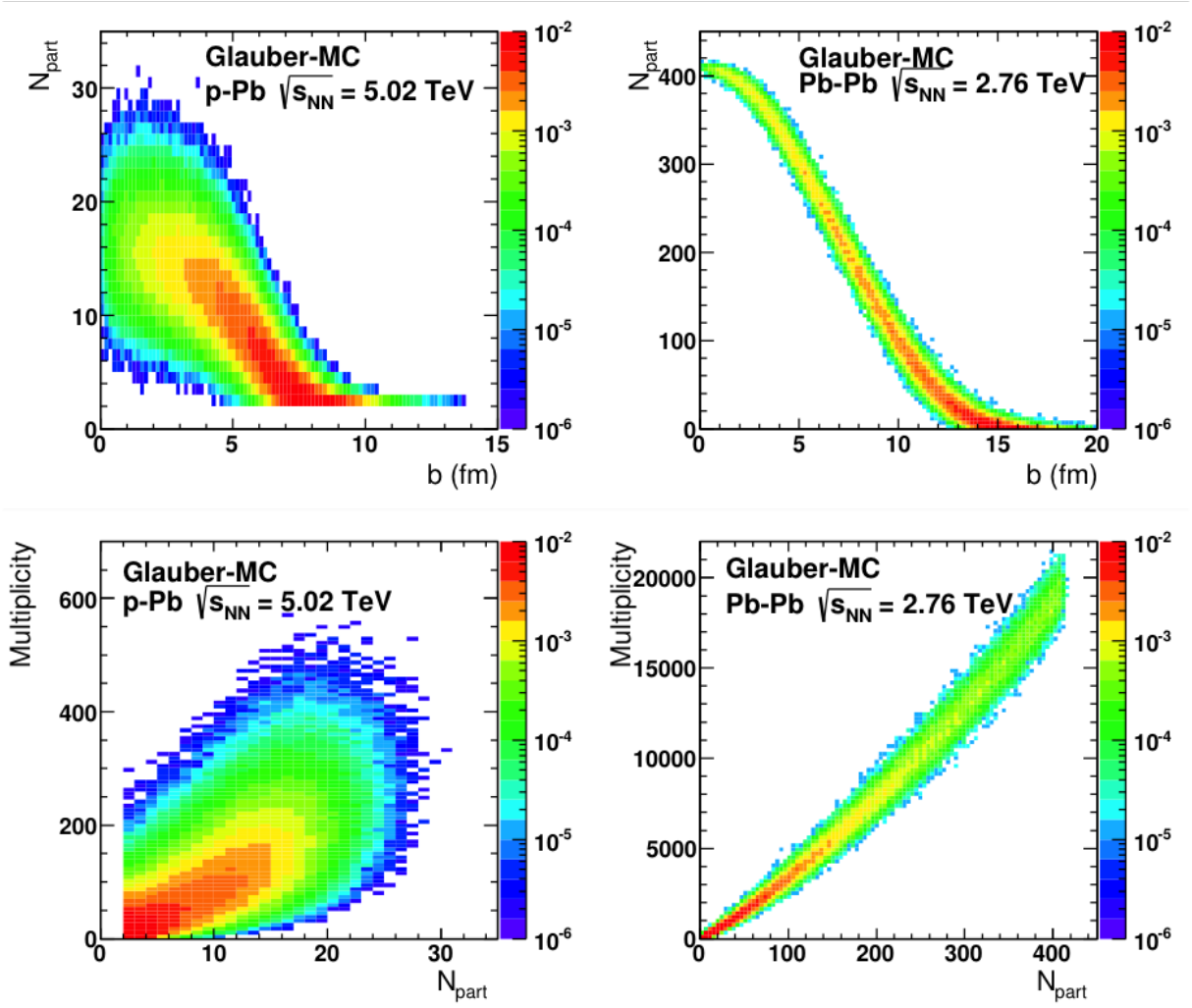

Figure C.1: Top: Scatter plot showing the realtionship of N_{part} to the impact parameter b in MC simulation for p-Pb (Left) and Pb-Pb (Right). Bottom: Scatter plot showing the realtionship of Multiplicity to N_{part} in MC simulation for p-Pb (Left) and Pb-Pb (Right). Adapted from [53].

In a Pb-Pb analysis, the term *Centrality* is defined as an interval of multiplicities

which corresponds to a particular percentile of all multiplcities measured in that system at a given energy. For example, a Pb-Pb collision resulting in a multiplicity of 5000 (which isn't the number of measured particles in the collision but rather the measure of some amplitude in a detector that is related to the number or particles and/or energy) might correspond to a centrality of 70%. This means when all Pb-Pb events are ordered in terms of multiplicity, this particular event falls between then 70^{th} and 71^{st} percentile. As shown in the right panels of figure C.1, there is a strong correlation between multiplicity and N_{part} and in turn a strong correlation between N_{part} and b for Pb-Pb collision. Thus, the centrality is strongly correlated to the impact parameter of the event. This is unfortunately not the case in p-Pb collisions as seen on the left panels of figure C.1. This is the primary reason why in this analysis multiplicity centrality class are favored instead of centrality as this strong correlation between multiplicity and impact parameter doesn't exist in p-Pb collisions. The multiplicity centrality class vs VZERO amplitude and ZDC amplitude are shown in figure C.2.

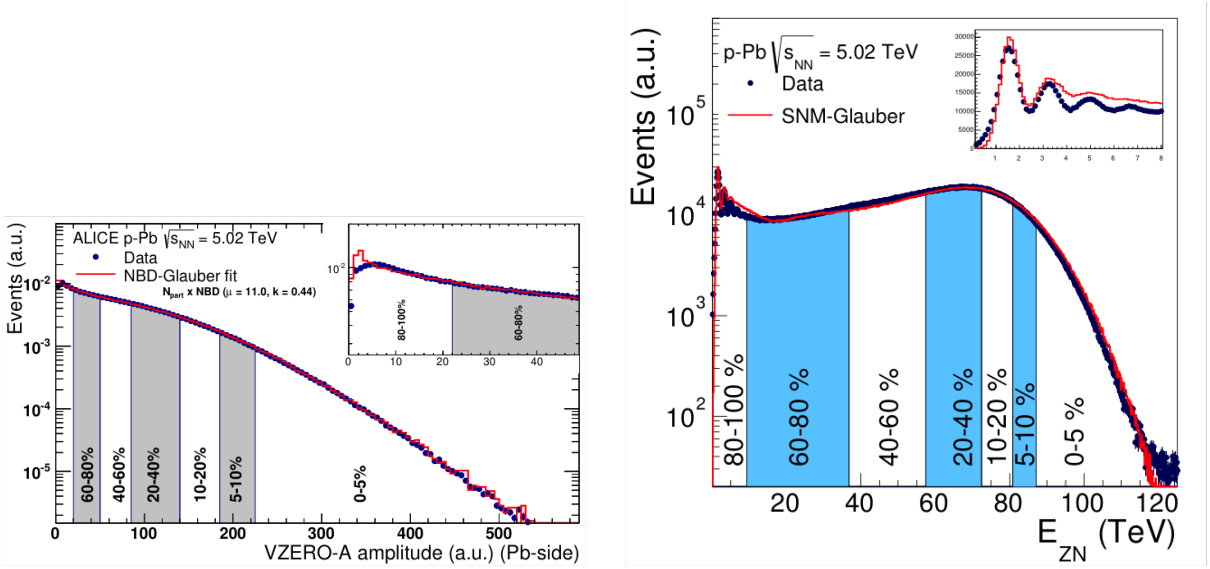

Figure C.2: Left: Frequency histogram of VZERO amplitudes. Right: Frequency histogram of ZN energy (energy from slow neutrons). Adapted from [53].

APPENDIX D

Centrality Integrated Jet Systematics (Cross-Section & R_{pPb}^{PYTHIA})

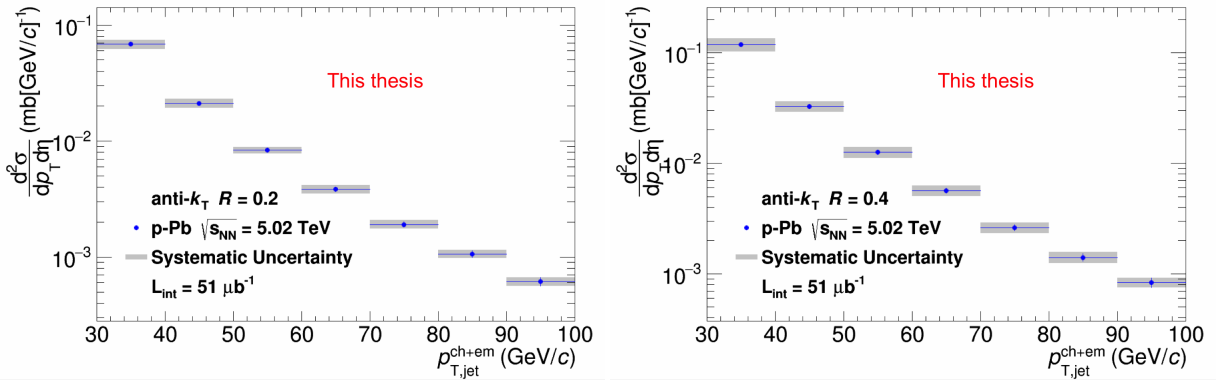

Figure D.1: Jet cross-section from p-Pb from ALICE at $\sqrt{s_{NN}} = 5.02$ TeV. There is an overall normalization uncertainty of 8.2%. Left: $R = 0.2$. Right: $R = 0.4$.

Systematic	$p_{T,jet}^{min}$	$p_{T,jet}^{max}$	**Min**	**Max**	**Mean**
Unfolding Systematics					
Unfolding Method	0.5	1.4	0.1	3.2	1.3
Unfolding Regularization	1.2	<0.1	<0.1	1.2	0.2
Unfolding Prior	2.3	1.2	0.3	3.4	<0.1
$p_{T,min}^{meas}$	4.5	0.5	<0.1	4.5	0.7
$p_{T,min}^{unf}$	negligible				
JES Systematics					
Tracking Efficiency	3.6	7.0	3.6	8.1	5.7
Hadronic Correction	3.3	0.7	0.1	3.3	0.8
Underlying Event Subtraction (UE)	4.8	2.0	1.7	6.1	3.5
Background Fluctuations (δp_T)	0.2	0.1	0.1	0.2	0.1
Detector Response	1.5	1.1	<0.1	3.7	0.8
Scale Factor	negligible				
Total Systematic	8.7%	7.7%	6.8%	8.7%	8.1%

Table D.1: Summary of systematic uncertainties for anti-k_T R = 0.2 MB jet spectrum and R_{pPb}^{PYTHIA}. The first column is the uncertainty at the minimum $p_{T,jet}^{min}$ = 30 GeV/c, the second column is the uncertainty at the $p_{T,jet}^{max}$ = 100 GeV/c. The minimum and maximum columns gives the extremes over the entire $p_{T,jet}^{ch+em}$ range, and the last column gives the mean systematic uncertainty over the entire $p_{T,jet}^{ch+em}$ range.

Systematic	$p_{T,jet}^{min}$	$p_{T,jet}^{max}$	**Min**	**Max**	**Mean**
Unfolding Systematics					
Unfolding Method	2.3	1.5	0.3	6.5	3.1
Unfolding Regularization	0.2	0.3	0.2	2.3	0.9
Unfolding Prior	3.7	0.2	0.2	3.7	0.2
$p_{T,min}^{meas}$	6.6	0.4	0.1	6.6	1.1
$p_{T,min}^{unf}$	negligible				
JES Systematics					
Tracking Efficiency	3.0	9.2	3.0	9.2	6.6
Hadronic Correction	1.1	3.1	0.1	3.1	0.6
Underlying Event Subtraction (UE)	5.7	4.0	4.0	6.4	5.2
Background Fluctuations (δp_T)	1.4	0.4	0.4	1.4	0.8
Detector Response	8.8	3.8	0.3	8.8	3.3
Scale Factor	0.5	0.2	0.1	0.6	0.4
Total Systematic	13.6%	11.3%	10.7%	13.6%	11.6%

Table D.2: Summary of systematic uncertainties for anti-k_T R = 0.4 MB jet spectrum and R_{pPb}^{PYTHIA}. The first column is the uncertainty at the minimum $p_{T,jet}^{min}$ = 30 GeV/c, the second column is the uncertainty at the $p_{T,jet}^{max}$ = 100 GeV/c. The minimum and maximum columns gives the extremes over the entire $p_{T,jet}^{ch+em}$ range, and the last column gives the mean systematic uncertainty over the entire $p_{T,jet}^{ch+em}$ range.

APPENDIX E

Jet Structure Ratio $\frac{R=0.2}{R=0.4}$ Systematics

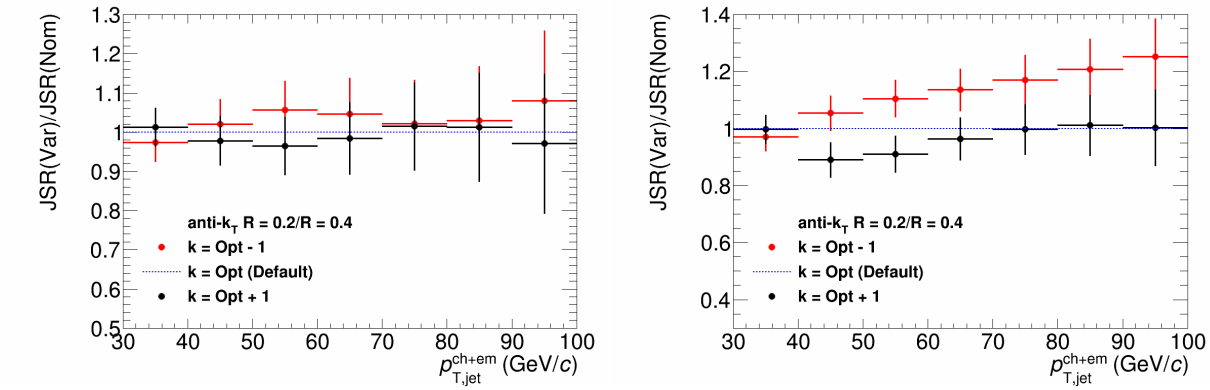

Figure E.1: Relative systematic uncertainty due to different regularizations in bayesian and SVD unfolding for the Jet Structure Ratio $\frac{R=0.2}{R=0.4}$. Left: Bayesian. Right: SVD

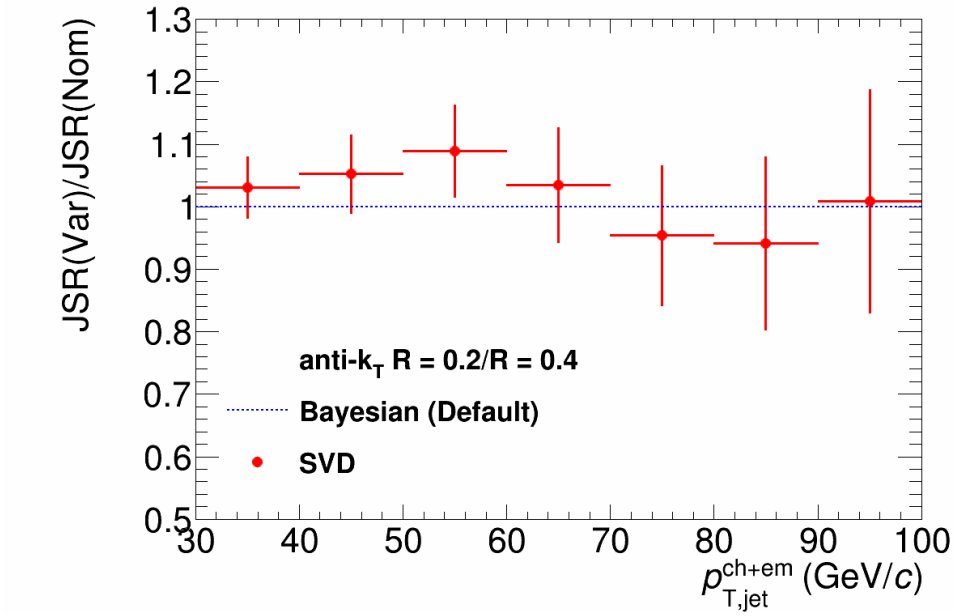

Figure E.2: Relative systematic uncertainty due to different unfolding methods for the Jet Structure Ratio $\frac{R=0.2}{R=0.4}$

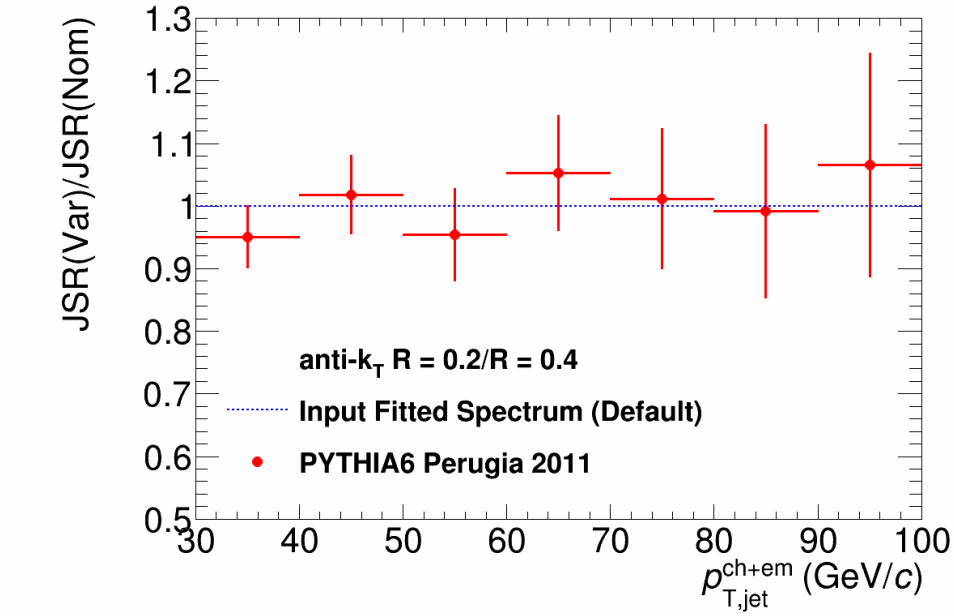

Figure E.3: Relative systematic uncertainty due to different priors being used for the Jet Structure Ratio $\frac{R=0.2}{R=0.4}$

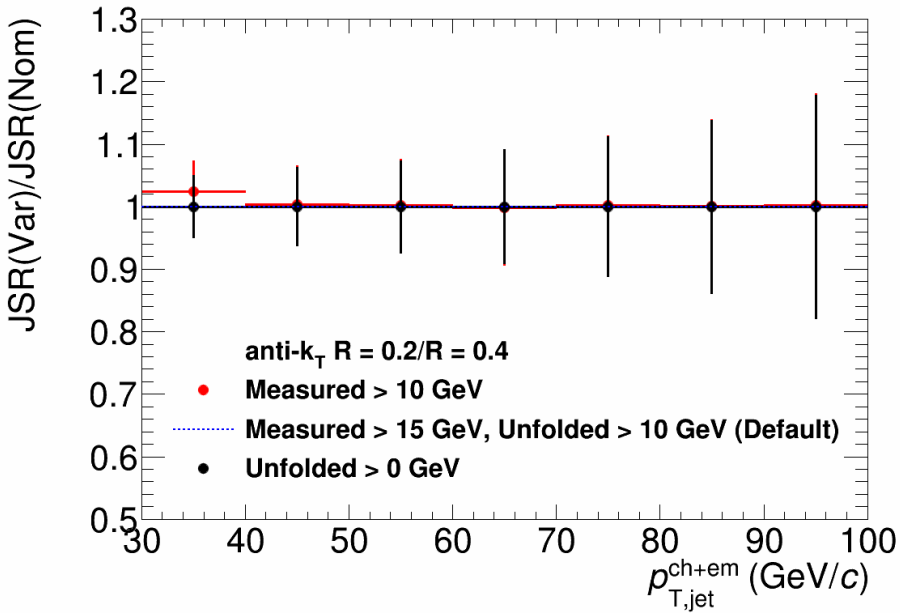

Figure E.4: Relative systematic uncertainty due to different minimum unfolding p_T cuts for the Jet Structure Ratio $\frac{R=0.2}{R=0.4}$

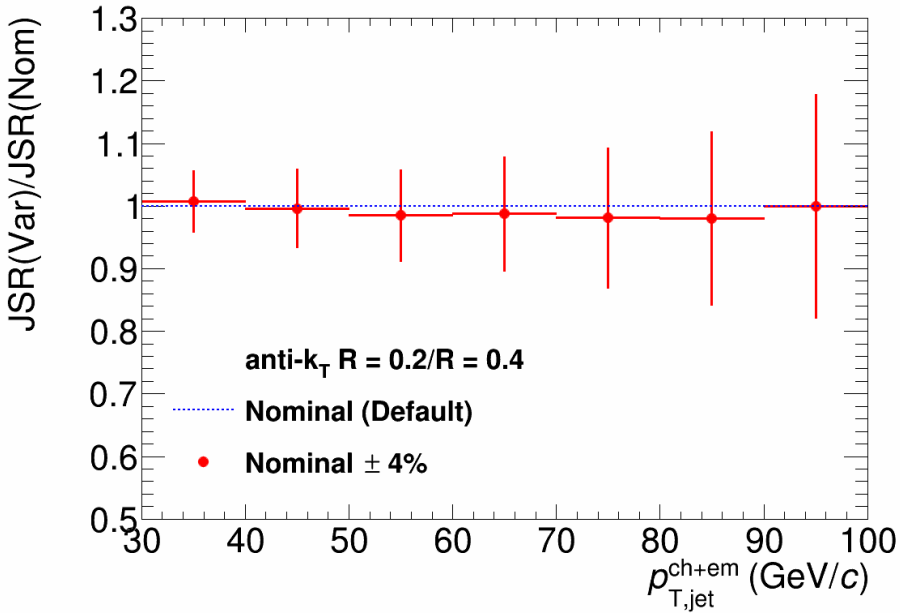

Figure E.5: Relative systematic uncertainty due to tracking efficiency for the Jet Structure Ratio $\frac{R=0.2}{R=0.4}$

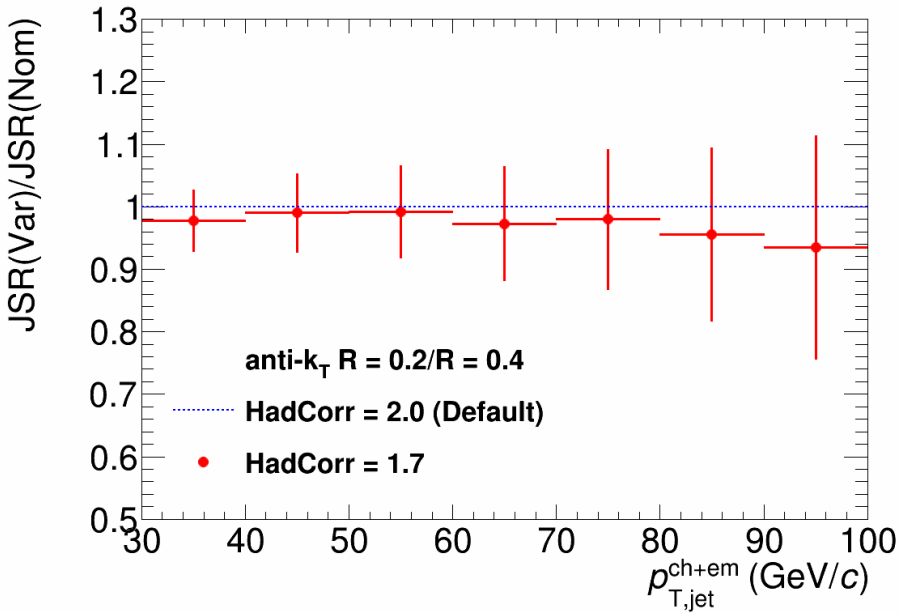

Figure E.6: Relative systematic uncertainty due to hadronic correction for the Jet Structure Ratio $\frac{R=0.2}{R=0.4}$

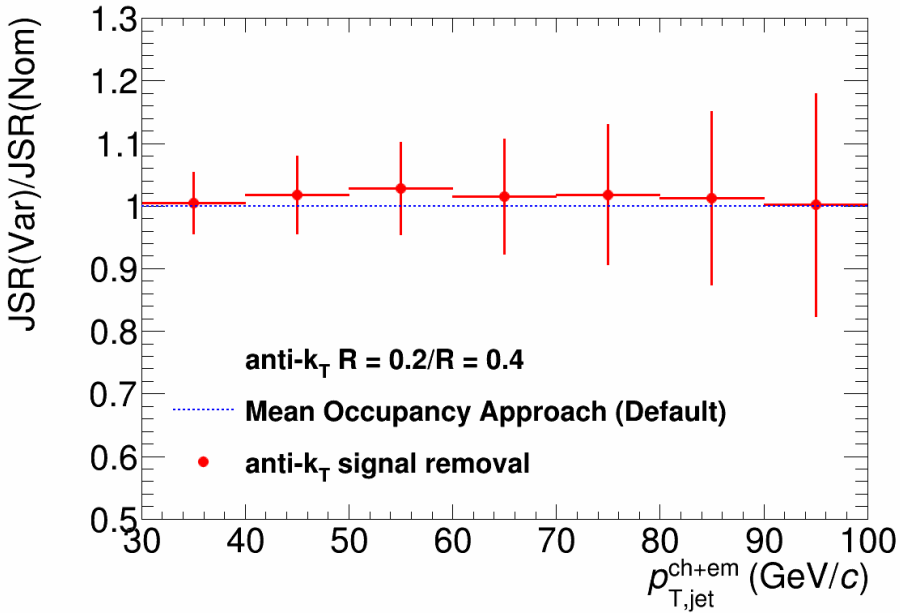

Figure E.7: Relative systematic uncertainty due to different UE subtraction methods for the Jet Structure Ratio $\frac{R=0.2}{R=0.4}$

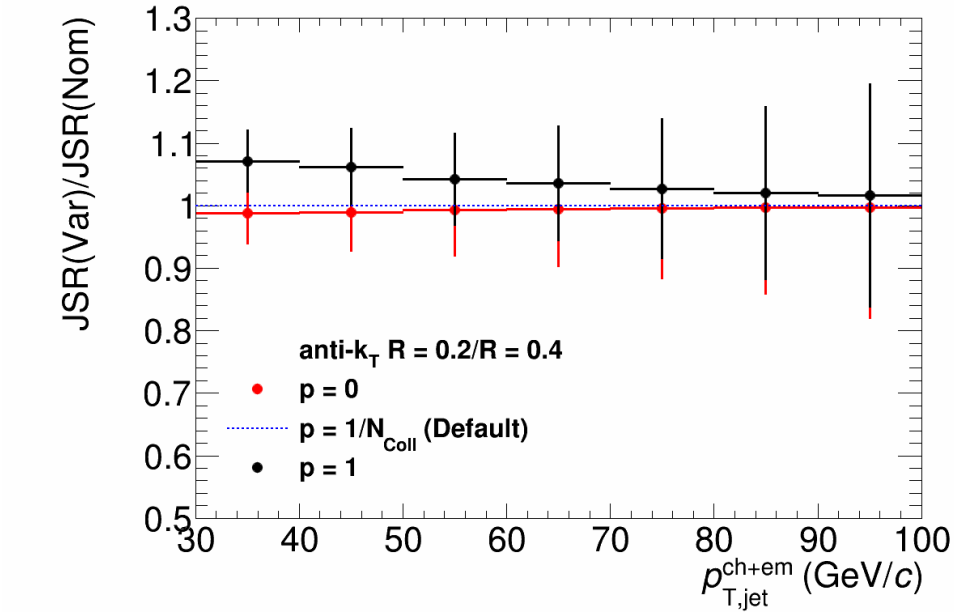

Figure E.8: Relative systematic uncertainty due to different δp_T definitions for the Jet Structure Ratio $\frac{R=0.2}{R=0.4}$. See section 4.6 for definitions of the p values.

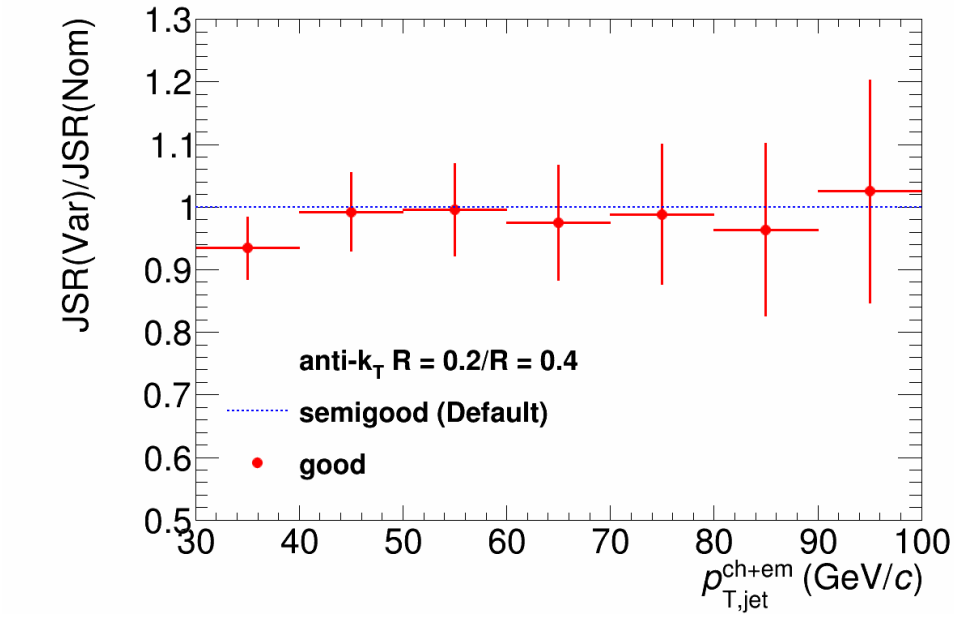

Figure E.9: Relative systematic uncertainty due to different unfolding response matricies used for detector conditions for the Jet Structure Ratio $\frac{R=0.2}{R=0.4}$

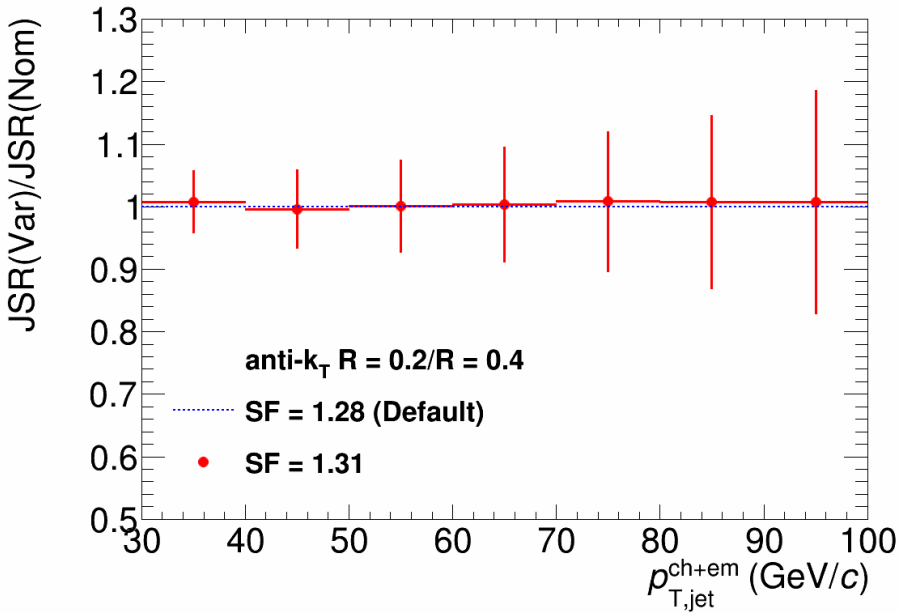

Figure E.10: Relative systematic uncertainty due to different scale factors for the Jet Structure Ratio $\frac{R=0.2}{R=0.4}$

Systematic	$p_{T,jet}^{min}$	$p_{T,jet}^{max}$	**Min**	**Max**	**Mean**
Unfolding Systematics					
Unfolding Method	3.0	5.9	3.0	8.9	1.7
Unfolding Regularization	1.3	1.2	1.2	3.6	0.6
Unfolding Prior	4.9	0.8	0.8	5.2	0.4
$p_{T,min}^{meas}$	2.4	0.1	0.1	2.4	0.5
$p_{T,min}^{unf}$	negligible				
JES Systematics					
Tracking Efficiency	0.7	2.0	0.4	2.0	1.1
Hadronic Correction	2.2	4.4	0.8	4.4	2.2
Underlying Event Subtraction (UE)	0.5	1.3	0.5	2.8	1.6
Background Fluctuations (δp_T)	1.1	0.3	0.3	1.1	0.7
Detector Response	6.6	3.6	0.4	6.6	2.5
Scale Factor	0.8	0.8	0.1	0.9	0.4
Total Systematic	9.6%	8.7%	6.2%	11.1%	8.3%

Table E.1: Summary of systematic uncertainties for the jet structure ratio $\frac{R=0.2}{R=0.4}$. The first column is the uncertainty at the minimum $p_{T,jet}^{min}$ = 30 GeV/c, the second column is the uncertainty at the $p_{T,jet}^{max}$ = 100 GeV/c. The minimum and maximum columns gives the extremes over the entire $p_{T,jet}^{ch+em}$ range, and the last column gives the mean systematic uncertainty over the entire $p_{T,jet}^{ch+em}$ range.

APPENDIX F

Centrality Dependent Jet Systematics

F.1 0-20% Jet Cross Section Systematics

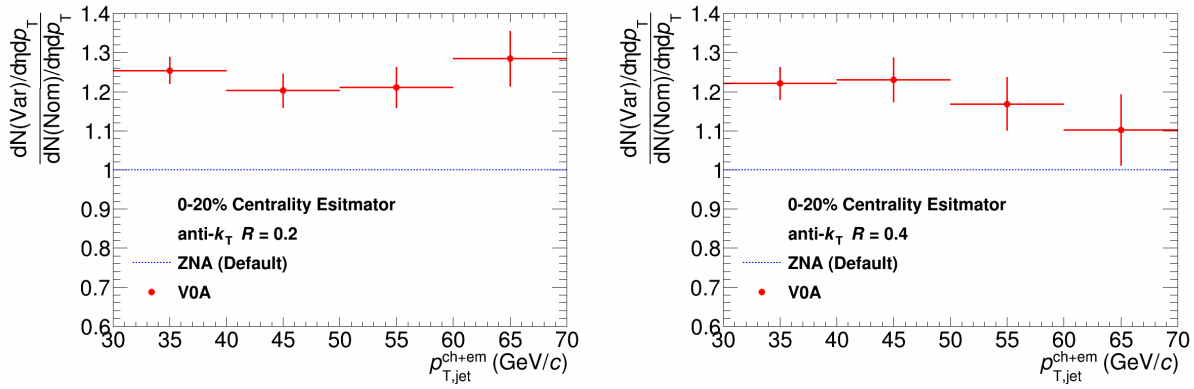

Figure F.1: Relative systematic deviation due to different centrality estimators. Left: $R = 0.2$. Right: $R = 0.4$

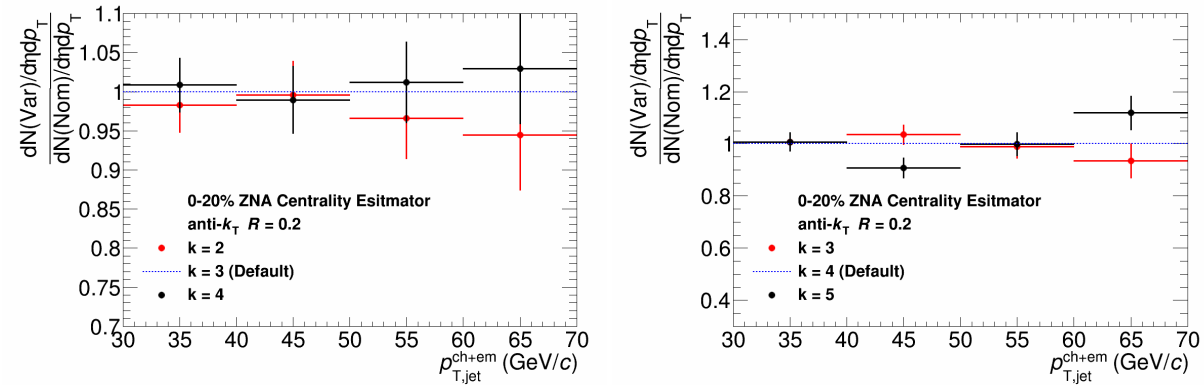

Figure F.2: Relative systematic uncertainty due to different regularizations in bayesian and SVD unfolding for $R = 0.2$. Left: Bayesian. Right: SVD

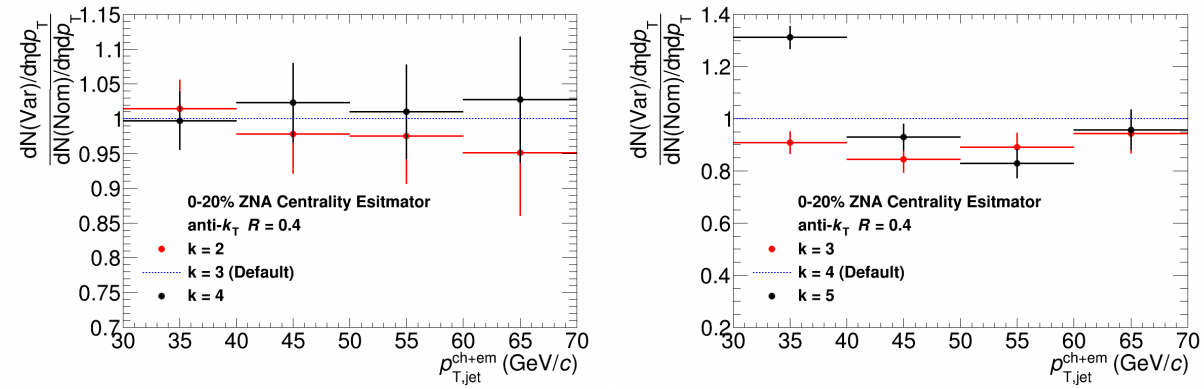

Figure F.3: Relative systematic uncertainty due to different regularizations in bayesian and SVD unfolding for $R = 0.4$. Left: Bayesian. Right: SVD

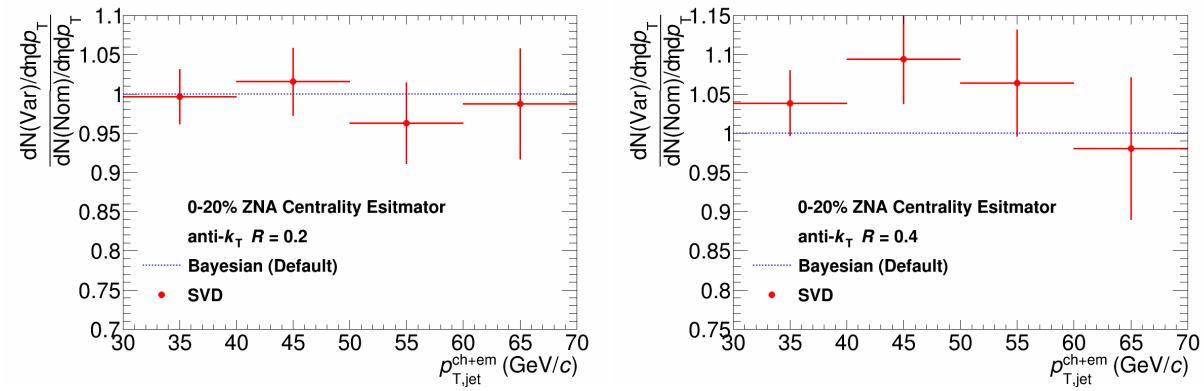

Figure F.4: Relative systematic uncertainty due to different unfolding methods. Left: $R = 0.2$. Right: $R = 0.4$

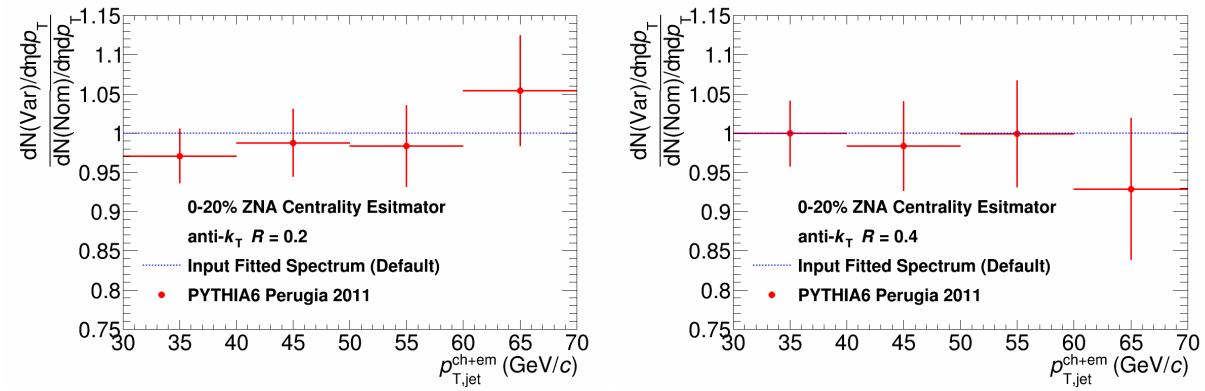

Figure F.5: Relative systematic uncertainty due to different priors being used. Left: $R = 0.2$. Right: $R = 0.4$

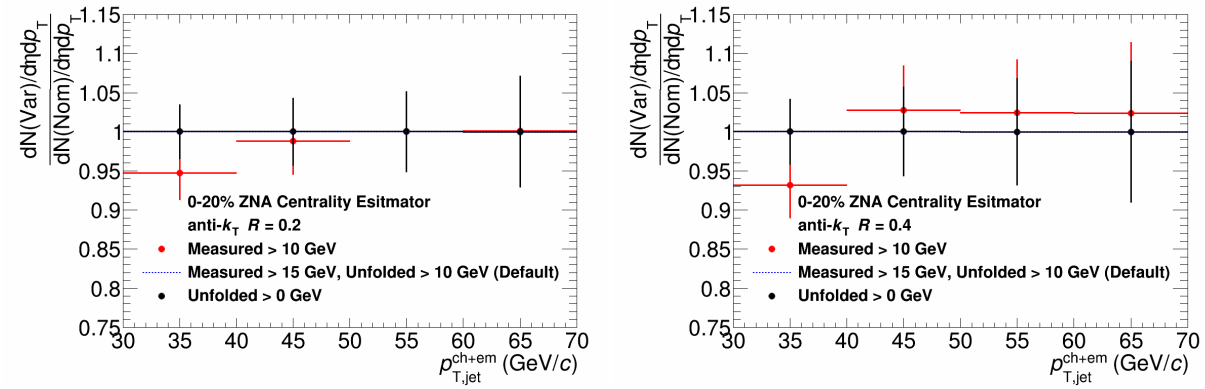

Figure F.6: Relative systematic uncertainty due to different minimum unfolding p_T cuts. Left: $R = 0.2$. Right: $R = 0.4$

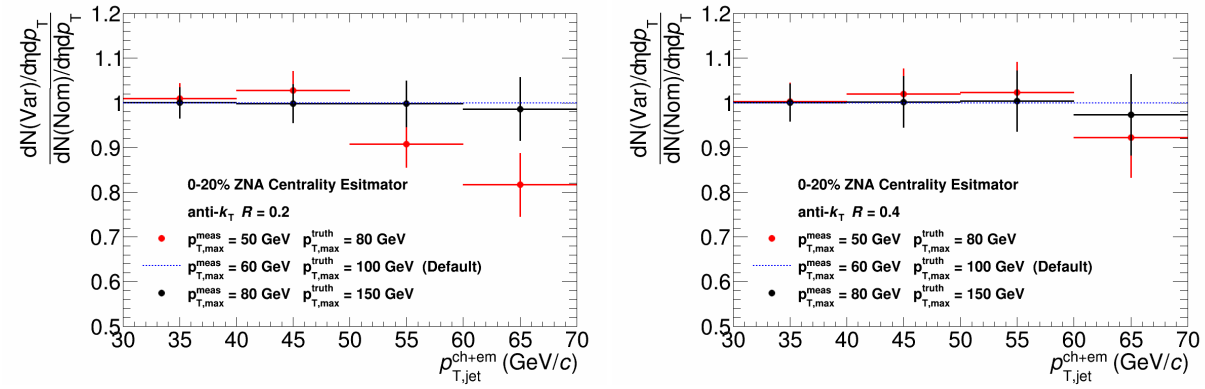

Figure F.7: Relative systematic deviation due to different $p^{meas}_{T,max}$ and $p^{unf}_{T,max}$. Left: $R = 0.2$. Right: $R = 0.4$

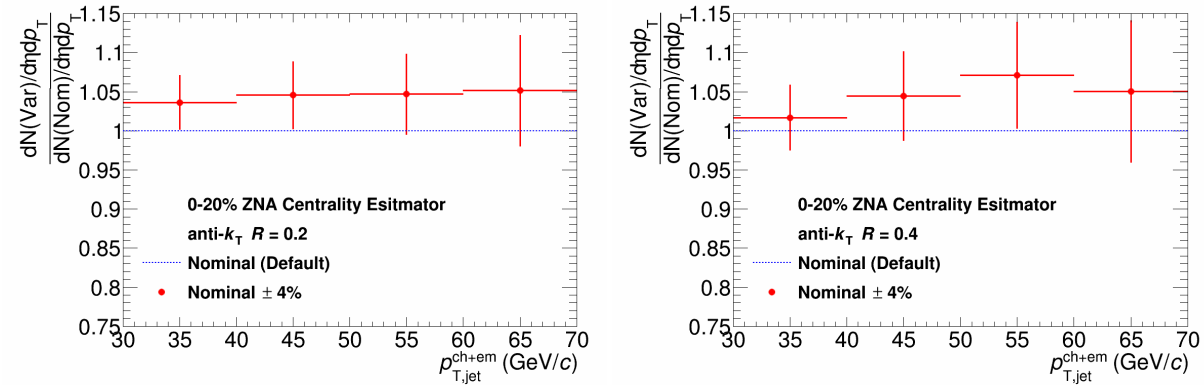

Figure F.8: Relative systematic uncertainty due to tracking efficiency. Left: $R = 0.2$. Right: $R = 0.4$

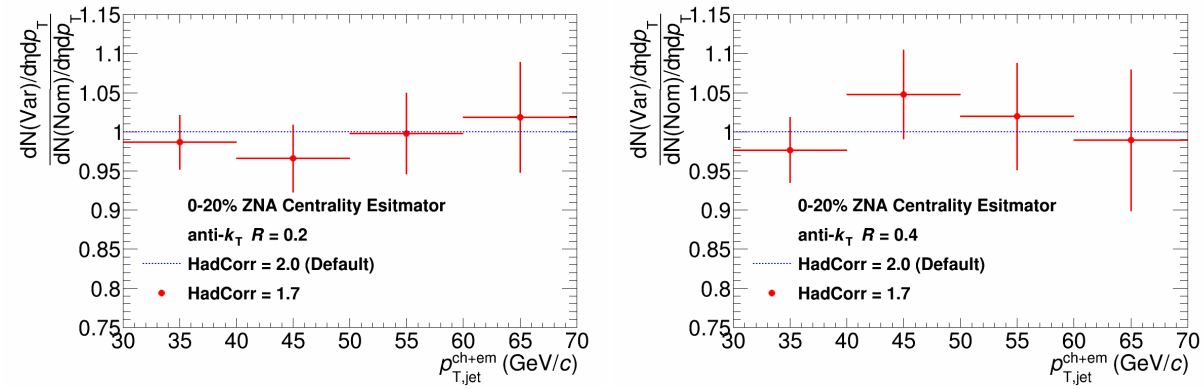

Figure F.9: Relative systematic uncertainty due to hadronic correction. Left: $R = 0.2$. Right: $R = 0.4$

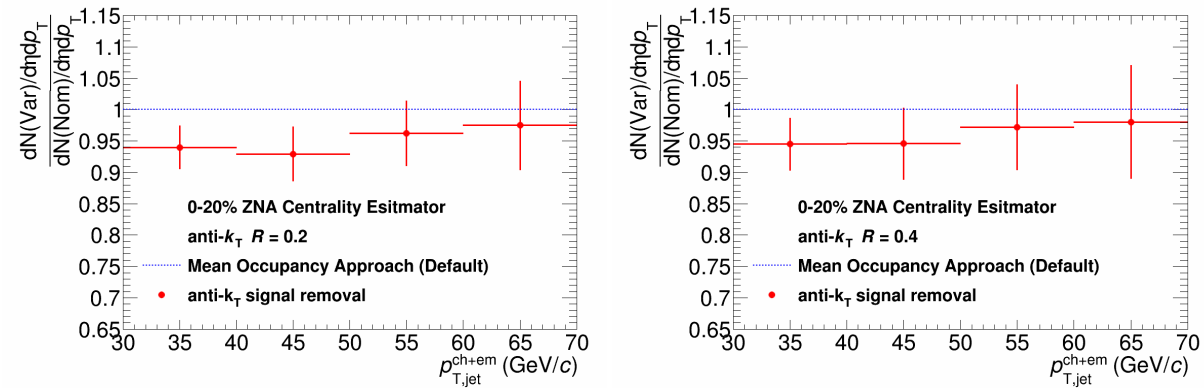

Figure F.10: Relative systematic uncertainty due to different UE subtraction methods. Left: $R = 0.2$. Right: $R = 0.4$

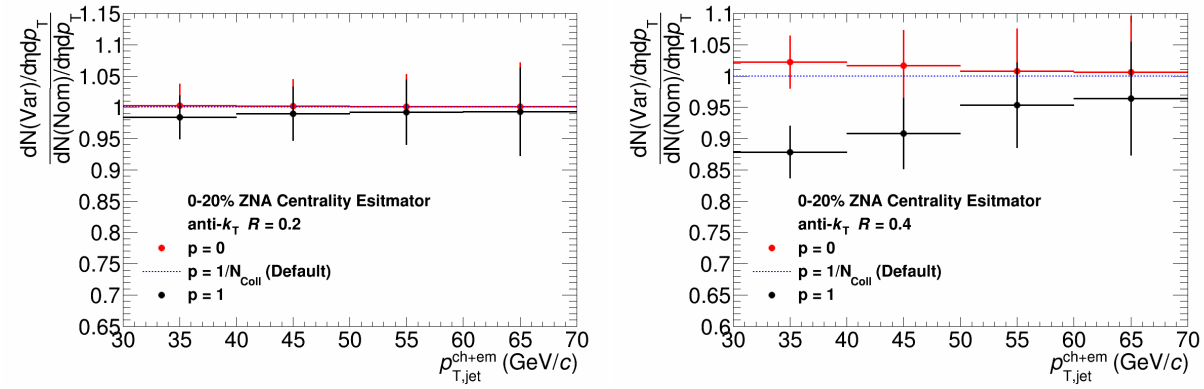

Figure F.11: Relative systematic uncertainty due to different δp_T definitions. See section 4.6 for definitions of the p values. Left: $R = 0.2$. Right: $R = 0.4$

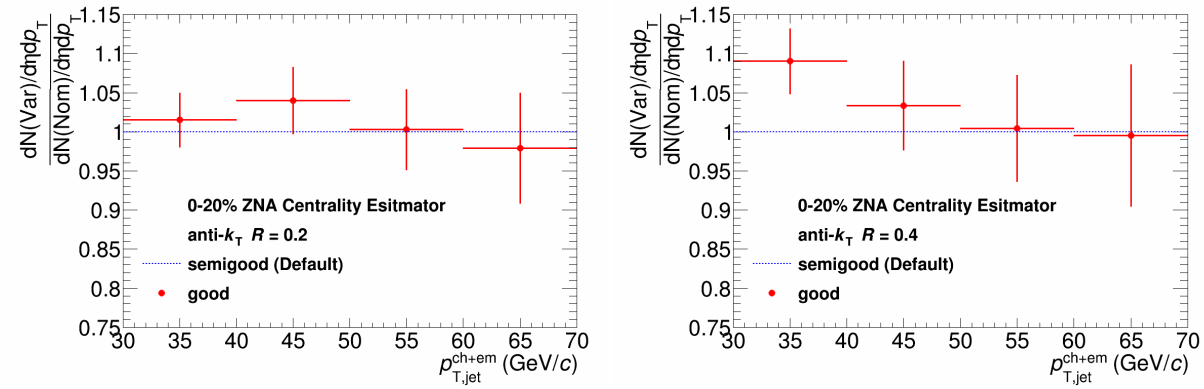

Figure F.12: Relative systematic uncertainty due to different unfolding response matricies used for detector conditions. Left: $R = 0.2$. Right: $R = 0.4$

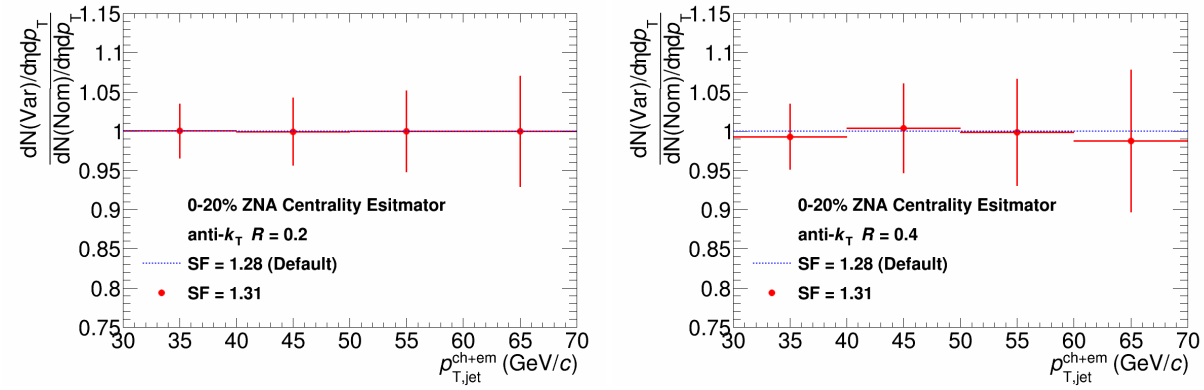

Figure F.13: Relative systematic uncertainty due to different scale factors. Left: $R = 0.2$. Right: $R = 0.4$

Systematic	$p_{T,jet}^{min}$	$p_{T,jet}^{max}$	**Min**	**Max**	**Mean**
Unfolding Systematics					
Unfolding Method	0.4	3.7	0.4	3.7	0.8
Unfolding Regularization	1.7	3.4	0.4	3.4	1.8
Unfolding Prior	2.9	1.7	1.2	2.9	1.9
$p_{T,min}^{meas}$	5.3	<0.1	<0.1	5.3	2.1
$p_{T,min}^{unf}$	negligible				
JES Systematics					
Tracking Efficiency	3.6	4.7	3.6	4.7	4.3
Hadronic Correction	1.3	0.2	0.2	3.4	1.6
Underlying Event Subtraction (UE)	6.0	3.8	3.8	7.1	5.6
Background Fluctuations (δp_T)	0.2	0.1	0.1	0.3	0.2
Detector Response	1.5	0.3	0.3	4.0	1.9
Scale Factor	<0.1				
Total Systematic	9.6%	8.0%	8.0%	10.2%	9.3%

Table F.1: Summary of systematic uncertainties for anti-k_T R = 0.2 0-20% jet spectrum. The first column is the uncertainty at the minimum $p_{T,jet}^{min}$ = 30 GeV/c, the second column is the uncertainty at the $p_{T,jet}^{max}$ = 70 GeV/c. The minimum and maximum columns gives the extremes over the entire $p_{T,jet}^{ch+em}$ range, and the last column gives the mean systematic uncertainty over the entire $p_{T,jet}^{ch+em}$ range.

Systematic	$p_{T,jet}^{min}$	$p_{T,jet}^{max}$	**Min**	**Max**	**Mean**
Unfolding Systematics					
Unfolding Method	3.8	6.4	3.8	9.5	6.6
Unfolding Regularization	0.3	1.0	0.3	2.3	1.0
Unfolding Prior	<0.1	<0.1	<0.1	1.6	0.6
$p_{T,min}^{meas}$	6.8	2.4	2.4	6.8	0.6
$p_{T,min}^{unf}$	negligible				
JES Systematics					
Tracking Efficiency	1.7	7.1	1.7	7.1	4.4
Hadronic Correction	2.3	2.0	2.0	4.8	1.5
Underlying Event Subtraction (UE)	5.5	2.8	2.8	5.5	4.6
Background Fluctuations (δp_T)	2.2	0.8	0.8	2.2	1.6
Detector Response	9.0	0.4	0.4	9.0	4.2
Scale Factor	0.7	0.1	0.1	0.7	0.2
Total Systematic	13.7%	10.5%	10.5%	13.8%	12.7%

Table F.2: Summary of systematic uncertainties for anti-k_T R = 0.4 0-20% jet spectrum. The first column is the uncertainty at the minimum $p_{T,jet}^{min}$ = 30 GeV/c, the second column is the uncertainty at the $p_{T,jet}^{max}$ = 70 GeV/c. The minimum and maximum columns gives the extremes over the entire $p_{T,jet}^{ch+em}$ range, and the last column gives the mean systematic uncertainty over the entire $p_{T,jet}^{ch+em}$ range.

F.2 40-90% Jet Cross Section Systematics

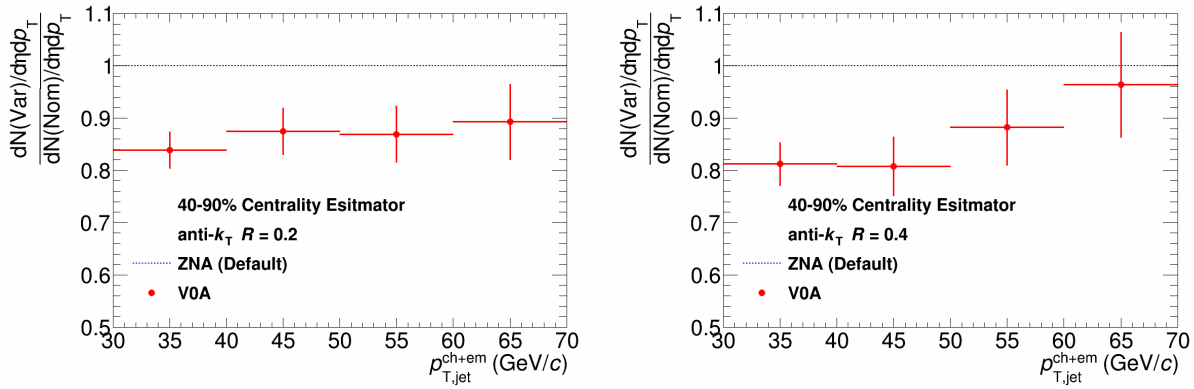

Figure F.14: Relative systematic deviation due to different centrality estimators. Left: $R = 0.2$. Right: $R = 0.4$

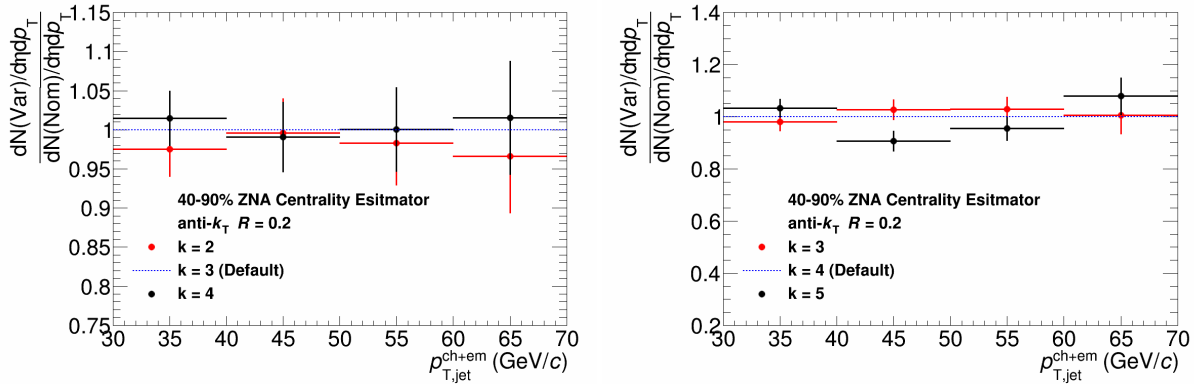

Figure F.15: Relative systematic uncertainty due to different regularizations in bayesian and SVD unfolding for $R = 0.2$. Left: Bayesian. Right: SVD

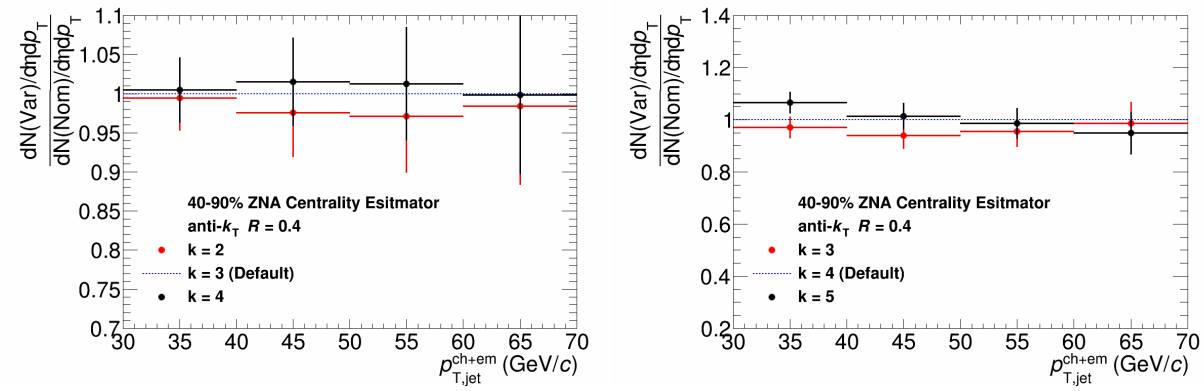

Figure F.16: Relative systematic uncertainty due to different regularizations in bayesian and SVD unfolding for $R = 0.4$. Left: Bayesian. Right: SVD

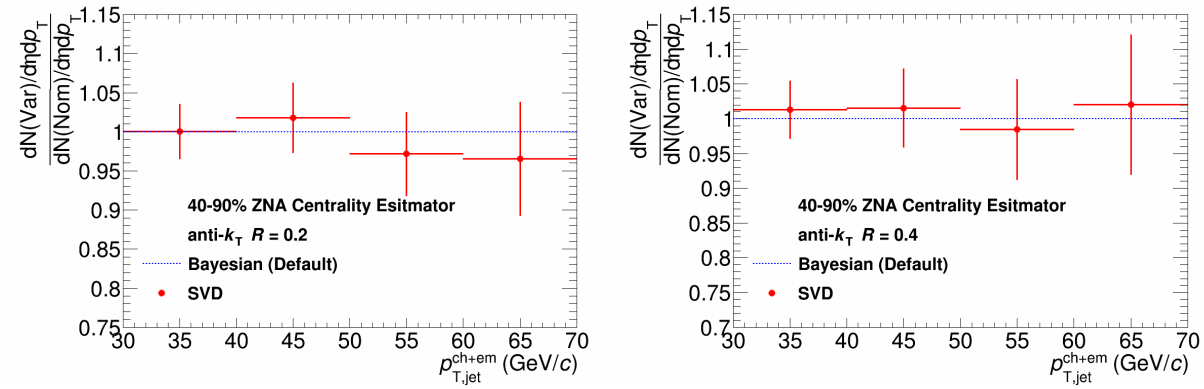

Figure F.17: Relative systematic uncertainty due to different unfolding methods. Left: $R = 0.2$. Right: $R = 0.4$

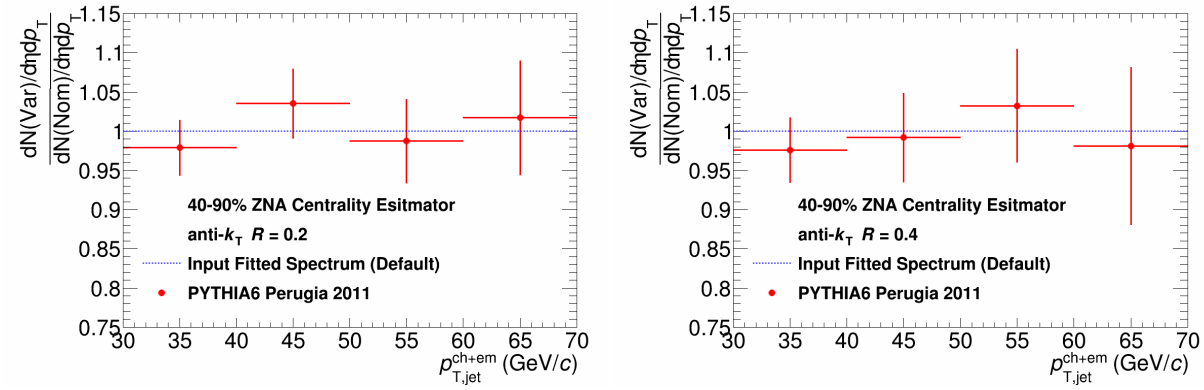

Figure F.18: Relative systematic uncertainty due to different priors being used. Left: $R = 0.2$. Right: $R = 0.4$

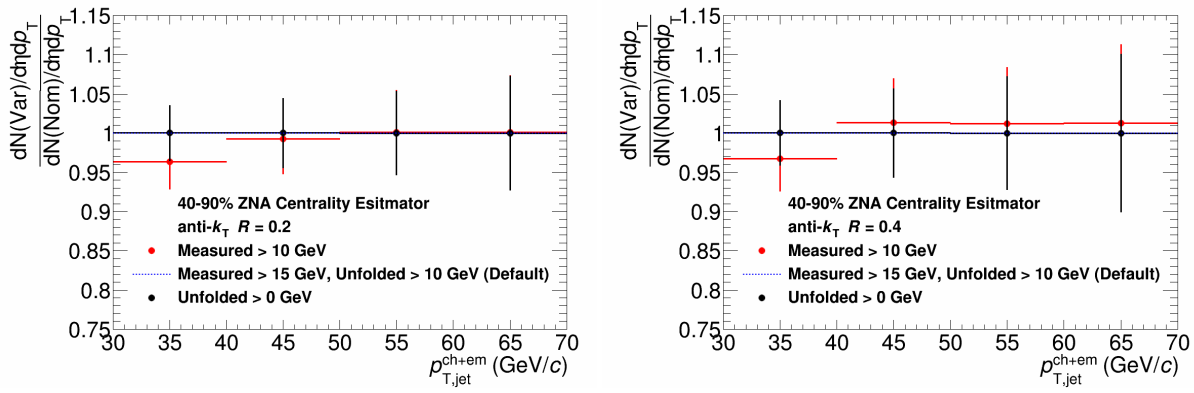

Figure F.19: Relative systematic uncertainty due to different minimum unfolding p_T cuts. Left: $R = 0.2$. Right: $R = 0.4$

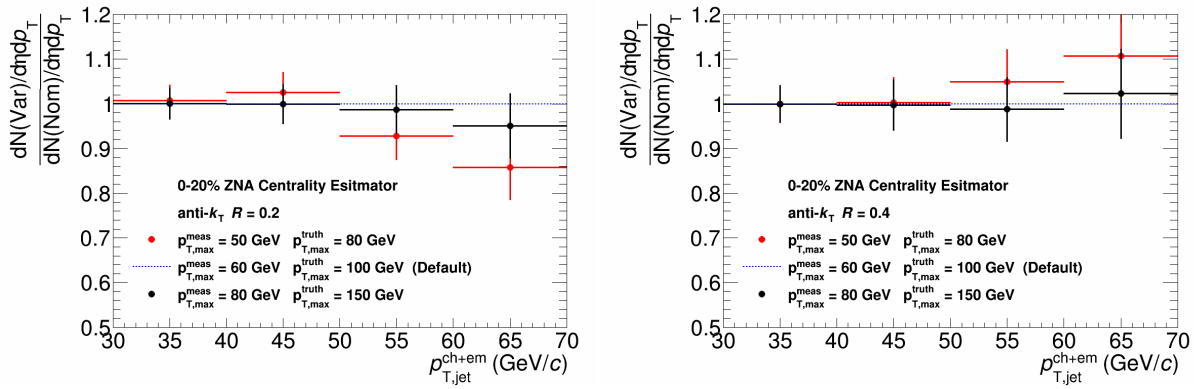

Figure F.20: Relative systematic deviation due to different $p^{meas}_{T,max}$ and $p^{unf}_{T,max}$. Left: $R = 0.2$. Right: $R = 0.4$

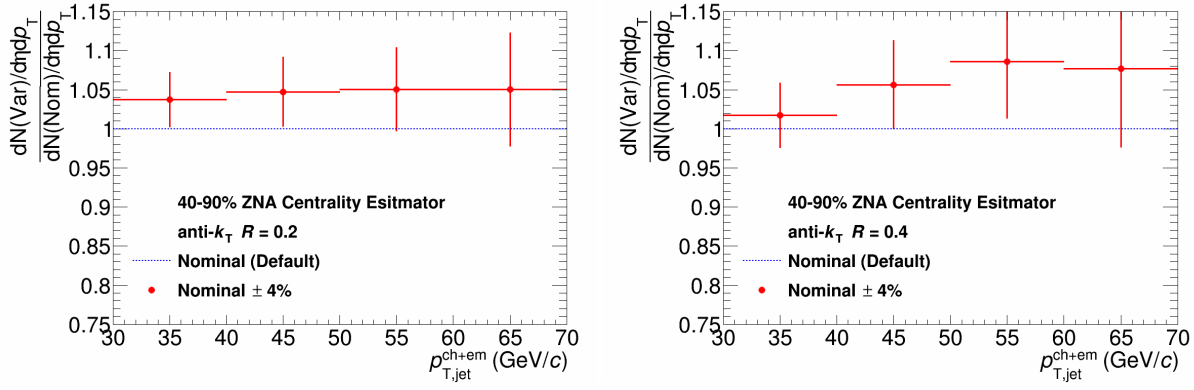

Figure F.21: Relative systematic uncertainty due to tracking efficiency. Left: $R = 0.2$. Right: $R = 0.4$

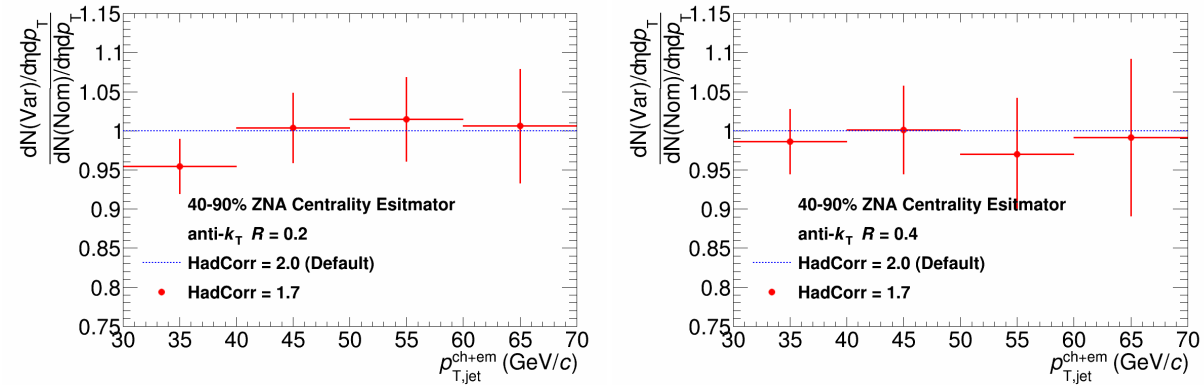

Figure F.22: Relative systematic uncertainty due to hadronic correction. Left: $R = 0.2$. Right: $R = 0.4$

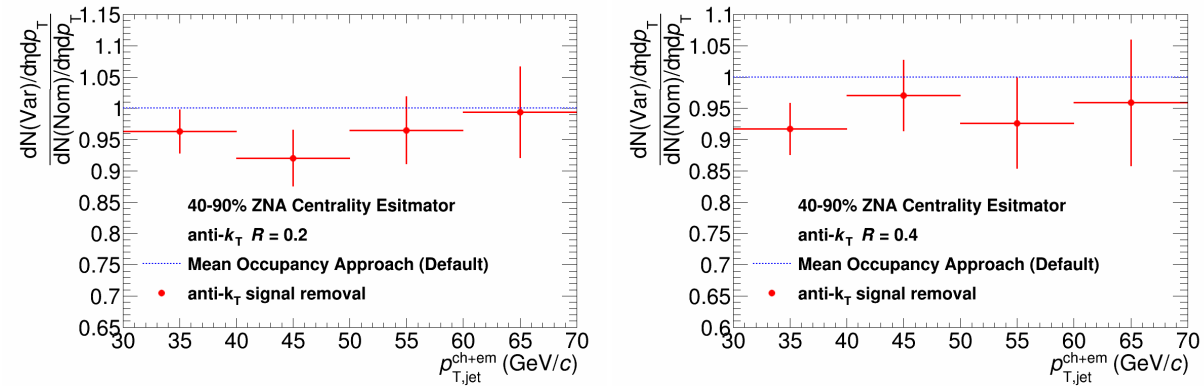

Figure F.23: Relative systematic uncertainty due to different UE subtraction methods. Left: $R = 0.2$. Right: $R = 0.4$

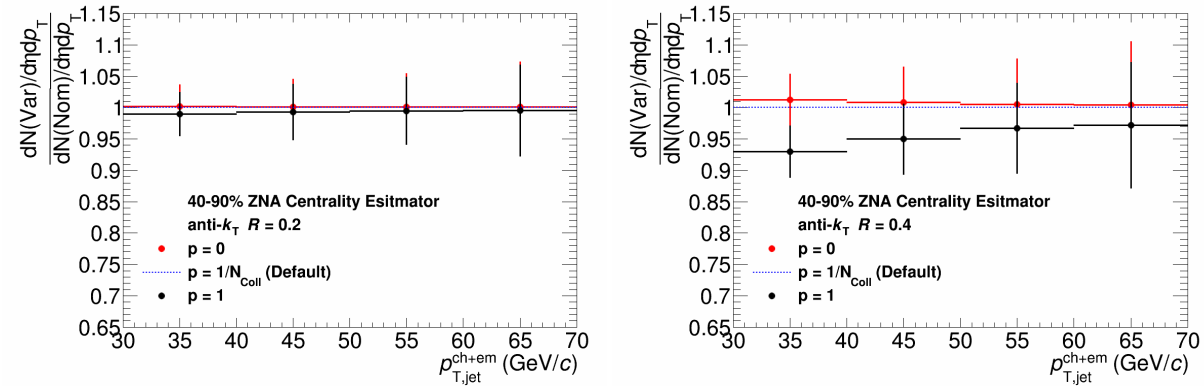

Figure F.24: Relative systematic uncertainty due to different δp_T definitions. See section 4.6 for definitions of the p values. Left: $R = 0.2$. Right: $R = 0.4$

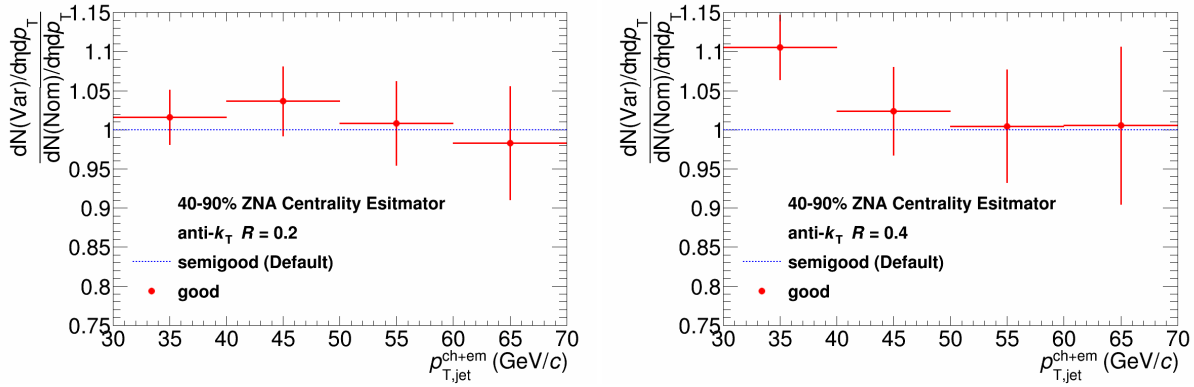

Figure F.25: Relative systematic uncertainty due to different unfolding response matricies used for detector conditions. Left: $R = 0.2$. Right: $R = 0.4$

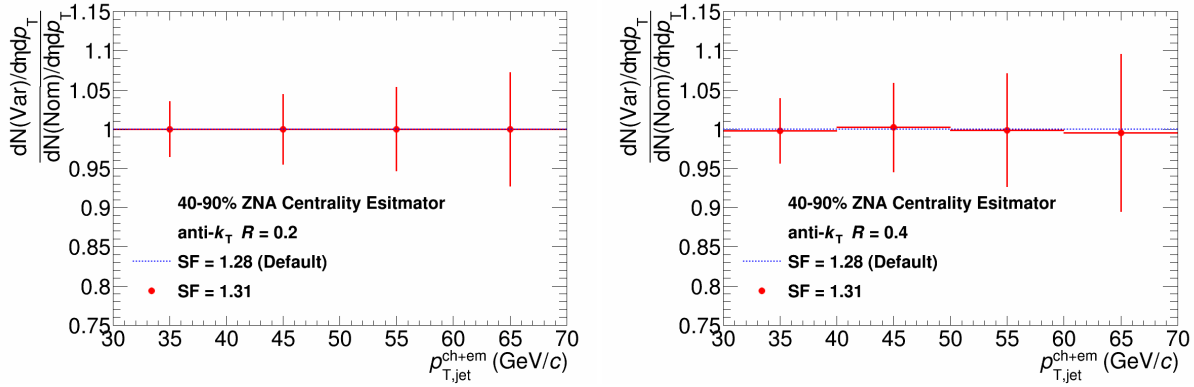

Figure F.26: Relative systematic uncertainty due to different scale factors. Left: $R = 0.2$. Right: $R = 0.4$

Systematic	$p_{T,jet}^{min}$	$p_{T,jet}^{max}$	**Min**	**Max**	**Mean**
Unfolding Systematics					
Unfolding Method	0.1	2.8	0.1	2.8	0.3
Unfolding Regularization	2.5	1.7	0.4	2.5	1.5
Unfolding Prior	2.1	1.3	1.3	3.5	<0.1
$p_{T,min}^{meas}$	3.6	0.1	0.1	3.6	1.4
$p_{T,min}^{unf}$	negligible				
JES Systematics					
Tracking Efficiency	3.8	5.0	3.8	5.0	4.5
Hadronic Correction	4.6	1.5	0.4	4.6	0.9
Underlying Event Subtraction (UE)	3.7	3.5	3.5	7.9	5.0
Background Fluctuations (δp_T)	0.2	0.1	0.1	0.2	0.1
Detector Response	1.6	0.8	0.8	3.6	2.0
Scale Factor	negligible				
Total Systematic	8.7%	7.3%	7.3%	10.7%	8.9%

Table F.3: Summary of systematic uncertainties for anti-k_T R = 0.2 40-90% jet spectrum. The first column is the uncertainty at the minimum $p_{T,jet}^{min}$ = 30 GeV/c, the second column is the uncertainty at the $p_{T,jet}^{max}$ = 70 GeV/c. The minimum and maximum columns gives the extremes over the entire $p_{T,jet}^{ch+em}$ range, and the last column gives the mean systematic uncertainty over the entire $p_{T,jet}^{ch+em}$ range.

Systematic	$p_{T,jet}^{min}$	$p_{T,jet}^{max}$	**Min**	**Max**	**Mean**
Unfolding Systematics					
Unfolding Method	1.3	1.5	1.3	1.5	0.4
Unfolding Regularization	0.5	1.3	0.5	1.5	1.1
Unfolding Prior	2.4	3.2	0.8	3.2	<0.01
$p_{T,min}^{meas}$	3.3	1.2	1.2	3.3	0.2
$p_{T,min}^{unf}$	negligible				
JES Systematics					
Tracking Efficiency	1.7	8.6	1.7	8.6	5.3
Hadronic Correction	1.4	3.0	0.1	3.0	1.4
Underlying Event Subtraction (UE)	8.3	7.4	3.0	8.3	6.2
Background Fluctuations (δp_T)	1.2	0.6	0.6	1.2	0.9
Detector Response	10.5	0.5	0.5	10.5	4.5
Scale Factor	0.2	0.1	0.1	0.2	<0.1
Total Systematic	14.3%	12.4%	7.4%	14.3%	11.3%

Table F.4: Summary of systematic uncertainties for anti-k_T R = 0.4 40-90% jet spectrum. The first column is the uncertainty at the minimum $p_{T,jet}^{min}$ = 30 GeV/c, the second column is the uncertainty at the $p_{T,jet}^{max}$ = 70 GeV/c. The minimum and maximum columns gives the extremes over the entire $p_{T,jet}^{ch+em}$ range, and the last column gives the mean systematic uncertainty over the entire $p_{T,jet}^{ch+em}$ range.

APPENDIX G

R_{CP} Systematics

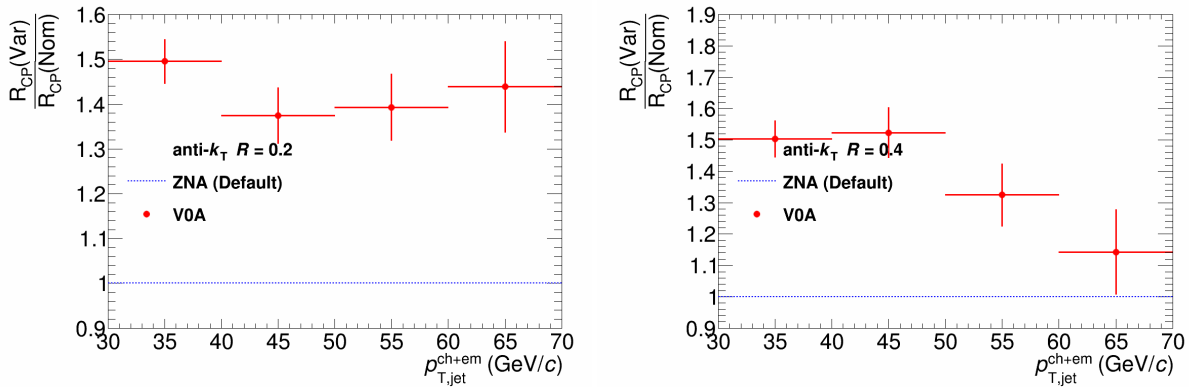

Figure G.1: Relative systematic deviation due to different centrality estimators. Left: $R = 0.2$. Right: $R = 0.4$

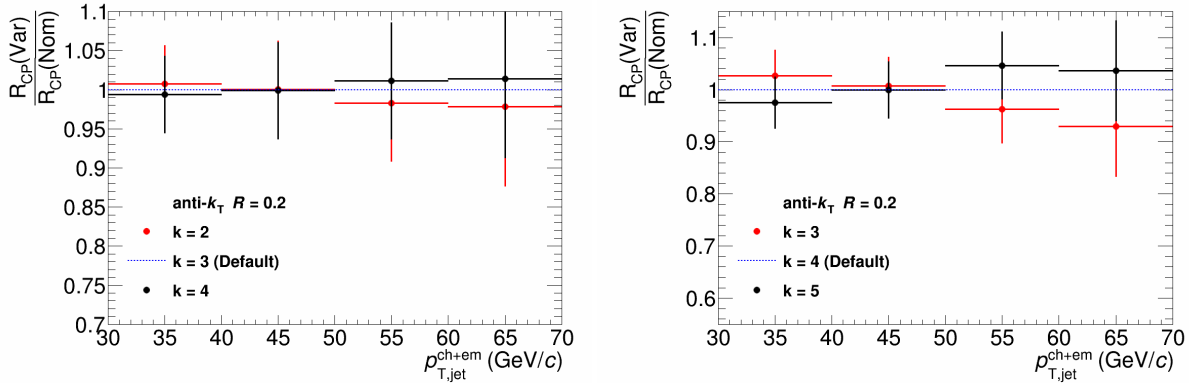

Figure G.2: Relative systematic uncertainty due to different regularizations in bayesian and SVD unfolding for $R = 0.2$. Left: Bayesian. Right: SVD

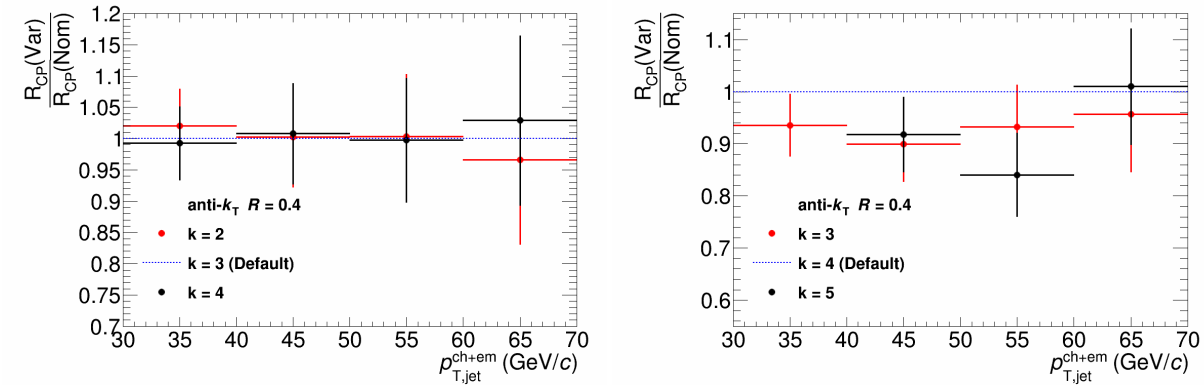

Figure G.3: Relative systematic uncertainty due to different regularizations in bayesian and SVD unfolding for $R = 0.4$. Left: Bayesian. Right: SVD

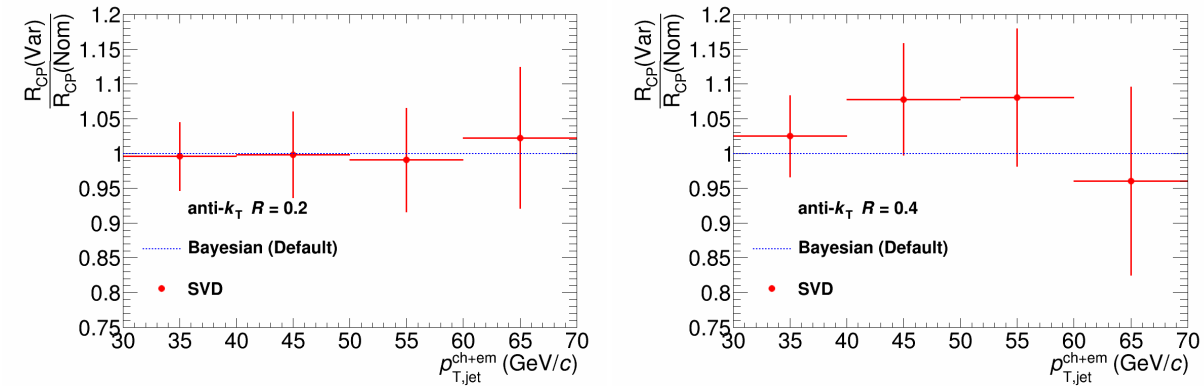

Figure G.4: Relative systematic uncertainty due to different unfolding methods. Left: $R = 0.2$. Right: $R = 0.4$

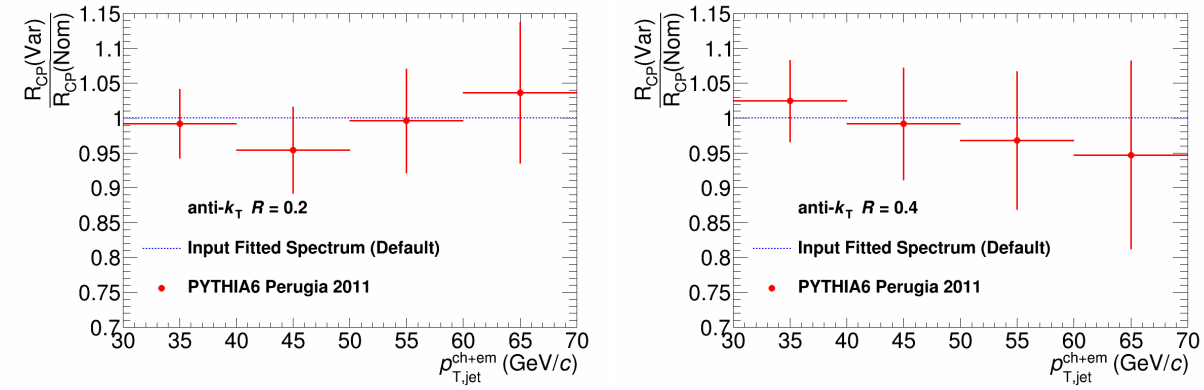

Figure G.5: Relative systematic uncertainty due to different priors being used. Left: $R = 0.2$. Right: $R = 0.4$

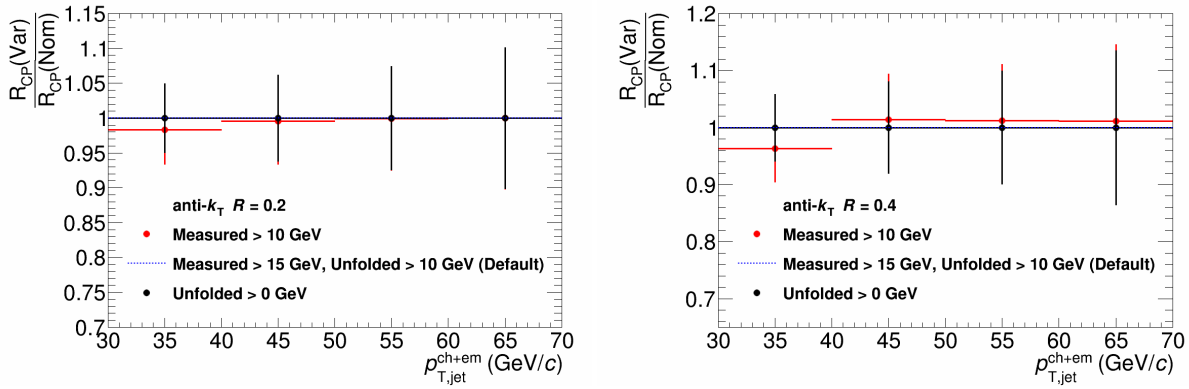

Figure G.6: Relative systematic uncertainty due to different minimum unfolding p_T cuts. Left: $R = 0.2$. Right: $R = 0.4$

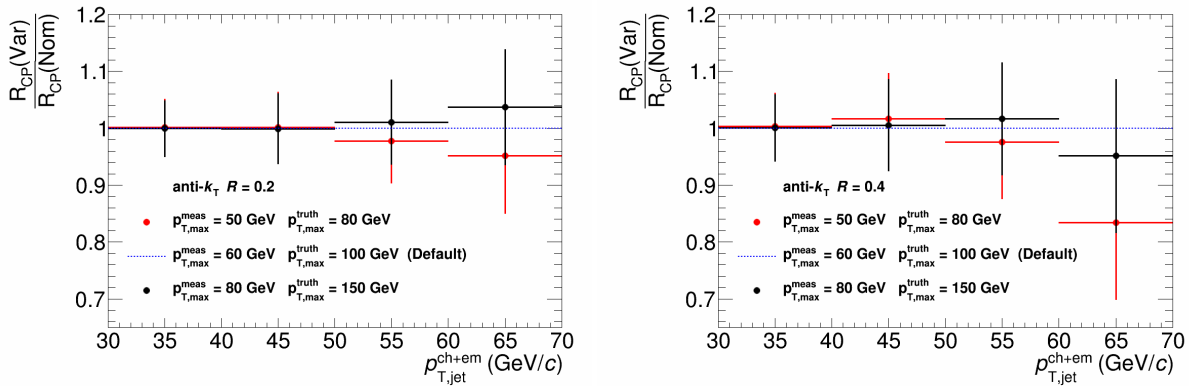

Figure G.7: Relative systematic deviation due to different $p_{T,max}^{meas}$ and $p_{T,max}^{unf}$. Left: $R = 0.2$. Right: $R = 0.4$

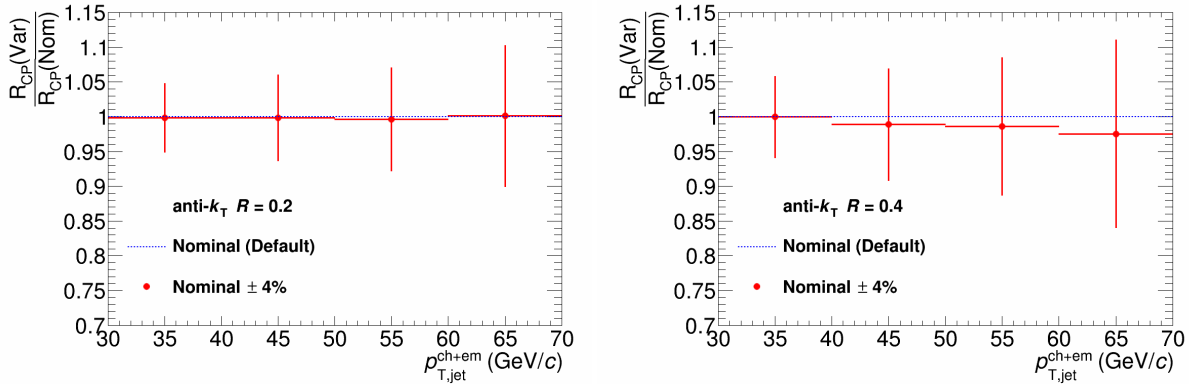

Figure G.8: Relative systematic uncertainty due to tracking efficiency. Left: $R = 0.2$. Right: $R = 0.4$

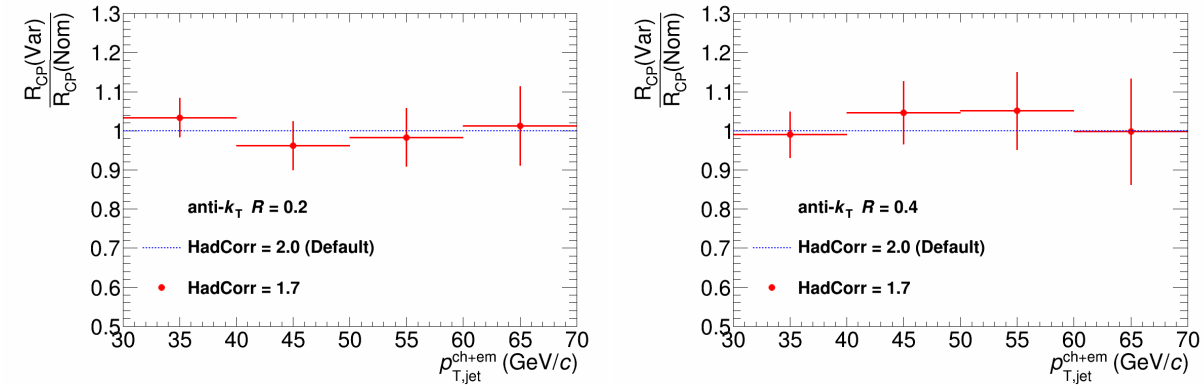

Figure G.9: Relative systematic uncertainty due to hadronic correction. Left: $R = 0.2$. Right: $R = 0.4$

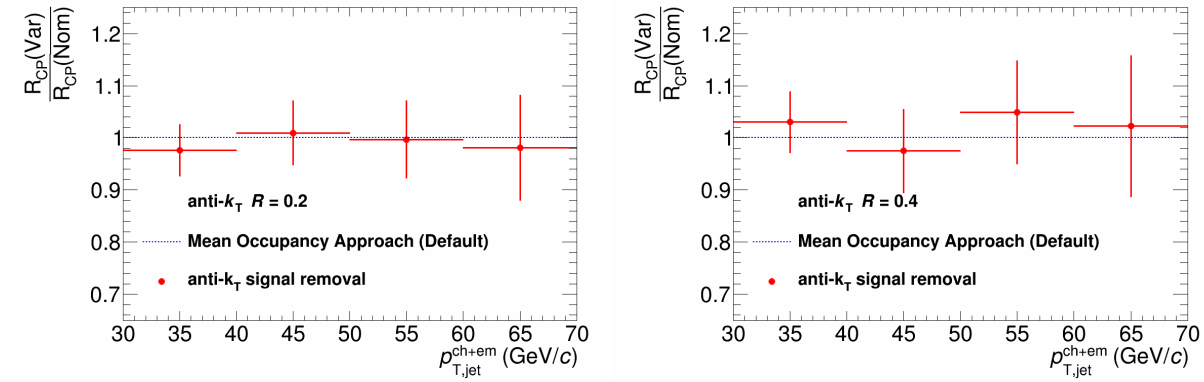

Figure G.10: Relative systematic uncertainty due to different UE subtraction methods. Left: $R = 0.2$. Right: $R = 0.4$

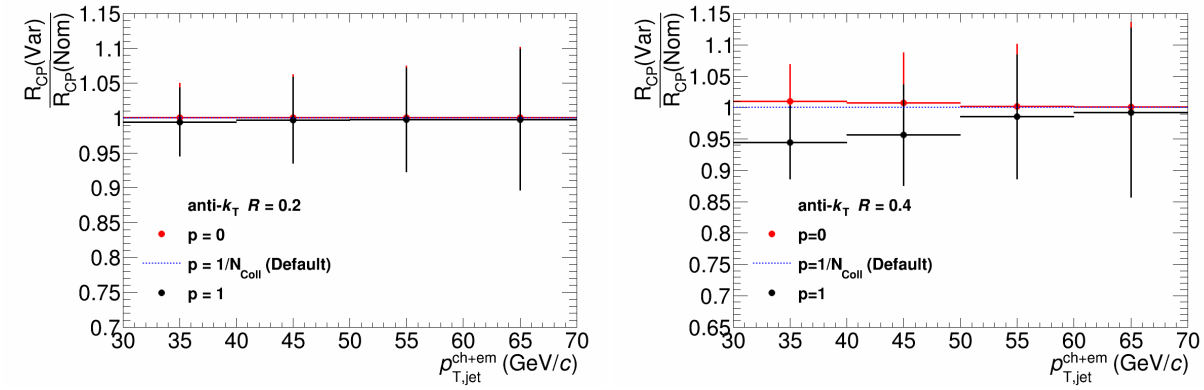

Figure G.11: Relative systematic uncertainty due to different δp_T definitions. See section 4.6 for definitions of the p values. Left: $R = 0.2$. Right: $R = 0.4$

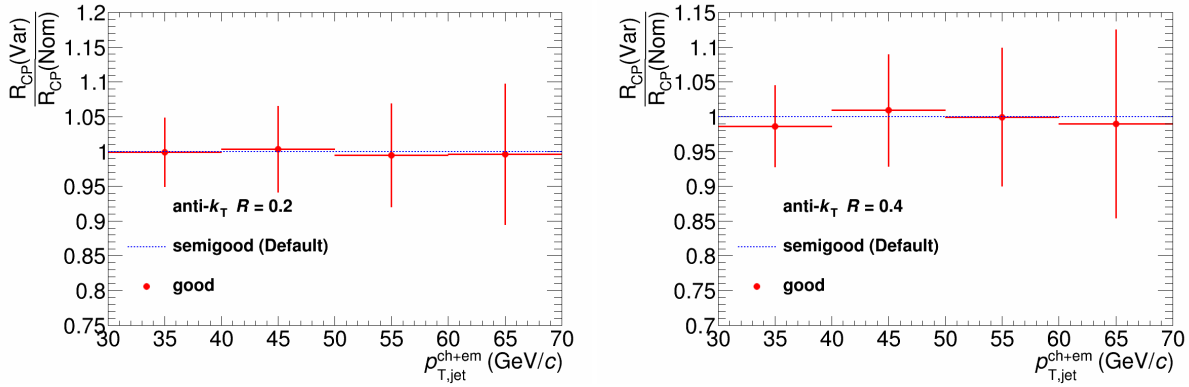

Figure G.12: Relative systematic uncertainty due to different unfolding response matricies used for detector conditions. Left: $R = 0.2$. Right: $R = 0.4$

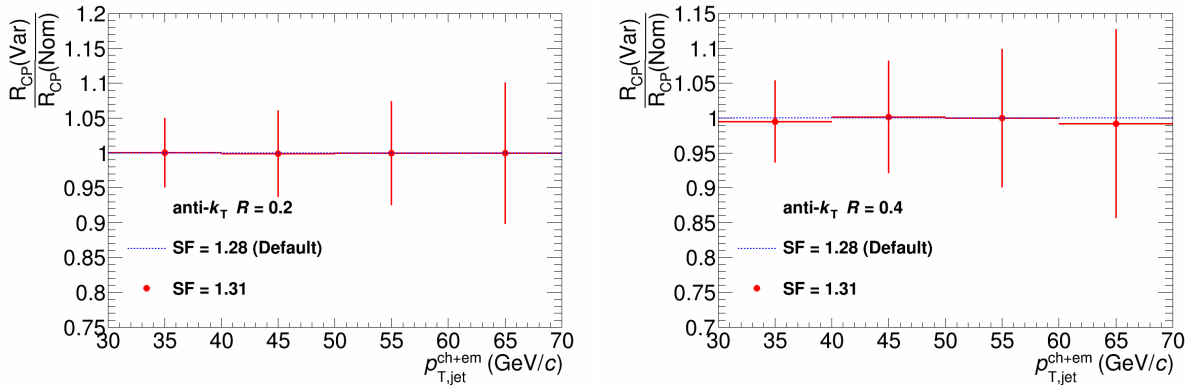

Figure G.13: Relative systematic uncertainty due to different scale factors. Left: $R = 0.2$. Right: $R = 0.4$

Systematic	$p_{T,jet}^{min}$	$p_{T,jet}^{max}$	**Min**	**Max**	**Mean**
Unfolding Systematics					
Unfolding Method	0.4	0.9	0.2	0.9	0.5
Unfolding Regularization	0.8	1.7	<0.1	1.7	0.3
Unfolding Prior	0.8	0.4	0.4	4.6	1.9
$p_{T,min}^{meas}$	1.7	0.1	0.1	1.7	0.7
$p_{T,min}^{unf}$	negligible				
JES Systematics					
Tracking Efficiency	0.1	0.3	0.1	0.3	0.2
Hadronic Correction	3.4	1.7	1.7	3.8	0.7
Underlying Event Subtraction (UE)	2.4	0.3	0.3	2.4	0.6
Background Fluctuations (δp_T)	0.1				
Detector Response	0.1	0.5	0.1	0.5	0.1
Scale Factor	negligible				
Total Systematic	4.6%	2.7%	2.7%	6.0%	4.5%

Table G.1: Summary of systematic uncertainties for anti-k_T R = 0.2 R_{CP} spectrum. The first column is the uncertainty at the minimum $p_{T,jet}^{min}$ = 30 GeV/c, the second column is the uncertainty at the $p_{T,jet}^{max}$ = 70 GeV/c. The minimum and maximum columns gives the extremes over the entire $p_{T,jet}^{ch+em}$ range, and the last column gives the mean systematic uncertainty over the entire $p_{T,jet}^{ch+em}$ range.

Systematic	$p_{T,jet}^{min}$	$p_{T,jet}^{max}$	**Min**	**Max**	**Mean**
Unfolding Systematics					
Unfolding Method	2.5	8.1	2.5	8.1	6.1
Unfolding Regularization	0.7	0.3	0.3	0.8	0.1
Unfolding Prior	2.5	3.2	0.8	3.2	0.5
$p_{T,min}^{meas}$	3.7	1.2	1.2	3.7	0.4
$p_{T,min}^{unf}$	negligible				
JES Systematics					
Tracking Efficiency	<0.1	1.4	<0.1	1.4	0.8
Hadronic Correction	1.0	5.1	1.0	5.1	2.9
Underlying Event Subtraction (UE)	3.0	4.9	2.5	4.9	1.8
Background Fluctuations (δp_T)	1.0	0.2	0.2	1.0	0.7
Detector Response	1.4	<0.1	<0.1	1.4	0.2
Scale Factor	0.5	<0.1	<0.1	0.5	0.1
Total Systematic	6.3%	11.4%	6.3%	11.4%	9.1%

Table G.2: Summary of systematic uncertainties for anti-k_T R = 0.4 R_{CP} spectrum. The first column is the uncertainty at the minimum $p_{T,jet}^{min}$ = 30 GeV/c, the second column is the uncertainty at the $p_{T,jet}^{max}$ = 70 GeV/c. The minimum and maximum columns gives the extremes over the entire $p_{T,jet}^{ch+em}$ range, and the last column gives the mean systematic uncertainty over the entire $p_{T,jet}^{ch+em}$ range.

BIBLIOGRAPHY

[1] Radboud University Nijmegen Theoretical High Energy Physics http://www.ru.nl/thef/research/vmresearch/standard_model/

[2] D. Griffiths *Introduction to Elementary Particles*. John Wiley & Sons. 1987. pg 280.

[3] K. Johnson et al, "The M.I.T. Bag Model", ACTA Physica Polonica B6, 865 (1975)

[4] PhysLink.com, http://www.physlink.com/news/101004NobelPrize.cfm

[5] J. Dirk Walecka, *Theoretical Nuclear and Subnuclear Physics* (Oxford University Press, New York, 1995)

[6] B. Mohanty, "Exploring the QCD landscape with high-energy nuclear collisions", New J. Phys. 13 (2011) 065031, arXiv: 1102.2495v1

[7] I. Arsene et al (BRAHMS), "Quark Gluon Plasma and Color Glass Condensate at RHIC? The perspective from the BRAHMS experiment.", Nucl. Phys. A757 (2004) 1, arXiv: 0410020v1

[8] J. Adams et al (STAR), "The STAR Collaboration's Critical Assessment of the Evidence from RHIC Collisions", Nucl. Phys. A757 (2005) 102, arXiv: 0501009v3

[9] J. Nagle, et. al., "Quark-Gluon Plasma at RHIC and the LHC: Perfect Fluid too Perfect?", New J.Phys.13:075004,2011, arXiv:1102.0680v1

[10] Physics Highlights from the D Collaboration, http://d0server1.fnal.gov/projects/results/runi/highlights/highlight_document/Highlig

[11] "Dynamics of isolated-photon plus jet production in pp collisions at $\sqrt{s}$ = 7 TeV with the ATLAS detector", Nucl. Phys. B 875 (2013) 483-535, arXiv:1307.6795v1

[12] R.J.Glauber, *Lectures in Theoretical Physics* v.1, ed. W.Brittain and L.G.Dunham. Interscience Publ., N.Y., 1959; R.J.Glauber and G.Matthiae, Nucl. Phys. B21 (1970) 135.

[13] D. d Enterria, "Jet quenching", Landolt-Boernstein, Springer-Verlag, Vol. 1-23A (2010) 99, arXiv: 0902.2011v2

[14] T. Renk, "Through the blackness - high p_T hadrons probing the central region of a 200 GeV Au-Au collisions", Phys. Rev. C74 (2006) 024903, arXiv: 0602045v3

[15] G. Aad et al., "Observation of a Centrality-Dependent Dijet Asymmetry in Lead-Lead Collisions at $\sqrt{s_{NN}}$ = 2.76 TeV with the ATLAS Detector at the LHC." Phys. Rev. Lett. 105, 252303

[16] K. Aamodt et al., "Suppression of Charged Particle Production at Large Transverse Momentum in Central PbPb Collisions at $\sqrt{s_{NN}}$ = 2.76 TeV." Phys. Lett., B696:3039, 2011.

[17] M. Gyulassy, X. Wang, "Multiple Collisions and Induced Gluon Bremsstrahlung in QCD", Nucl.Phys.B420:583-614,1994, arXiv:nucl-th/9306003v1

[18] D. Antonov, H.-J. Pirner, "Jet quenching parameter $\hat{q}$ in the stochastic QCD vacuum with Landau damping", Eur. Phys. J. C55:439-447 (2008), arXiv:0710.1540v2

[19] S. Brodsky, G. Teramond (SLAC), "ADS/CFT and QCD", arXiv: 0702205v1

[20] PHENIX plot summary, `http://www.phenix.bnl.gov/WWW/info/released_plots/`

[21] B. Abelev, et. al., "J/psi suppression at forward rapidity in Pb-Pb collisions at $\sqrt{s_{NN}} = 2.76$ TeV", Phys. Rev. Lett. 109 (2012) 072301, arXiv:1202.1383v2

[22] W. Horowitz, M. Gyulassy, "Quenching and Tomography from RHIC to LHC", arXiv:1107.2136v1

[23] J. Adams et al, "Evidence from d+Au measurements for final-state suppression of high p_T hadrons in Au+Au collisions at RHIC", Phys. Rev. Lett .91:072304 (2003), arXiv: 0306024v3

[24] R. Reed (ALICE), "Full Jet Reconstruction in 2.76 TeV pp and Pb-Pb collisions in the ALICE experiment", J. Phys.: Conf. Ser. (2013) 446 012006

[25] F. Liu, K. Werner, "On QGP Formation in pp Collisions at 7 TeV", arXiv:1106.5909v1

[26] F.D. Aaron, et al, [H1 and ZEUS Collaborations], "A Precision Measurement of the Inclusive ep Scattering Cross Section at HERA", JHEP 1001, 109 (2010).

[27] H. Honkanen, et al, "Modeling nuclear parton distribution functions", arXiv: 1310.5879v2

[28] K. Escola, et. al, "A New Generation of NLO and LO Nuclear Parton Distribution Functions", arXiv: 0902.4154v2

[29] S. Brodsky, H. Lu, "Shadowing and Anti-Shadowing of Nuclear Structure Functions", Phys. Rev. Lett. 64, 1342 (1990)

[30] J. Blaizot et. al., "High energy pA collisions in the color glass condensate approach I. Gluon production and the Cronin effect", arXiv:hep-ph/0402256v1

[31] Brookhaven National Laboratory, "Background on color glass condensate", http://www.bnl.gov/bnlweb/pubaf/pr/2003/colorglasscondensate-background.htm

[32] F. Gelis, "Color Glass Condensate and Glasma", Int. J. Mod. Phys. A28 (2013) 1330001, arXiv: 1211.3327v2

[33] E. Iancu, *QCD in heavy ion collisions*, CERN-2014-003, pp. 197-266, arXiv:1205.0579v1

[34] ATLAS detector and physics performance : Technical Design Report, 1, ATLAS-TDR-14 ; CERN-LHCC-99-014.

[35] ATLAS detector and physics performance : Technical Design Report, 2, ATLAS-TDR-15 ; CERN-LHCC-99-015.

[36] CMS: Technical Design Report, Volume 1, CERN/LHCC 2006-001, CMS TDR 8.1

[37] CMS: Technical Design Report, Volume 2, 2007 J. Phys. G: Nucl. Part. Phys. 34 995, http://http://iopscience.iop.org/0954-3899/34/6/S01

[38] ALICE: Physics Performance Report, Volume I, 2004 J. Phys. G: Nucl. Part. Phys. 30 1517, http://iopscience.iop.org/0954-3899/30/11/001

[39] ALICE: Physics Performance Report, Volume 2, 2006 J. Phys. G: Nucl. Part. Phys. 32 1295, http://iopscience.iop.org/0954-3899/32/10/001

[40] G. Dellacasa, et al., ALICE: Technical design report of the Time Projection Chamber (TPC).

[41] G. Dellacasa, et al., ALICE: Technical design report of the Inner Tracking System (ITS).

[42] P. Cortese, et al., ALICE techinical design report on Forward Detectors: FMD, T0, V0.

[43] M. Gallio, et al., ALICE: Technical design report of the Zero Degree Calorimeter (ZDC)

[44] V. Manko, et al., ALICE technical design report of the Photon Spectrometer (PHOS).

[45] U. Abeysekara, et al., ALICE EMCal Physics Performance Report.

[46] C. Grupen, B. Shwartz, Particle Detectors, www.cambridge.org/9780521840064.

[47] M. Cacciari, G. Salam, "Dispelling the N^3 myth for the k_T jet-finder". *Phys. Lett.*, B641 57-61, 2006

[48] M. Cacciari et al, "FastJet user manual". 2011

[49] M. Verweij. *Analysis Note: Measurement of jet spectra with charged particles in Pb-Pb collisions at* $\sqrt{s_{NN}} = 2.76$ *TeV with the ALICE detector at the LHC*.

[50] R. Reed, S. Aiola. *Analysis Note: Fully Reconstructed Jets in* $\sqrt{s_{NN}} = 2.76$ *TeV Pb-Pb Collisions*.

[51] The CMS Collaboration, "Measurement of the underlying event activity in pp collisions at $\sqrt{s} = 0.9 and 7$ TeV with the novel jet-area/median approach", JHEP 08 (2012) 130, arXiv:1207.2392.

[52] Betty Abelev et al, "Measurement of Event Background Fluctuations for Charged Particle Jet Reconstruction in Pb-Pb collisions at $\sqrt{s_{NN}} = 2.76$ TeV", JHEP, 1203:053, 2012.

[53] ALICE https://twiki.cern.ch/twiki/bin/viewauth/ALICE/PACentStudies

[54] R. Haacke, "Analysis Note: Minimum bias charged jets in pPb collisions at $\sqrt{s_{NN}} = 5.02$ TeV"

[55] R. Ma, P. Jacobs, "Analysis Note: Measurement of the inclusive differential jet cross section for pp collisions at $\sqrt{s_{NN}} = 2.76$ TeV"

[56] T. Sjostrand, S. Mrenna, P. Skands, "PYTHIA 6.4 Physics and Manual", JHEP, 0605:026, 2006, arXiv:hep-ph/0603175v2

[57] S. Agostinelli et al., "Geant4 - A Simulation Toolkit", Nuclear Instruments and Methods A506 (2003) 250-303

[58] G. D'Agostini, "Bayesian Inference in Processing Experimental Data Principals and Basic Applications", arXiv:physics/0304102

[59] A. Hocker, V. Kartvelishvili, "SVD approach to data unfolding", Nucl.Instrum.Meth. A372 469-481

[60] T. Adye, "Unfolding algorithms and tests using `RooUnfold`", arXiv:1105.1160

[61] "Centrality determination of Pb-Pb collisions at $\sqrt{s_{NN}} = 2.76$ TeV with ALICE", Phys. Rev. C 88 (2013) 044909, arXiv:1301.4361v3

[62] "Measurement of inelastic, single and double-diffraction cross sections in proton-proton collisions at the LHC with ALICE", Eur.Phys.J. C73 (2013) 2456, arXiv:1208.4968v1

[63] "Measurement of visible cross sections in proton-lead collisions at $\sqrt{s_{NN}} = 5.02$ TeV in van der Meer scans with the ALICE detector", JINST 9 (2014) 1100, arXiv:1405.1849v3

[64] "Centrality and rapidity dependence of inclusive jet production in $\sqrt{s_{NN}} = 5.02$ TeV protonlead collisions with the ATLAS detector", Nucl. Phys. A931 (2014) 416-421, arXiv:1412.4092v1

[65] "Measurement of inclusive jet nuclear modification factor in pPb collisions at $\sqrt{s_{NN}} = 5.02$ TeV with CMS", CMS (2014), CMS-PAS-HIN-14-001

[66] "Tuning Monte Carlo Generators: The Perugia Tunes", CERN PH-TH, Case 01600, arXiv:1005.3457v5

[67] F. Sikler, "Centrality control of hadron-nucleus interactions by detection of slow nucleons", arXiv:hep-ph/0304065v1

[68] A. Artamonov, et. al, "The ATLAS Forward Calorimeter", (2008) JINST 3 P02010

[69] J. E. Huth et al., "Toward a standardization of jet definitions", FNAL-C-90-249-E, published in the proceedings of the 1990 Summer Study on High Energy Physics, Research Directions for the Decade, Snowmass, Colorado, June 25 July 13, 1990.

[70] G. Salam, "Towards Jetography". *Eur. Phys. J* C67 637-686, 2010, arXiv:0906:1833v2

[71] M. Cacciari et al., "The anti-k_T jet clustering algorithm", JHEP 0804 (2008) 063, arXiv:0802.1189v2

[72] M. Cacciari et al., "The catchment area of jets", JHEP 04 (2008) 005, arXiv:0802.1188

[73] M. Miller, et al.,"Glauber Modeling in High Energy Nuclear Collisions", Rev. Nucl. Part. Sci. 57, 205 (2007), arXiv:nucl-ex/0701025

ABSTRACT

ESTIMATING COLD NUCLEAR MATTER EFFECTS USING JETS IN p-Pb COLLISIONS AT $\sqrt{s_{NN}} = 5.02$ TeV WITH THE ALICE DETECTOR

by

CHRIS YALDO

August 2015

Advisor: Joern Putschke
Major: Physics
Degree: Doctor of Philosophy

In heavy-ion collisions at RHIC and the LHC, a suppression of the nuclear modification factor for jets along with other strongly interacting particles has been observed relative to proton-proton collisions. To unambiguously determine if this suppression is due to the creation of a strongly interacting medium of de-confied partons referred to as the *Quark-Gluon Plasma*, or due to *Cold Nuclear Matter* effects, a "control experiment" is required. Proton-lead collisions serve as this control experiment, because these collisions are expected to be sensitive to cold nuclear matter effects while not producing a QGP at this collision energy ($\sqrt{s_{NN}} = 5.02$ TeV). Presented in this defense are the first measurements of charged + neutral jets in p-Pb collisions using the ALICE detector at the LHC.

Measurements of CNM effects are done via the nuclear modification factor for jets: R_{pPb}, R_{CP}, and the jet structure ratio. Measurements of the jet spectrum along with a detailed and proper discussion of the statistical, systematic, and normalization uncertainties will be presented. Also a comparison of R_{pPb} and R_{CP} measured in this analysis to other measured R_{pPb} and R_{CP} from ATLAS and CMS will be presented.

All the measurements performed in this analysis indicate that no strong cold nuclear matter effects are observed in p-Pb collisions using the ALICE detector at the LHC.

AUTOBIOGRAPHICAL STATEMENT

Name: Christopher G. Yaldo

Education:
B.S. Mathematics, Wayne State University, Detroit, MI, 2005
M.S. Physics, Wayne State University, Detroit, MI, 2012

Born in Marysville, MI on June 6, 1984, Christopher G. Yaldo is the 3^{rd} child of Monir and Helen Yaldo, immigrants from Iraq. Form an early age, Chris showed considerable interest in astronomy and excelled in mathematics. At age 10, do to business opportunities, the family moved to West Bloomfield, MI where Chris was enrolled in the West Bloomfield Public School systems. While in high school, Chris continued to exceled in math and physics, completing advance placement courses and taking courses at Wayne State University in mathematics. Completing his high school diploma in 2003, Chris enrolled in Wayne State University and completed a B.S. in Mathematics in 2005, in only 2 years. Afterwards, Chris began his Masters in Physics in 2006. After 2 years enrolled in the physics program, Chris left the physics program to begin a retail warehouse outlet. After encountering difficulties due to the economic recession, Chris left this industry and continued his masters completing it in 2012. In subsequent 3 years, after several trip to CERN, Chris completed his PhD in 2015.